

**DYNAMIC SUBGRID-SCALE MODELING FOR LARGE-EDDY
SIMULATION OF TURBULENT FLOWS WITH A STABILIZED
FINITE ELEMENT METHOD**

By

Andrés E. Tejada-Martínez

A Thesis Submitted to the Graduate
Faculty of Rensselaer Polytechnic Institute
in Partial Fulfillment of the
Requirements for the Degree of
DOCTOR OF PHILOSOPHY
Major Subject: Applied Mechanics

Approved by the
Examining Committee:

Dr. Kenneth E. Jansen, Thesis Adviser

Dr. Luciano Castillo, Member

Dr. Joseph E. Flaherty, Member

Dr. Mark S. Shephard, Member

Rensselaer Polytechnic Institute
Troy, New York

November 2002
(For graduation December 2002)

**DYNAMIC SUBGRID-SCALE MODELING FOR LARGE-EDDY
SIMULATION OF TURBULENT FLOWS WITH A STABILIZED
FINITE ELEMENT METHOD**

By

Andrés E. Tejada-Martínez

An Abstract of a Thesis Submitted to the Graduate

Faculty of Rensselaer Polytechnic Institute

in Partial Fulfillment of the

Requirements for the Degree of

DOCTOR OF PHILOSOPHY

Major Subject: Applied Mechanics

The original of the complete thesis is on file
in the Rensselaer Polytechnic Institute Library

Examining Committee:

Dr. Kenneth E. Jansen, Thesis Adviser

Dr. Luciano Castillo, Member

Dr. Joseph E. Flaherty, Member

Dr. Mark S. Shephard, Member

Rensselaer Polytechnic Institute
Troy, New York

November 2002
(For graduation December 2002)

© Copyright 2002
by
Andrés E. Tejada-Martínez
All Rights Reserved

CONTENTS

LIST OF TABLES	iv
LIST OF FIGURES	v
ABSTRACT	xiii
1. INTRODUCTION	1
1.1 Turbulence simulation	1
1.1.1 Physical description of turbulence	1
1.1.2 Mathematical description of turbulence	3
1.1.3 Numerical approach to turbulence	6
1.1.3.1 Direct numerical simulation (DNS)	6
1.1.3.2 Reynolds-averaging: Reynolds-averaged Navier-Stokes simulation (RANSS)	7
1.1.3.3 Spatial filtering: Large-eddy simulation (LES)	9
1.2 Turbulence subgrid-scale modeling in LES with stabilized finite element methods	14
1.2.1 Chapter description	16
2. THE MODELED FILTERED NAVIER-STOKES EQUATIONS	19
2.1 The filtered Navier-Stokes equations and the residual (subgrid-scale) stress	20
2.2 Modeling the residual (subgrid-scale) stress	22
2.2.1 The constant coefficient Smagorinsky model	22
2.2.2 The dynamic model	26
2.3 Chapter summary	29
3. DISCRETE TEST FILTERS ON FINITE ELEMENT TOPOLOGIES	31
3.1 The box, Gaussian, and sharp spectral filters	31
3.1.1 Filter widths	35
3.2 Discrete approximations of the box filter	36
3.2.1 Discrete box filters in one-dimension	37
3.2.1.1 Example: Approximations using one-point quadrature	38
3.2.1.2 Example: Approximations using two-point quadrature	39
3.2.2 Discrete box filters in multi-dimension	42

3.2.2.1	Example: Two-dimensional approximations of the box filter	43
3.2.2.2	Example: Three-dimensional approximations of the box filter	44
3.2.3	Filter widths	44
3.3	Continuous piecewise polynomial approximations as filters	47
3.3.1	L_2 -projections as filters	49
3.3.1.1	Example: L_2 -projection onto a linear grid of 9 vertices	50
3.3.2	Interpolations as filters	53
3.3.2.1	Example: Interpolation onto a linear grid of 9 vertices	53
3.4	Chapter summary	55
4.	EFFECT OF TEST FILTER TYPE AND FILTER WIDTH RATIO IN DYNAMIC MODEL LES	57
4.1	An assumption for the filter width ratio	57
4.2	Experiments with decaying isotropic turbulence	59
4.2.1	Initial conditions	60
4.2.2	LES of decaying isotropic turbulence on hexes	62
4.2.3	LES of isotropic turbulence on tets and wedges	65
4.3	Experiments with turbulent channel flow at $Re_\tau = 180$	67
4.3.1	Basic relationships for turbulence statistics	70
4.3.2	LES of turbulent channel flow on hexes	71
4.3.3	Comparison between dynamic model results with finite element-based (3-D) and finite difference-based (2-D) test filters	78
4.4	Chapter summary	86
5.	DYNAMIC FORMULATION OF THE FILTER WIDTH RATIO	87
5.1	Dynamic formulation of the filter width ratio. Part I	90
5.1.1	Numerical results with decaying isotropic turbulence	94
5.1.2	Test filter widths in the DFWR	96
5.2	Dynamic formulation of the filter width ratio. Part II: A parameter-free model	97
5.2.1	Numerical results with decaying isotropic turbulence	103
5.2.2	Numerical results with wall-modeled turbulent channel flow	107
5.3	Chapter summary	111

6. A MODIFIED DYNAMIC MODEL BASED ON SUPG STABILIZATION . . .	112
6.1 Mathematical preliminaries	115
6.1.1 Resolved kinetic energy	115
6.1.2 Weak form – Finite element discretization with the SUPG method	115
6.1.3 Numerical dissipation	118
6.2 A modification to the dynamic model based on SUPG	120
6.2.1 Channel flow at $Re_\tau = 180$	120
6.3 Turbulent channel LES with the SUPG-modified dynamic model	126
6.3.1 Channel flow at $Re_\tau = 180$ with model using filter S1	126
6.3.2 Channel flow at $Re_\tau = 180$ with model using filter W1	129
6.3.3 Channel flow at $Re_\tau = 395$ with model using filter S1	134
6.4 Turbulent channel LES with the SUPG-modified, parameter-free dynamic model	135
6.5 Chapter summary	141
7. DISCUSSION AND CONCLUSION	145
REFERENCES	151

LIST OF TABLES

3.1	Table outlining widths for finite element-based test filters on regularly connected hexes with constant spacing h between grid points in the x -, y -, and z -directions. Q-PT EVALS stands for quadrature point evaluations.	47
3.2	Table outlining widths for finite element-based test filters on regularly connected tets with constant spacing h between grid points in the x -, y -, and z -directions.	48
3.3	Table outlining widths for finite element-based test filters on regularly connected wedges with constant spacing h between grid points in the x -, y -, and z -directions.	48
4.1	Summary of filter width ratios used for simulations on hexes. All test filter widths are based on $G(\mathbf{k}^*) = 0.75$	63
4.2	Summary of filter width ratios used for simulations on tets. All test filter widths are based on $G(\mathbf{k}^*) = 0.85$	66
4.3	Summary of filter width ratios used for simulations on wedges. All test filter widths are based on $G(\mathbf{k}^*) = 0.85$	66
5.1	Limiting values of test filter width ratios $\tilde{\Delta}/\hat{\Delta}$ for filters on hexes.	97
5.2	Limiting values of test filter width ratios $\tilde{\Delta}/\hat{\Delta}$ for filters on tets.	97

LIST OF FIGURES

1.1	One-dimensional sketch of a filter kernel.	10
1.2	Sketch of function $f(x)$ and its filtered component $\bar{f}(x)$	11
1.3	Sketch of the Kolmogorov energy spectrum. $E(k)$ is the energy contained in scales of size inversely proportional to k	13
2.1	Sketch of energy spectrum in terms of resolved scales and in terms of all the scales (resolved plus residual). The energy spectrum based on the resolved scales is able to approximate the energy spectrum of the full scales up to the inertial range.	22
2.2	Sketch of the Kolmogorov energy spectrum. $E(k)$ is the energy contained in scales of size inversely proportional to k	30
3.1	Kernels for commonly used filters. — : box ; ---- : Gaussian; - · - : sharp spectral.	34
3.2	Transfer functions for commonly used filters. — : box ; ---- : Gaussian; - · - : sharp spectral.	34
3.3	Sketch of function evaluations for filter S1 and W1. Each quadrature point is located at the middle of an element (the interval between two vertices). The spacing between vertices is h	38
3.4	Sketch of function evaluations for filter S2 and W2. The spacing between vertices is h . Each quadrature point is located at a distance of αh away from its nearest vertex, where $\alpha = 0.211324865$	40
3.5	Transfer functions for one-dimensional filters. — : filter S1; ---- : filter W1; - · - : filter S2; ····· : filter W2; ○ : filter FD1; + : filter FD2.	41
3.6	Box and witch's hat filter kernels. Length h corresponds to the constant spacing between vertices in Figure 3.3 and Figure 3.4.	42
3.7	Sketch of regularly connected triangular and rectangular grids. Each quadrature point is located at the centroid of its element. Quadrature point locations are symmetric ($\mathbf{x}_i = -\mathbf{x}_{-i}$) about the center vertex.	44
3.8	Transfer functions of finite element-based filters on triangles and quadrilaterals with one-point quadrature approximation (a) Transfer function of filter S1 on triangles. (b) Contours of (a). (c) Transfer function of filter S1 on quadrilaterals. (d) Contours of (c).	45

3.9	Finite element-based transfer function contours defined by $G(\mathbf{k}^*) = 0.75$ on hexahedral elements. (a) Contour for standard filter S1. (b) Contour for wide filter W1. (c) Contour for standard filter S2. (d) Contour for wide filter W2.	45
3.10	Finite element-based transfer function contours defined by $G(\mathbf{k}^*) = 0.85$ on tetrahedral elements. (a) Contour for standard filter S1. (b) Contour for wide filter W1. (c) Contour for standard filter S2. (d) Contour for wide filter W2.	46
3.11	Finite element-based transfer function contours defined by $G(\mathbf{k}^*) = 0.85$ on wedge and tet elements. (a) Contour for standard filter S2 on wedges. (b) Contour for wide filter W2 on wedges. (c) Contour for standard filter S2 on tets. (d) Contour for wide filter W2 on tets.	46
3.12	Sketch of L_2 -projection filter kernel. The points $y = x_i$ are equally spaced.	51
3.13	L_2 -projection filter kernels for different amounts of mass lumping. — : $\theta = 1.0$; ---- : $\theta = 0.75$; - · - : $\theta = 0.5$; : $\theta = 0.25$; ◦ : $\theta = 0.0$.	52
3.14	Sketch showing effect of interpolation. Vertices along the x' - and x -axis are equally spaced.	54
4.1	Effect of the filter width ratio squared (α) on dynamic model results of isotropic turbulence. — : initial condition matching the data at t_{42} . Data at t_{42} (\diamond), and at t_{98} (\square). Simulations with $\alpha = 2$ (—), $\alpha = 3$ (----), $\alpha = 4$ (- · -), and $\alpha = 5$ (.....). The test filter in all the simulations is filter S1 on hexes.	63
4.2	Sets of simulations on hexes comparing dynamic model results with different test filters. (a) Two simulations, one with filter S1, the other with filter W1, and both with $\kappa = 0.680$. (b) Two simulations, one with filter S2, the other with filter W2, and both with $\kappa = 0.680$. (c) Two simulations, one with filter S1, the other with filter W1, and both with $\kappa = 0.544$. (d) Two simulations, one with filter S2, the other with filter W2, and both with $\kappa = 0.544$. In all four plots, — : standard filter S1 or S2; · · · : wide filter W1 or W2.	64
4.3	Sets of simulations on tets comparing dynamic model results with different test filters. (a) Two simulations, one with filter S1, the other with filter W1, and both with $\kappa = 1.0$. (b) Two simulations, one with filter S2, the other with filter W2, and both with $\kappa = 1.0$. (c) Two simulations, one with filter S1, the other with filter W1, and both with $\kappa = 0.588$. (d) Two simulations, one with filter S2, the other with filter W2, and both with $\kappa = 0.588$. In all for plots, — : standard filter S1 or S2; · · · : wide filter W1 or W2.	67
4.4	Sets of simulations on wedges comparing dynamic model results with different test filters. (a) Simulations with $\kappa = 1.0$. (b) Simulations with $\kappa = 0.370$. In both plots, — : standard filter S2; · · · : wide filter W2.	68
4.5	Sketch of domain used for LES of turbulent channel flows	69

4.6	Wall force histories with dynamic model using (a) filter S1 and (b) filter W1. The mean wall force should be approximately 0.435.	74
4.7	Comparison between dynamic model coefficients with filter S1 and filter W1. (a) $\langle(C_s \bar{\Delta})^2\rangle$ with filter S1 (—) and filter W1 (----). (b) $\langle(C_s \bar{\Delta})^2\rangle$ with filter S1 divided by $\langle(C_s \bar{\Delta})^2\rangle$ with filter W1. The straight line in (a) denotes a y^{+3} profile.	74
4.8	Mean streamwise velocity in wall coordinates (scaled by the computed friction velocity) with dynamic model using filter S1 (—) and filter W1 (----). \circ : mean velocity in the DNS in [34].	75
4.9	Mean streamwise velocity in wall coordinates (scaled by the expected friction velocity) with dynamic model using filter S1 (—) and filter W1 (----). \circ : mean velocity in the DNS in [34].	76
4.10	Rms of velocity fluctuations in wall coordinates. Rms of velocities with dynamic model using filter S1 (—) and filter W1 (----); \circ : rms of fluctuations in the DNS in [34].	76
4.11	Reynolds stress component, $\langle u'_1 u'_2 \rangle / u_\tau^2$, with dynamic model using filter S1 (—), and filter W1 (----). \circ : Reynolds stress component in the DNS in [34].	77
4.12	Wall force histories with dynamic model using 2-D and 3-D filtering. Forces with (a) 3-D filter S1, (b) 3-D filter W1, (c) 2-D filter FD1, and (d) wide version of 2-D filter FD1. The mean wall force should be approximately 0.435.	80
4.13	Comparison between dynamic model coefficients with 2-D and 3-D filters. (a) $\langle(C_s \bar{\Delta})^2\rangle$ with 3-D filter S1 (—), 3-D filter W1 (----), 2-D filter FD1 (- · -), and wide version of FD1 (· · ·). (b) $\langle(C_s \bar{\Delta})^2\rangle$ with filter S1 divided by $\langle(C_s \bar{\Delta})^2\rangle$ with filter W1 (—) and $\langle(C_s \bar{\Delta})^2\rangle$ with filter FD1 divided by $\langle(C_s \bar{\Delta})^2\rangle$ with wide version of FD1 (----).	81
4.14	Comparison of L_{ij} tensor in the dynamic model with 2-D and 3-D filters — : L_{ij} with 3-D filter S1; ---- : L_{ij} with 3-D filter W1. - · - : L_{ij} with 2-D filter FD1; · · · : L_{ij} with wide version of FD1. $L_{ij} = L_{ji}$ and $\langle L_{13} \rangle$ and $\langle L_{23} \rangle$ are approximately 0.	82
4.15	Comparison of M_{ij} tensor in the dynamic model with 2-D and 3-D filters — : M_{ij} with 3-D filter S1; ---- : M_{ij} with 3-D filter W1. - · - : M_{ij} with 2-D filter FD1; · · · : M_{ij} with wide version of FD1. $M_{ij} = M_{ji}$ and $\langle M_{13} \rangle$ and $\langle M_{23} \rangle$ are approximately 0.	83
4.16	Rms of velocities in wall coordinates. Rms of velocity fluctuations with dynamic model using filter S1 (—), filter W1 (----), filter FD1 (- · -), and wide version of filter FD1 (· · ·). \circ : rms of fluctuations in the DNS in [34].	84

4.17	Reynolds stress component, $\langle u_1 u_2 \rangle / u_\tau^2$, with dynamic model using filter S1 (—), filter W1 (----), filter FD1 (-·-), and wide version of filter FD1 (···). \circ : component 12 of the stress in the DNS in [34].	85
4.18	Mean streamwise velocity in wall coordinates with dynamic model using filter S1 (—), filter W1 (----), filter FD1 (-·-), and wide version of filter FD1 (···). \circ : mean velocity in the DNS in [34].	85
5.1	Dynamic model simulations on hexes with DFWR. Energy spectra at t_{98} are shown on the left and temporal evolution of the filter width ratios squared are shown on the right. — : DFWR with $(\tilde{\Delta}/\hat{\Delta})^2 = 2.9$ and filters S1 and W1; ---- : DFWR with $(\tilde{\Delta}/\hat{\Delta})^2 = 2.4$ and filters S2 and W2.	95
5.2	Dynamic model simulations on tets with DFWR. Energy spectra at t_{98} are shown on the left and temporal evolution of the filter width ratios squared are shown on the right. — : DFWR with $(\tilde{\Delta}/\hat{\Delta})^2 = 2.9$ and filters S1 and W1; ---- : DFWR with $(\tilde{\Delta}/\hat{\Delta})^2 = 2.6$ and filters S2 and W2.	96
5.3	Dynamic model simulations on wedges with DFWR and $(\tilde{\Delta}/\hat{\Delta})^2 = 2.6$. Energy spectra at t_{98} are shown on the left and temporal evolution of the filter width ratio squared is shown on the right. DFWR uses filters S2 and W2. . .	96
5.4	Ratio between dynamic model coefficients in decaying isotropic turbulence on hexes obtained using standard and wide filters. These results correspond to the simulations in sub-section 4.2.2 of Chapter 4.	100
5.5	Energy of the initial condition at t_{42} and energy at t_{98} after simulations with DFWR1 and DFWR2 on the hexahedral grid. — : initial energy for all simulations; — : DFWR2 with filters S1 and W1; ---- : DFWR2 with S2 and W2; -·- : DFWR1 with S1 and W1; ··· : DFWR1 with S2 and W2; \diamond : data at t_{42} ; \square : data at t_{98}	104
5.6	Temporal evolution of predicted filter width ratios in the simulations on the hexahedral grid. — : DFWR2 with filters S1 and W1; ---- : DFWR2 with S2 and W2; -·- : DFWR1 with S1 and W1; ··· : DFWR1 with S2 and W2. In DFWR1 $\zeta = 1$	104
5.7	Energy of the initial condition at t_{42} and energy at t_{98} after simulations with DFWR1 and DFWR2 on the tetrahedral grid. — : initial energy for all simulations; — : DFWR2 with filters S1 and W1; ---- : DFWR2 with S2 and W2; -·- : DFWR1 with S1 and W1; ··· : DFWR1 with S2 and W2; \diamond : data at t_{42} ; \square : data at t_{98}	105

5.8	Temporal evolution of predicted filter width ratios in the simulations on the tetrahedral grid. — : DFWR2 with filters S1 and W1; ---- : DFWR2 with S2 and W2; - · - : DFWR1 with S1 and W1; · · · : DFWR1 with S2 and W2. In DFWR1 $\zeta = 1$	105
5.9	Energy of the initial condition at t_{42} and energy at t_{98} after simulations with DFWR1 and DFWR2 on the wedge grid. — : initial energy for all simulations; — : DFWR2 with filters S2 and W2; ---- : DFWR1 with S2 and W2.	106
5.10	Temporal evolution of predicted filter width ratios in the simulations on the wedge grid. — : DFWR2 with filters S2 and W2; ---- : DFWR1 with S2 and W2. In DFWR1 $\zeta = 1$	106
5.11	Wall force histories with (a) no model, (b) classical model with standard filter S1, (c) classical model with wide filter W1, (d) DFWR2. The mean wall force should be approximately 0.435.	108
5.12	Mean streamwise velocities in wall coordinates with DFWR2 (—), classical dynamic model with standard filter S1 (----), classical model with wide filter W1 (· · ·), and no model (- · -). \circ : mean velocity in the DNS in [34].	108
5.13	(a), (b) $\langle (C_s \bar{\Delta})^2 \rangle$ in DFWR2 (—), in the classical dynamic model with S1 (----), and in the model with W1 (- · -). In (a), the solid, straight line denotes the theoretical y^{+3} profile. (c) Filter width ratio in DFWR2, $\langle \alpha \zeta \rangle \equiv \langle (C_s^{\hat{\Delta}} / C_s^{\bar{\Delta}})^2 (\hat{\Delta} / \bar{\Delta})^2 \rangle$. In (b), — : clipped DFWR2 coefficient used in simulations; · · · : DFWR2 coefficient showing negative values. . . .	110
6.1	Components of the SUPG tensor τ_{ij}^{SUPG} . — : $c_1 = 16$ (strong SUPG) and strong dynamic model; ---- : $c_1 = 64$ (weak SUPG) and strong model; · · · : $c_1 = 16$ (strong SUPG) and weak model.	121
6.2	(a) SUPG dissipation on the left and (b) dynamic model/SGS dissipation on the right, both in wall units. Solid: $c_1 = 16$ (strong SUPG) and strong model; dashed: $c_1 = 64$ (weak SUPG) and strong model; dotted: $c_1 = 16$ (strong SUPG) and weak model.	122
6.3	Eddy viscosity in wall units. Solid: $c_1 = 16$ and strong model; dashed: $c_1 = 64$ (weak SUPG) and strong model	123
6.4	(a) Force histories with strong model and with varying SUPG. — : $c_1 = 16$ (strong SUPG); ---- : $c_1 = 64$ (weak SUPG). (b) Force history with weak model and with $c_1 = 16$ in the stabilization (strong SUPG). The mean wall force should be approximately 0.435.	123

6.5	(a) Dynamic model coefficient versus y^{+3} . (b) Dynamic model coefficient versus y . For (a) and (b), — : strong model and $c_1 = 16$ (strong SUPG); \cdots : strong model and $c_1 = 64$ (weak SUPG).	124
6.6	Components of the SUPG tensor τ_{ij}^{SUPG} with and without SUPG correction in the dynamic model with filter S1. — : $c_1 = 16$ and SUPG correction; ---- : $c_1 = 64$ and SUPG correction. - · - : $c_1 = 16$ and no SUPG correction; \cdots : $c_1 = 64$ and no SUPG correction.	127
6.7	(a) SUPG dissipation on the left and (b) dynamic model/SGS dissipation on the right, both in wall units. Here results are with and without SUPG correction in the dynamic model with filter S1. — : $c_1 = 16$ and SUPG correction; ---- : $c_1 = 64$ and SUPG correction. - · - : $c_1 = 16$ and no SUPG correction; \cdots : $c_1 = 64$ and no SUPG correction.	128
6.8	Eddy viscosity in wall units with and without SUPG correction in the dynamic model with filter S1. — : $c_1 = 16$ and SUPG correction; ---- : $c_1 = 64$ and SUPG correction. - · - : $c_1 = 16$ and no SUPG correction; \cdots : $c_1 = 64$ and no SUPG correction.	128
6.9	(a) Wall forces without SUPG correction on the top and (b) wall forces with SUPG correction on the bottom. In all cases the model was computed with filter S1. — : $c_1 = 16$; dashed: $c_1 = 64$	129
6.10	Components of the SUPG tensor τ_{ij}^{SUPG} with and without SUPG correction in the dynamic model with the filter W1. — : $c_1 = 16$ and SUPG correction; ---- : $c_1 = 64$ and SUPG correction. - · - : $c_1 = 16$ and no SUPG correction; \cdots : $c_1 = 64$ and no SUPG correction.	130
6.11	(a) SUPG dissipation on the left and (b) dynamic model/SGS dissipation on the right, both in wall units. Here results are with and without SUPG correction in the dynamic model with filter W1. — : $c_1 = 16$ and SUPG correction; ---- : $c_1 = 64$ and SUPG correction. - · - : $c_1 = 16$ and no SUPG correction; \cdots : $c_1 = 64$ and no SUPG correction.	131
6.12	Eddy viscosity in wall units with and without SUPG correction in the dynamic model with filter W1. — : $c_1 = 16$ and SUPG correction; ---- : $c_1 = 64$ and SUPG correction. - · - : $c_1 = 16$ and no SUPG correction; \cdots : $c_1 = 64$ and no SUPG correction.	131
6.13	(a) Wall forces without SUPG correction on the top and (b) wall forces with SUPG correction on the bottom. In all cases the model was computed with filter W1. — : $c_1 = 16$; ---- : $c_1 = 64$	132

6.14	Mean streamwise velocity in wall coordinates with dynamic model using filter S1 and SUPG correction(——), filter W1 and SUPG correction (----), filter S1 and no SUPG correction (- · -), and filter W1 and no SUPG correction (· · ·). \circ : mean velocity in the DNS in [34].	133
6.15	Rms of velocity fluctuations in wall coordinates. Rms of velocities with dynamic model using filter S1 and SUPG correction(——), filter W1 and SUPG correction (----), filter S1 and no SUPG correction (- · -), and filter W1 and no SUPG correction (· · ·). \circ : rms of fluctuations in the DNS in [34]. . .	133
6.16	Reynolds stress component $\langle u'_1 u'_2 \rangle$ with dynamic model using using filter S1 and SUPG correction(——), filter W1 and SUPG correction (----), filter S1 and no SUPG correction (- · -), and filter W1 and no SUPG correction (· · ·). \circ : Reynolds stress component in the DNS in [34].	134
6.17	Components of the SUPG tensor τ_{ij}^{SUPG} with and without SUPG correction in the dynamic model with filter S1. — : $c_1 = 16$ and SUPG correction; ---- : $c_1 = 64$ and SUPG correction. - · - : $c_1 = 16$ and no SUPG correction; · · · : $c_1 = 64$ and no SUPG correction.	136
6.18	(a) SUPG dissipation on the left and (b) dynamic model/SGS dissipation on the right, both in wall units. Here results are with and without SUPG correction in the dynamic model with filter S1. — : $c_1 = 16$ and SUPG correction; ---- : $c_1 = 64$ and SUPG correction. - · - : $c_1 = 16$ and no SUPG correction; · · · : $c_1 = 64$ and no SUPG correction.	137
6.19	(a) Wall forces without SUPG correction on the top and (b) wall forces with SUPG correction on the bottom. In all cases the model was computed with filter S1. The expected mean wall force is approximately 0.133. — : $c_1 = 16$; dashed: $c_1 = 64$	137
6.20	Wall force histories with classical dynamic models (CDM) and with DFWR2. Forces with (a) CDM with filter S1 and SUPG correction, (b) CDM with filter W1 and SUPG correction, (c) DFWR2 with no SUPG correction, and (d) DFWR2 with SUPG correction. The mean wall force should be approximately 0.435.	138
6.21	(a), (b) $\langle (C_s \bar{\Delta})^2 \rangle$ in DFWR2 with SUPG correction (——), in CDM with S1 and SUPG correction (----), and in CDM with W1 and SUPG correction (- · -). In (a), the solid, straight line denotes the theoretical y^{+3} profile. (c) Filter width ratio in DFWR2, $\langle \alpha \zeta \rangle \equiv \langle (C_s^{\hat{\Delta}} / C_s^{\bar{\Delta}})^2 (\hat{\Delta} / \bar{\Delta})^2 \rangle$. In (b), — : clipped DFWR2 coefficient used in simulations; · · · : DFWR2 coefficient showing negative values.	139

6.22	(a) SUPG dissipation on the left and (b) dynamic model/SGS dissipation on the right, both in wall units. — : DFWR2 with SUPG correction; ---- : classical dynamic model (CDM) with filter S1 and SUPG correction; - · - : CDM with filter W1 and SUPG correction.	141
6.23	Eddy viscosity in wall units. — : DFWR2 with SUPG correction; ---- : classical dynamic model (CDM) with filter S1 and SUPG correction; - · - : CDM with filter W1 and SUPG correction.	142
6.24	Mean streamwise velocity in wall coordinates with DFWR2 and SUPG correction (—), classical dynamic model (CDM) with filter W1 and SUPG correction (· · ·), and CDM with filter S1 and SUPG correction (----). ○ : mean velocity in the DNS in [34].	142
6.25	Rms of velocity fluctuations in wall coordinates. Rms of velocities with with DFWR2 and SUPG correction (—), classical dynamic model (CDM) with filter W1 and SUPG correction (· · ·), and CDM with filter S1 and SUPG correction (----). ○ : rms of fluctuations in the DNS in [34].	143
6.26	Reynolds stress component $\langle u'_1 u'_2 \rangle$ with DFWR2 and SUPG correction (—), classical dynamic model (CDM) with filter W1 and SUPG correction (· · ·), and CDM with filter S1 and SUPG correction (----). ○ : Reynolds stress component in the DNS in [34].	143

ACKNOWLEDGMENTS

This work was made possible due to the active participation of a number of individuals. Their support has manifested itself in many different ways, ranging from expert advice to moral encouragement:

Professor Kenneth Jansen, adviser in my research pursuits, was the first person to introduce me to the fields of large-eddy simulation and finite element methods for fluid dynamics. His careful guidance and leadership by personal example have helped me overcome the numerous difficulties one encounters in close contact with unknown terrain. For this I am infinitely grateful. Members of Prof. Jansen's research group, former and present provided necessary help and expressed genuine interest in this research topic, especially Jurijs Bazilevs and Sunitha Nagrath, with whom I had many fruitful discussions. Prof. Cesar Mendoza, my adviser during my studies at Columbia University, was the first person to introduce me to fluid mechanics through his research and courses. Andrés Antonio and Maria Teresa, my parents, instilled in me the value of an education as well as the value of hard work, without which this undertaking would not have been successful.

Special thanks to my wife and best friend Judit Yvette, who has shown a tremendous level of understanding and was extremely accommodating at times when it was much needed.

ABSTRACT

This thesis is concerned with large-eddy simulation (LES) of turbulent flows in which the large scales of the flow are resolved numerically, while their interactions with the small scales or subgrid-scales are modeled. The goal is to understand and better model the dynamics of the subgrid-scales. In the simulations considered here, the subgrid-scales are represented by a physical LES model, namely the popular dynamic Smagorinsky model (or simply dynamic model), as well as by a numerical model in the form of the well-known streamline upwind / Petrov-Galerkin (SUPG) stabilization for finite element discretizations of advection-diffusion systems. The latter is not a physical model, as its purpose is to provide sufficient algorithmic dissipation for a stable, consistent, and convergent numerical method.

In the first part of this work, various “finite element-based”, low-pass, spatial test filters, required for computing the dynamic model, are proposed and analyzed. A number of simulations of decaying isotropic turbulence are performed to understand the dependence of the dynamic model on the test filter of choice. From these numerical experiments, key assumptions are extracted leading to the derivation of two new dynamic models in which the sole model parameter is computed dynamically. The second of these models is parameter-free. Traditionally, the dynamic model parameter has been taken as a constant. Both new dynamic models are tested on decaying isotropic turbulence and the parameter-free model is also tested on turbulent channel flow.

In the latter part of this work, the interaction between the physical and numerical models is studied by analyzing energy dissipation associated to these two. Based on this study, a modified dynamic model is proposed, characterized by a coupling between the previously mentioned physical model and the numerical model. The modified dynamic model is shown to be successful in simulations of turbulent channel flow.

The physical models proposed herein provide accounting of the numerical method’s implicit filtering characteristics as well as discounting of the numerical method’s dissipative nature.

CHAPTER 1

INTRODUCTION

1.1 Turbulence simulation

In this first section we introduce the reader to key aspects in turbulence and turbulence simulations of concern in this work.

Turbulence is experienced by us every day. Fluid flows around cars, ships and airplanes can be turbulent. Atmospheric flows, water currents below the ocean's surface and rivers can be characterized as turbulent as well. Many other examples of turbulent flows arise in aeronautics, hydraulics, nuclear and chemical engineering, environmental sciences, oceanography, meteorology, and others. The incompressible Navier-Stokes equations contain a full description of turbulence given that they describe the motion of every Newtonian incompressible fluid based on conservation principles without further assumptions.

Unfortunately, except for very simple flows, there is no analytical solution to these equations. Moreover, the Navier-Stokes equations can exhibit great sensitivity to initial and boundary conditions leading to unpredictable chaotic behavior. Although the fundamental laws behind the Navier-Stokes equations are purely deterministic, these equations, similar to other simpler deterministic equations, can often behave chaotically under certain conditions. A popular example is that of the Lorenz equations, which are known to exhibit a random nature under slight perturbations of initial conditions. More on the Lorenz equations can be found in the books of Gleick [19] and Moon [46]. For laminar flows, analytical or numerical solutions can be directly compared to experimental results. However, due to the randomness in turbulent flows, it is hopeless to track instantaneous behavior. Instead, the goal is to measure this behavior in the temporal or spatial mean.

1.1.1 Physical description of turbulence

There is no widely accepted definition of turbulence, as it is one of the least-known physical processes. A good way to become familiar with the appearance of turbulence is through the "Album of Fluid Motion" by Van Dyke [12], which presents pictures of

a myriad of turbulent flows. Another way is to describe its features as is done in most turbulence books such as those of Pope [53], Hinze [23], and Frisch [13]. Here are some of these characteristic features.

1. Turbulent flows are irregular. This is a very important feature, appearing in almost any definition of turbulence. Because of irregularity, the deterministic approach to turbulence becomes impractical, in that it appears impossible to describe the turbulent motion in all details as a function of space and time. However, it is believed possible to indicate average (in time and/or space) velocity and pressure.
2. Turbulent flows are diffusive. This causes rapid mixing and increased rates of momentum, heat and mass transfer. Turbulent flows should be able to mix passive transported quantities such as temperature, density, etc. much more rapidly than if only molecular diffusion processes were involved. For example, if a passive scalar is being transported by the flow, a certain amount of mixing will occur due to molecular diffusion. In a turbulent flow, a similar mixing occurs, but with a much greater amount than predicted by molecular diffusion. From the practical stand point, diffusivity is very important. The engineer, for instance, is mainly concerned with the knowledge of turbulent heat diffusion coefficients, or the turbulent drag (depending on turbulent momentum diffusion in the flow).
3. Turbulent flows are rotational. For a large class of flows, turbulence arises due to the presence of boundaries or obstacles, which create vorticity inside a flow which was initially irrotational. Turbulence is thus associated to vorticity, and it is impossible to imagine a turbulent irrotational flow.
4. Turbulent flows occur at high Reynolds numbers. The Reynolds number represents the ratio between inertial forces and viscous forces in the flow. Turbulence often arises from instabilities in laminar flows when the Reynolds number becomes high enough. These instabilities are related to the complex interaction of viscous and convective (inertial) influences.
5. Turbulent flows are dissipative. Viscosity affects result in the conversion of kinetic energy of the flow into heat. If there is no external source of energy to make up for

this kinetic energy loss, the turbulent motion will decay.

6. Turbulent flows are characterized by a wide range of scales of motions, unlike in laminar flows in which there are usually a few scales. As per Kolmogorov's theory (see [53]), which has been demonstrated countless of times through experiments as well as computations, energy is transferred from the largest to the smallest scales at which point viscosity acts as a converter of energy into heat. Throughout this work, the term "scales of motion" will be referred to as simply "scales".
7. Turbulent flows are continuum phenomena. Even the smallest scales in a turbulent flow are ordinarily far larger than any molecular length scale.
8. Turbulence is a feature of fluid flows, and not of fluids. If the Reynolds number is high enough, most of the dynamics associated to the smaller scales in the turbulence is the same in all fluids. In short, the main characteristics of turbulent flows are not controlled by the molecular properties of the particular fluid.

Given that the Navier-Stokes equations represent the basis for understanding turbulence and analytical solutions are difficult, we must turn to numerical procedures to help us extract answers. First, let us take a look at the equations that govern turbulent flows.

1.1.2 Mathematical description of turbulence

The non-dimensionalized equations describing any incompressible Newtonian fluid motion including turbulence in a bounded domain Ω are the well-known Navier-Stokes equations:

$$\begin{aligned} \nabla \cdot \mathbf{u} &= 0 \\ \frac{\partial \mathbf{u}}{\partial t} + \nabla \cdot (\mathbf{u} \otimes \mathbf{u}) &= -\nabla p + \nabla \cdot \boldsymbol{\tau}^\nu, \end{aligned} \tag{1.1}$$

where the molecular viscous stress tensor is

$$\boldsymbol{\tau}^\nu = \frac{1}{Re} (\nabla \mathbf{u} + (\nabla \mathbf{u})^T). \tag{1.2}$$

Here, Re is the Reynolds number defined as $Re = UL/\nu$. U and L are characteristic velocity and length scales, respectively, and ν is the kinematic eddy viscosity, defined from the molecular viscosity as $\nu = \mu/\rho$, where ρ is density and μ is molecular viscosity. Variable \mathbf{u} is the velocity vector and variable p is pressure. The symbol \otimes denotes a tensor product, thus $[\mathbf{u} \otimes \mathbf{u}]_{ij} = u_i u_j$. Throughout this work, the velocity vector will be taken as $\mathbf{u} = (u_1, u_2, u_3)$ and the gradient vector as $\nabla = (\partial_{x_1}, \partial_{x_2}, \partial_{x_3})$.

Often, the continuity equation (the first equation in (1.1)), is used to represent the convection (or advection) and viscous terms as

$$\nabla \cdot (\mathbf{u} \otimes \mathbf{u}) = \mathbf{u} \cdot \nabla \mathbf{u} \quad (1.3)$$

and

$$\nabla \cdot \boldsymbol{\tau}^\nu = \frac{1}{Re} \Delta \mathbf{u}, \quad (1.4)$$

respectively, where Δ is the Laplacian defined as $\Delta = (\partial_{x_1}^2 + \partial_{x_2}^2 + \partial_{x_3}^2)$. In the present work, the simplification in (1.4) will never be made. If the simplification in (1.3) is made, the equations will be referred to as being in advective form. If the simplification in (1.3) is not made, then the equations will be referred to being in conservation form. Differences in the two forms as they relate to the numerical method used in this work will be discussed at a later point.

The Navier-Stokes equations in (1.1) must be supplemented by boundary and initial conditions. Moreover, given that pressure only appears in the form of its gradient, the incompressible Navier-Stokes equations can only determine pressure up to a constant. To ensure the uniqueness of pressure we impose

$$\int_{\Omega} p(\mathbf{x}, t) d\mathbf{x} = 0, \quad (1.5)$$

which is the equivalent of imposing a zero spatial mean for all times. Uniqueness of pressure also can be ensured by setting pressure weakly at a boundary. As mentioned before, the Navier-Stokes equations are derived directly from conservation principles. The first equation in (1.1) represents conservation of mass, and the second equation in (1.1) repre-

sents conservation of momentum. Thus, these equations do not represent a model. Furthermore, every incompressible Newtonian flow, be it laminar or turbulent, must satisfy the Navier-Stokes equations.

In the mathematical setting of the Navier-Stokes equations, the only control parameter is the Reynolds number (Re), which makes the difference between laminar and turbulent flows; laminar flows occur at low Reynolds numbers, whereas turbulent flows occur at high Reynolds numbers. Thus, since all turbulent flows satisfy the Navier-Stokes equations, it seems natural to use a mathematical approach in trying to understand turbulence.

However, the present state of the mathematical theory of the Navier-Stokes equations is not encouraging. Except for very simple settings like Couette flow or Poiseuille flow, we do not have an analytical solution. In this respect, the following 1949 quote of John von Neumann, as it appears in [13], is very appropriate:

The entire experience with the subject indicates that the purely analytical approach is beset with difficulties, which at this moment are still prohibitive. The reason for this is probably as was indicated above: That our intuitive relationship to the subject is still too loose - not having succeeded at anything like deep mathematical penetration in any part of the subject, we are still quite disoriented as to the relevant factors, and as to the proper analytical machinery to be used.

Under these conditions there might be some hope to “break the deadlock” by extensive, well-planned, computational efforts. It must be admitted that the problems in question are too vast to be solved by a direct computations attack, that is, by an outright calculation of a representative family of special cases. There are, however, strong indications that one could name certain strategic points on this complex, where relevant information must be obtained by direct calculations. If this is properly done, and then the operation is repeated on the basis of broader information then becoming available, etc., there is a reasonable chance of effecting real penetrations in this complex of problems and gradually developing a useful, intuitive relationship to it.

Given that the Navier-Stokes equations represent the basis for understanding turbulence and analytical solutions are difficult, we must turn to numerical procedures to help

us extract answers.

1.1.3 Numerical approach to turbulence

As we have seen from the previous two sections, both approaches (mathematical and physical) are pretty far from giving a complete answer to the understanding of turbulence. However, mainly due to efforts in the engineering and geophysics communities, the numerical simulation of turbulent flows emerged as an essential approach in tackling turbulence. Even though the numerical approach has undeniable accomplishments, it is by no means an easy and straightforward one.

1.1.3.1 Direct numerical simulation (DNS)

The most natural approach to turbulence is direct numerical simulation (DNS), in which all the scales of motion are simulated or resolved by the numerical method solely using the Navier-Stokes equations. As discussed earlier, the range of scales of motions in a turbulent flow grows with the Reynolds number. More specifically, small scales exist down to $O(Re^{-3/4})$, as per Kolmogorov's theory discussed in any introductory turbulence text such as [53]. Thus, in order to capture all of the scales on a grid, a grid size of $h \approx Re^{-3/4}$ is required, translating to a grid of approximately $Re^{9/4}$ vertices. To give the reader an idea of the large numbers of vertices required in a DNS, below are some typical Reynolds numbers encountered in turbulent flows of interest.

- Flow around a model airplane with characteristic length and velocity scales of 1 m and 1 m/s, respectively:

$$Re \approx 7 \cdot 10^4.$$

- Flow around cars with characteristic velocity of 3 m/s:

$$Re \approx 6 \cdot 10^5.$$

- Flow around airplanes with characteristic velocity of 30 m/s:

$$Re \approx 2 \cdot 10^7.$$

- Atmospheric flows:

$$Re \approx 2 \cdot 10^7.$$

Other examples can be found in [23]. Thus, for $Re \approx 10^6$, a reasonable number for many flows of practical interest, the number of vertices would be about $10^{13.5}$. Present computational resources make such calculations impractical.

Even though DNS is unsuited for most simulations of interest, in some cases it can be a useful tool to validate turbulence models. For example Kim *et al.* in [34] present a DNS of channel flow, and Le *et al.* in [37] present a DNS of flow over a backward-facing step. Both of these studies were conducted to gain new insight into the physical mechanisms involved in turbulent flow. The results in [34] and others will be used to validate the new models to be proposed in this work.

Because the DNS approach, based solely on the Navier-Stokes equations, is not suitable for most turbulent flows, early scientists had to find different approaches. If a full description of all of the scales in a turbulent flow is not possible, perhaps it is possible to derive equations which govern the large scales, while the affect of the smaller scales on the large ones is modeled. The first of such approaches is that of the Reynolds-averaged Navier-Stokes equations.

1.1.3.2 Reynolds-averaging: Reynolds-averaged Navier-Stokes simulation (RANSS)

As was pointed out earlier, irregularity is one of the most important features in turbulent flows. Even though it seems impossible to describe the turbulent motion in all details as a function of time and space coordinates, it appears possible to indicate average values of the flow variables (velocity and pressure). As is pointed out in [23], mere observation of turbulent flows and time histories of turbulent quantities show that these averages exist because of the following reasons:

1. At a given point in the turbulent flow domain a distinct pattern is repeated more or less regularly in time.
2. At a given instant a distinct pattern is repeated more or less irregularly in space; so turbulence, broadly speaking, has the same over-all structure throughout the domain considered.

Furthermore, although general assumptions regarding the behavior of the smallest scales lead to turbulence models, details of the motion at this level are not of interest for most

applications in engineering and geophysics. Motivated by the latter, Osborne Reynolds developed a statistical approach in 1895 and derived the famous equations that bear his name to describe the dynamics of the mean or average flow, otherwise the largest of the scales. Formally, the Reynolds equations are obtained from the Navier-Stokes equations in (1.1) by decomposing the velocity \mathbf{u} and the pressure p into mean (average) and fluctuation components as

$$\mathbf{u} = \langle \mathbf{u} \rangle + \mathbf{u}' \quad p = \langle p \rangle + p', \quad (1.6)$$

where the fluctuations reflect the turbulent intensities of the variables. There are essentially two ways to define the mean components $\langle \mathbf{u} \rangle$ and $\langle p \rangle$. These are ensemble averaging and time averaging:

1. **Ensemble Averaging:** This is done by performing many physical experiments on the same problem, measuring the velocity and pressure at every time and at every point in the domain, and then averaging over this set of experimental data. Ensemble averaging can be done via multiple realizations of a physical experiment or via multiple computational simulations with white noise introduced into the problem data such as boundary and initial conditions.
2. **Time Averaging:** This was Reynolds' original approach, who defined the mean flow variables as

$$\langle \mathbf{u} \rangle(\mathbf{x}, t) = \frac{1}{T} \int_t^{t+T} \mathbf{u}(\lambda, \mathbf{x}) d\lambda \quad \text{and} \quad \langle p \rangle(\mathbf{x}, t) = \frac{1}{T} \int_t^{t+T} p(\lambda, \mathbf{x}) d\lambda. \quad (1.7)$$

The time scale T has to be sufficiently long that choosing a larger time scale would produce the same mean components. At the same time, T should be short enough relative to temporal variations in the mean not associated with turbulence as vortex shedding. For statistically stationary turbulence, the means are time independent thus they can be defined as

$$\langle \mathbf{u} \rangle(\mathbf{x}) = \frac{1}{T} \int_t^{t+T} \mathbf{u}(\mathbf{x}, t) dt \quad \text{and} \quad \langle p \rangle(\mathbf{x}) = \frac{1}{T} \int_t^{t+T} p(\mathbf{x}, t) dt. \quad (1.8)$$

In the limit as $T \rightarrow \infty$ the following properties hold for the means and fluctuations of \mathbf{u} and p :

$$\langle\langle \mathbf{u} \rangle\rangle = \langle \mathbf{u} \rangle, \quad \langle\langle p \rangle\rangle = \langle p \rangle, \quad \langle \mathbf{u}' \rangle = \mathbf{0} \quad \text{and} \quad \langle p' \rangle = 0. \quad (1.9)$$

The previous conditions are often imposed when approximating a sufficiently large T .

Substitution of the decomposition in (1.6) into the Navier-Stokes equations leads to the well-known Reynolds-averaged Navier-Stokes equations. These are of the same form as the original ones, except that they describe the behavior of $(\langle \mathbf{u} \rangle, \langle p \rangle)$ instead of (\mathbf{u}, p) . Furthermore, in addition to the mean viscous stress in terms of the gradient of $\langle \mathbf{u} \rangle$, the Reynolds-averaged Navier-Stokes equations also possess a second stress, namely the Reynolds stress, representing the influence of the fluctuating components upon the mean flow components $(\langle \mathbf{u} \rangle, \langle p \rangle)$. The entries of the Reynolds stress tensor are

$$\tau_{ij} = \langle u_i u_j \rangle - \langle u_i \rangle \langle u_j \rangle. \quad (1.10)$$

As can be seen in (1.10), the Reynolds stress tensor requires knowledge of \mathbf{u} , an unknown entity since the Reynolds-averaged equations govern $\langle \mathbf{u} \rangle$. Knowledge of \mathbf{u} is required to form $\langle u_i u_j \rangle$ in (1.10). Thus, to get a closed system the Reynolds stress tensor must be modeled in terms of the variables in the Reynolds averaged equations, $(\langle \mathbf{u} \rangle, \langle p \rangle)$. Numerical solution of the Reynolds-averaged Navier-Stokes equations together with a model for the Reynolds stress is what is referred to as Reynolds-averaged Navier-Stokes simulation (RANS). The present work will not focus on the Reynolds-averaged Navier-Stokes equations and its closure problem. Instead, it will focus on an analogous set of equations referred to as the filtered Navier-Stokes equations, introduced in the following subsection.

1.1.3.3 Spatial filtering: Large-eddy simulation (LES)

In the spatial filtering approach to turbulence, a low-pass, local, spatial filter is applied to the Navier-Stokes equations, instead of an ensemble or temporal average. The main idea is similar to that of Reynolds-averaging in which the equations governing the mean components of the flow are derived. The mean components can be thought of as

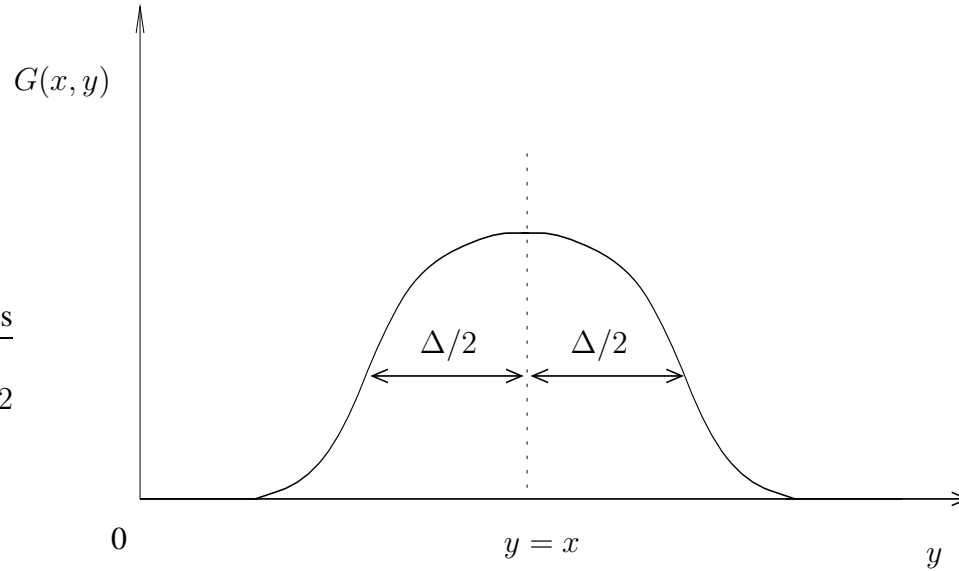


Figure 1.1: One-dimensional sketch of a filter kernel.

the *largest* of the scales in the turbulence. With spatial filtering, the equations governing the *larger* components of the turbulent scales are derived. Spatial filtering decomposes the variables into two components as

$$\mathbf{u} = \bar{\mathbf{u}} + \mathbf{u}' \quad \text{and} \quad p = \bar{p} + p', \quad (1.11)$$

where $\bar{\mathbf{u}}$ and \bar{p} are the resolved (filtered or larger) components and \mathbf{u}' and p' are the residual (subgrid or smaller) components. The reason why the residual components are sometimes referred to as subgrid components will be made clear in later chapters when we discuss the discretization and we let the grid determine $(\bar{\mathbf{u}}, \bar{p})$. The resolved components, originally defined by Leonard in [38], can be written as

$$\bar{\mathbf{u}}(\mathbf{x}, t) = \int_{\Omega} G(\mathbf{x}, \mathbf{y}) \mathbf{u}(\mathbf{y}, t) d\mathbf{y} \quad \text{and} \quad p(\mathbf{x}, t) = \int_{\Omega} G(\mathbf{x}, \mathbf{y}) p(\mathbf{y}, t) d\mathbf{y}, \quad (1.12)$$

where $G(\mathbf{x}, \mathbf{y})$ is usually a symmetric function about $\mathbf{y} = \mathbf{x}$ (as seen in Figure 1.1 whose shape remains constant when moving $\mathbf{y} = \mathbf{x}$). When this is the case, such a function is said to be a homogenous filter kernel, and the operation a homogenous filter. Furthermore, the kernel $G(\mathbf{x}, \mathbf{y})$ is of small compact support, as it decays rapidly in the limit $|\mathbf{y} - \mathbf{x}| \rightarrow \infty$. The effect of filtering can be seen in the sketch shown in Figure 1.2 in which the filtered

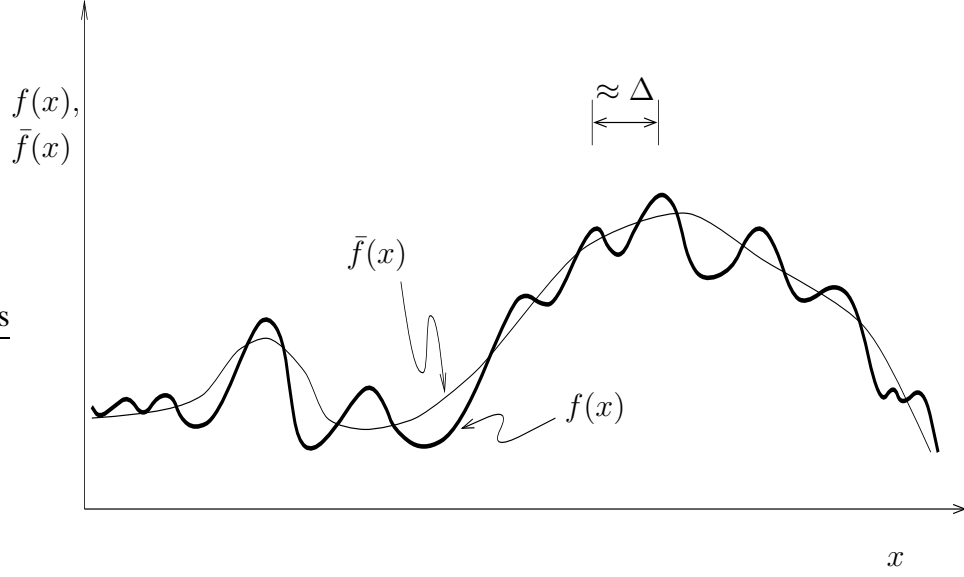


Figure 1.2: Sketch of function $f(x)$ and its filtered component $\bar{f}(x)$.

component of a function and the original function are depicted. The filtering operation serves to damp scales on the order of the filter width denoted as Δ . The width is a certain characteristic length of the filter. In the next chapter we will give details on different filters and how to compute their widths. The filter kernel $G(\mathbf{x}, \mathbf{y})$ is scaled such that if the function to be filtered is a constant, the resulting filtered function is that same constant. Note that in general,

$$\bar{\bar{\mathbf{u}}} \neq \bar{\mathbf{u}}, \quad \bar{\bar{p}} \neq \bar{p}, \quad \overline{\mathbf{u}'} \neq \mathbf{0}, \quad \text{and} \quad \overline{p'} \neq 0, \quad (1.13)$$

even if the flow is statistically stationary.

Filtering the Navier-Stokes equations leads to the governing equations for the resolved components $(\bar{\mathbf{u}}, \bar{p})$. These are of the same form as the original Navier-Stokes equations except that they are in terms of $(\bar{\mathbf{u}}, \bar{p})$. Furthermore, in addition to the filtered viscous stress term in terms of $\bar{\mathbf{u}}$, the filtered Navier-Stokes equations possess a second stress, namely the residual stress, representing the influence of the small (residual) components upon the resolved (large) ones. The entries of the residual (subgrid-scale (SGS)) stress

tensor are

$$\tau_{ij} = \overline{u_i u_j} - \bar{u}_i \bar{u}_j. \quad (1.14)$$

As can be seen in (1.14), the SGS stress tensor requires knowledge of \mathbf{u} , an unknown variable since the filtered Navier-Stokes equations govern $\bar{\mathbf{u}}$. Knowledge of \mathbf{u} is required to form $\overline{u_i u_j}$ in (1.14). Thus, to get a closed system, the SGS stress tensor must be modeled in terms of the variables in the filters equations, $(\bar{\mathbf{u}}, \bar{p})$. A presentation of specific SGS stress models will be delayed until the next chapter. Numerical solution of the filtered Navier-Stokes equations together with a model for the residual (SGS) stress (in other words, the LES equations) is what is referred to large-eddy simulation.

LES is a compromise between DNS and RANSS. In LES, the computational grid is sufficiently fine to resolve some of the turbulent structures, unlike in RANSS, but not fine enough to resolve the energy-dissipating motions, like in DNS. In LES, the motions and interactions of large eddies are computed directly, while the effects of the the small eddies on the large eddies are modeled. This approach is motivated by one of the most important features of turbulent flows, irregularity. Indeed, homogenous, isotropic turbulence (when sufficiently far away from the walls) is believed to have a random nature. This belief is consistent with experiments. The fact that it is random suggests that it has a universal character and the effects of the smaller scales should be capable of being represented by a model and thus predictable. On the other hand, the larger eddies in a turbulent flow are widely believed to be deterministic, hence predictable once the effects of the smaller eddies on them is known. Furthermore, these larger eddies are often the most important flow structures and carry the most energy. These notions provide the foundation for LES: to model the mean effects of the small scales on the larger ones using the universal features of the former, and then numerically simulate the motion of the latter.

The main objective in modeling the effects of the smaller scales on the larger scales is to provide proper energy dissipation. As discussed earlier and first proposed by Kolmogorov (see [52]), the role of the smallest of the scales is to receive energy transferred from the larger-scales and dissipate it in the form of heat, due to viscosity effects. The energy dissipating small scales are not present in the filtered equations, thus without a model to account for dissipation associated to this small scales, the filtered equations would give

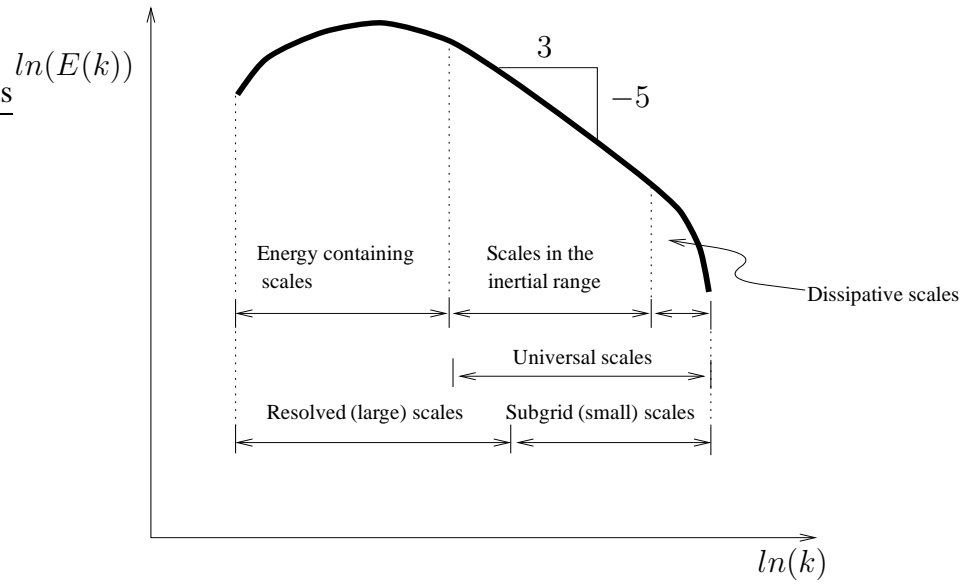


Figure 1.3: Sketch of the Kolmogorov energy spectrum. $E(k)$ is the energy contained in scales of size inversely proportional to k .

rise to an accumulation of energy in the smallest resolved scales.

Modeling the dissipative mechanism of the smallest scales is based on their universality as well as the universality of the mid-range small scales. This mid-range is often referred to as the inertial range. A sketch of the so-called Kolmogorov energy spectrum, depicting the universality of the scales in the inertial range in terms of the energy contained in them is seen in Figure 1.3. The sole purpose of the scales in the inertial range is to transfer energy from the energy containing scales down to the dissipative (smallest) scales. Most turbulent flows possess an inertial range where the energy contained in the scales in this range decreases as the size of the scales decreases following a $-5/3$ power law behavior. This was originally hypothesized by Kolmogorov and proved experimentally a number of times. For example, see Reference [61]. The size of the inertial range increases with increasing Reynolds number. The sketch in Figure 1.3 also provides the reader an idea of the nominal range of the resolved (large) scales and the modeled subgrid (small) scales in an LES. Ideally, the smallest of the resolved scales should fall within the inertial range as dictated by one of the modeling assumptions to be discussed in Chapter 2.

Not necessarily in order of importance, it is the opinion of the author that the fundamental issues in LES are:

1. **Numerical algorithms.** By their very nature, turbulent flows are strongly unstable and often dominated by strong advection. Advancing the understanding of turbulence requires specialized algorithms requiring artificial (numerical) dissipation due to their unstable nature in the presence of advection-dominated flows.
2. **Modeling the SGS stress tensor** representing the interaction between the small (sub-grid) scales and the large (resolved) ones. The model should be faithful to the physics of the turbulent flow, as it provides dissipation due to the missing smallest dissipative scales. Traditionally, modelers have adhered to this condition. In this work, we adhere to the condition that the model should also be robust enough to adjust properly in the presence of numerical dissipation.
3. **Proper boundary conditions.** Since spatial filtering is not a pointwise operation (as it involves integration), special care has to be taken to imposing boundary conditions on the resolved variables. New approaches consistent with the physics of the flow are presented in [15]. Alternatively, a new approach to LES in which filtering is not required, and thus by-passing the issue of boundary conditions, is proposed in [27]. In this work, we will assume the same boundary conditions on the resolved velocity $\bar{\mathbf{u}}$ as those of the entire field \mathbf{u} . However, future research should consider proper boundary conditions in conjunction with models to be proposed.
4. **Mathematical foundations.** Even though LES has greatly evolved in the engineering and geophysical communities, its mathematical foundations are yet to be set. This is a stringent challenge and some research in this area has been done in references [15] and [14].

This thesis is concerned with issues 1) and 2) which are further introduced in the next section.

1.2 Turbulence subgrid-scale modeling in LES with stabilized finite element methods

Over the last two decades, stabilized finite element methods for fluid dynamics have grown in popularity. Led by the streamline upwind / Petrov-Galerkin (SUPG) method of

Brooks and Hughes in [5] through the work of Hughes *et al.* in [26] on the Galerkin / least squares (GLS) method, and the streamline diffusion method (related to the SUPG method) of Hansbo and Szepessy in [21], a number of stabilized formulations have been proposed. Jansen in [31] has pioneered applications of stabilized finite elements to LES of turbulent flows using the SUPG method. Prior to [31], LES had only been explored by the finite-difference and spectral methods communities. Given that applications of stabilized finite elements to LES are recent, no one has ventured into a detailed study of dynamic subgrid-scale LES modeling (herein referred to as physical modeling) with stabilized methods. Furthermore, the recent uncovering of stabilized methods as numerical subgrid-scale models (herein referred to as numerical models) in [3], [28], and [8] among others, has driven the need to understand the interplay between physical and numerical modeling.

It is important to stress the difference between a physical and a numerical subgrid-scale model. The physical model is derived based on the physics describing the turbulence of the missing subgrid-scales in an LES. The numerical model is derived based purely on the mathematics of splitting the space of scales into resolved scales and subgrid-scales. This splitting occurs in all discretizations of any (laminar or turbulent) flow, without regard for the possibility of existing turbulent subgrid-scales. The numerical model attempts to describe the subgrid-scales from the point of view that in all discretizations there will always be resolved scales and subgrid-scales. In fact, the discretization can be thought of as an implicit filter given that it will always split the scales into two: 1) those that are resolved by the discretization and 2) those that are not. More on the discretization's implicit filtering characteristic, specifically as to how it relates to the filtered Navier-Stokes equations, will be discussed in subsequent chapters.

It is the goal of this thesis to understand and better model the dynamics of the subgrid-scales. Here the subgrid-scales will be represented by a physical model, namely the popular dynamic Smagorinsky model (or simply dynamic model) in [18] and [40], as well as by a numerical model in the form of the SUPG method referenced earlier. The former provides dissipation based on physical modeling assumptions related to the universality of the subgrid-scales, and the latter provides sufficient algorithmic dissipation for a stable, consistent, convergent numerical method in the presence of advection-dominated flows, such as turbulent flows.

The dynamic model requires application of a low-pass, homogenous, spatial test filter for its computation. After a thorough understanding of the effect of several proposed spatial filters (suitable for finite element discretizations) on the dynamic model, two new dynamic models will be derived and tested. These new physical models are distinguished by a dynamic computation of their sole parameter. Traditionally, the dynamic model parameter has been taken as a constant. Here, we view its dynamic computation as a way for the physical (dynamic) model to account for the numerical method's implicit filtering behavior.

In the latter part of this work we investigate the roles of physical and numerical subgrid-scale modeling directly. Here we study the interaction between the physical and numerical models by analyzing energy dissipation associated to the two. Based on this study, a modification to the dynamic model is made as a way to discount the numerical method's algorithmic dissipation from the total subgrid-scale dissipation.

The different forms of physical subgrid-scale modeling presented in this work are based on the tenet that the models should be robust enough to adapt to changes in the way they are computed or to changes in the numerical subgrid-scale model. This tenet is reflected through the following statement: Up to some degree determined by the modeler, LES results should be independent of

1. a change in the physical (dynamic) model brought about by changing the spatial filter required in the dynamic model, and
2. a change in the numerical model brought about by the tuning of SUPG parameters so as to provide sufficient stabilization.

1.2.1 Chapter description

The work will be presented as follows. Chapter 2 will provide the reader with the preliminaries of the filtered Navier-Stokes equations as a well as an introduction to the Smagorinsky model and its variations, especially the dynamic model. Assumptions made in deriving the dynamic model will be detailed with special emphasis on the assumption of scale-invariance based on the universality principle describing the subgrid-scales. Furthermore, key problematic aspects of the dynamic model will be identified which will be addressed throughout the thesis.

In Chapter 3, several discrete, “finite element-based” test filters required in dynamic model computations and suited for finite element discretizations are proposed and characterized by their widths. Knowledge of the test filter width is required for setting the dynamic model parameter. Two of the “finite element-based” filters, suited for finite element discretizations with tri-linear basis functions, will prove to be the workhorse behind the different dynamic models derived in this thesis. The rest of the filters discussed in Chapter 3 will be identified for potential use in LES with finite element discretizations employing hierarchic basis functions, such as those in [67], [69], and [68].

In Chapter 4, several of the discrete test filters presented in Chapter 3 will be used in dynamic model LES of decaying isotropic turbulence and turbulent channel flow in an effort to understand the dependence of the model on the filter of choice. In the case of decaying isotropic turbulence, it will be concluded that dynamic model results are independent of the filter type, as long as the width of the filter used in each simulation is consistently computed based on a given definition. In Chapter 5, this result will lead to the derivation of a new dynamic model in which the model parameter involving the width of the test filter is dynamically computed. The new dynamic model will be tested on decaying isotropic turbulence on hexahedral, tetrahedral, and wedge grids. In addition to validating the new dynamic model, these tests will demonstrate that at least for simulations of truly isotropic turbulence which exists far away from boundaries, grid topology is not an issue.

Based on the results of channel flow presented in Chapter 3, it will be concluded that regardless of a consistent calculation of the test filter width of choice, simulations with different test filters can yield different results in near-wall regions. Consequently, assumptions made in the previously discussed new dynamic model fail in near-wall regions. In the second half of Chapter 5, assumptions which fail in near-wall regions are abandoned and a stronger, generalized version of the new dynamic model put forth in the first half of the chapter, will be derived. Decaying isotropic turbulence and turbulent channel flow results will be presented validating this second new model. Just like the first new model, the second new model is also characterized by its dynamic computation of the model parameter. Furthermore, unlike the first new model, the second new model requires no information regarding the width of test filters. Such an attribute renders the second model parameter-free. This attribute is important given that widths of filters on potential com-

plex grids can be cumbersome if not impossible to obtain. Moreover, the parameter-free model is derived without the scale-invariance assumption made in the traditional dynamic model. Thus, the parameter-free model can be considered scale-dependent, a characteristic which will lead us to its comparison with the scale-dependent model of Porté-Agel and collaborators in [54] and [44]. A third attribute of the second model, also enjoyed by the first model, is that by definition of the model parameter, its dynamic computation can be viewed as accounting for the numerical method's implicit filtering characteristic.

Next, Chapter 6 will explicitly consider the interaction between the physical (dynamic) subgrid-scale model and the numerical subgrid-scale model. To that extent, an *ad hoc* definition of the numerical dissipation due to the SUPG method will be proposed. Studies of physical model and numerical model dissipations will lead to a modified dynamic model able to properly adjust to parameter changes in SUPG stabilization controlling the strength of numerical dissipation. The modified dynamic model will be validated on turbulent channel flow.

Finally, conclusions and future research directions will be given in Chapter 7, and the contributions of the present research will be summarized.

CHAPTER 2

THE MODELED FILTERED NAVIER-STOKES EQUATIONS

Developed by the engineering and geophysics communities, LES has emerged as one of the most promising approaches in the numerical simulation of turbulent flows. The steps in LES can be summarized as follows:

1. A homogenous filtering operation is defined to decompose the velocity $\mathbf{u}(\mathbf{x}, t)$ into the sum of a filtered (or resolved) component $\bar{\mathbf{u}}(\mathbf{x}, t)$ and a residual or subgrid-scale (SGS) component $\mathbf{u}'(\mathbf{x}, t)$. The filtered component represents the motions of the large eddies.
2. The evolution equations for the filtered velocity field are derived by filtering the Navier-Stokes equations. These filtered equations are of the same form as the Navier-Stokes equations, with the momentum equation containing an unknown residual stress (subgrid-scale) tensor that arises from the residual motions.
3. Closure is obtained by modeling the residual stress tensor; in our case the dynamic Smagorinsky model is used.
4. The modeled filtered equations are solved numerically for $\bar{\mathbf{u}}(\mathbf{x}, t)$, which provides an approximation to the large-scale motions of the turbulent flow.

In this chapter we will focus on the first two steps as we introduce the filtered Navier-Stokes, the Smagorinsky model, and its dynamic version, the dynamic model. But before proceeding to the next sub-section, we point out that throughout this chapter we will continue to refer to subgrid-scales as residual scales. The term “residual scales” is more appropriate because we have yet to introduce the discretization (given by the SUPG) method. Once we do, then we will use the term “subgrid-scales” instead of “residual-scales”.

2.1 The filtered Navier-Stokes equations and the residual (subgrid-scale) stress

The incompressible Navier-Stokes equations in conservation form written in indicial notation take the following form:

$$\begin{aligned} \frac{\partial u_i}{\partial x_i} &= 0 \\ \frac{\partial u_i}{\partial t} + \frac{\partial u_i u_j}{\partial x_j} &= -\frac{1}{\rho} \frac{\partial p}{\partial x_i} + \frac{\partial \tau_{ij}^\nu}{\partial x_j}, \end{aligned} \quad (2.1)$$

where the viscous stress is

$$\tau_{ij}^\nu = \nu \left(\frac{\partial u_i}{\partial x_j} + \frac{\partial u_j}{\partial x_i} \right). \quad (2.2)$$

Consider application of any **arbitrary** homogenous filter with kernel $G_{\bar{\Delta}}$ and of width $\bar{\Delta}$ (as described in Chapter 1) to the Navier-Stokes equations. Let us take the width $\bar{\Delta}$ such that it falls within the inertial range. Herein this filter will be referred to as the primary filter. Consequently, the filtered Navier-Stokes equations are rendered as:

$$\begin{aligned} \frac{\partial \bar{u}_i}{\partial x_i} &= 0 \\ \frac{\partial \bar{u}_i}{\partial t} + \frac{\partial \bar{u}_i \bar{u}_j}{\partial x_j} &= -\frac{\partial \bar{p}}{\partial x_i} + \frac{\partial \bar{\tau}_{ij}^\nu}{\partial x_j}. \end{aligned} \quad (2.3)$$

As can be seen, the filtering operation commutes with differentiation, which is brought about by the homogeneity of the applied filter. The issue of commutation is treated extensively in Refs. [43], [65], and [66]. Returning to the filtered equations in (2.3), the filtered viscous stress is given in terms of the filtered velocity \bar{u}_i as

$$\bar{\tau}_{ij}^\nu = \nu \left(\frac{\partial \bar{u}_i}{\partial x_j} + \frac{\partial \bar{u}_j}{\partial x_i} \right). \quad (2.4)$$

In the case of compressible flows, the compressible Navier-Stokes equations are filtered using a generalized filtering procedure known as Favre (or density weighted) filtering. The interested reader is encouraged to consult Moin et al in Ref. [45].

The equations in (2.3) differ from the Navier-Stokes equations in terms of filtered

variables because the filtered product $\overline{u_i u_j}$ is different from the product of the filtered velocities $\bar{u}_i \bar{u}_j$. The difference is the residual or subgrid-scale stress tensor defined by

$$\tau_{ij} = \overline{u_i u_j} - \bar{u}_i \bar{u}_j. \quad (2.5)$$

Substituting

$$\overline{u_i u_j} = \tau_{ij} + \bar{u}_i \bar{u}_j \quad (2.6)$$

into the second equation in (2.3), expressing the deviatoric or traceless part of residual stress, τ_{ij}^d , as

$$\tau_{ij}^d = \tau_{ij} - \frac{1}{3} \tau_{kk} \delta_{ij}, \quad (2.7)$$

and adding the trace of the residual stress to the pressure as

$$\bar{P} = \bar{p} + \frac{1}{3} \rho \tau_{kk}, \quad (2.8)$$

the filtered momentum equation in (2.3) can be re-written as

$$\frac{\partial \bar{u}_i}{\partial t} + \frac{\partial \bar{u}_i \bar{u}_j}{\partial x_j} = -\frac{\partial \bar{P}}{\partial x_i} + \frac{\partial (\overline{\tau_{ij}^v} - \tau_{ij}^d)}{\partial x_j}. \quad (2.9)$$

If $\tau_{ij}^d(\mathbf{x}, t)$ is given by a residual (subgrid-scale) stress model, the filtered continuity equation (the first equation in (2.3)) and the filtered momentum equation in (2.9), herein referred to as the filtered Navier-Stokes equations, can be solved numerically to determine $\bar{\mathbf{u}}(\mathbf{x}, t)$ and $\bar{P}(\mathbf{x}, t)$.

The filtered Navier-Stokes equations in terms of $(\bar{\mathbf{u}}, \bar{P})$ are of the same form as the original Navier-Stokes equations in terms of (\mathbf{u}, p) , except for the presence of the residual (subgrid-scale) stress in the right hand side of the momentum equation in (2.9).

A sketch comparing the energy contained in all of the scales of a high-Reynolds number turbulent flow to the energy contained in the resolved scales in an LES of the same flow is made in Figure 2.1. Notice that the energy of the resolved scales can only represent the energy spectrum of all the scales only up to the inertial range. The reason

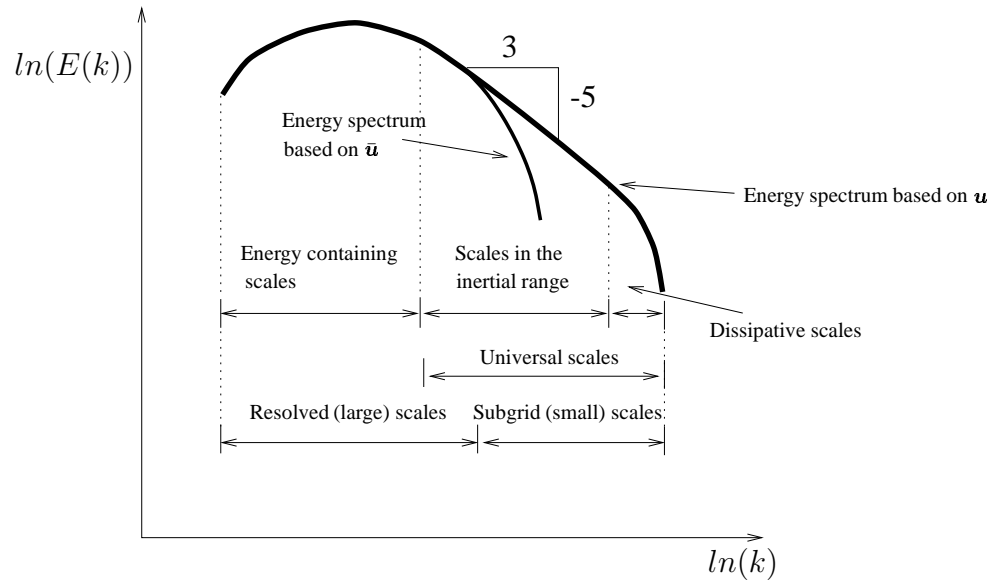


Figure 2.1: Sketch of energy spectrum in terms of resolved scales and in terms of all the scales (resolved plus residual). The energy spectrum based on the resolved scales is able to approximate the energy spectrum of the full scales up to the inertial range.

for this is that by construction, the width of the primary filter used to obtain the filtered Navier-Stokes equations falls within the inertial range. This condition will be used in the next sub-section for the derivation of the Smagorinsky model and its dynamic version, the dynamic model.

2.2 Modeling the residual (subgrid-scale) stress

2.2.1 The constant coefficient Smagorinsky model

The filter applied to the Navier-Stokes equations is meant to remove the small scales of motion. At the smallest of these small scales is where motion is converted to heat via viscous dissipation, thus, the dissipation of motion must be modeled due to the missing smallest scales. By Kolmogorov's first hypothesis (see [53]), the behavior of the absent smallest (or Kolmogorov) scales is universal, and as a result, it should be possible to construct a model applicable to all types of flows. A simple model was proposed by Smagorinsky in [59] to account for the dissipation of motion. Here we review its derivation closely following Ref. [7], as it will prove to be beneficiary in light of the development of new models in later chapters.

Smagorinsky assumed a gradient-diffusion-type model for the deviatoric part of the unknown residual (subgrid-scale) stress in (2.7) by expressing it as

$$\tau_{ij}^d = -2\nu_T \bar{S}_{ij}, \quad (2.10)$$

where

$$\bar{S}_{ij} = \frac{1}{2} \left(\frac{\partial \bar{u}_i}{\partial x_j} + \frac{\partial \bar{u}_j}{\partial x_i} \right) \quad (2.11)$$

is the filtered rate of strain tensor. Note that (2.10) is mathematically consistent from the point of view that the left and right hand sides are both trace-free. The eddy viscosity, ν_T , just like the kinematic viscosity, has dimensions of L^2/T , where L is a length scale and T is a time scale. Given that this is a model for the absent subgrid-scales, and given that these scales are on the order of the width of the primary filter, $\bar{\Delta}$, the only logical choice is to set $L = \bar{\Delta}$. Next, let us assume that scales on the order of $\bar{\Delta}$ fall within the inertial range, as depicted in Figure 2.1. According to Kolmogorov's hypothesis (see [52]), scales within the inertial range serve as middle-ground to transfer energy from the energy containing, possibly energy producing largest scales down to the energy dissipating, viscous scales. Hence, the only important quantity affecting scales in the inertial range is the rate of energy transfer. Based on this and using dimensional analysis, Smagorinsky took the time scale T as that given by a combination of the length scale $\bar{\Delta}$ and by the rate of energy transfer within the inertial range, \mathcal{E} . Thus, he took $T = (\bar{\Delta}^2/\mathcal{E})^{1/3}$ since the rate of energy transfer has dimensions of L^2/T^3 . Recalling the dimensions of eddy viscosity given above, the following expression for the eddy viscosity holds

$$\nu_T = C_k \mathcal{E}^{1/3} \bar{\Delta}^{4/3}, \quad (2.12)$$

where C_k is the non-dimensional Kolmogorov proportionality constant.

Next, Smagorinsky proposed to set the rate of energy transfer within the inertial range approximately equal to the subgrid-scale dissipation defined as $-\tau_{ij}^{(d)} \bar{S}_{ij}$. (This definition of the subgrid-scale dissipation can be obtained from the equation governing the resolved kinetic energy, to be presented in a later chapter.) Hence, the following relations

hold

$$\mathcal{E} \approx -\tau_{ij}^{(d)} \bar{S}_{ij} = \nu_T |\bar{S}|^2, \quad (2.13)$$

where $|\bar{S}|^2 = 2\bar{S}_{ij}\bar{S}_{ij}$ is the square of the norm of the filtered rate of strain tensor. The equality in (2.13) can be seen by inserting (2.10) for $\tau_{ij}^{(d)}$. The relation in (2.13) is a good approximation if it is integrated over the flow domain since nearly all the dissipation will be accounted for by the subgrid-scale model when the primary filter width, $\bar{\Delta}$, falls in the inertial range. However, Smagorinsky invoked a local equilibrium assumption between energy production and dissipation, thereby taking the approximation in (2.13) at every point in the domain. Solving for \mathcal{E} in (2.12) and substituting the resulting expression into (2.13), and then solving for ν_T leads to the Smagorinsky model for the eddy viscosity,

$$\nu_T = (C_s \bar{\Delta})^2 |\bar{S}|, \quad (2.14)$$

and furthermore, the Smagorinsky model for the residual (subgrid-scale) stress,

$$\tau_{ij}^d = -2(C_s \bar{\Delta})^2 |\bar{S}| \bar{S}_{ij}, \quad (2.15)$$

where $C_s = C_k^3$ is the Smagorinsky coefficient.

The Smagorinsky model is valid only if scales of size on the order of the primary filter width, $\bar{\Delta}$, are within the inertial range. As discussed earlier, scales in the inertial range are larger than the dissipative scales, yet smaller than the scales which contain most of the energy.

Furthermore, as discussed in [50], the model is not suitable to represent the possible energy transfers from the missing dissipative, viscous scales to the larger scales, an occurrence known as *backscatter*. The reason for such deficiency is that backscatter occurs on time scales smaller than those represented by the model.

Lastly, and most important of all are the following statements. **Recall that the homogenous primary filter used to obtain the filtered Navier-Stokes equation is arbitrary as long as its width, $\bar{\Delta}$, falls within the inertial range. Specifically, the LES equations, given by the first equation in (2.3) and equation (2.9) together with a model**

such as the Smagorinsky model, are solely in terms of the primary filtered variables (\bar{u}, \bar{P}) and no specific choice for the primary filter is required as long as it is homogeneous and its width falls in the inertial range. Thus, the precise width of the primary filter, which appears as a parameter in the Smagorinsky model, is not defined. The previous statements are crucial in the current work, as most of the efforts here will attempt to resolve the ambiguity set by the arbitrary primary filter width. All of past research with the Smagorinsky model has not focused on the primary filter width, and instead has focused on obtaining an appropriate value of the Smagorinsky coefficient, C_s . A summary of this past research follows. A detailed presentation of the evolution of the Smagorinsky model is given in [1] and [56]. We will just mention the main developments related to the models considered in this thesis.

The Smagorinsky model and its variants have been used with success. Departing from the condition that scales of $O(\bar{\Delta})$ are within the inertial range, Lilly in [39], was able to approximate the norm of the filtered rate of strain tensor, $|\bar{S}|$, and determine that the Smagorinsky coefficient, C_s should vary between 0.17 and 0.21, depending on the numerical approximation for \bar{S}_{ij} . Other investigators were able to approximate C_s based on numerical experiments. In Refs. [36], [57], and [2], numerous LES of decaying isotropic turbulence were performed with the goal of finding C_s by matching computational results with the experimental data of [9]. For several discretizations, C_s was found to be in the range of 0.19 to 0.24.

For LES of high-Reynolds number turbulent channel flow, Deardoff in [10] found that using the value of C_s estimated by Lilly leads to a very strong model causing excessive damping of the turbulence intensities. Deardoff also found that a value of C_s at 0.1 gives better results. In [11], Deardoff performed LES of in-homogeneous flows without mean shear and with buoyancy as the driving force and found C_s at 0.21 to be an appropriate value. From this, he concluded that differences in C_s can be attributed to mean shear, given that in Lilly's estimation the effect of mean shear was not taken into account.

Throughout the late 70s and 80s, a number of variants of the Smagorinsky model were proposed. A good survey of such variants is given in [56]. From these early applications of LES, it became clear that the Smagorinsky coefficient, C_s , needed to be different in different flows, and furthermore, within the flow itself it needed to be different in dif-

ferent flow regions. These requirements led to the dynamic Smagorinsky model (dynamic model) first proposed in 1991 by Germano in [18] and later modified in 1992 by Lilly in [40]. In the next section we describe the dynamic model in detail.

2.2.2 The dynamic model

As previously discussed, one of the problems with the implementation of the Smagorinsky model is that the appropriate value of the coefficient C_s is different in different flow regimes. More precisely, it should be zero in laminar flow, and it should be attenuated near walls compared to its value (0.17–0.24) in high Reynolds number free turbulent flows. To relieve the non-adaptive nature of the constant coefficient model, Germano in [17] developed a procedure for calculating the model coefficient locally. Consider the application of a homogenous secondary or test filter (with kernel $G_{\hat{\Delta}}$ and of width $\hat{\Delta} > \bar{\Delta}$ in the inertial range) to the once-filtered Navier-Stokes equations in (2.3). As expected, the continuity and momentum equations take the following form:

$$\begin{aligned} \frac{\partial \hat{u}_i}{\partial x_i} &= 0 \\ \frac{\partial \hat{u}_i}{\partial t} + \frac{\partial \widehat{u_j u_i}}{\partial x_j} &= -\frac{1}{\rho} \frac{\partial \hat{p}}{\partial x_i} + \frac{\partial \widehat{\tau_{ij}^\nu}}{\partial x_j}. \end{aligned} \quad (2.16)$$

The residual (subtest-scale) stress created by the application of the test filter is expressed as

$$T_{ij} = \widehat{u_i u_j} - \hat{u}_i \hat{u}_j. \quad (2.17)$$

The twice-filtered Navier-Stokes equations in (2.16) were obtained by test-filtering the once-filtered equations in (2.3). However, looking at the twice-filtered equations in (2.16) we notice that these equations could have also been obtained by simply filtering the original (un-filtered) equations in (2.1) with a single homogenous filter of kernel $G_{\hat{\Delta}}$. This filter, of width $\hat{\Delta}$ is precisely the filter resulting from two successive applications of the primary and test filters with kernels $G_{\bar{\Delta}}$ and $G_{\hat{\Delta}}$, respectively. Note that the width of the new filter, $\hat{\Delta}$, is assumed to fall within the inertial range and is larger than the width of the primary filter, $\bar{\Delta}$, and the width the test filter, $\hat{\Delta}$.

Thus, analogous to the Smagorinsky model for the deviatoric portion of the residual (subgrid-scale) stress in (2.10), the Smagorinsky model for the deviatoric portion of the residual (subtest-scale) stress in (2.17) takes shape as

$$T_{ij}^d \equiv T_{ij} - \frac{1}{3}T_{kk}\delta_{ij} = -2(C_s\hat{\Delta})^2|\hat{S}|\hat{S}_{ij}, \quad (2.18)$$

where \hat{S}_{ij} and $|\hat{S}|$ are defined straightforwardly based on $\hat{\mathbf{u}}$. Note that the coefficient C_s in (2.18) is taken exactly as the coefficient in the Smagorinsky model for the subgrid-scale stress in (2.10). This assumption is called the *scale-invariance* assumption and its motivation lies behind the fact that the widths of the primary filter $G_{\bar{\Delta}}$, $\bar{\Delta}$, and the width of the filter with kernel $G_{\hat{\Delta}}$, $\hat{\Delta}$, both fall within the inertial range in which self-similarity arguments are valid. However, this justification holds only if these two filters are self-similar themselves. The self-similarity condition, as described in [6], implies that $G_{\bar{\Delta}}$ and $G_{\hat{\Delta}}$ have identical shapes and may only differ by their widths. We shall return to the scale-invariance assumption later when we derive one of our new models.

Next, an identity due to Germano is obtained by applying the test filter to (2.5) and subtracting the result from (2.17):

$$L_{ij} \equiv T_{ij} - \hat{\tau}_{ij} = \widehat{\bar{u}_i \bar{u}_j} - \hat{u}_i \hat{u}_j. \quad (2.19)$$

The significance of this identity is that L_{ij} (called the resolved stress tensor) is known in terms of $\bar{\mathbf{u}}$, whereas T_{ij} and τ_{ij} are not. Thus, the deviatoric part of L_{ij} can be expressed in terms of the resolved field (as seen in (2.19)) as well as in terms of the modeled stresses. Taking the Smagorinsky coefficient as roughly constant in the neighborhood where the filter kernel is non-zero, the relations in (2.10) and (2.18) lead to

$$L_{ij}^d \equiv T_{ij}^d - \widehat{\tau_{ij}^d} = 2(C_s\bar{\Delta})^2 M_{ij}, \quad (2.20)$$

in terms of the modeled stresses, where L_{ij}^d is the deviatoric portion of L_{ij} ,

$$L_{ij}^d = L_{ij} - \frac{1}{3}L_{kk}\delta_{ij}, \quad (2.21)$$

and

$$M_{ij} = |\widehat{S}| \widehat{S}_{ij} - \left(\frac{\widehat{\Delta}}{\Delta} \right)^2 |\widehat{S}| \widehat{S}_{ij}. \quad (2.22)$$

As originally proposed by Lilly in [40], least squares minimization of the difference between the resolved L_{ij}^d , obtained from (2.19) and (2.21), and the modeled L_{ij}^d in (2.20), leads to the following expression for the coefficient $(C_s \bar{\Delta})^2$:

$$(C_s \bar{\Delta})^2 = \frac{1}{2} \frac{L_{ij}^d M_{ij}}{M_{kl} M_{kl}} = \frac{1}{2} \frac{L_{ij} M_{ij}}{M_{kl} M_{kl}}, \quad (2.23)$$

where the last equality holds due to the symmetry of M_{ij} . Finally, both L_{ij} and M_{ij} (given in (2.19) and (2.22) are known in terms of $\bar{\mathbf{u}}(\mathbf{x}, t)$, thereby completing the expression in (2.10). Recall that the filtered continuity equation, the first equation in (2.3), and the filtered momentum equation in (2.9) together with the Smagorinsky model in (2.10) are the LES equations we solve numerically for the set of variables $(\bar{\mathbf{u}}, \bar{P})$. Now, the coefficient $(C_s \Delta)^2$ in the Smagorinsky model is determined dynamically through (2.23).

In most cases, as will be done in the present work, the denominator and numerator in (2.23) are averaged over homogeneous directions of the flow (ie. directions over which temporal mean quantities of the flow are constant) resulting in a time dependent Smagorinsky coefficient as a function of the directions in which the flow is in-homogeneous. Averaging is an *ad hoc* operation performed as a way to avoid numerical instabilities. These instabilities can occur because in some instances, the fluctuations of M_{ij} between negative and positive values result in a vanishing of the denominator in (2.23). Furthermore, averaging the numerator and denominator in (2.23) reduces the likelihood of negative values of $(C_s \bar{\Delta})^2$. Such negative values would give rise to a parasitic energy transfer due to the fact that the Smagorinsky model is not able to properly describe transfers of energy from small to large scales.

Note that application of the test filter G_{Δ} appears explicitly in the computation of dynamic model components M_{ij} and L_{ij} . This operation is denoted with an over-hat ($\widehat{\cdot}$). To that extent, we will need to consider specific choices for the test filter.

The next statement identifies a key problematic issue of great concern in this work.

In addition to the arbitrary primary filter $G_{\bar{\Delta}}$, as a result of the dynamic model procedure we have gained a second arbitrary filter, denoted as $G_{\hat{\Delta}}$. Although the homogenous test filter appears explicitly (and thus can be chosen to be a certain shape and width), the sequential application of the primary filter and the test filter, resulting in the filter with kernel $G_{\hat{\Delta}}$, is arbitrary due to the arbitrariness of the primary filter. Notice that the ratio between the filter widths of these two filters, $\hat{\Delta}/\bar{\Delta}$, appears as a parameter in the computation of the dynamic model in (2.22). Thus, this model parameter, herein referred to as the filter width ratio, is not well-defined. One of the main contributions of this work will be to derive new models in which this parameter is computed dynamically based on the resolved velocity \bar{u} . Traditionally, the filter width ratio has been taken as simply $\hat{\Delta}/\bar{\Delta}$, where the test filter width $\hat{\Delta}$ is well-defined and $\bar{\Delta}$ is approximated as the local grid size in a discretization.

Despite the arbitrariness of the filter width ratio, the dynamic model is an improvement over the constant coefficient Smagorinsky model, as it computes the coefficient C_s as part of an expression that varies in space and time. As depicted in Figure 2.2 the dynamic procedure essentially extracts spectral information existing between the subgrid-scale level and the subtest-scale level to obtain $(C_s\bar{\Delta})^2$ dynamically. Applications of the dynamic model have shown that $(C_s\bar{\Delta})^2$ nearly vanishes in near-wall and laminar flow regions, a decisive advantage over taking this coefficient as a constant, such as in the original Smagorinsky model.

2.3 Chapter summary

In this chapter we introduced the filtered Navier-Stokes equations modeled with the constant coefficient Smagorinsky model or with the dynamic coefficient Smagorinsky model (dynamic model). Emphasis was placed on key assumptions in the derivation of the dynamic model and its predecessor (the constant coefficient Smagorinsky model) as we will be referring to these assumptions in later chapters.

Furthermore, we have stressed a major difficulty in computing the dynamic model coefficient, in the form of the undefined filter width ratio. In later chapters we will identify the filter width ratio with the numerical method used to discretize the LES equations, and we will derive a new dynamic model in which this ratio is computed dynamically.

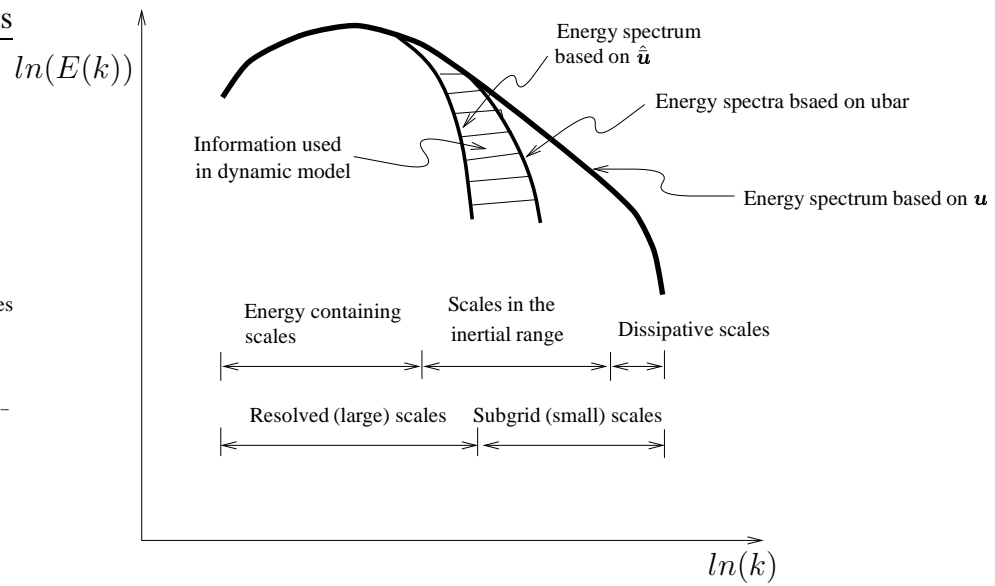


Figure 2.2: Sketch of the Kolmogorov energy spectrum. $E(k)$ is the energy contained in scales of size inversely proportional to k .

CHAPTER 3

DISCRETE TEST FILTERS ON FINITE ELEMENT TOPOLOGIES

In the previous chapter we discussed in detail the dynamic Smagorinsky model, for which a test filter had to be applied to resolved fields in order to obtain the dynamic model coefficient, $(C_s \bar{\Delta})^2$ in (2.23). In this chapter we will discuss in detail potential candidates to serve as the test filter. Specifically we will propose and study several test filters suited for finite element topologies. These filters will be understood or better yet characterized in terms of their widths.

3.1 The box, Gaussian, and sharp spectral filters

As discussed in the Introduction, the general spatial filtering operation, introduced by Leonard [38], is defined as

$$\bar{f}(x) = \int_{\Omega} G(x, y) f(y) dy. \quad (3.1)$$

For now we will focus on filtering in one-dimension as three-dimensional filtering follows straightforward. The filter kernel $G(x, y)$ is centered about the point $y = x$ (as was shown in Figure 1.1) and is chosen to have small compact support in y thereby reducing the region of integration to be much smaller than the flow domain. The simplest filter kernels are homogenous, thus they are symmetric in y about x and their shapes remain constant as $y = x$ varies. This homogeneity property implies that they can be expressed as $G(r)$, where $r = x - y$. Furthermore, these filters are normalized such that they preserve constant functions, thus they satisfy the following condition:

$$\int G(r) dr = 1. \quad (3.2)$$

In general, a well-defined filter kernel will decay symmetrically as r moves away from the origin.

A second way to look at a homogenous filter is through its transfer function, which is essentially the Fourier transform of the filter kernel scaled by 2π . Thus, the transfer function of our filter kernel $G(r)$ is defined as

$$\mathcal{F}\{G(r)\} = \int_{-\infty}^{\infty} G(r)e^{-ikr} dr. \quad (3.3)$$

Application of the filtering operation in (3.1) together with the Fourier transform, and making use of the convolution theorem (see [52]), leads to the following expression for the Fourier transform of a filtered function

$$\begin{aligned} \mathcal{F}\{\bar{f}(x)\} &= \mathcal{F}\{G(r)\} \mathcal{F}\{f(x)\} \\ &= \mathcal{G}(k)\varphi(k), \end{aligned} \quad (3.4)$$

where $\mathcal{G}(k)$ is the transfer function of kernel $G(r)$, which decays rapidly as $|k| \rightarrow \infty$, and $\varphi(k)$ is the Fourier transform of $f(x)$. In general, a well-defined filter kernel will possess a transfer function which is unity at $k = 0$ and decays symmetrically about $k = 0$ as $|k| \rightarrow \infty$. Thus, from (3.4) it is seen that filtering essentially damps high wavenumber content while preserving low wavenumber content of the original function. The Fourier transform of a filter kernel may result in a transfer function with real and an imaginary components. However, the homogeneity of the filters discussed here yields a purely real transfer function. Filter kernels with Fourier transforms having a non-zero imaginary component do not act as true filters and ideally should be avoided. The reason for this is that in addition to damping the amplitude components of a field (which is what a true filter should do), kernels with complex Fourier transform components act on the phase components as well.

The most common spatial filters used in LES are the box, Gaussian and sharp spectral filters. The kernels and the transfer functions for these filters are listed below.

- The **box** filter kernel of width Δ is defined as

$$G(r) = \frac{1}{\Delta} H(\Delta/2 - |r|), \quad (3.5)$$

where $H(\cdot)$ is the Heaviside function. Box filtering the function $f(x)$ is simply taking the average of $f(y)$ in the interval $x - \Delta/2 < y < x + \Delta/2$. The transfer

function of the box filter is expressed as

$$\mathcal{F}\{G(r)\} = \frac{\sin(k\Delta/2)}{k\Delta/2}. \quad (3.6)$$

- The **Gaussian** filter kernel is defined as

$$G(r) = \left(\frac{6}{\pi\Delta}\right)^{1/2} \exp\left(\frac{-6r^2}{\Delta^2}\right). \quad (3.7)$$

The Gaussian filter kernel is the Gaussian distribution with zero mean and a variance of $\Delta^2/12$. This value of the variance, which involves the width the box filter kernel in (3.5), was chosen by Leonard in [38], so as to match the second moment,

$$\int_{-\infty}^{\infty} r^2 G(r) dr, \quad (3.8)$$

of the Gaussian kernel to that of the box kernel. The transfer function of the Gaussian filter is given as

$$\mathcal{F}\{G(r)\} = \exp\left(\frac{-k^2\Delta^2}{24}\right). \quad (3.9)$$

- Finally we have the **sharp spectral** filter with kernel defined as

$$G(r) = \frac{\sin(\pi r/\Delta)}{\pi r}, \quad (3.10)$$

and with transfer function given as

$$\mathcal{F}\{G(r)\} = H(k_c - |k|), \quad \text{where } k_c \equiv \pi/\Delta. \quad (3.11)$$

Looking at (3.4), we see that all of the filters attenuate the high wavenumber content of the un-filtered function $f(x)$. The sharp spectral filter of width Δ is defined such that it completely annihilates wavenumber content beyond a certain cutoff wavenumber denoted as $k_c = \pi/\Delta$.

The previous filter kernels and their transfer functions are plotted in Figure 3.1 and Figure 3.2.

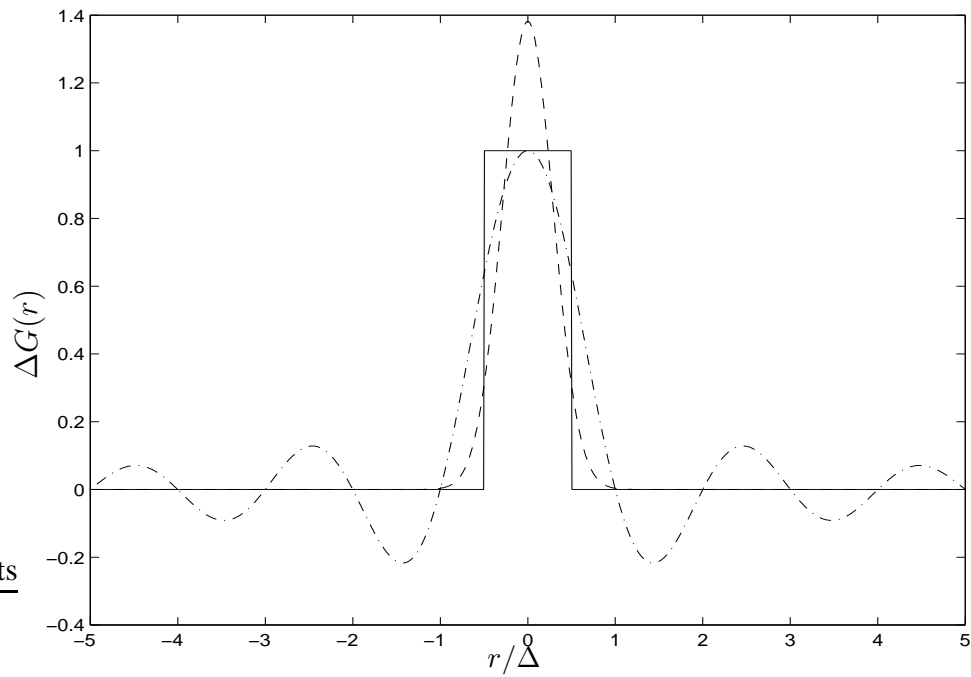


Figure 3.1: Kernels for commonly used filters. — : box ; ---- : Gaussian; - . - : sharp spectral.

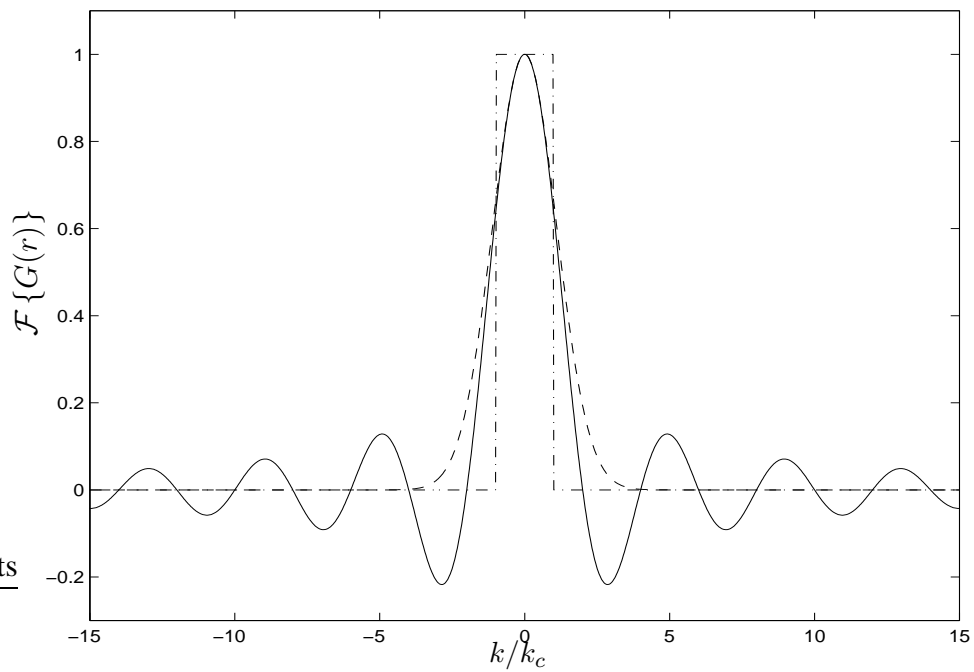


Figure 3.2: Transfer functions for commonly used filters. — : box ; ---- : Gaussian; - . - : sharp spectral.

3.1.1 Filter widths

As previously discussed, the Gaussian filter kernel in (3.7) was chosen such that it has the same second moment as the box filter kernel in (3.5). Furthermore, the box kernel at $y = x$ of width Δ was defined to be unity in the interval $x - \Delta/2 < y < x + \Delta/2$ and zero elsewhere. This admits a natural way of categorizing filters by their widths, taken as Δ . Just like the Gaussian filter, other homogenous non-negative symmetric filters (with non-vanishing second moments) can be required to match their second moments with that of the box filter, resulting in the following general definition of their widths:

$$\Delta = \left(12 \int_{-\infty}^{\infty} r^2 G(r) dr \right)^{1/2}. \quad (3.12)$$

The previous definition is applicable to the box and Gaussian filters, but not to the sharp spectral filter as it possesses a vanishing second moment. Definition (3.12) is extensively discussed by Lund [41] and will be used in this chapter to help characterize potential test filters for our dynamic model simulations.

A second approach to defining the widths of filters is through their transfer functions. In the case of the sharp spectral filter, the width is naturally defined through the cutoff wavenumber $k_c = \pi/\Delta$. Any wavenumber content greater than a given cutoff wavenumber, k_c , is annihilated by the sharp spectral filter, and any wavenumber content less than k_c is completely preserved. In the case of the box or Gaussian filter, its width can be defined through $k^* = \pi/\Delta$, where k^* is the wavenumber at which the filter transfer function achieves a set value between zero and one. As seen through Figure 3.2, by choosing this value of the transfer function closer to zero, the value for the filter width admitted by the definition becomes larger.

The previous two definitions will be used in the following sections to characterize the filters used in our simulations. Furthermore, definitions of the filter widths are not unique, and use of different definitions will lead to different values. Recall that the filter width ratio parameter in the classical dynamic model in (2.23) and (2.22) requires knowledge of the test filter width. It will be one of the accomplishments of this thesis to derive models which are independent of these definitions.

3.2 Discrete approximations of the box filter

In this sub-section we will consider quadrature approximations of the box filter with kernel given in (3.5), and furthermore, we will obtain definitions for the widths of the discrete filters resulting from these approximations. We begin with one-dimensional approximations and proceed to three-dimensional approximations on different finite element topologies.

Regardless of the topology, we will assume the following generalized definition of the box filter. A generalized box filtered function evaluated at vertex A is given as

$$\hat{f}(\mathbf{x}_A) = \frac{1}{\text{meas}(\Omega_A)} \int_{\Omega_A} f(\mathbf{y}) d\mathbf{y}. \quad (3.13)$$

where Ω_A is the union of elements which share vertex A . Here the box filter kernel has been generalized such that at vertex A it becomes

$$G(\mathbf{x}_A, \mathbf{y}) = \begin{cases} \frac{1}{\text{meas}(\Omega_A)} & \text{if } \mathbf{y} \text{ is in } \Omega_A \\ 0 & \text{otherwise.} \end{cases} \quad (3.14)$$

Before we begin our discussion on approximations of filters, it would be helpful to recall the numerical method we will use to solve the modeled filtered Navier-Stokes equations. The spatial discretization in our large-eddy simulations is brought about by the Galerkin approximation to the weak form of the filtered Navier-Stokes equations augmented by the Streamline Upwind Petrov-Galerkin (SUPG) stabilization, herein referred to as the SUPG method. (see [31] and [68]). The Galerkin approximation is often made by representing the flow variables as a linear combination of continuous piecewise polynomial basis functions of order p . In turn, these velocity fields are used to calculate the dynamic model, which requires the test filtering of numerous flow quantities including the product of two components of the velocity (see (2.19)). In our case, these flow quantities are products of piecewise tri-linear ($p = 1$) velocity fields, thus they will be piece-wise tri-quadratics or higher.

3.2.1 Discrete box filters in one-dimension

Consider performing the filtering integrations using the box filter kernel (of width $\Delta = 2h$ where h is the constant grid spacing), as depicted in Figure 3.6, integrated by different quadrature rules. Such quadrature rules admit a family of discrete approximations to a box filtered function evaluated at a particular vertex in the grid. In one-dimension this family can be represented as

$$\hat{f}(x_0) = \sum_{i=-J}^J W_i f(x_i). \quad (3.15)$$

Here the filtered function $\hat{f}(x)$ is evaluated at a vertex whose spatial location is denoted as x_0 with neighboring quadrature points located at $x_1 = x_0 + L_1$, $x_2 = x_0 + L_2, \dots, x_J = x_0 + L_J$ to the right and $x_{-1} = x_0 - L_1$, $x_{-2} = x_0 - L_2, \dots, x_{-J} = x_0 - L_J$ to the left, where the $\{L_i\}$ are constants determined by the quadrature rule and the grid spacing h . The $\{L_i\}$ are representable in the form $L_i = \alpha_i h$ where $0 < \alpha_i < 1$. Furthermore, the weights are non-negative, symmetric (ie. $W_i = W_{-i}$), and satisfy the condition

$$\sum_{i=-J}^J W_i = 1. \quad (3.16)$$

Therefore, this family of discrete filters preserves constants. Examples of several discrete approximations to the box will be given in sub-sequent sections. The family of discrete kernels corresponding to the family of discrete filters in (3.15) can be expressed as

$$G(x - y) = h \sum_{i=-J}^J W_i \delta(x - y + \alpha_i), \quad (3.17)$$

where $\alpha_{-i} = -\alpha_i$ and $\delta(x)$ is the Dirac delta function. The previous relation can be inserted into (3.12) to obtain a general expression for the filter width:

$$\Delta = h \left(12 \sum_{i=-J}^J W_i \alpha_i^2 \right)^{1/2}. \quad (3.18)$$

3.2.1.1 Example: Approximations using one-point quadrature

We point the reader to the sketch in Figure 3.3 as an example. Using one-point Gaussian quadrature to evaluate the filtering operation in (3.13), we obtain that a filtered function at vertex 0 (located at $x = x_0$) can be written as

$$\int_{x_{-1}}^{x_1} f(y)dy \approx \hat{f}_0 = \frac{1}{2}(f_{-1/2} + f_{1/2}), \quad (\text{S1}) \quad (3.19)$$

where $f_0 = f(x_0)$, $f_{-1/2} = f(x_{-1/2})$, $f_{1/2} = f(x_{1/2})$, and S1 stands for standard filter with rule 1 quadrature (one-point quadrature). The transfer function induced by this “finite element-based” filtering operation is

$$G(kh) = \cos(khx_{1/2}), \quad (3.20)$$

where k is the wavenumber and h is the constant spacing between vertices. Note that the previous expression is the Fourier transform of the discrete kernel induced by the operation in (3.19) scaled by 2π . Next, let us assume that \hat{f} is a piecewise continuous linear function,

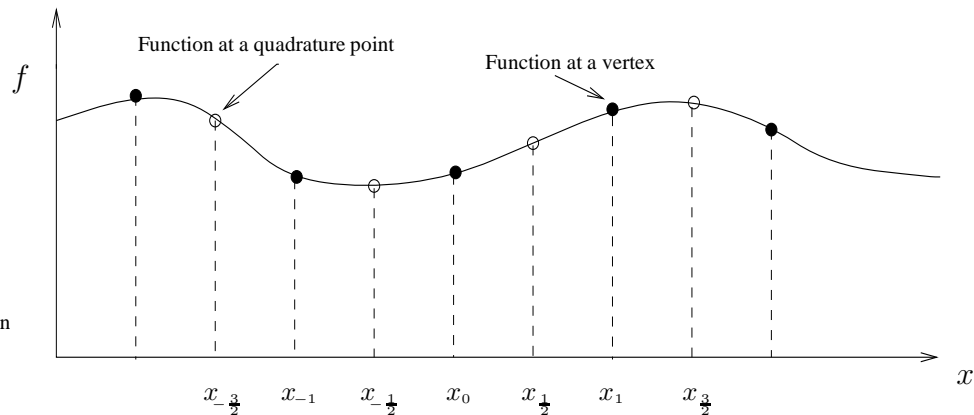


Figure 3.3: Sketch of function evaluations for filter S1 and W1. Each quadrature point is located at the middle of an element (the interval between two vertices). The spacing between vertices is h .

and let us filter it again with the box filter of (3.13) and (3.14) using either a one-point or a two-point quadrature rule, which for this one-dimensional case are both equivalent to the trapezoidal rule. We will refer to this second filter as the “finite element-based” trapezoidal

filter. Hence, we obtain the following filtered function at vertex 0:

$$\tilde{f}_0 = \frac{1}{8}f_{-3/2} + \frac{3}{8}f_{-1/2} + \frac{3}{8}f_{1/2} + \frac{1}{8}f_{3/2}, \quad (\text{W1}) \quad (3.21)$$

where W1 is short notation for wide filter with rule 1. Filter W1 has resulted from sequential applications of the filter S1 and the finite element-based trapezoidal rule. Note that filter W1 filters scales larger than filter S1, hence the name wide filter. The transfer function induced by this filtering operation is

$$G(kh) = \frac{3}{4} \cos(khx_{1/2}) + \frac{1}{4} \cos(khx_{3/2}). \quad (3.22)$$

The widths of filters S1 and W1 can be obtained through their transfer functions in (3.20) and (3.22), respectively or through their second moments using (3.18). If using the latter, we obtain $\Delta = \sqrt{3}h$ as the width of filter S1 and $\Delta = \sqrt{9}h$ as the width of filter W1.

3.2.1.2 Example: Approximations using two-point quadrature

Looking at Figure 3.4, we can think of performing the previous two filtering operations with two-point quadrature (or rule 2) instead of one-point quadrature. If so, we obtain the following filtering operations:

$$\hat{f}_0 = \frac{1}{4}(f_{-2/3} + f_{-1/3} + f_{1/3} + f_{2/3}), \quad (\text{S2}) \quad \text{and} \quad (3.23)$$

$$\begin{aligned} \tilde{\hat{f}}_0 &= \frac{1}{16}(f_{-5/3} + f_{-4/3}) + \frac{3}{16}(f_{-2/3} + f_{-1/3}) \\ &\quad + \frac{3}{16}(f_{1/3} + f_{2/3}) + \frac{1}{16}(f_{4/3} + f_{5/3}). \quad (\text{W2}) \end{aligned} \quad (3.24)$$

The transfer functions corresponding to filters S2 and W2 are

$$G(kh) = \frac{1}{2}[\cos(kh/3) + \cos(2kh/3)] \quad \text{and} \quad (3.25)$$

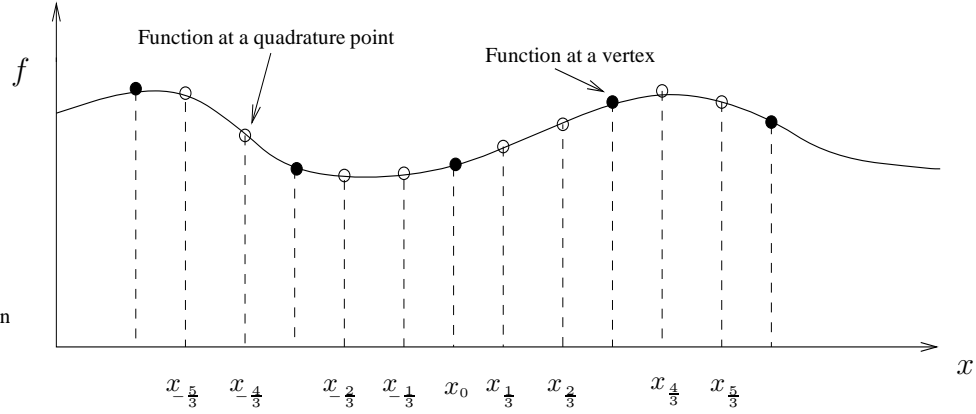


Figure 3.4: Sketch of function evaluations for filter S2 and W2. The spacing between vertices is h . Each quadrature point is located at a distance of αh away from its nearest vertex, where $\alpha = 0.211324865$.

$$G(kh) = \frac{1}{8}[\cos(5kh/3) + \cos(4kh/3)] + \frac{3}{8}[\cos(2kh/3) + \cos(kh/3)], \quad (3.26)$$

respectively.

The widths of filters S2 and W2 can be obtained through their their transfer functions in (3.25) and (3.26) or through their second moments using (3.18). If using the latter, we obtain $\Delta = \sqrt{4}h$ as the width of filter S2 and $\Delta = \sqrt{10}h$ as the width of filter W2.

The transfer functions for the one-dimensional filters S1, S2, W1, and W2 are plotted in Figure 3.5 along with the transfer functions for the box filter approximated using the trapezoidal and Simpson's rules. The previous two filter approximations, which are often employed in finite difference discretizations, lead to

$$\hat{f}_0 = \frac{1}{4}f_{-1} + \frac{1}{2}f_0 + \frac{1}{4}f_1 \quad (\text{FD1}) \quad \text{and} \quad (3.27)$$

$$\hat{f}_0 = \frac{1}{6}f_{-1} + \frac{2}{3}f_0 + \frac{1}{6}f_1, \quad (\text{FD2}) \quad (3.28)$$

respectively. The transfer function for filter FD1 is

$$G(kh) = \frac{1}{2}[1 + \cos(kh)] \quad (3.29)$$

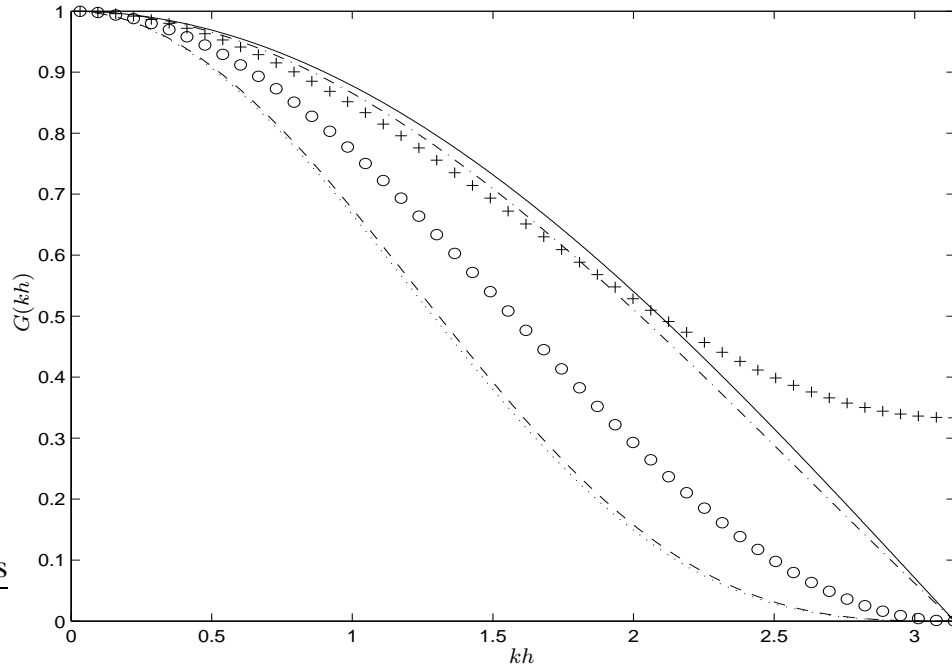


Figure 3.5: Transfer functions for one-dimensional filters. — : filter S1; ---- : filter W1; - · - : filter S2; : filter W2; ○ : filter FD1; + : filter FD2.

and for filter FD2 is

$$G(kh) = \frac{2}{3} + \frac{1}{3} \cos(kh). \quad (3.30)$$

The main difference between the “finite difference-based” filters (FD1 and FD2) and the “finite element-based filters” (S1, S2, W1, and W2) is that the latter group takes into account the function space underlying the finite element method (FEM). The importance of this comes into play when computing the dynamic model. For example, if the FEM uses continuous piecewise linear basis functions, the finite element-based filters act to filter continuous piecewise quadratic functions such as the products between \bar{u}_i and \bar{u}_j . To see this, the reader is directed to the term $\widehat{\bar{u}_i \bar{u}_j}$ appearing in the dynamic model given by equations (2.19), (2.22), and (2.23).

In real space, filters S1, S2, FD1, and FD2 are discrete approximations of the one-dimensional box filter kernel shown in Figure 3.6. Filters W1 and W2 can be shown to be discrete approximations of the one-dimensional “witch’s hat” filter with kernel shown

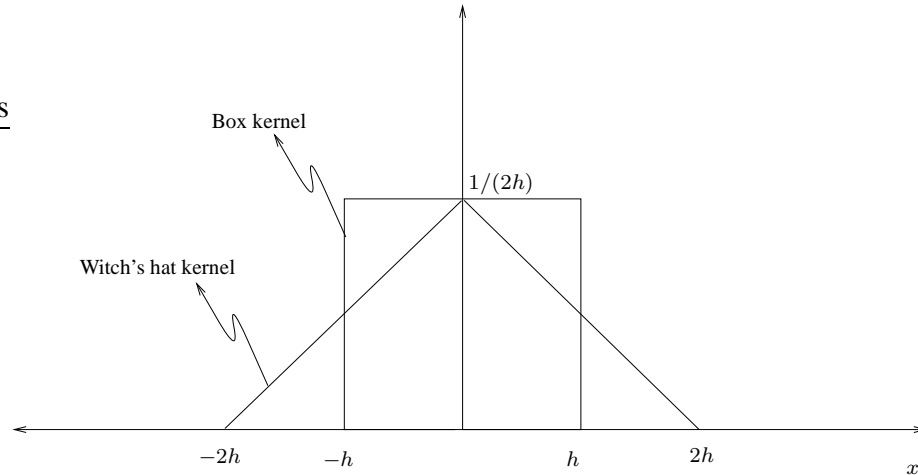


Figure 3.6: Box and witch's hat filter kernels. Length h corresponds to the constant spacing between vertices in Figure 3.3 and Figure 3.4.

also in Figure 3.6. By construction, the wide filters are approximations of the filter resulting from two successive applications of the box filter. As was shown earlier, the Fourier transform of a filtered function is simply the product between the filter transfer function and the Fourier transform of the original function. Hence, twice application of the box filter in Fourier space is given by the product between the square of the box filter transfer function and the Fourier transform of the original function. It follows that the transfer function of the filter resulting from sequential applications of the box filter is the square of the box filter transfer function. Application of the inverse Fourier transform to the square of the box filter transfer function yields the witch's hat kernel of Figure 3.6.

In conclusion, each wide filter (W1 or W2), denoted with a over-hat/over-tilde, $\widehat{\cdot}$, $\widetilde{\cdot}$, can be obtained from a standard filter (S1 or S2) by sequential applications of the standard filter denoted with an over-hat, $\widehat{\cdot}$, and the finite element-based trapezoidal filter denoted with an over-tilde, $\widetilde{\cdot}$.

3.2.2 Discrete box filters in multi-dimension

The finite element-based filters on regularly connected quadrilateral (two-dimensional) or hexahedral (three-dimensional) elements reduce to products of their one-dimensional counterparts in the x -, y -, and/or z -directions. However, this is not the case for triangular (two-dimensional) or tetrahedral (three-dimensional) topologies. In general, multi-

dimensional finite element-based filters S1, S2, W1, and W2 can be constructed in the same fashion as their one-dimensional counterparts described in the previous sub-section. Furthermore, any multi-dimensional finite element-based test filtered function (with test filter S1, S2, W1, or W2) at vertex location $\mathbf{x} = \mathbf{x}_0$ on two- or three-dimensional regularly connected topologies takes the form

$$\hat{f}(\mathbf{x}_0) = \sum_{i=-N/2}^{N/2} W_i f(\mathbf{x}_i), \quad (3.31)$$

where $f(\mathbf{x}_i)$ is $f(\mathbf{x})$ evaluated at the i^{th} quadrature point neighboring x_0 and the filter weights, W_i , sum to one. The symmetry between quadrature points ($\mathbf{x}_i = -\mathbf{x}_{-i}$) due to the regularity of the topologies leads to the following purely real transfer functions:

$$G(\mathbf{k}) = 2 \sum_{i=1}^{N/2} W_i \cos(\mathbf{k} \cdot \mathbf{x}_i), \quad (3.32)$$

where the non-dimensionalized wavenumber vector \mathbf{k} is given as $(k_1 h_1, k_2 h_2, k_3 h_3)$ or $(k_x h_x, k_y h_y, k_z h_z)$ with $k_z h_z = 0$ for two-dimensional topologies. Length h_i is the constant spacing between grid points in the i^{th} direction and k_i is the wavenumber in that direction. Throughout this work, the absolute value of the wavenumber vector, \mathbf{k} , will be referred to as the radial wavenumber, k_r .

3.2.2.1 Example: Two-dimensional approximations of the box filter

As an example of finite element-based test filters in two dimensions, consider test filtering a function on the regularly connected triangular and quadrilateral grids shown in Figures 3.7a and 3.7b using one-point quadrature. Such approximations lead to filter S1 on triangles and filter S1 on quadrilaterals. Filter S1 on triangles and filter S1 on quadrilaterals and their transfer function on these two-dimensional grids reduce to (3.31) and (3.32) with $(N = 6, W_i = 1/6)$ and $(N = 4, W_i = 1/4)$, respectively, for all i . The transfer functions for these two cases with $h_x = h_y$ ($h_1 = h_2$) are shown in Figure 3.8. Notice the direction bias introduced by the transfer function on triangles, as it filters more in one direction than in others.

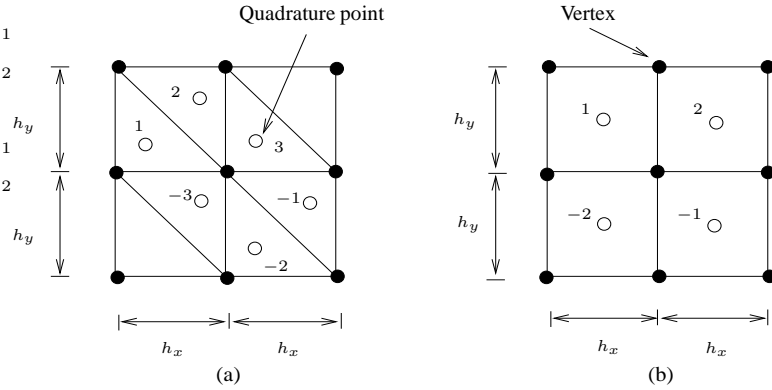


Figure 3.7: Sketch of regularly connected triangular and rectangular grids. Each quadrature point is located at the centroid of its element. Quadrature point locations are symmetric ($x_i = -x_{-i}$) about the center vertex.

3.2.2.2 Example: Three-dimensional approximations of the box filter

Transfer functions of two-dimensional filters can be plotted as closed curve contours such as the ones in Figure 3.8. Transfer functions of three-dimensional filters can be plotted as closed iso-surfaces. In the next three figures we show examples of such contours for filters S1, S2, W1, and W2 on regularly connected grids composed of hexahedral (“hex”), tetrahedral (“tet”) and wedge elements with equal spacing in the x , y , and z -directions.

Similar to filters on triangles, filters on tets and wedges introduce a directional bias by filtering in one direction more than in others, as can be seen from Figures 3.10 and 3.11. Notice the different orientation bias between the filters on tets and wedges. in Figure 3.10. Only looking at the transfer function contours in Figures 3.9, 3.10 and 3.11, one might be led to think that there is not much difference between wide and standard filters. To appreciate the vast difference, the reader is directed to Tables 3.1, 3.2, 3.3 highlighting the disparity existing between wide and standard filters in their widths and in their number of quadrature point (or function) evaluations.

3.2.3 Filter widths

As discussed previously, widths for one-dimensional filters can be easily obtained through the second moment of their filter kernels. This is also the case for the multi-dimensional filters on quadrilateral and hexahedral grids, given that they can be obtained from sequential applications of one-dimensional filters in the x - y - and z -directions. However, in the

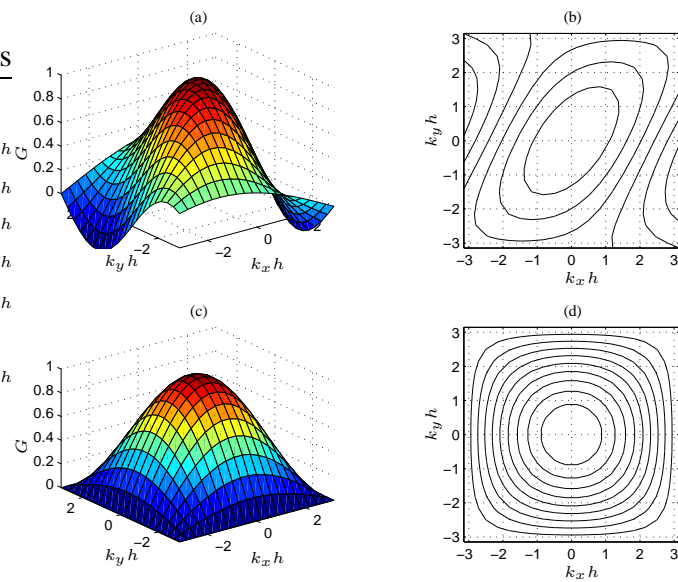


Figure 3.8: Transfer functions of finite element-based filters on triangles and quadrilaterals with one-point quadrature approximation (a) Transfer function of filter S1 on triangles. (b) Contours of (a). (c) Transfer function of filter S1 on quadrilaterals. (d) Contours of (c).

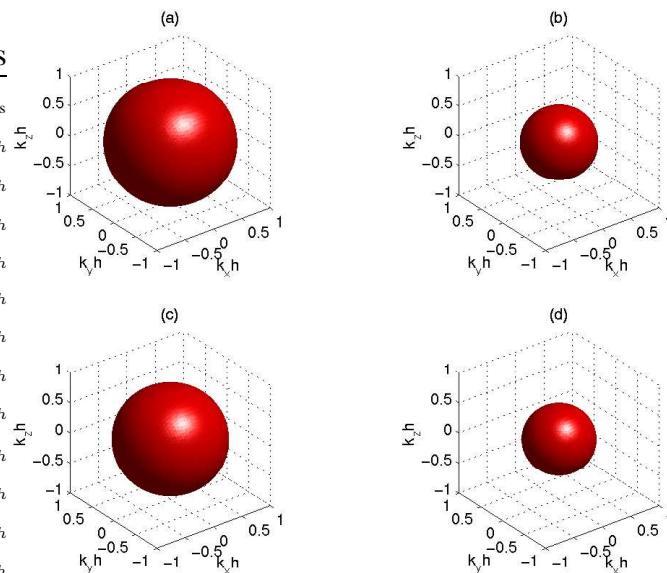


Figure 3.9: Finite element-based transfer function contours defined by $G(\mathbf{k}^*) = 0.75$ on hexahedral elements. (a) Contour for standard filter S1. (b) Contour for wide filter W1. (c) Contour for standard filter S2. (d) Contour for wide filter W2.

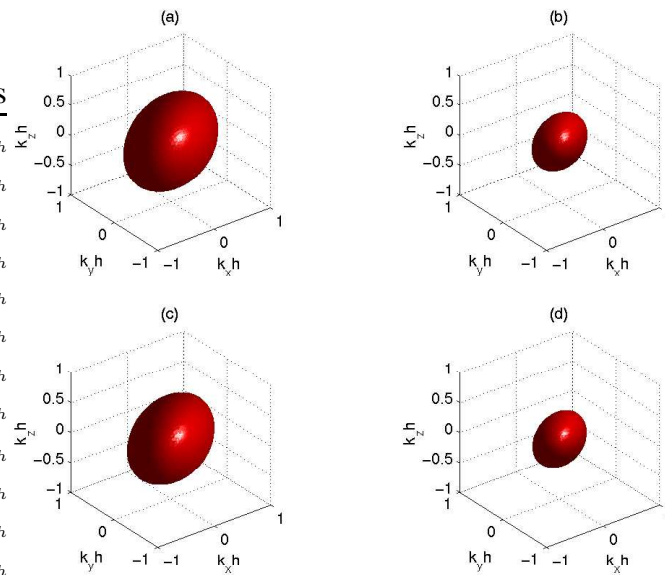


Figure 3.10: Finite element-based transfer function contours defined by $G(\mathbf{k}^*) = 0.85$ on tetrahedral elements. (a) Contour for standard filter S1. (b) Contour for wide filter W1. (c) Contour for standard filter S2. (d) Contour for wide filter W2.

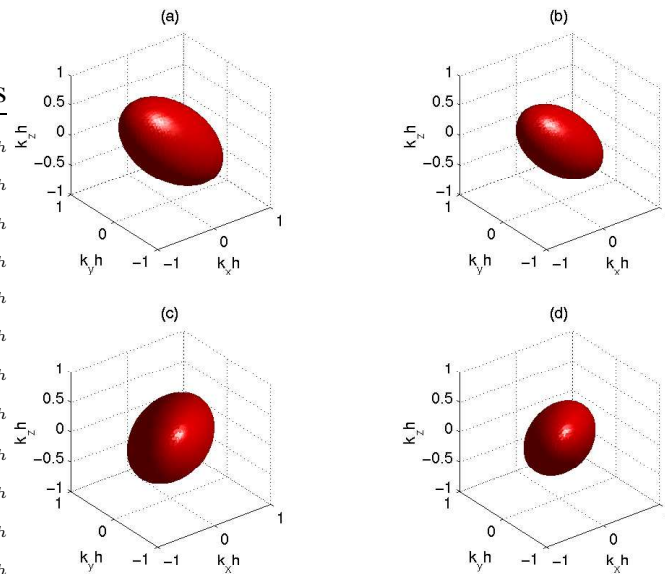


Figure 3.11: Finite element-based transfer function contours defined by $G(\mathbf{k}^*) = 0.85$ on wedge and tet elements. (a) Contour for standard filter S2 on wedges. (b) Contour for wide filter W2 on wedges. (c) Contour for standard filter S2 on tets. (d) Contour for wide filter W2 on tets.

FILTER TYPE	Q-PT EVALS	FILTER WIDTH SQUARED $(\hat{\Delta}/h)^2$			
		$G(\mathbf{k}^*) = 0.5$	$G(\mathbf{k}^*) = 0.65$	$G(\mathbf{k}^*) = 0.75$	$G(\mathbf{k}^*) = 0.85$
S1	8	3.28	5.04	7.36	12.7
S2	64	4.20	6.50	9.57	16.6
W1	64	9.03	14.4	21.1	37.0
W2	512	9.97	15.8	23.4	41.5

Table 3.1: Table outlining widths for finite element-based test filters on regularly connected hexes with constant spacing h between grid points in the x -, y -, and z -directions. Q-PT EVALS stands for quadrature point evaluations.

case of the multi-dimensional filters on triangles, tetrahedral or wedge topologies, obtaining their widths based on the second moment of their kernels might not be so practical due to the need to perform a large number of integrations. For these cases it is simpler to obtain filter widths based on the kernels' transfer functions. For example, the width of any of the one-dimensional filters with transfer function shown in Figure 3.5 can be computed from the non-dimensional wavenumber kh , for which its transfer function equals a specified value. Here, we generalize this approach to evaluate the widths of the three-dimensional finite element-based filters. We define the filter width for such filters as the size of scales corresponding to the average radial wavenumber k_r^* , for which the filter transfer function assumes a specified value between 0 and 1. We proceed by setting the filter width as $\hat{\Delta} = \pi/k_r^*$. For purposes of dynamic estimation of the filter width ratio in the model, the specified value of $G(\mathbf{k}^*)$ will be shown later to be unimportant. Instead, the ratio between widths of the wide and standard test filters will be shown to be important. In Tables 3.1, 3.2, 3.3 we tabulate widths of finite element-based filters based on different values of their transfer functions. Here we present the square of test filter widths, since this is a more appropriate representation in light of the dynamic model parameter $\alpha = (\hat{\Delta}/\bar{\Delta})^2$.

3.3 Continuous piecewise polynomial approximations as filters

The three-dimensional discrete filters presented in the previous section will be used extensively in the new models derived here. In this section we will propose several filters which will not be used for the large-eddy simulation results presented in this thesis. However, the filters proposed in this section have great potential for application to LES on fi-

FILTER TYPE	Q-PT EVALS	FILTER WIDTH SQUARED $(\hat{\Delta}/h)^2$			
		$G(\mathbf{k}^*) = 0.5$	$G(\mathbf{k}^*) = 0.65$	$G(\mathbf{k}^*) = 0.75$	$G(\mathbf{k}^*) = 0.85$
S1	24	1.88	2.86	4.15	7.17
S2	96	2.15	3.33	4.90	8.51
W1	192	5.09	8.06	12.0	21.0
W2	768	5.40	8.57	12.7	22.4

Table 3.2: Table outlining widths for finite element-based test filters on regularly connected tets with constant spacing h between grid points in the x -, y -, and z -directions.

FILTER TYPE	Q-PT EVALUATIONS	FILTER WIDTH SQUARED $(\hat{\Delta}/h)^2, G(\mathbf{k}^*) = 0.85$
S2	72	10.8
W2	576	27.7

Table 3.3: Table outlining widths for finite element-based test filters on regularly connected wedges with constant spacing h between grid points in the x -, y -, and z -directions.

nite elements with hierarchic (higher order) basis functions. A possible advantage of using higher order basis functions is to enable the efficient, accurate representation of turbulent flows on coarser grids than required for simulation with tri-linear basis functions. If we use the box filter as the test filter in the same manner it was used in the previous sub-section when performing LES with hierarchic basis functions, the resulting filter width could potentially be greater than the inertial range scales due to the coarseness of the grids, thereby making the Smagorinsky model invalid. Thus, we would like to define a special class of filters such that their widths can potentially fall on the inertial range even on coarse hierarchic grids. For this we make reality notions first discussed by Leonard [38] and Pope [52], who envision a filtered function as a finite dimensional projection of an infinite dimensional function.

Consider a random function $f(x)$ characterized by high frequencies. The motivation for using polynomial approximations of $f(x)$ as a way to filter $f(x)$ is that a polynomial can be made to represent $f(x)$ up to certain scales. More precisely, the higher the order the polynomial is, the better it can represent the smaller scales of $f(x)$. An example of such

polynomial approximations is

$$\hat{f} = \sum_{n=1}^N a_n \phi_n(x) \quad (3.33)$$

where the $\{\phi_n\}$ are continuous piece-wise polynomial basis functions and the coefficients $\{a_n(x)\}$ are to be determined.

3.3.1 L_2 -projections as filters

A family of filters can be obtained by determining the basis function coefficients $\{a_n\}$ in (3.33) such that they minimize the square of the L_2 -norm of the difference between the filtered and original functions over the domain of interest:

$$R = \frac{1}{L} \int_0^L (\hat{f}(x) - f(x))^2 dx, \quad (3.34)$$

where L is the distance of our domain. By substituting (3.33) into (3.34) and differentiating with respect to the $\{a_m\}$, it is seen that the coefficients satisfy the matrix equation

$$\sum_{n=1}^N B_{mn} a_n = v_m, \quad (3.35)$$

with

$$B_{mn} = \frac{1}{L} \int_0^L \phi_m(x) \phi_n(x) dx, \quad (3.36)$$

and

$$v_m = \frac{1}{L} \int_0^L \phi_m(x) f(x) dx. \quad (3.37)$$

From (3.3.1)

$$a_n = \sum_{m=1}^N B_{mn}^{-1} v_m, \quad (3.38)$$

where B_{mn}^{-1} are the entries of the inverse of the mass matrix \mathbf{B} with entries B_{mn} defined in (3.36). Substituting (3.37) into (3.38) and inserting the result into (3.33) we see that the family of filters in question admits the following family of kernels:

$$G(x, y) = \sum_{n=1}^N \sum_{m=1}^N B_{mn}^{-1} \phi_n(x) \phi_m(y). \quad (3.39)$$

Note that

$$\phi_m^*(x) = \sum_{n=1}^N B_{mn}^{-1} \phi_n(x) \quad (3.40)$$

are the well-known conjugate basis functions, which appear in other applications of L_2 -projections. Thus, the kernel in (3.39) can be expressed in terms of the conjugate basis functions as

$$G(x, y) = \sum_{m=1}^N \phi_m^*(x) \phi_m(y) \quad (3.41)$$

The L_2 -projection filter is similar to the sharp spectral filter in that it completely annihilates scales smaller than a specific size. More specifically, the L_2 -projection filter annihilates scales which can not be represented by the set of basis functions $\{\phi_n(x)\}$.

3.3.1.1 Example: L_2 -projection onto a linear grid of 9 vertices

We would like to get an idea of how the L_2 -projection filter kernel looks on a simple one-dimensional domain. To that extent, we consider a periodic domain split by 9 equally spaced vertices along the y -axis as shown in Figure 3.12. Furthermore, we let the basis functions $\{\phi_m(x)\}$ be the piecewise continuous linear Lagrangian functions, denoted as $\{N_m(x)\}$. In that case, the L_2 -projection filter kernel may be written as

$$G(x, y) = \sum_{m=1}^9 N_m^*(x) N_m(y). \quad (3.42)$$

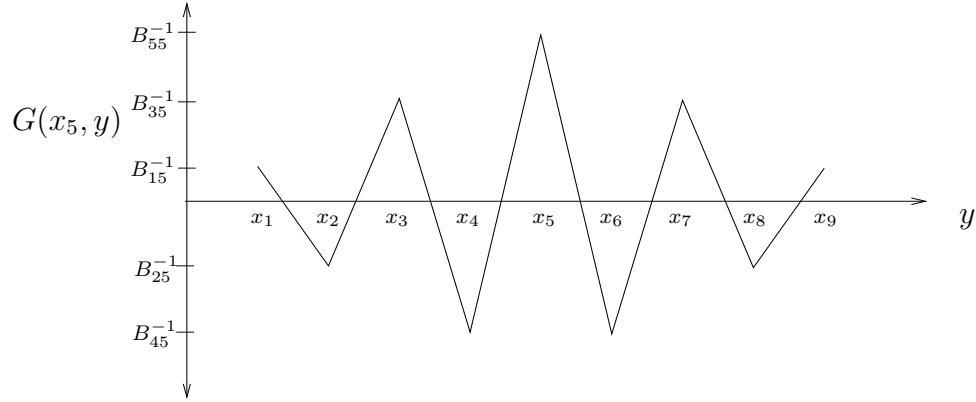


Figure 3.12: Sketch of L_2 -projection filter kernel. The points $y = x_i$ are equally spaced.

Looking at Figure 3.12, let us take position at the middle of the grid at the vertex given by $y = x_5$. In that case the L_2 -projection kernel becomes

$$G(x_5, y) = \sum_{m=1}^9 N_m^*(x_5)N_m(y) = \sum_{m=1}^9 B_{m5}^{-1}N_m(y). \quad (3.43)$$

where the second equality is brought about by

$$N_m^*(x_5) = \sum_{n=1}^9 B_{mn}^{-1}N_n(x_5) = \sum_{n=1}^9 B_{mn}^{-1}\delta_{n5} = B_{m5}^{-1}. \quad (3.44)$$

The linear basis functions possess the characteristic that $N_m^*(x_n) = \delta_{mn}$, where δ_{mn} is the Kronecker delta function which evaluates to 1 if $m = n$ or 0 if $m \neq n$. In Figure 3.12 we see a sketch of the symmetric kernel $G(x_5, y)$ about $y = x_5$. Notice that the kernel decays away from its line of symmetry.

Next, we would like to see how the transfer function corresponding to an L_2 -projection filter, such as the one sketched in Figure 3.12, behaves. It turns out that if we were to evaluate every integration in our L_2 -projection filter exactly, the transfer function corresponding to this filter would not be a filter at all. Instead of damping the high wave number content of a function, it would amplify it! However, we can recover a true filter behavior out of the L_2 -projection by partially lumping the mass matrix in (3.36) via the row sum technique in [29], and by evaluating (3.37) using one-point Gaussian quadrature. For simplicity, let $x_9 - x_1 = 2\pi$ in the grid shown in Figure 3.12. Furthermore let us evaluate (3.37) with

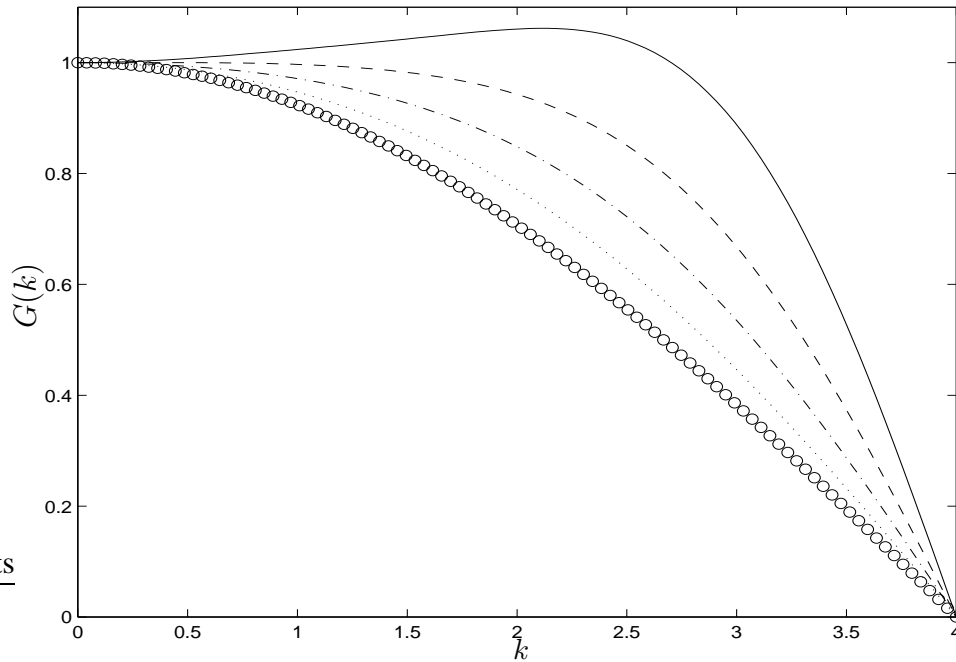


Figure 3.13: L_2 -projection filter kernels for different amounts of mass lumping. — : $\theta = 1.0$; ---- : $\theta = 0.75$; - · - : $\theta = 0.5$; : $\theta = 0.25$; ○ : $\theta = 0.0$.

one-point quadrature and replace the mass matrix \mathbf{B} in (3.36) with

$$\mathbf{B}' = \theta \mathbf{B} + (1 - \theta) \mathbf{B}^l, \quad (3.45)$$

where \mathbf{B}^l is the lumped mass matrix, \mathbf{B} is the mass matrix evaluated exactly, and θ is a parameter between 0 and 1. Under these modifications, the transfer functions corresponding to our L_2 -projection filter for different values of θ are shown in Figure 3.13. As can be seen from Figure 3.13, when the exact mass matrix is used (corresponding to $\theta = 1.0$), the resulting L_2 -projection amplifies high wave number content. This no longer occurs as higher fractions of the lumped mass matrix are used in (3.45), and the resulting L_2 -projection behaves like a true filter. When the mass matrix is completely lumped (corresponding to $\theta = 0.0$), the L_2 -projection filter reduces to the box filter approximated with one-point quadrature, denoted as filter S1 in (3.19).

3.3.2 Interpolations as filters

A second family of finite-dimensional projection filters can be obtained by picking the coefficients $\{a_n\}$ in (3.33) such that the filtered function interpolates the original function through N pre-determined points. As an example of this type of filters we take the filtered function $\hat{f}(x)$ to be the piecewise linear polynomial interpolating the original function $f(x)$ through the N grid points:

$$\hat{f} = \sum_{n=1}^N f_n \phi_n(x), \quad (3.46)$$

where $f_n = f(x_n)$, and the $\{\phi_n(x)\}$ are the Lagrangian piecewise linear basis functions. The kernel associated to this filtering operation can be written as

$$G(x, y) = \sum_{n=1}^N \delta(y - x_n) \phi_n(x) \quad (3.47)$$

In large-eddy simulation involving hierarchic basis functions (such as those performed by the author in [32]), it is common to linearly interpolate the solution onto finer grids for purposes of interpreting results in wave (or Fourier) space. Thus, it would be beneficial to quantify any loss of scales present in the original solution. Furthermore, as discussed earlier, it would be helpful if linear interpolation could serve as a test filter for dynamic model LES.

3.3.2.1 Example: Interpolation onto a linear grid of 9 vertices

In large-eddy simulation involving hierarchic basis functions (such as those performed by the author in [32]), it is common to linearly interpolate the solution onto finer grids for purposes of interpreting results in wave (or Fourier) space. Thus, it would be beneficial to quantify any loss of scales present in the original solution. Furthermore, as discussed earlier, it would be helpful if linear interpolation could serve as a test filter for dynamic model LES.

Consider a 2π -periodic function, $f(x)$, as shown in Figure 3.14. Without any loss of generality, let us assume that the $f(x)$ is reasonably approximated by a Fourier series

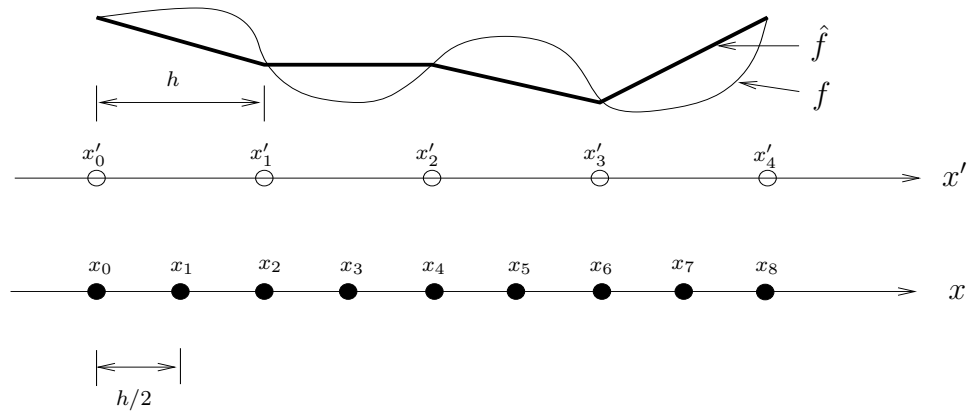


Figure 3.14: Sketch showing effect of interpolation. Vertices along the x' - and x -axis are equally spaced.

whose coefficients are given by

$$\begin{aligned}
 c_k &= \frac{1}{4} \sum_{j=0}^3 f(x'_j) e^{-ikx'_j} \\
 &= \frac{1}{4} (f(x_0) e^{-ikx_0} + f(x_2) e^{-ikx_2} + f(x_4) e^{-ikx_4} + f(x_6) e^{-ikx_6})
 \end{aligned} \tag{3.48}$$

Let us take the filtered component of f as \hat{f} , also shown in Figure 3.14. The coefficients in the Fourier series of \hat{f} can be expressed as

$$\hat{c}_k = \frac{1}{8} \sum_{j=0}^7 \hat{f}(x_j) e^{-ikx_j}, \tag{3.49}$$

where

$$\hat{f}(x_i) = \begin{cases} f(x_i) & \text{for } i = 0, 2, 4, 6 \\ \frac{f(x_{i-1}) + f(x_{i+1})}{2} & \text{for } i = 1, 3, 5, 7 \end{cases} \tag{3.50}$$

and $f(x_8) = f(x_0)$. Note that the Fourier series representation of \hat{f} , with coefficients defined in (3.50), is not unique as more terms could be taken. However, here we simply want to show that taking \hat{f} as a linear interpolation of f can be regarded as a filtering of the latter.

Next, let us compare the Fourier coefficients of f and \hat{f} . To that extent, let us see

what has happened to a generic term in the Fourier series of f as it was filtered by the interpolation process. Let us take the second term in the series for c_k in (3.48).

$$c_k : \quad \frac{1}{4}f(x_2)e^{-ikx_2}. \quad (3.51)$$

We proceed by collecting all the terms in the series for the Fourier coefficients of \hat{f} in (3.49) which possess $f(x_2)$ as a common factor. Thus,

$$\hat{c}_k : \quad \frac{1}{4}f(x_2) \left(\frac{1}{4}e^{-ikx_1} + e^{-ikx_2} + \frac{1}{4}e^{-ikx_3} \right). \quad (3.52)$$

By substituting $x_1 = x_2 - h/2$ and $x_3 = x_2 + h/2$, and making use of the identity $\cos(z) = [\exp(iz) + \exp(-iz)]/2$, the term in (3.52) can be re-expressed as

$$\hat{c}_k : \quad \left\{ \frac{1 + \cos(kh/2)}{2} \right\} \frac{1}{4}f(x_2)e^{-ikx_2} \quad (3.53)$$

Comparing the terms in (3.51) and (3.53) we conclude that in general

$$\hat{c}_k = \left\{ \frac{1 + \cos(kh/2)}{2} \right\} c_k. \quad (3.54)$$

Thus, the transfer function induced by the linear interpolation of f , \hat{f} , is precisely

$$\mathcal{F} \{G(r)\} = \frac{1 + \cos(kh/2)}{2} \quad (3.55)$$

Note that $\mathcal{F} \{G(r)\} \rightarrow 1$ as $kh \rightarrow 0$, hence the interpolation filter preserves the largest scale in f . Additionally, $\mathcal{F} \{G(r)\} \rightarrow 0$ as $kh \rightarrow 2\pi$, hence the interpolation filter damps the smaller scales of f .

3.4 Chapter summary

In this chapter we have introduced numerous filters as possible candidates for the test filter required in computations of the dynamic model coefficient in (2.23). We showed how to obtain discrete approximations of the box filter based on quadrature rules on different finite element topologies such as hexahedral, tetrahedral, and wedge topologies. Fur-

thermore, the filter widths of these discrete approximations of the box filter were obtained based on the second moments of the filter kernels or based on the transfer functions of the filters. The quadrature rule approximations of the box filter, which we have referred to as finite element-based filters will be used extensively in the simulations presented in this work. Two additional filters, which are more appropriate for dynamic model LES on hierarchic grids, were proposed and analyzed. These filters, denoted as the L_2 -projection filter and the interpolation filter, are members of a class of filters based on finite dimensional projections.

CHAPTER 4

EFFECT OF TEST FILTER TYPE AND FILTER WIDTH RATIO IN DYNAMIC MODEL LES

In this chapter we will use the three-dimensional finite element-based filters, previously described, as test filters for the dynamic model in large-eddy simulations. The goal is to understand the role of the test filter type and the filter width ratio on dynamic model results. To that extent we perform LES of decaying isotropic turbulence, which is homogenous in all spatial directions, and turbulent channel flow which behaves similar to isotropic turbulence in the middle or core region far from its bounding walls but behaves differently in regions approaching the walls. Additionally, we use turbulent channel flow to compare the dynamic model using finite element-based filtering with the dynamic model using traditional finite difference-based filtering.

4.1 An assumption for the filter width ratio

Of particular interest in this chapter is to understand the role of the square of the filter width ratio, defined as

$$\alpha = \left(\frac{\hat{\Delta}}{\bar{\Delta}} \right)^2, \quad (4.1)$$

which is intertwined with the test filter denoted with an over-hat, $\hat{\cdot}$, both appearing in the dynamic model given by (2.23), (2.22) and (2.19). An understanding of the role that these two play is essential to large-eddy simulations, especially those performed on coarse grids on which the dynamic model strongly affects the results as will be shown later in Figure 4.1.

Because any numerical discretization operates on the modeled filtered equations (given by the first equation in (2.3) and equations (2.9), (2.15), and (2.23)), applications of the primary filter with kernel $G_{\bar{\Delta}}$ and the filter with kernel $G_{\hat{\Delta}}$ do not appear explicitly in the discretized modeled filtered equations. Prior to discretization, these two filters are arbitrary, as was pointed out in Chapter 2. Yet, computation of the dynamic model in (2.23)

requires knowledge of the widths of these two filters in the form of the filter width ratio squared, noted in (4.1). In practice, the primary filter kernel $G_{\bar{\Delta}}$ is inherently present in the discretization because the discretization itself filters scales smaller than the scales present at its resolution threshold. In fact, the stabilized finite element method used in the discretization in this work, namely the Streamline Upwind / Petrov-Galerkin (SUPG) method, has been identified in [3], [28], and [8] among others, as a numerical model accounting for the effect of unresolved scales on those that are resolved. If a tri-linear finite element method (as is our case) or a typical finite difference method is used, the size of the unresolved scales is approximately equal to the grid size (which is why unresolved, residual motions are often referred to as subgrid-scale motions). Consequently, $\bar{\Delta}$ (the width of the primary, implicit numerical filter kernel, $G_{\bar{\Delta}}$), can be set proportional to the grid size, which has been done traditionally. However, in reality, the width of the primary filter kernel, $\bar{\Delta}$, as well as $\hat{\Delta}$ (the width of $G_{\hat{\Delta}}$) may depend on an unknown combination of the test filter, the dynamic model, the grid size, the polynomial order of the basis functions, and the discretization method, which together comprise the numerical discretization. Thus, we are left with one question when using the dynamic model: How can we compute the filter width ratio squared, $\alpha = (\hat{\Delta}/\bar{\Delta})^2$, correctly? Accurate determination of this parameter is important given that results may depend heavily on it.

The application of the test filter with kernel $G_{\hat{\Delta}}$ and width $\hat{\Delta}$ does appear explicitly in the calculation of the dynamic model coefficient in (2.23) and can help assess α . In Chapter 3 we showed how to calculate $\hat{\Delta}$ on regularly connected grids. In this chapter we will make use of this information by assuming that the filter width ratio squared can be expressed as

$$\alpha \equiv \left(\frac{\hat{\Delta}}{\bar{\Delta}} \right)^2 = \kappa \left(\frac{\hat{\Delta}}{h} \right)^2, \quad (4.2)$$

where h is the approximate size of scales resolved by the discretization, or better yet, the grid size, and κ is a positive parameter that may potentially depend on the the implicit filter due to numerical discretization and the test filter. In expressing the filter width ratio as is done in (4.2), we are attempting to clarify its dependence on the test and implicit numerical filters. As results will show in the next section, the only question in setting α will be that

due to the unknown implicit numerical filter, reflected through κ , and the dependence of α on the test filter will be fully understood.

4.2 Experiments with decaying isotropic turbulence

Under certain conditions, large-scale motions can become turbulent. More precisely, the large-scale motions become unstable and break into smaller scale motions which take energy from the larger ones. Energy is passed down to such small scales at which it is dissipated by the action of molecular viscosity. At high enough Reynolds numbers, the small-scale motions cease to depend on the nature of the large-scale flow, leading to the universality of small-scale motions mentioned in the introduction. Furthermore, these scales lose all directional orientation, thus becoming isotropic. The energy contained in the inertial scales (defined in Chapters 1 and 2) is characterized by what is usually referred to as the *five-thirds law*. In other words, the energy at these scales behaves as $k_r^{-5/3}$, where k_r , the radial wavenumber, is proportional the inverse of the size of the scales. The radial wavenumber was defined as the magnitude of wavenumber \mathbf{k} .

In the up-coming sub-sections we simulate a flow which is nearly isotropic at all scales. Our results are compared to the experimental data of Comte-Bellot and Corrsin in [9], who represented an infinite space of isotropic motions decaying in time because of a lack of kinetic energy production (in the absence of shear flows) to balance the viscous dissipation. They accomplished this by obtaining a turbulent field behind a regular grid of bars spanning a steady, uniform duct flow. By moving at the speed of the mean flow behind the grid, they correctly surmised that an observer would see something like true isotropic turbulence evolving in time.

Due to the homogeneity of the flow, the domain is taken as a cube with sides of length 2π , and the boundary conditions are taken as periodic in the x_1 -, x_2 -, and x_3 -directions. Furthermore, the cube is represented by a grid with 33 equally spaced vertices in each direction. We will explore three topologies for this grid: 1) a hexahedral (hex) topology, 2) a tetrahedral (tet) topology, and 3) a wedge topology. A well resolved direct numerical simulation (DNS) of this flow would require a grid with about 256 vertices in each direction.

Results are compared to the experimental data of Comte-Bellot and Corrsin in the

form of energy spectrum, or better yet, energy contained in the different scales of the flow. The initial condition for our simulations is obtained such that its energy spectrum matches filtered experimental spectrum at a particular non-dimensional time station of the Comte-Bellot and Corrsin experiment, denoted as t_{42} . The simulation is run for 56 time units, at steps of size 0.1, up to a second non-dimensional time station, denoted as t_{98} , and the energy spectrum of the solution at this time is compared to the energy spectrum of the measured data corresponding to that same time station. In all of the simulations performed in this chapter and throughout this work, the SUPG method is used in the spatial discretization and the generalized- α method, discussed in [33], is used in the temporal discretization. The reader is reminded not to confuse the α in the term “generalized- α method” with the α denoting the filter width ratio squared in (4.2). These two α s are distinct. Assigning initial conditions in this problem is not a simple, straightforward step, and thus deserves further discussion.

4.2.1 Initial conditions

The Fourier transform of a velocity field is complex, unless that field is symmetric about some point, which is certainly not the case for a turbulent field. Consider

$$\mathcal{F}\{u_i(x_j, t_{42})\} = A_i(k_r, t_{42}) \exp\{I \theta_i(k_r, t_{42})\} \quad (4.3)$$

as the Fourier transform of the initial velocity field in our simulations, where I , instead of i , has been chosen as $\sqrt{-1}$ so as to not confuse it with the indicial notation in u_i . From the available Comte-Bellot and Corrsin experimental data at t_{42} we can obtain the amplitude components of our initial field in (4.3), $A_i(k_r, t_{42})$. By doing this we automatically ensure that the energy spectrum of our initial condition matches the energy spectrum of the experimental data at t_{42} because by definition, the spectrum is strictly assembled from the amplitude components of the field and not the phase components. However, the phase components of our initial field, $\theta_i(k_r, t_{42})$ in (4.3), are not available from the experimental data. Thus, at first, the best we can do is assign random, uncorrelated numbers to $\theta_i(k_r, t_{42})$. Once we have the initial velocity, partly experimental and partly random, the initial pressure is obtained by solving the Poisson equation for pressure in Fourier or wave space. Next, we apply the inverse Fourier transform to obtain the initial velocity and pres-

sure fields in real space. Note that these initial conditions are not truly turbulent as their random, uncorrelated phases are not consistent with the Navier-Stokes equations.

After running the simulation for 56 time units up to t_{98} , we transform our solution to Fourier space where we decompose it into its amplitude and phase component as

$$\mathcal{F}\{u_i(x_j, t_{98})\} = A_i(k_r, t_{98}) \exp\{I \theta_i(k_r, t_{98})\}. \quad (4.4)$$

At this point, we build the energy spectrum of our numerical solution using $A_i(t_{98}, k_r)$ and notice that this energy spectrum does not approximate the spectrum of the experimental data at this same time station. This is due to the fact that the uncorrelated phase components of the initial conditions did not satisfy the Navier-Stokes equations. Despite that true turbulent amplitudes were assigned initially at t_{42} , the uncorrelated phases led to a deterioration of the amplitude components during the simulation. However, during the simulation, the phase components of our velocity field, $\theta_i(k_r, t)$, developed partial correlation between them due to the fact that they were forced to satisfy the governing equations throughout the simulation. Consequently, we re-scale our solution at t_{98} such that we obtain a new initial condition at t_{42} assembled as

$$\mathcal{F}\{u_i(x_j, t_{42})\} = A_i(k_r, t_{42}) \exp\{I \theta_i(k_r, t_{98})\}. \quad (4.5)$$

We have discarded the deteriorated amplitudes at t_{98} and kept the partially correlated phase of the velocity vector field at t_{98} . The deteriorated amplitudes have been replaced by true turbulent amplitudes at t_{42} . By doing this, the energy in our new initial condition matches the energy of the measured experimental data at t_{42} , and we are ready to re-start our simulation. A new initial pressure is obtained by solving the the Poisson equation for pressure once again, this time using the velocity field in (4.5).

As the previous procedure is repeated, the energy spectrum at t_{98} of the numerical solution improves relative to the energy spectrum of the experimental data at this time station because the phase components become correlated and truly turbulent. Furthermore, the iterative process is stopped once the spectrum at t_{98} does not change much from iteration to iteration.

Other re-scaling procedures for obtaining the initial conditions have been performed

by researchers, as communicated in [30], and were attempted for the present work. However, the previously described new way of re-scaling was found to work best.

4.2.2 LES of decaying isotropic turbulence on hexes

We begin by demonstrating the strong impact that the filter width ratio parameter can have on dynamic model LES results. Figure 4.1 shows the effect of changing the filter width ratio squared, α in (4.2), on dynamic model LES of isotropic turbulence with the hexahedral grid discussed earlier. The results in Figure 4.1 were obtained using finite element-based filter S1 on hexes described in Chapter 3. Notice the strong effect of this parameter on the energy spectrum in the inertial region, thus its accurate prediction is of primordial importance. Furthermore, as α is increased, the magnitude of the model coefficient decreases and the effect of the model is lessened, leading to accumulation of energy at the high wavenumbers, or better yet at the smallest resolvable scales. The discretization by itself can not represent the energy cascade of energy from large to small scales, thus requiring an accurate dynamic model. Additionally, in Figure 4.1 we show the energy spectrum of the initial velocity at t_{42} matching the experimental spectrum.

Next, using the same hexahedral grid, we perform two sets of simulations. The two sets, both composed of simulations performed with the finite element-based S1, W1, S2, and W2 filters, are distinguished by different values of parameter κ in (4.2). In both sets, the test filter widths are computed based on the average radial wavenumber ($k_r^* = |\mathbf{k}^*|$) of the filter transfer function iso-surface defined by $G(\mathbf{k}^*) = 0.75$, where $G(\mathbf{k})$ is the transfer function for each of the test filters. Recall that based on this definition, test filter widths are determined as $\hat{\Delta} = \pi/k_r^*$. A list of the test filter widths, divided by the grid spacing h appears in Table 3.1. We use these widths to compute the filter width ratio squared based on the assumption in (4.2) as $\alpha = \kappa(\hat{\Delta}/h)^2$. For example, in the first set of the simulations we fix κ at 0.680, which for the dynamic model with test filter S1 yields $\alpha = 5.00$. In Table 4.1, we list the squared filter width ratios in the dynamic model with the various finite element-based test filters for the two sets of simulations on hexes. In Figure 4.2 we plot simulation results corresponding to the filter width ratios and test filters noted in Table 4.1. Here we are not concerned with agreement with the experimental data, but rather we focus on the fact that results are independent of the test filter as long as its filter width is

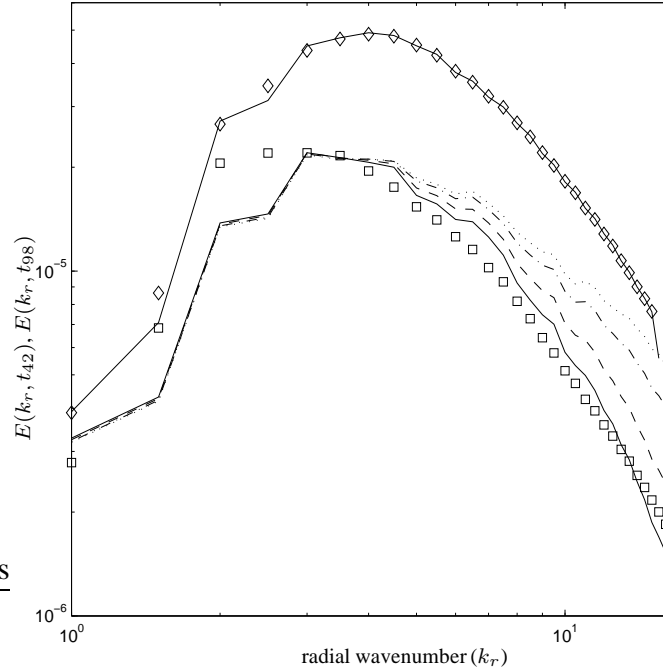


Figure 4.1: Effect of the filter width ratio squared (α) on dynamic model results of isotropic turbulence. — : initial condition matching the data at t_{42} . Data at t_{42} (\diamond), and at t_{98} (\square). Simulations with $\alpha = 2$ (—), $\alpha = 3$ (----), $\alpha = 4$ (- · -), and $\alpha = 5$ (·····). The test filter in all the simulations is filter S1 on hexes.

FILTER TYPE	$\alpha \equiv (\hat{\Delta}/\bar{\Delta})^2 = \kappa(\hat{\Delta}/h)^2$	
	SET 1 ($\kappa = 0.680$)	SET 2 ($\kappa = 0.544$)
S1	5.00	4.00
W1	14.3	11.5
S2	6.51	5.21
W2	15.9	12.7

Table 4.1: Summary of filter width ratios used for simulations on hexes. All test filter widths are based on $G(\mathbf{k}^*) = 0.75$

consistently computed. For a fixed value of κ , the dynamic model is robust enough that it gives nearly identical results for all test filters regardless of the vast difference between the filters. This vast difference can be seen in the transfer functions and filter kernels of standard and wide filters, depicted in Figure 3.9, as well as in the widths of such filters, noted in Table 4.1.

The previous conclusion made about the invariance of results under different finite element-based test filters on hexes is also made by the author in [64], where filter widths

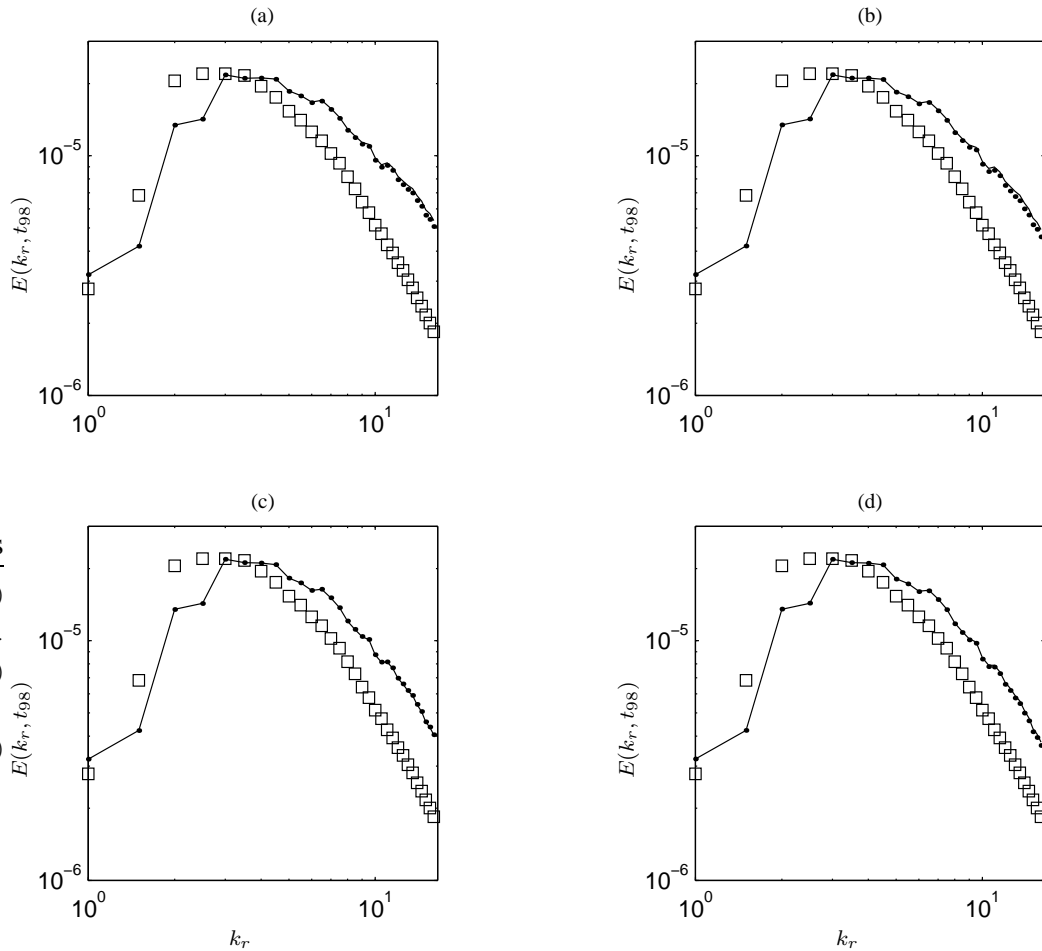


Figure 4.2: Sets of simulations on hexes comparing dynamic model results with different test filters. (a) Two simulations, one with filter S1, the other with filter W1, and both with $\kappa = 0.680$. (b) Two simulations, one with filter S2, the other with filter W2, and both with $\kappa = 0.680$. (c) Two simulations, one with filter S1, the other with filter W1, and both with $\kappa = 0.544$. (d) Two simulations, one with filter S2, the other with filter W2, and both with $\kappa = 0.544$. In all four plots, — : standard filter S1 or S2; \cdots : wide filter W1 or W2.

are computed using the expression based on the second moments of the filter kernels in (3.18), instead of the filter transfer functions as is done here. When the second moments of the filter kernels are used, equation (3.18) yields $\hat{\Delta} = \sqrt{3}h$, $\hat{\Delta} = \sqrt{4}h$, $\hat{\Delta} = \sqrt{4}h$, and $\hat{\Delta} = \sqrt{10}h$ for filters S1, W1 S2, and W2 on hexes, respectively. Recall that on hexes, these filters reduce to applications of their one-dimensional counterparts in the x_1 -, x_2 -, and x_3 -directions. Hence, the filter widths of the 1-D versions of S1, W1, S2, and W2 based on (3.18) can be used to obtain their widths on hexes. Furthermore, in [64] the as-

sumption for the filter width ratio in (4.2) is made and the constant κ is varied leading to the same conclusions made here. In the case $\kappa = 1$ is taken, the energy spectra with filters S1, W1, S2, and W2 are nearly indistinguishable. For the simulation with filter S1, in which $\alpha = (\hat{\Delta}/\bar{\Delta})^2 = \kappa(\hat{\Delta}/h)^2 = 1 \cdot (\sqrt{3})^2$, the energy spectrum of the solution at t_{98} is precisely the curve in Figure 4.1 corresponding to $\alpha = 3$. Clearly, when using the test filter width based on the second moment and making the assumption in (4.2), setting $\kappa = 1$ is not a good choice because the resulting energy spectrum over-predicts the expected spectrum at t_{98} . As evinced by Figure 4.2 and other figures to follow, parameter κ can be tuned to give better results. However, this is deemed undesirable and in this work we derive models for which tuning of input parameters is not required.

In the next sub-sections we will use the filter transfer functions to compute filter widths because they are more convenient to use for filters on tets and wedges, as discussed in Chapter 3.

4.2.3 LES of isotropic turbulence on tets and wedges

Here we present sets of simulations with tetrahedral and wedge elements. In all sets, the test filter widths are computed based on the average radial wavenumber of the iso-surface defined by $G(\mathbf{k}^*) = 0.85$. Note that in the previous sub-section we used $G(\mathbf{k}^*) = 0.75$, instead of $G(\mathbf{k}^*) = 0.85$, to obtain widths of test filters on hexes. The reason we did not use $G(\mathbf{k}^*) = 0.85$ for hexes is that it leads to high filter widths compared to tets and wedges. For example, looking at Tables 3.1 and 3.2 we see that $G(\mathbf{k}^*) = 0.85$ leads to filter widths which for hexes are approximately two times greater than for tets. For consistency regardless of topology, we choose a value of $G(\mathbf{k}^*)$ which leads to filter widths which are of the same order for hexes, tets, and wedges. Looking at Tables 3.1, 3.2, and 3.3, we see that $G(\mathbf{k}^*) = 0.75$ for hexes leads to filter widths which are of the same order as those for tets and wedges with $G(\mathbf{k}^*) = 0.85$. It must be said that although we have chosen specific values of the filter transfer functions, $G(\mathbf{k})$, for computing filter widths, and this might seem biased, ultimately these values will not have an impact on the results with the new models derived in Chapter 5. Tables 4.2 and 4.3 contain information regarding the widths of the test filters used in the simulations. In Figure 4.3 we plot simulation results on tets corresponding to the filter width ratios noted in Table 4.2. Once again, we

FILTER TYPE	$\alpha \equiv (\hat{\Delta}/\bar{\Delta})^2 = \kappa(\hat{\Delta}/h)^2$	
	SET 1 ($\kappa = 1.0$)	SET 2 ($\kappa = 0.558$)
S1	7.17	4.00
W1	21.0	11.7
S2	8.51	4.75
W2	22.4	12.5

Table 4.2: Summary of filter width ratios used for simulations on tets. All test filter widths are based on $G(\mathbf{k}^*) = 0.85$.

FILTER TYPE	$\alpha \equiv (\hat{\Delta}/\bar{\Delta})^2 = \kappa(\hat{\Delta}/h)^2$	
	SET 1 ($\kappa = 1.0$)	SET 2 ($\kappa = 0.370$)
S2	10.8	4.00
W2	27.7	10.2

Table 4.3: Summary of filter width ratios used for simulations on wedges. All test filter widths are based on $G(\mathbf{k}^*) = 0.85$.

see the robustness of the dynamic model as it gives nearly identical results for a fixed value of κ regardless of the test filter. In Figure 4.4 we plot simulation results on wedges corresponding to the filter width ratios noted in Table 4.3. Again, results are nearly identical for a fixed value of κ regardless of the test filter.

We have shown that results of dynamic model LES of decaying isotropic turbulence are invariant as long as the filter widths are consistently computed with definitions given. This is an important conclusion because as was originally discussed in [41], often in the literature differences in simulation results have been incorrectly attributed to using test filters of different shapes as a result of not computing test filter widths with a proper definition. Isotropic turbulence LES results here are invariant to test filters on a set or fixed topology. Thus, for a fixed topology we can say that the optimal value of parameter κ (κ_{opt}) such that results match experimental data well, is independent of the test filter used and solely dependent on the discretization excluding the test filter. The difficulty now shifts to finding the value of κ_{opt} , or better yet, finding the optimal value of the filter width ratio squared (α).

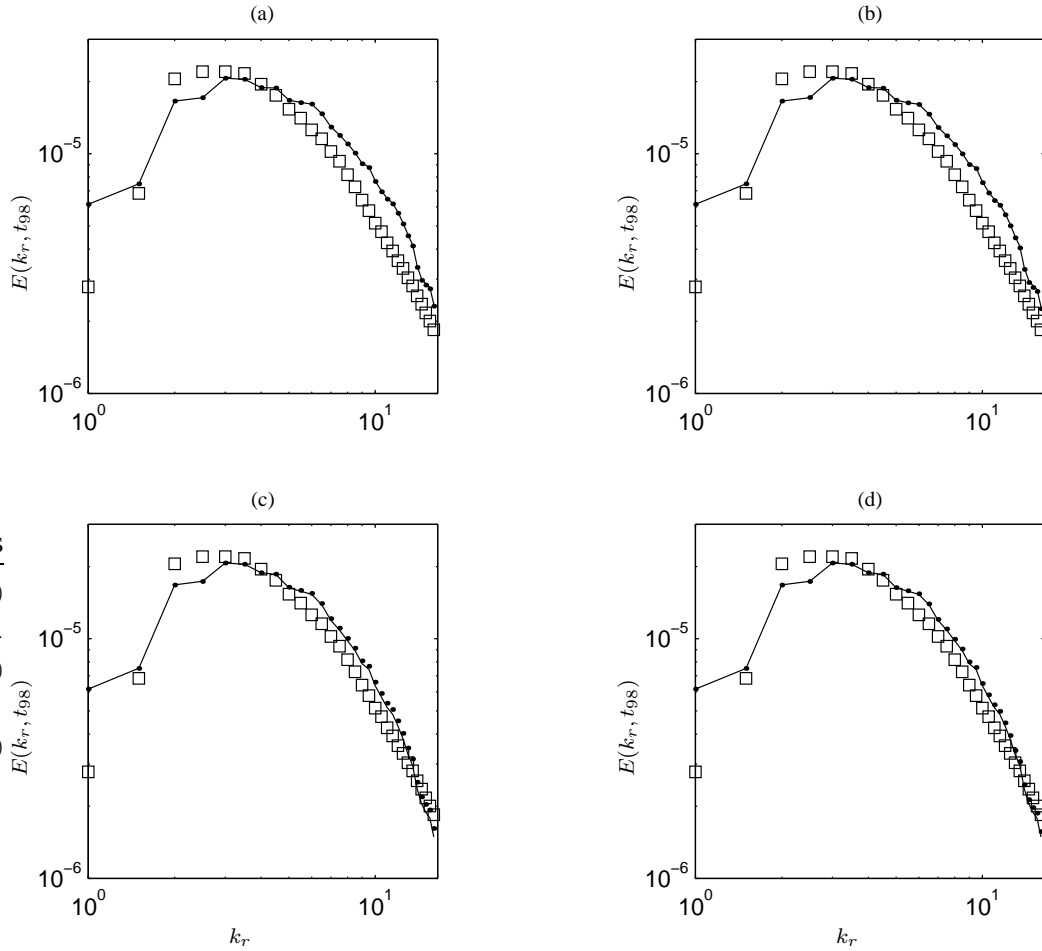


Figure 4.3: Sets of simulations on tets comparing dynamic model results with different test filters. (a) Two simulations, one with filter S1, the other with filter W1, and both with $\kappa = 1.0$. (b) Two simulations, one with filter S2, the other with filter W2, and both with $\kappa = 1.0$. (c) Two simulations, one with filter S1, the other with filter W1, and both with $\kappa = 0.588$. (d) Two simulations, one with filter S2, the other with filter W2, and both with $\kappa = 0.588$. In all for plots, — : standard filter S1 or S2; \cdots : wide filter W1 or W2.

4.3 Experiments with turbulent channel flow at $Re_\tau = 180$

In this section we will present dynamic model simulation results of turbulent channel flow between parallel plates using the finite element-based test filters that were previously tested on decaying isotropic turbulence. The channel flow is chosen to have a Reynolds number, Re_τ , (based on the friction velocity, u_τ , and the channel half-width, h) at 180 for the purpose of comparison with the benchmark direct numerical simulation (DNS) results of Kim, Moin, and Moser in [34]. The friction velocity is defined as $u_\tau^2 = (\tau_w/\rho)$, where

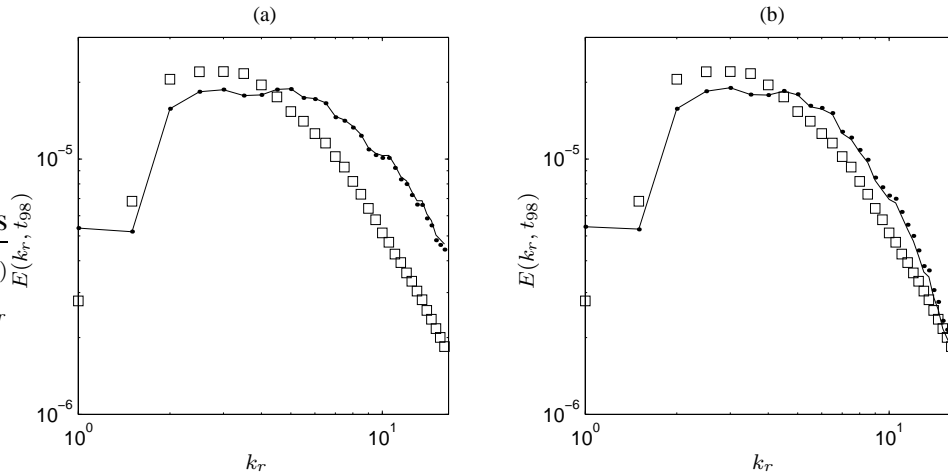


Figure 4.4: Sets of simulations on wedges comparing dynamic model results with different test filters. (a) Simulations with $\kappa = 1.0$. (b) Simulations with $\kappa = 0.370$. In both plots, — : standard filter S2; \cdots : wide filter W2.

τ_w is the shear stress at the walls. By Dean's suggested correlation, as given in [34], $Re_\tau = 180$ corresponds to a bulk Reynolds number, Re (based on the bulk streamwise velocity and channel half-width) of 2800. Using the previous Reynolds number with bulk velocity assumed to be unity together with the definition of Re_τ and the relation between the friction velocity, u_τ , and the wall shear stress, τ_w , the expected wall shear stress corresponding to $Re_\tau = 180$ is calculated as 0.00413.

The geometry of the problem, as sketched in Figure 4.5, is composed of no-slip walls at $y = \pm h$ with periodic boundary conditions in the spanwise (z -) and streamwise (x -) directions. Thus, the spanwise and streamwise directions are considered spatially homogeneous and the numerator and denominator in the dynamic model coefficient in (2.23) are averaged over these directions. For the channel domain depicted in Figure 4.5, $L_x = 4\pi h$ and $L_z = (4/3)\pi h$. In our LES, the grid is composed of 33 vertices in the x -direction, 65 vertices in the y -direction, and 33 vertices in the z -direction. The DNS of Kim, Moin, and Moser was carried out on a domain of same dimensions as our LES, but on a much finer grid of 192 vertices in the x -direction, 129 vertices in the y -direction, and 160 vertices in the z -direction. For our channel grid, a hyperbolic stretching function is employed in the y -direction such that the first vertex off the wall is set at a distance $\Delta y^+ = u_\tau \Delta y / \nu = 1$ away from the wall, where y is non-dimensionalized by h , and $\nu = 1/Re$ is the non-dimensionalized kinematic viscosity. Using the stretching function, the grid spacings in

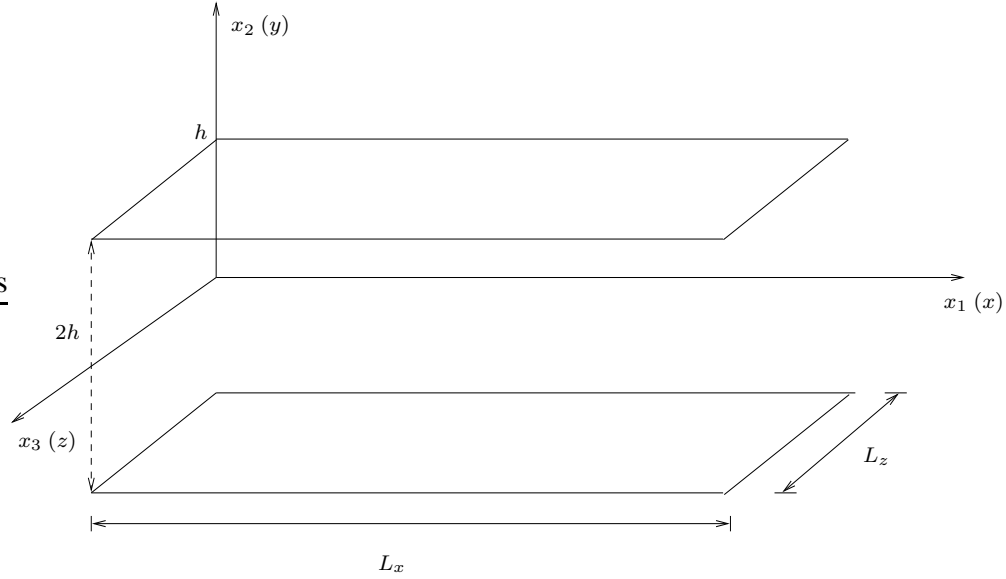


Figure 4.5: Sketch of domain used for LES of turbulent channel flows

the y -direction become smaller near the walls, yielding higher resolution in these regions. Due to the no-slip boundary conditions, strong gradients occur in the near-wall region, thus a higher resolution is required near walls. In summary, the grid vertices are uniformly spaced over homogenous directions of the flow. However, this is not the case over the inhomogenous direction (normal to the walls), as the grid is non-uniform, characterized by an accumulation of vertices in the near wall-regions. Finally, the $Re_\tau = 180$ channel simulations are made with a constant time step at 0.1 to satisfy the Courant, Friedrichs, Levy (CFL) condition and maintain temporal accuracy.

It is important to note that the body force, which is essentially the pressure gradient in this problem, is commonly chosen such that in a control volume setting it balances the targeted wall shear stress determined by the choice of Re_τ . Instead, in our simulations we determine the body force dynamically so that it keeps the streamwise mass flux, or better yet the bulk velocity, nominally constant. Thus, we set the body force such that the mass flux satisfies

$$\frac{h}{2L_z} \int_{-1}^1 \int_0^{L_z/h} u_1 d\left(\frac{z}{h}\right) d\left(\frac{y}{h}\right) \approx 1. \quad (4.6)$$

When the body force is not used to control the mass flux, the mass flux is observed to experience oscillations which slow convergence of statistics (space and time-averaged quan-

tities) of interest.

The initial conditions for this problem are obtained by first running the simulation with zero initial pressure and random perturbations superimposed on a streamwise parabolic velocity profile. In time, the perturbations grow, leading to a fully developed turbulent channel flow. Here, fully developed means that the flow is steady in the temporal mean (or stationary) and is spatially homogenous in the streamwise and spanwise directions. Throughout the transition to turbulence period, the simulation is performed without any LES model. Once the channel is fully developed we use the fully developed solution at a particular time step as the initial condition for the simulations with the dynamic model. We will refer to this initial condition as a “no-model” initial condition.

4.3.1 Basic relationships for turbulence statistics

Consider the filtered, resolved velocity decomposed into time-averaged and fluctuating components as

$$\bar{u}_i = \langle \bar{u}_i \rangle + \text{fluctuation}, \quad (4.7)$$

where the time-averaged velocity is

$$\langle \bar{u}_i \rangle = \frac{1}{T} \int_{t_0}^{t_0+T} \bar{u}_i dt. \quad (4.8)$$

Here the averaging period T is chosen so that the flow has adjusted after transitioning from a no-model initial condition or better yet, a no-model flow, to a modeled flow. For simplicity, we drop the bar notation and refer to the resolved component, \bar{u}_i , as u_i . Thus, (4.7) is re-expressed as

$$u_i = \langle u_i \rangle + u'_i, \quad (4.9)$$

where u'_i is the fluctuation of u_i . Furthermore, in computations, the temporal average of the velocity in (4.8) is commonly computed by performing a numerical average over N

discrete time steps as

$$\langle u_i \rangle = \frac{1}{N} \sum_{k=1}^N u_i(\mathbf{x}, t_k), \quad (4.10)$$

where $u_i(\mathbf{x}, t_k)$ is the flow velocity of interest at the k^{th} time step.

To gain insight into the dynamics of the turbulent flow, various quantities based on the decomposition in (4.9) are collected during a simulation. In addition to this temporal averaging, spatial averaging over homogenous directions is also used to increase the statistical sampling, allowing fewer time steps to achieve what is commonly referred to as statistically steady behavior. Thus, the $\langle \cdot \rangle$ notation will denote spatial averaging over spatially homogenous directions in addition to temporal averaging as originally presented.

Several averaged quantities are of particular interest, starting with the mean quantities themselves such as the mean wall force and the mean velocity, followed by the turbulence intensities such as the root-mean-square (rms) of the velocity fluctuations, denoted as

$$u_i^{rms} = \sqrt{\langle u'_{(i)} u'_{(i)} \rangle}, \quad (4.11)$$

where the notation (i) denotes no sum on i . Also of interest is the Reynolds stress component defined as

$$\langle u'_1 u'_2 \rangle, \quad (4.12)$$

which for stationary turbulence, such as the turbulent channel flow considered here, is equivalent to the Reynolds stress in (1.10) with $i = 1$ and $j = 2$.

4.3.2 LES of turbulent channel flow on hexes

In this sub-section we present dynamic model LES results on hexes of the turbulent channel flow at $Re_\tau = 180$ previously described. Of concern here is to understand the effect of filter type on the results. We restrict attention to the standard and wide finite element-based filters on hexes with one-point quadrature rule (S1 and W1), as their counterparts with two-point quadrature (S2 and W2) yield similar results. More specifically,

filter S2 yields similar results to S1, and W2 yields similar results to W1. For the filter width ratio in the dynamic model we assume the approximation in (4.2) with $\kappa = 1$. Furthermore, for simplicity the test filter widths computed are based on the second moment of the kernels. Recall that on hexes, the finite element-based filters reduce to sequential applications in the x -, y -, and z -directions of their one-dimensional counterparts in (3.19) and (3.21). Thus, we can obtain the test filter widths using (3.18), from which we find that the width of filter S1 is $\hat{\Delta} = \sqrt{3}h$ and the width of filter W1 is $\hat{\Delta} = \sqrt{9}h$. Recall that in the x - and z -directions the grid is uniformly spaced. However, this is not the case in the y -direction due to the hyperbolic stretching of vertices. Consequently, the symmetry of the finite element-based test filters is slightly distorted. An analysis of asymmetric filters and their effects is presented in [43], [65], and [66] in which it is concluded that asymmetry effects are negligible if the distribution of vertices is sufficiently smooth. Given that the stretching function used for our channel grid is smooth, the slight asymmetries developed by the test filters do not produce adverse effects, as will be shown later.

In Figure 4.6 we plot the x -component of the force on the channel walls exerted by the flow versus non-dimensional time for two cases of the dynamic model. In the first case, corresponding to Figure 4.6a, the dynamic model uses filter S1 as the test filter and in the second case (Figure 4.6b) the model uses filter W1. As can be seen, the dynamic model with the wide filter (filter W1) leads to higher wall forces than the model with the standard filter (filter S1). This is directly due to the fact that in the near-wall region the dynamic model coefficient, $(C_s \bar{\Delta})^2$, is greater in the case of the standard test filter, as seen in Figure 4.7b, leading to a less energetic flow, and thus lower wall forces. In the core (middle) region of the channel flow, the ratio between the model coefficients is nearly one, thus we can say that in this region the model coefficient is somewhat independent of the test filter, similar to what was observed in the decaying of isotropic turbulence problem. However, this conclusion can not be made for the model coefficient in the near-wall region.

For presentation purposes, in Figure 4.7, we time-average the numerator and denominator of the dynamic model coefficient in (2.23) in addition to their space-average. We denote the model coefficient with space- and time-averaged numerator and denominator

as

$$\langle (C_s \bar{\Delta})^2 \rangle \equiv \frac{1}{2} \frac{\langle L_{ij} M_{ij} \rangle}{\langle M_{kl} M_{kl} \rangle}. \quad (4.13)$$

Recall that during the simulations, the numerator and denominator of the model coefficient are not time-averaged and are only space-averaged over homogenous directions, in this case the x - and z -directions. In Figure 4.7a we examine the near-wall profile of the dynamic model coefficient with filters S1 and W1. Theoretically, the model coefficient should exhibit a behavior close to y^{+3} near walls (see [52]). However, in the cases of the finite element-based filters, the model coefficient deviates slightly away from the y^{+3} profile as it approaches the walls. In the next sub-section, the reason for this slight deviation will be explained and it will be shown that it does not have a negative impact on the results. Overall, both simulations, show that the dynamic model under-predicts the expected mean wall force of 0.435, computed based on the expected wall shear stress. This is common for the dynamic model, as observed in [48] among others.

Next, we examine the mean streamwise velocity (as the other two mean velocities are zero in this problem), the root-mean-square of the velocity fluctuations and the Reynolds stress component, $\langle u'_1 u'_2 \rangle$. In Figure 4.8 we plot the time- and space-averaged streamwise velocity in wall coordinates, $\langle u_1 \rangle^+$, as a function of y^+ , where

$$\langle u_1 \rangle^+ = \langle u_1 \rangle / u_\tau \quad \text{and} \quad y^+ = \frac{(1 - |y/h|) u_\tau}{\nu}. \quad (4.14)$$

The friction velocity is obtained through the wall shear stress as $u_\tau = \sqrt{\tau_w / \rho}$. In each simulation, the wall shear stress is obtained from the computed mean wall force. As can be seen in Figure 4.8, the dynamic model using the wide test filter, W1, gives a better approximation of the mean streamwise velocity in wall coordinates compared to the dynamic model with the standard test filter, S1, especially in the core region of the channel, relative to the DNS data in [34]. The difference in the mean streamwise velocity prediction can be attributed to the fact that the dynamic model with filter W1 results in a better approximation of the mean wall force, as seen in Figure 4.6. The mean wall force plays a direct role in the computation of the mean streamwise velocity in wall coordinates, defined in (4.14), through its determination of the friction velocity u_τ . To see the impor-

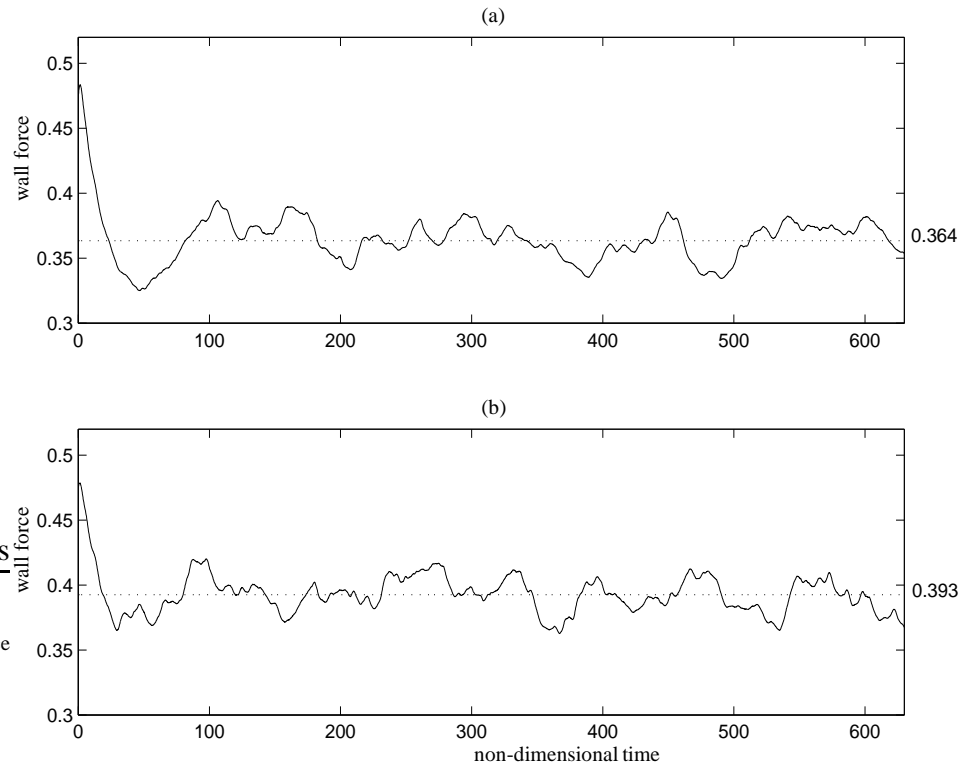


Figure 4.6: Wall force histories with dynamic model using (a) filter S1 and (b) filter W1. The mean wall force should be approximately 0.435.

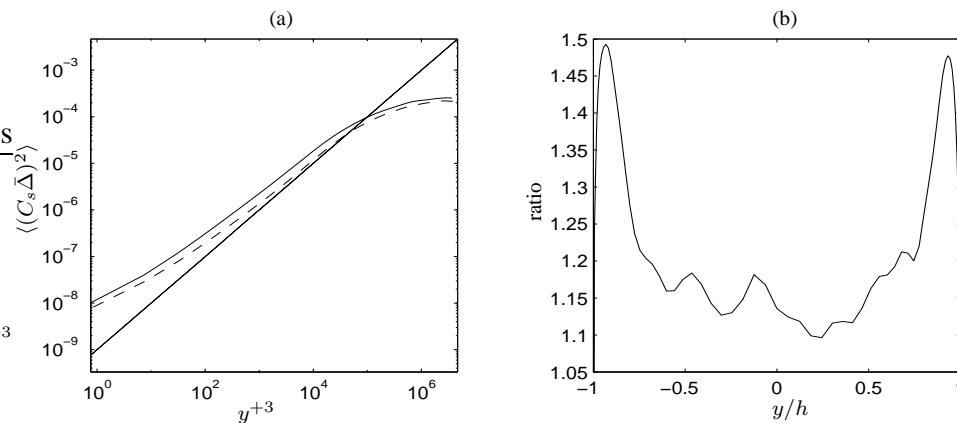


Figure 4.7: Comparison between dynamic model coefficients with filter S1 and filter W1. (a) $\langle (C_s \bar{\Delta})^2 \rangle$ with filter S1 (—) and filter W1 (----). (b) $\langle (C_s \bar{\Delta})^2 \rangle$ with filter S1 divided by $\langle (C_s \bar{\Delta})^2 \rangle$ with filter W1. The straight line in (a) denotes a y^+3 profile.

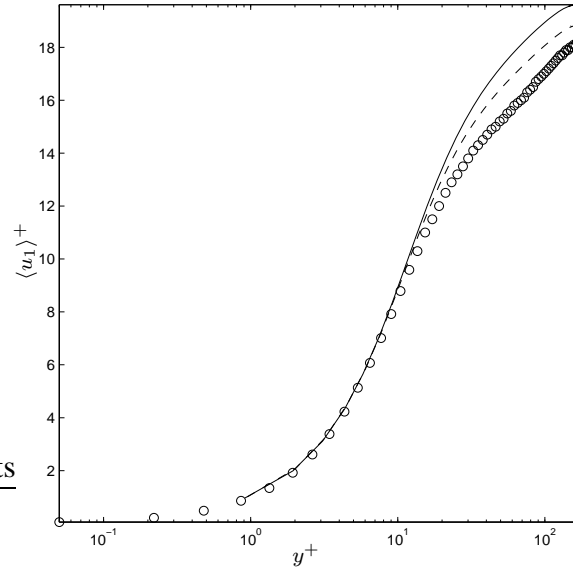


Figure 4.8: Mean streamwise velocity in wall coordinates (scaled by the computed friction velocity) with dynamic model using filter S1 (—) and filter W1 (----). \circ : mean velocity in the DNS in [34].

tance of determining an accurate mean wall shear stress and thereby and accurate mean friction velocity we direct the reader to Figure 4.9, where we plot mean streamwise velocities in wall coordinates using the theoretical or expected value of the friction velocity, $u_\tau = 0.064$. Notice that the mean velocities scaled by the expected friction velocity are closer to the mean velocity recorded in the DNS compared to the mean velocities scaled by the predicted (or computed) mean friction velocities in Figure 4.8. Throughout this work all results in wall coordinates will use computed mean friction velocities, and furthermore given the importance of predicting good friction velocities, computed mean wall forces will be stressed. In Figure 4.10 and Figure 4.11, we plot the root-mean-square of the velocity fluctuations and the Reynolds stress component, $\langle u'_1 u'_2 \rangle$, respectively. The former is scaled by u_τ and the latter is scaled by u_τ^2 . Although not shown, the Reynolds stress component is anti-symmetric about $y = 0$ and the root-mean-square of the fluctuations are symmetric about $y = 0$. Once again, we see that the dynamic model with the wide filter W1 yields better results compared to the dynamic model with the standard filter S1 relative to the DNS data, most likely due to a better approximation of u_τ . In Figure 4.10, the upper three curves correspond to u_1^{rms} , the middle three curves correspond to u_2^{rms} , and the lower three curves correspond to u_3^{rms} . Here we see that the root-mean-squares of

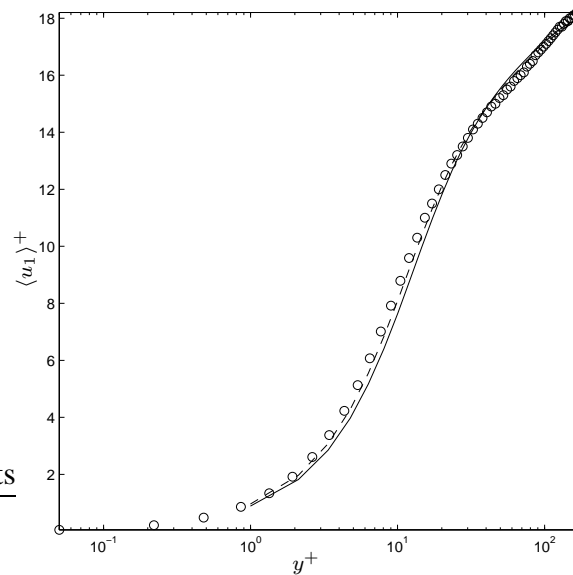


Figure 4.9: Mean streamwise velocity in wall coordinates (scaled by the expected friction velocity) with dynamic model using filter S1 (—) and filter W1 (----). \circ : mean velocity in the DNS in [34].

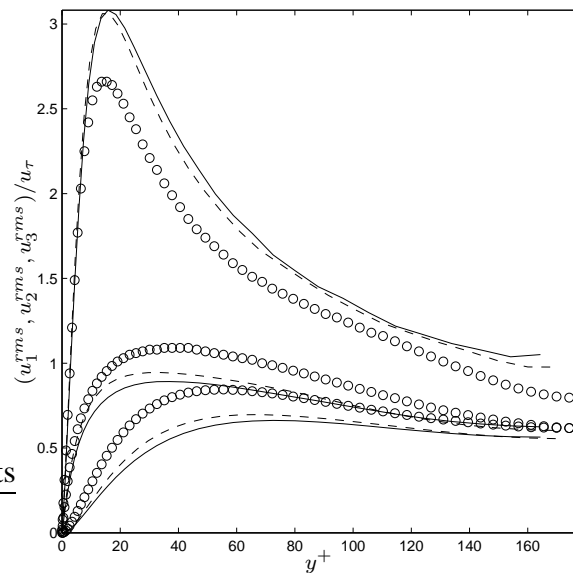


Figure 4.10: Rms of velocity fluctuations in wall coordinates. Rms of velocities with dynamic model using filter S1 (—) and filter W1 (----); \circ : rms of fluctuations in the DNS in [34].

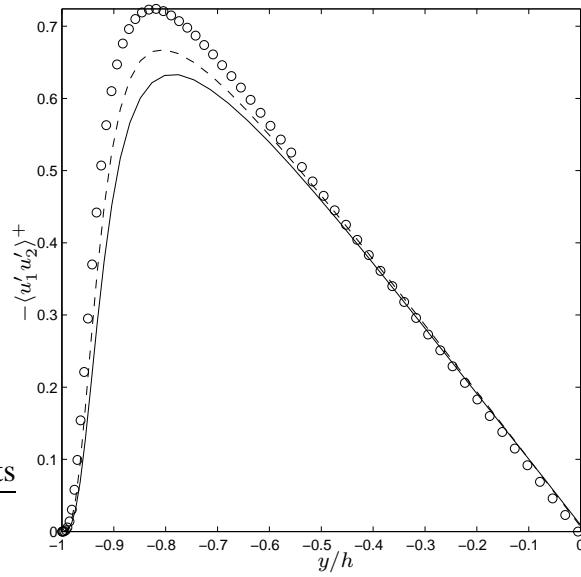


Figure 4.11: Reynolds stress component, $\langle u'_1 u'_2 \rangle / u_\tau^2$, with dynamic model using filter S1 (—), and filter W1 (----). \circ : Reynolds stress component in the DNS in [34].

the spanwise and normal to the walls velocity fluctuations are under-predicted. This is not surprising given that the numerical solution represents the filtered component of the velocity with fluctuations that should be weaker than those of the full velocity resolved by the DNS. An under-prediction should occur for the root-mean-square of the streamwise fluctuations as well. However, here the low wall shear stress predicted by the dynamic model with both finite element-based filters (S1 and W1) serves to shift the root-mean-square of the streamwise fluctuations above that of their DNS counterpart. Thus, the mean wall shear stress has a greater impact on the root-mean-square of the streamwise fluctuations than on the root-mean-square of the fluctuations in the other two directions. Furthermore, over-prediction of u_1^{rms} / u_τ seems to indicate the need for a model stronger than the current models in the core region, yet weaker near the walls, so as to yield higher mean wall forces. Recall that in the current models with test filters S1 and W1, the filter width ratio assumption in (4.2) is made with $\kappa = 1$ and the filter widths are based on the second moment of the test filters. These same models yielded an over-prediction of the energy in LES of decaying isotropic turbulence, consistent with their over-prediction of u_1^{rms} / u_τ in the current problem. Finally, the under-prediction of the Reynolds stress component, $\langle u'_1 u'_2 \rangle / u_\tau^2$, in Figure 4.17, by the model with any of the filters (S1 or W1) can perhaps be attributed to its under-prediction of u_2^{rms} / u_τ , despite its over-prediction of u_1^{rms} / u_τ .

The trends discussed here regarding mean streamwise velocity, rms of velocity fluctuations, and Reynolds stress have also been observed in other simulations with the dynamic model such as those in [48] and [20].

4.3.3 Comparison between dynamic model results with finite element-based (3-D) and finite difference-based (2-D) test filters

We would like to compare dynamic model results with the finite element-based filters to dynamic model results with traditional filters used in finite difference simulations. In the case of the turbulent channel flow studied here, the LES community has traditionally applied finite difference-based filtering in the spanwise and streamwise directions as

$$\hat{u}_i(\mathbf{x}, t) = \int G(\mathbf{x}, y_1, y_3) \mathbf{u}(y_1, x_2, y_3, t) dy_1 dy_3, \quad (4.15)$$

where $\mathbf{y} = (y_1, y_2, y_3)$, $\mathbf{x} = (x_1, x_2, x_3)$, and $\mathbf{u}(y_1, x_2, y_3, t)$ is $\mathbf{u}(\mathbf{y}, t)$ restricted to the plane $y_2 = x_2$. In terms of the channel's (x, y, z) -coordinate system, the filtering integration is applied in planes of constant y . The main reason behind this is to avoid non-uniformities in the grid. As discussed earlier, in the current problem, the grid vertices are uniformly distributed in the directions of flow homogeneity (the streamwise and spanwise directions), however, this is not the case in the direction normal to the walls. If filtering is applied along a direction in which the grid is non-uniform, the filter will no longer be symmetric. Thus, to preserve symmetry of the filter it is common to apply it over directions of the flow which are homogenous. However, in the channel simulations performed so far in this work, finite element-based filters have been applied in all three directions as

$$\hat{u}_i(\mathbf{x}, t) = \int G(\mathbf{x}, \mathbf{y}) \mathbf{u}(\mathbf{y}, t) dy_1 dy_2 dy_3. \quad (4.16)$$

The reason we choose to filter over all three directions is that in general, a turbulent flow might not have homogenous directions leading to a completely non-uniform grid, in which case we have no other choice but to filter in three-dimensions (3-D).

To understand the effect of 3-D filtering and the problems it may potentially bring due to its asymmetries, we compare the results of the previous sub-section with results obtained using finite difference-based filters applied only over the spanwise and stream-

wise directions. To that extent, we employ the trapezoidal filter (FD1) in (3.27) applied on (x, z) -planes. This filter will be referred to as the trapezoidal, in-plane (2-D) filter. A second, wider version of the trapezoidal, in-plane filter is also used. This wider version is obtained by applying the trapezoidal, in-plane filter twice. To summarize, we will be comparing four simulations: 1) with the standard finite element-based (3-D) filter S1, 2) with the wide finite element-based (3-D) filter W1, 3) with the trapezoidal, in-plane (2-D), finite difference-based filter FD1, and 4) with the wide trapezoidal, in-plane (2-D), finite difference-based filter. Recall that in cases 1) and 2), the filter width ratio was taken as

$$\frac{\hat{\Delta}}{\bar{\Delta}} \approx \frac{\hat{\Delta}}{h}, \quad (4.17)$$

stemming from the assumption in (4.2) with $\kappa = 1$. This same approximation is used for cases 3) and 4) as well. For 1) and 2), $\hat{\Delta}/h = \sqrt{3}$ and $\hat{\Delta}/h = \sqrt{9}$, respectively, based on the second moment of the filter kernels used in (3.18). Similarly, for cases 3) and 4), the filter width based on the second moment leads to $\hat{\Delta}/h = \sqrt{6}$ and $\hat{\Delta}/h = \sqrt{12}$, respectively.

In Figure 4.12 we plot time histories of the wall forces for the dynamic model using the 2-D and 3-D filters in cases 1), 2), 3), and 4). Overall, the wide, 3-D, finite element-based filter, W1, leads to a better prediction of the expected mean wall force. Additionally, the difference between mean forces with filter S1 and its wide version, filter W1, is larger than the difference between mean forces with filter FD1 and its wide version. The reason for this can be seen by examining the space- and time-averaged model coefficient $(C_s \bar{\Delta})^2$ in Figure 4.13. In Figure 4.13b we see that in the core of the channel, $(C_s \bar{\Delta})^2$ with filter S1 (viz. FD1) is slightly larger (about 1.1 to 1.2 times larger) than with W1 (viz. the wider version of FD1). In the near-wall region, the same can be said for the ratio between $(C_s \bar{\Delta})^2$ obtained with FD1 and $(C_s \bar{\Delta})^2$ obtained with the wider version of FD1. However, near the wall, the difference in $(C_s \bar{\Delta})^2$ with the 3-D filters, S1 and W1, is much larger, as $(C_s \bar{\Delta})^2$ with S1 reaches a maximum value of about 1.5 times larger than $(C_s \bar{\Delta})^2$ with W1.

The fact that the finite element-based filters lead to a $(C_s \bar{\Delta})^2$ which deviates from its expected y^{+3} profile in the near-wall region can be attributed to their three-dimensionality, given that $(C_s \bar{\Delta})^2$ with the finite difference-based, 2-D in-plane filters do follow the y^{+3}

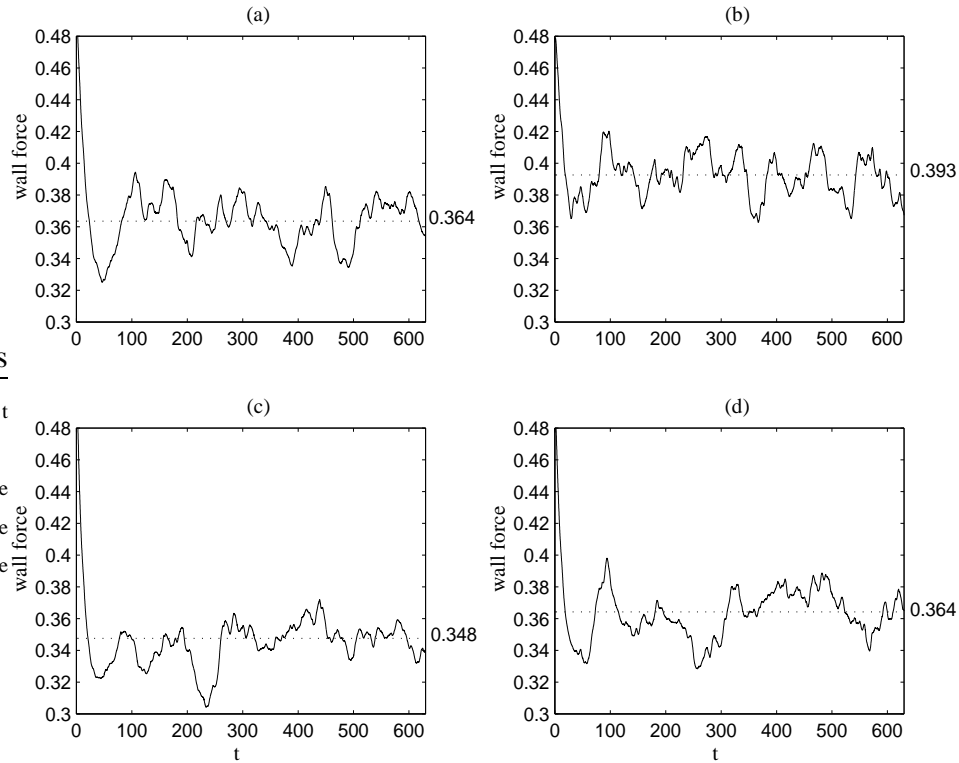


Figure 4.12: Wall force histories with dynamic model using 2-D and 3-D filtering. Forces with (a) 3-D filter S1, (b) 3-D filter W1, (c) 2-D filter FD1, and (d) wide version of 2-D filter FD1. The mean wall force should be approximately 0.435.

profile, as seen in Figure 4.13a. This deviation of $(C_s \bar{\Delta})^2$ with the 3-D filters does not have a negative impact, as results with the 3-D filters are shown to be of the same quality or better than results with the 2-D filters.

Differences in the behavior of the dynamic model coefficient, $(C_s \bar{\Delta})^2$, obtained with the 2-D and 3-D filters can be traced to the L_{ij} and M_{ij} tensors in the calculation of $(C_s \bar{\Delta})^2$ in (4.13). Although not shown, the components of these tensors are symmetric about the channel at $y = 0$, except for L_{12} and M_{12} which are anti-symmetric about $y = 0$. From Figure 4.14 and Figure 4.15, we conclude that the most dominant factor why the S1 and FD1 filters lead to larger values of $(C_s \bar{\Delta})^2$ than their wider counterparts is the magnitude of M_{12} , which is much greater for the wider filters, especially in the approach to the walls. Recall that M_{ij} contracted with itself appears in the denominator of $(C_s \bar{\Delta})^2$ in (4.13). Thus, larger magnitudes of M_{ij} lead to smaller values of $(C_s \bar{\Delta})^2$, even in the presence of larger magnitudes of L_{ij} appearing in the numerator, which is the case for the wider

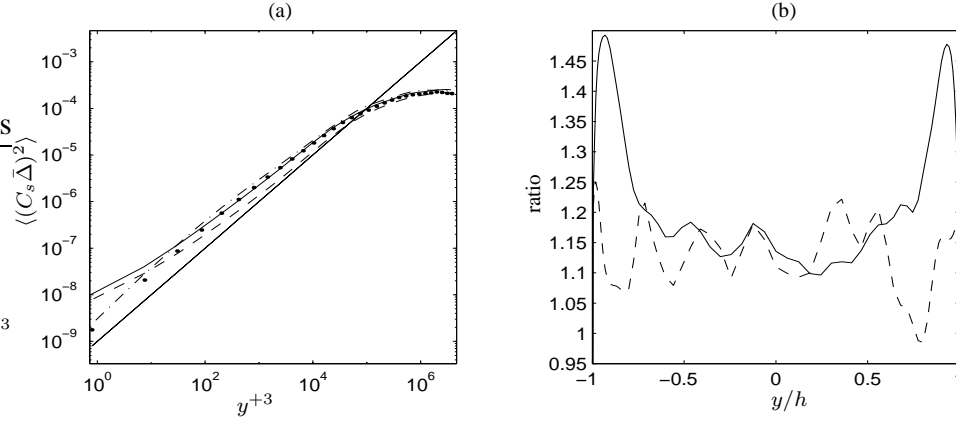


Figure 4.13: Comparison between dynamic model coefficients with 2-D and 3-D filters. (a) $\langle (C_s \bar{\Delta})^2 \rangle$ with 3-D filter S1 (—), 3-D filter W1 (----), 2-D filter FD1 (-·-), and wide version of FD1 (···). (b) $\langle (C_s \bar{\Delta})^2 \rangle$ with filter S1 divided by $\langle (C_s \bar{\Delta})^2 \rangle$ with filter W1 (—) and $\langle (C_s \bar{\Delta})^2 \rangle$ with filter FD1 divided by $\langle (C_s \bar{\Delta})^2 \rangle$ with wide version of FD1 (----).

filter. For all the cases, M_{12} dominates over all the components of L_{ij} . Consequently, this leads to a weaker dynamic model coefficient and a more energetic flow, producing a higher mean wall force.

The magnitude difference in M_{12} with the 3-D filters, S1 and W1, is greater than the magnitude difference of M_{12} with the 2-D filters, FD1 and its wider version. This might be due to the fact that the relative width between filters W1 and S1 is greater than the relative width between FD1 and its wider version. As seen in (2.22), the magnitude of M_{ij} is proportional to the filter width ratio which is set proportional to the test filter width.

However, the filter width ratio, and thus the width of the test filter, are not the sole factors controlling the behavior of M_{ij} , as the M_{12} and M_{22} components with filter W1 are for the most part greater in magnitude than those with the wide version of filter FD1, yet the filter width ratio used with W1 is smaller at $\sqrt{9}$ than the filter width ratio used with the wider version of FD1 at $\sqrt{12}$. Thus, the only logical choice is to attribute this to the three-dimensionality of W1. Recall that the magnitude of M_{12} in (2.22) is proportional to the gradient of the streamwise velocity normal to the walls ($u_{1,2}$). At any point in the channel domain, the three dimensionality of the wide filter W1 enables it to sample flow on planes closer to the walls with larger gradients $u_{1,2}$, compared to the wide 2-D filter which only samples flow on a single plane parallel to the walls.

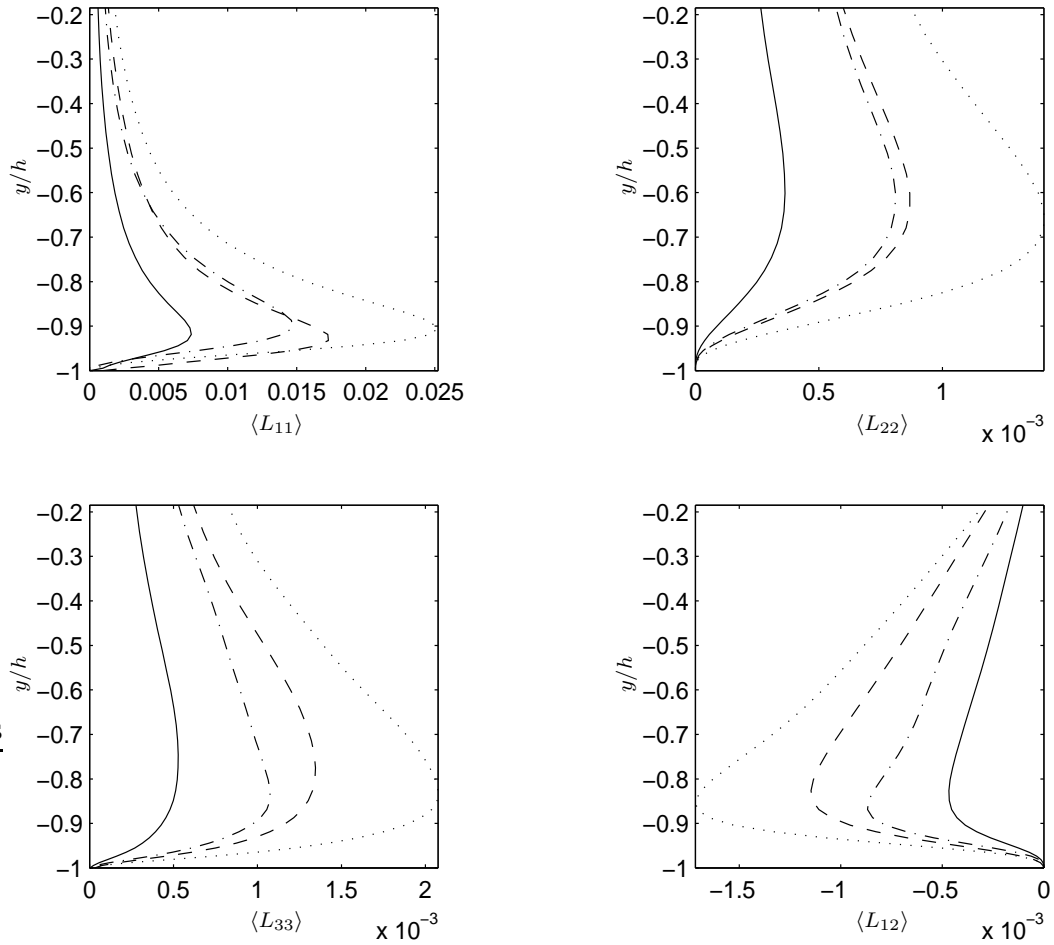


Figure 4.14: Comparison of L_{ij} tensor in the dynamic model with 2-D and 3-D filters — : L_{ij} with 3-D filter S1; ---- : L_{ij} with 3-D filter W1. - · - : L_{ij} with 2-D filter FD1; · · · : L_{ij} with wide version of FD1. $L_{ij} = L_{ji}$ and $\langle L_{13} \rangle$ and $\langle L_{23} \rangle$ are approximately 0.

An interesting question to ask is: why does the wide version of the 2-D filter FD1 lead to nominally the same mean wall force as the 3-D filter S1, even though the magnitude of M_{12} with the former is greater than with the latter? The answer lies behind the components of the L_{ij} tensor shown in Figure 4.14. All of the components of this tensor are greater in magnitude with the wide version of filter FD1 than with filter S1. Even though the wide version of filter FD1 tends to lower the model coefficient with its greater values of M_{12} (compared to those of S1), this effect is balanced by its greater values in L_{ij} (compared to those of S1) tending to increase the model coefficient.

The fact that the wide version of the 2-D filter FD1 leads to nominally the same mean

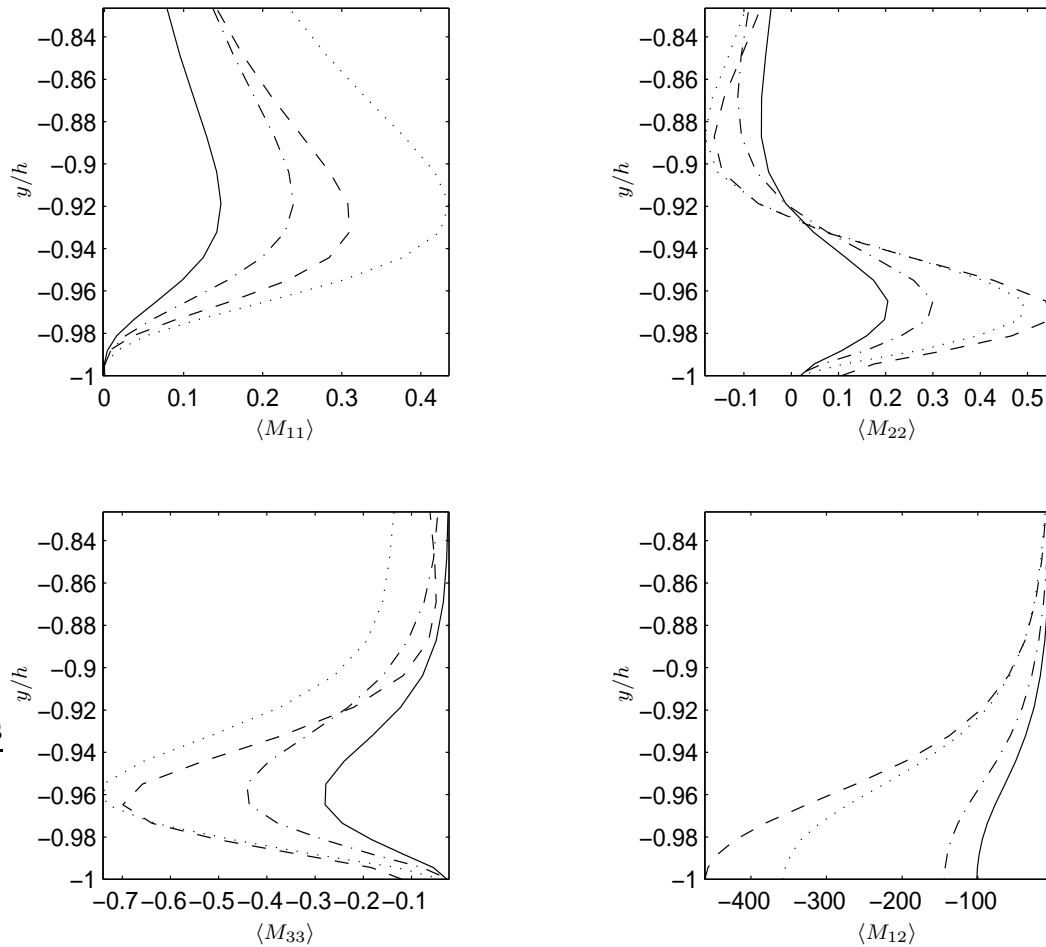


Figure 4.15: Comparison of M_{ij} tensor in the dynamic model with 2-D and 3-D filters — : M_{ij} with 3-D filter S1; ---- : M_{ij} with 3-D filter W1. - · - : M_{ij} with 2-D filter FD1; · · · : M_{ij} with wide version of FD1. $M_{ij} = M_{ji}$ and $\langle M_{13} \rangle$ and $\langle M_{23} \rangle$ are approximately 0.

wall force as the 3-D filter S1 further proves that the strength of the dynamic model coefficient is not solely based on the width of the filter and thereby the test filter width. The magnitude of the model coefficient is inversely proportional to the filter width ratio, which would make one expect that a larger filter width ratio would lead to a lower model coefficient. Certainly this is not the case with the wide version of 2-D filter FD1 with filter width ratio at $\sqrt{12}$ and with the 3-D filter S1 with filter width ratio at $\sqrt{3}$, as evinced by their corresponding mean wall forces in Figure 4.6. However, it should be pointed out that if the filter is kept fixed, the model coefficient does indeed decrease when the filter width ratio is increased and vice versa.

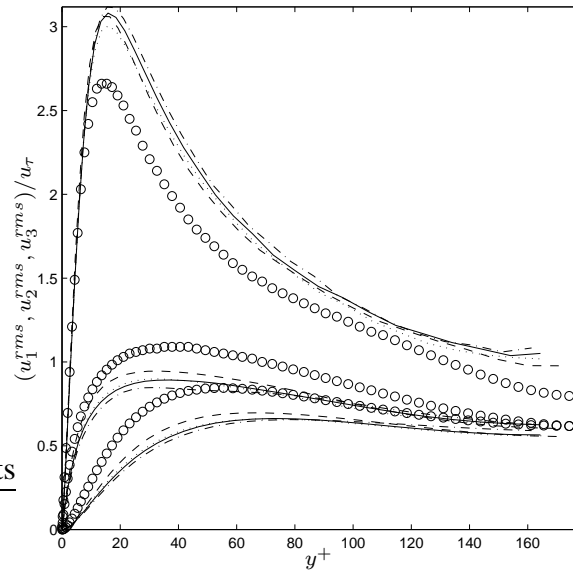


Figure 4.16: Rms of velocities in wall coordinates. Rms of velocity fluctuations with dynamic model using filter S1 (—), filter W1 (----), filter FD1 (— · —), and wide version of filter FD1 (· · ·). \circ : rms of fluctuations in the DNS in [34].

In conclusion, differences in the strength of the dynamic model are not solely based on the influence of the filter width ratio and thereby the width of the test filter, as it is also based on the dimensionality of the test filter. Furthermore, the asymmetry introduced by the 3-D, finite element-based filters, as discussed earlier, does not create adverse effects, most likely due to the smoothness of the grid. In fact, the wide 3-D filter, W1, yields better results than the 2-D, finite difference-based filters, as was shown in terms of the mean wall forces.

In Figures 4.16, 4.17 and 4.18 we compare the root-mean-square (rms) of the velocity fluctuations, the Reynolds stress component, $\langle u'_1 u'_2 \rangle$, and the mean streamwise velocity, respectively, resulting from the dynamic model with the 2-D and 3-D filters. As was discussed earlier, obtaining an accurate mean wall force leads to better results in terms of the previous three quantities. Thus, the finite element-based 3-D filter W1 yields better results due to its much better approximation of the mean force compared to the other filters. Furthermore, although the mean wall force with the wider version of filter FD1 is slightly higher than the mean wall force with FD1 itself, this slight difference is not enough to cause a really noticeable improvement especially in terms of Reynolds stress. However, slight improvements are seen in terms of rms fluctuations and mean streamwise velocity.

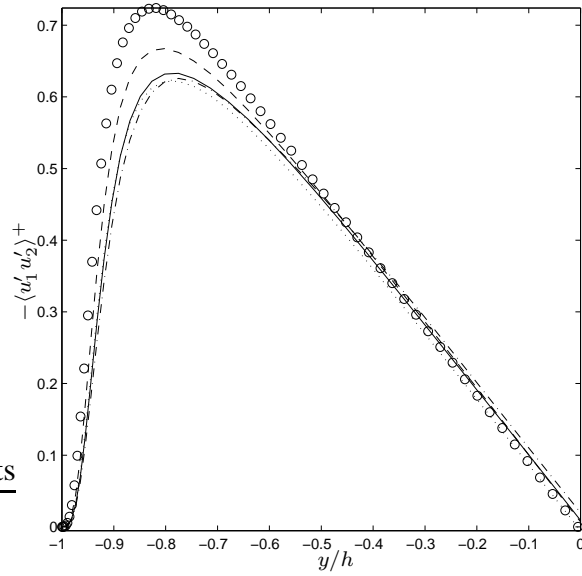


Figure 4.17: Reynolds stress component, $\langle u_1' u_2' \rangle^+$, with dynamic model using filter S1 (—), filter W1 (----), filter FD1 (- · -), and wide version of filter FD1 (···). ○ : component 12 of the stress in the DNS in [34].

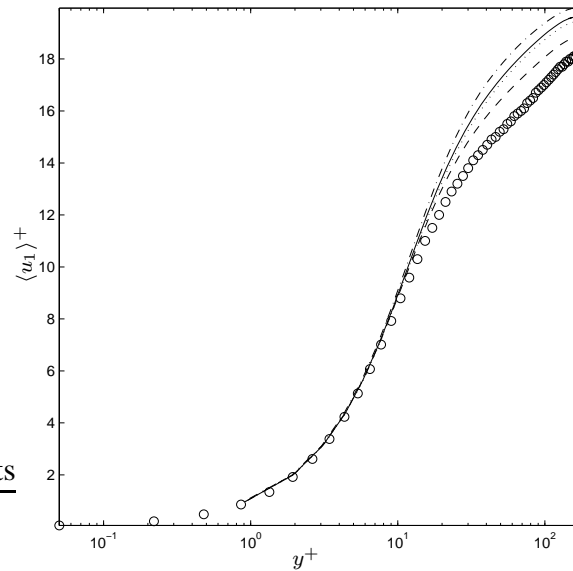


Figure 4.18: Mean streamwise velocity in wall coordinates with dynamic model using filter S1 (—), filter W1 (----), filter FD1 (- · -), and wide version of filter FD1 (···). ○ : mean velocity in the DNS in [34].

4.4 Chapter summary

In this chapter we studied the effect of the test filter on dynamic model LES results of decaying isotropic turbulence and turbulent channel flow. For isotropic turbulence, it was concluded that on a fixed topology results are independent of the filter of choice, as long as its width is computed consistently with formulas based on either the second moment of the filter kernel or the filter transfer function. In the case of turbulent channel flow, similar conclusions were made in the core region of the flow, away from the walls. Near the walls, the filter of choice did play a role, as it was concluded that wider filters yield better results. This was the case for the proposed 3-D, finite element-based filters. In the case of traditional 2-D, finite difference-based filters, the width of the filter did not play such an important role, as results did not change as much when the width was changed.

Turbulent channel simulations in this chapter and throughout this work have been and will be restricted to hexahedral topologies. The reason is that the characteristics of near-wall turbulence are better represented with hexes than with tets or wedges. The latter two introduce a directional bias which negatively impact the near-wall numerical solution. In the case of isotropic turbulence, tet and wedge elements introduce directional bias, but the bias does not affect the solution because the flow is isotropic and thus directionally independent. The same can not be said for near-wall turbulent flow. A study on the effect of element topology on near-wall turbulence is merited, but is beyond the scope of this work.

CHAPTER 5

DYNAMIC FORMULATION OF THE FILTER WIDTH RATIO

The formulation of the dynamic model requires the successive application of two homogeneous filters on the Navier-Stokes equations, namely the primary filter, with kernel $G_{\bar{\Delta}}$, and the test filter, with kernel $G_{\hat{\Delta}}$, leading to a third filter, denoted by $G_{\hat{\Delta}}$. Knowledge of the shapes and widths of $G_{\bar{\Delta}}$ and $G_{\hat{\Delta}}$ is required when assigning the model's only adjustable parameter. This parameter, denoted as the filter width ratio, is defined as the width of kernel $G_{\hat{\Delta}}$ divided by the width of kernel $G_{\bar{\Delta}}$: $\hat{\Delta}/\bar{\Delta}$. When numerically solving the LES equations, the discretization can only represent scales down to its resolution level, and thus implicitly assumes the role of the primary filter $G_{\bar{\Delta}}$, herein referred to as the numerical filter or the grid filter. Unlike the primary filter, the test filter, $G_{\hat{\Delta}}$, is explicit. The damping of small scales in upwind and stabilized finite element methods by introducing an artificial viscosity or some form of dissipation along streamlines (as is done in the Streamline Upwind / Petrov-Galerkin (SUPG) method used here) further suggests that these methods can be interpreted as an implicit filter. Consequently, the name “subgrid-scale motions” becomes appropriate when referring to “residual motions”. In general, the implicit numerical filter is not well-characterized, as discussed in [17], giving rise to a major difficulty when assigning the filter width ratio for the dynamic model. In other words, not knowing the shape and thereby the width of the grid filter, renders it and the filter width ratio unknown. Additionally, results can be sensitive to the filter width ratio as was shown in Chapter 4, thus motivating the need for its accurate determination. This sensitivity issue deserves special attention specifically for cases when LES grids are coarsened, leading to stronger subgrid-scale model dissipations.

To bypass the difficulty of the filter width ratio, if the discretization involves finite differences, the grid filter is often assumed to be twice the characteristic size of the grid, such as

$$\bar{\Delta} = 2(h_1 h_2 h_3)^{1/3} \quad \text{or} \quad \bar{\Delta} = 2(h_1^2 + h_2^2 + h_3^2)^{1/2}, \quad (5.1)$$

where h_i is the grid spacing in the i^{th} -direction. There exists a loose equivalence between

the exact derivative of a filtered variable and the central difference derivative of the unfiltered variable (see [56] [41] and [65]), leading to the conclusion that the implicit numerical filter behaves like the well-known box filter of width twice the grid size. In brief, after choosing the test filter and assuming a specific form for the implicit numerical filter, the filter width ratio can be computed as is shown in [70]. However, in general an assumption regarding the form of the numerical filter can not be made, leaving one to estimate its width.

Explicit filtering of nonlinear terms in the filtered equations has been suggested to remove the indeterminacy of the numerical discretization. However, a study on how it can remove this indeterminacy has not been made. Indeterminacy of the numerical discretizations has not been the main trust behind proponents of explicit filtering of nonlinear terms. The main thrust has been based on the fact that information from the smallest resolvable scales is used to model the unresolvable residual stress, and if such resolvable scales are affected by numerical error, so will the model. Explicit filtering of nonlinear terms can remove the smallest scales polluted by numerical error, thus helping the performance of the residual stress model. However, as observed in [42], there is some benefit from including additional smaller scales in the simulations even if they are contaminated by numerical error. It is suggested by the authors in [42] that this benefit is likely due to the fact that the error is pushed out to small scales which have relatively weak impact on low-order statistics. Instead of exploring explicit filtering of nonlinear terms in the filtered equations, we focus on how to avoid the indeterminacy of the numerical filter by formulating new dynamic models, without directly impacting the equations.

Without the benefit of an equivalence between the stabilized method used here (or for that matter any other method of discretization) and its implied filter, we have chosen to represent the square of the filter width ratio as

$$\alpha \equiv \left(\frac{\hat{\Delta}}{\Delta} \right)^2 = \kappa \left(\frac{\hat{\Delta}}{h} \right)^2, \quad (5.2)$$

where $\hat{\Delta}$ is the width of the well-defined test filter, and h is the size of the grid, appropriate for simulations with tri-linear basis functions. Under this assumption, we have been able to show that for isotropic turbulence, results are independent of the test filter, and κ is a

constant representing the effect of the implicit numerical filter. However, this conclusion did not hold for wall-bounded, in-homogeneous turbulence. In order to potentially obtain a similar result for in-homogeneous turbulence, κ should be a function of the in-homogeneous direction(s) and of the finite element-based test filter. In the core region, far from the walls, κ may cease to depend on the test filter of choice, if test filter widths are computed consistently with one definition, as supported by results in the previous chapter. This implies that the filter width ratio should be a function of in-homogeneous directions as well, giving rise to the notion that perhaps it should be dynamically computed!

Recent works such as [48] and [60] have attempted to address the fact that the dynamic model formulation presupposes that the implicit numerical filters denoted by kernels $G_{\bar{\Delta}}$ and $G_{\hat{\Delta}}$ are self-similar, thus enabling the model's scale-invariance assumption. However, all hopes of knowing in advance the shape of the test filter based on the shape of the primary filter are eliminated because the unknown numerical filter acts as the primary filter. To that extent, the previous two references have investigated several test filters in an effort to find the best filter shape corresponding to best simulation results. Unfortunately, in these studies favorable results have been incorrectly attributed to certain filter shapes due to an inaccurate determination of filter widths, as discussed in [41].

In this chapter, we derive two new dynamic models under the assumption that if the filter width ratio is obtained accurately, the model should be robust enough so that it is independent of the test filter, as it should be in principle. The goal of these new models is to compute the filter width ratio dynamically, thereby accounting for the implicit filter characteristic of the SUPG method. Furthermore, in the derivation of the second of these models it is seen how the lengths scales present in the filter width ratio, $\bar{\Delta}$ and $\hat{\Delta}$, are related to the scale-invariance assumption made in the classic dynamic model. The dynamic formulation of the filter width ratio leads to a scale-dependent, parameter-free dynamic model in which the scale-invariance assumption is not made, thereby eliminating the self-similarity condition between the unknown, implicit, numerical filters, $G_{\bar{\Delta}}$ and $G_{\hat{\Delta}}$.

5.1 Dynamic formulation of the filter width ratio. Part I

Recall the once- and twice-filtered momentum equations,

$$\frac{\partial \bar{u}_i}{\partial t} + \frac{\partial \bar{u}_i \bar{u}_j}{\partial x_j} = -\frac{\partial \bar{p}}{\partial x_i} + \frac{\partial \bar{\tau}_{ij}^\nu}{\partial x_j} \quad (5.3)$$

and

$$\frac{\partial \hat{u}_i}{\partial t} + \frac{\partial \widehat{\bar{u}_i \bar{u}_j}}{\partial x_j} = -\frac{1}{\rho} \frac{\partial \hat{p}}{\partial x_i} + \frac{\partial \widehat{\bar{\tau}_{ij}^\nu}}{\partial x_j}. \quad (5.4)$$

As discussed earlier, the once-filtered equation in (5.3) is obtained by applying a filter with kernel $G_{\bar{\Delta}}$ to the un-filtered momentum equation and the twice-filtered equation in (5.4) is obtained by applying a homogenous test filter with kernel $G_{\hat{\Delta}}$ to the once-filtered equation. Alternatively, the twice-filtered equations can be thought of as resulting from the application of a filter with kernel $G_{\hat{\Delta}}$ to the un-filtered momentum equation. The filter represented by $G_{\hat{\Delta}}$ is obtained from successive applications of the primary filter with kernel $G_{\bar{\Delta}}$ and the test filter, represented by $G_{\hat{\Delta}}$. Now, consider applying a second homogenous test filter with kernel $G_{\tilde{\Delta}}$ to the twice-filtered equations. In that case we obtain

$$\frac{\partial \tilde{u}_i}{\partial t} + \frac{\partial \widetilde{\bar{u}_i \bar{u}_j}}{\partial x_j} = -\frac{1}{\rho} \frac{\partial \tilde{p}}{\partial x_i} + \frac{\partial \widetilde{\bar{\tau}_{ij}^\nu}}{\partial x_j}. \quad (5.5)$$

The thrice-filtered momentum equation in (5.5) can be thought of as resulting from the application of a homogenous filter with kernel $G_{\tilde{\Delta}}$ to the un-filtered momentum equation. This filter is obtained from successive applications of the primary filter denoted by $G_{\bar{\Delta}}$, the test filter, $G_{\hat{\Delta}}$, and the second test filter $G_{\tilde{\Delta}}$.

Recall that the residual stress generated after filtering the momentum equation with the primary filter:

$$\tau_{ij} = \overline{u_i u_j} - \bar{u}_i \bar{u}_j, \quad (5.6)$$

and recall the subtest-scale stress resulting from successive filtering of the momentum

equation with the primary filter and the test filter:

$$T_{ij} = \widehat{\overline{u_i u_j}} - \widehat{\overline{u_i}} \widehat{\overline{u_j}}. \quad (5.7)$$

Analogously, successive filtering of the momentum equation with the primary, test, and the second test filter yields the following secondary subtest-scale stress:

$$\mathcal{T}_{ij} = \widetilde{\overline{\overline{u_i u_j}}} - \widetilde{\overline{\overline{u_i}}} \widetilde{\overline{\overline{u_j}}}. \quad (5.8)$$

Throughout this chapter, the often-named subgrid-scale stress in (5.6) will be referred to as the stress at the $G_{\overline{\Delta}}$ -level, and the stress in (5.7) will be referred to as the stress at the $G_{\widehat{\Delta}}$ -level. Similarly, the stress in (5.8) will be referred to as the stress at the $G_{\widetilde{\Delta}}$ -level.

Under the assumption of scale-invariance, the deviatoric portions of the stresses at the $G_{\overline{\Delta}}$ -level and at the $G_{\widehat{\Delta}}$ -level are represented through the Smagorinsky model as

$$\tau_{ij}^d = -2(C_s \overline{\Delta})^2 |\overline{S}| \overline{S}_{ij}, \quad (5.9)$$

and

$$T_{ij}^d = -2(C_s \widehat{\Delta})^2 |\widehat{S}| \widehat{S}_{ij}, \quad (5.10)$$

respectively. Analogously, the deviatoric portion of the stress at the $G_{\widetilde{\Delta}}$ -level can be modeled as

$$\mathcal{T}_{ij}^d = -2(C_s \widetilde{\Delta})^2 |\widetilde{S}| \widetilde{S}_{ij}, \quad (5.11)$$

where the strain rate tensor, \widetilde{S}_{ij} , and its norm, $|\widetilde{S}|$, are based on the thrice-filtered velocity $\widetilde{\overline{\overline{u_i}}}$. Note that here we have assumed scale-invariance, thus the modeled stresses in (5.9), (5.10), and (5.11) share the same Smagorinsky coefficient, C_s .

The Germano identity in (2.19) used for the classical dynamic model involves the stresses at the $G_{\overline{\Delta}}$ -level and the $G_{\widehat{\Delta}}$ -level. An analogous identity to that of Germano, this

time between the stresses at the $G_{\widehat{\Delta}}$ -level and the $G_{\widetilde{\Delta}}$ -level, leads to

$$Q_{ij} = \mathcal{T}_{ij} - \widetilde{T}_{ij}, \quad (5.12)$$

which can be modeled through the Smagorinsky-type expressions in (5.10) and (5.11) and can be expressed through resolved quantities as

$$Q_{ij} = \widetilde{\widehat{u}}_i \widetilde{\widehat{u}}_j - \widetilde{\widetilde{u}}_i \widetilde{\widetilde{u}}_j \quad (5.13)$$

by using (5.7) and (5.8). The square of the difference between the modeled and resolved expressions for the the deviatoric portion of Q_{ij} (Q_{ij}^d) is given as $D_{ij}D_{ij}$, where

$$D_{ij} = Q_{ij}^d - 2(C_s \widehat{\Delta})^2 N_{ij}, \quad (5.14)$$

and Q_{ij}^d is the deviatoric portion of the resolved tensor Q_{ij} in (5.13). Tensor N_{ij} is

$$N_{ij} = |\widetilde{\widehat{S}}| \widetilde{\widehat{S}}_{ij} - \gamma |\widetilde{\widetilde{S}}| \widetilde{\widetilde{S}}_{ij}, \quad (5.15)$$

where $\gamma = (\widetilde{\widehat{\Delta}}/\widehat{\Delta})^2$. Minimization of (5.14) with respect to C_s leads to

$$(C_s \widehat{\Delta})^2 = \frac{1}{2} \frac{\langle Q_{ij} N_{ij} \rangle}{\langle N_{kl} N_{kl} \rangle}, \quad (5.16)$$

where Q_{ij} in (5.13) is used. The brackets denote averaging over spatially homogenous directions, such as is done for $(C_s \widehat{\Delta})^2$ in (2.23). Notice that tensor N_{ij} requires knowledge of a ratio between filter widths, γ , analogous to tensor M_{ij} in (2.22). The ratio γ can be expressed as

$$\gamma = \left(\frac{\widetilde{\widehat{\Delta}}}{\widehat{\Delta}} \right)^2 = \frac{(\widetilde{\widehat{\Delta}}/\widehat{\Delta})^2}{(\widehat{\Delta}/\widetilde{\widehat{\Delta}})^2}. \quad (5.17)$$

The denominator in the previous expression can be thought of as the square of the filter width ratio, α , appearing in tensor M_{ij} in (2.22) of the classical dynamic model when finite element-based, standard filter S1 or S2 is used as the test filter. The numerator can be

thought of as α when finite element-based, wide filter W1 or W2 is used as the test filter. Re-defining α in the way of (4.2), γ becomes

$$\gamma = \frac{(\widetilde{\Delta}/\bar{\Delta})^2}{(\widehat{\Delta}/\bar{\Delta})^2} = \frac{\kappa_1(\widetilde{\Delta}/h)^2}{\kappa_2(\widehat{\Delta}/h)^2} = \frac{\kappa_1}{\kappa_2} \left(\frac{\widetilde{\Delta}}{\widehat{\Delta}} \right)^2, \quad (5.18)$$

where $\widetilde{\Delta}$ is the width of the wide test filter and $\widehat{\Delta}$ is the width of the standard test filter. It was concluded in the Chapter 4 that for isotropic turbulence, dynamic model results are independent of the test filter (S1, S2, W1, or W2) as long as the test filter width is computed accurately and consistently. Dynamic model results of isotropic turbulence with the standard and wide finite element-based filters have been shown to be nearly indistinguishable, thus $\kappa_1 \approx \kappa_2$ can be taken, leading to

$$\gamma = \frac{\kappa_1}{\kappa_2} \left(\frac{\widetilde{\Delta}}{\widehat{\Delta}} \right)^2 = \left(\frac{\widetilde{\Delta}}{\widehat{\Delta}} \right)^2, \quad (5.19)$$

where the last ratio involves solely the widths of the explicitly applied wide and standard test filters. This ratio between test filters can be computed with definitions shown and used earlier, giving rise to at least an approximate expression for γ and thus the right hand side of (5.16) ($\langle\langle Q_{ij}N_{ij} \rangle\rangle / \langle\langle N_{kl}N_{kl} \rangle\rangle$). Note that for near-wall turbulence, $\kappa_1 \neq \kappa_2$, as their optimal values may be unknown functions of the in-homogenous direction and the test filter used.

Next, we divide the expression in (5.16) by that in (2.23) leading to

$$\alpha = \left(\frac{\widehat{\Delta}}{\bar{\Delta}} \right)^2 = \frac{\langle\langle Q_{mn}N_{mn} \rangle\rangle \langle\langle M_{kl}M_{kl} \rangle\rangle}{\langle\langle N_{pq}N_{pq} \rangle\rangle \langle\langle L_{ij}M_{ij} \rangle\rangle}. \quad (5.20)$$

Recall that $\langle\langle Q_{mn}N_{mn} \rangle\rangle / \langle\langle N_{mn}N_{mn} \rangle\rangle$ can be approximately computed as was previously described, and M_{ij} in (2.22) is a function of α . Hence, expansion of (5.20) leads to the following quadratic algebraic equation for α :

$$c_0 - c_1\alpha + c_2\alpha^2 = 0, \quad (5.21)$$

where

$$\begin{aligned}
c_2 &= \frac{\langle Q_{mn}N_{mn} \rangle}{\langle N_{pq}N_{pq} \rangle} \left\langle |\widehat{S}|^2 \left(\widehat{S}_{ij} \right)^2 \right\rangle + \langle L_{ij}|\widehat{S}|\widehat{S}_{ij} \rangle \\
c_1 &= 2 \frac{\langle Q_{mn}N_{mn} \rangle}{\langle N_{pq}N_{pq} \rangle} \left\langle |\widehat{S}|\widetilde{S}_{ij}|\widehat{S}|\widetilde{S}_{ij} \right\rangle + \langle L_{ij}|\widehat{S}|\widetilde{S}_{ij} \rangle \\
c_0 &= \frac{\langle Q_{mn}N_{mn} \rangle}{\langle N_{pq}N_{pq} \rangle} \left\langle \left(|\widehat{S}|\widetilde{S}_{ij} \right)^2 \right\rangle.
\end{aligned} \tag{5.22}$$

Solution of the quadratic equation in (5.21) yields a dynamic filter width ratio, which can be used to calculate the dynamic model coefficient in (2.23). The only input parameter is the ratio between the widths of the test filters in (5.19), $(\widehat{\Delta}/\widetilde{\Delta})^2$, which can be directly computed once the standard and wide test filters have been defined. Note that the width of the numerical filter is no longer required.

5.1.1 Numerical results with decaying isotropic turbulence

As can be seen, the finite element-based filters presented in Chapter 3 lend perfectly for implementation of the previously derived dynamic filter width ratio (DFWR) formulation. In expressions (5.16) (5.21) and (5.22), filter S1 or S2 can act as the first test filter, denoted with an over-hat, $\widehat{\cdot}$. Furthermore, the finite element-based (FE-based) trapezoidal filter can act as the second test filter denoted with an over-tilde, $\widetilde{\cdot}$. Recall that application of filter S1 (viz. S2) followed by application of the FE-based trapezoidal filter yields wide filter W1 (viz. W2). Thus, we refer to using filters S1 and the FE-based trapezoidal rule to compute the dynamic model parameter α through (5.21) as DFWR with S1 and W1. Furthermore, we refer to using filters S2 and the FE-based trapezoidal rule to compute the dynamic filter width ratio α through (5.21) as DFWR with S2 and W2.

In Figures 5.1, 5.2, and 5.3, we present isotropic turbulence simulations results using the dynamic Smagorinsky model with DFWR on the hex, tet, and wedge grids discussed in Chapter 4. Recall that these grids have 33 vertices in each direction, x_1 , x_2 , and x_3 . Furthermore, the domain is 2π -periodic in each of these directions. The initial conditions at non-dimensional time station t_{42} are those described in Chapter 4, and results are compared in terms of energy spectrum to the experiments of Comte-Bellot and Corrsin in [9] at t_{98} .

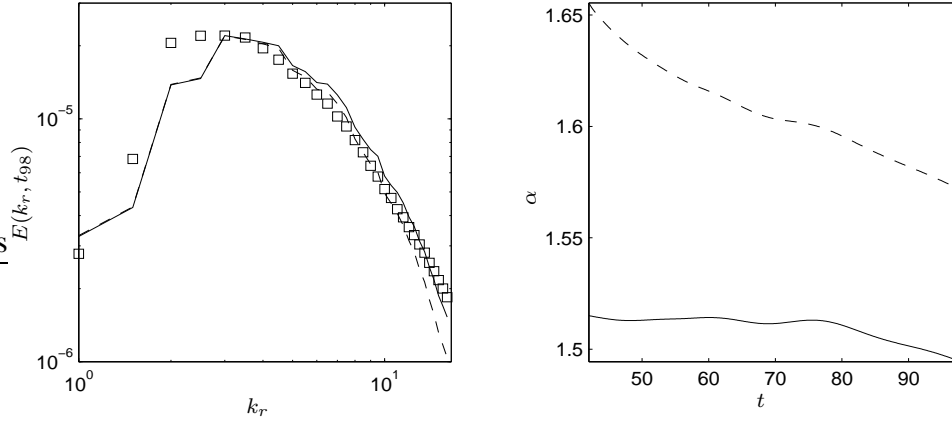


Figure 5.1: Dynamic model simulations on hexes with DFWR. Energy spectra at t_{98} are shown on the left and temporal evolution of the filter width ratios squared are shown on the right. — : DFWR with $(\tilde{\Delta}/\hat{\Delta})^2 = 2.9$ and filters S1 and W1; ---- : DFWR with $(\tilde{\Delta}/\hat{\Delta})^2 = 2.4$ and filters S2 and W2.

From the previous three figures we see that the energy spectra at t_{98} of the numerical solutions match the experimental spectrum quite well, demonstrating the success of the dynamic model with the DFWR formulation. Compared to the dynamic models with fixed filter width ratios based on the assumption in (5.2) with $\kappa = 1$ and test filter widths based on the second moment of the filter transfer function, DFWR yields higher values of the model coefficient, leading to a less energetic flow at t_{98} reflected in the energy spectrum. This can be seen by comparing the over-predicted energy spectrum at t_{98} in Figure 4.1 corresponding to $\alpha = 3$ to the improved energy spectra with DFWR in Figure 5.1.

The DFWR has essentially obviated the importance of the width of the undefined grid filter by spectrally sampling the resolved field and inherently extracting this information. Furthermore, with the difficulty of determining the dynamic model parameter α out of the way, we can truly say that the dynamic model on grids of hexahedral, tetrahedral, and wedge elements performs equally well at least for decaying isotropic turbulence. In Figures 5.1, 5.2, and 5.3, we see that the energy spectra on hexes, tets and wedges predicted with DFWR are very similar, especially in the inertial range around $k_r = 9$. Despite the vast difference between standard and wide test filters and despite the directional bias introduced by the tet and wedge grids and the test filters on these topologies, the model can adequately represent the cascading transfer of energy that occurs in decay of isotropic

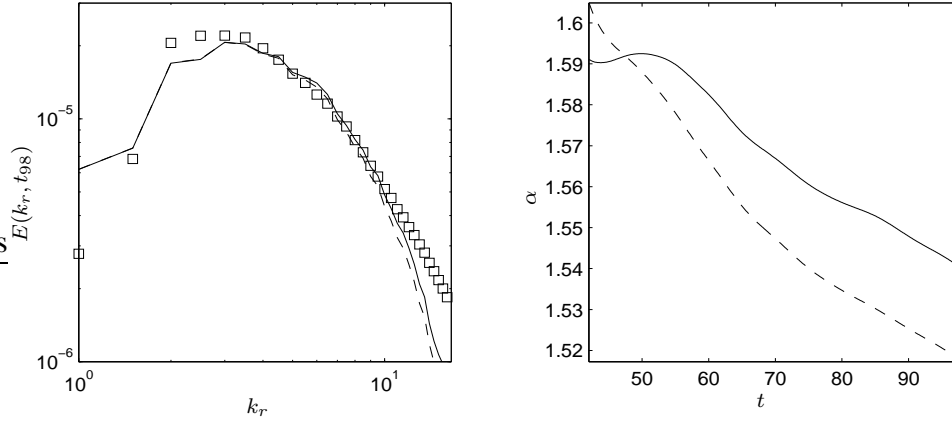


Figure 5.2: Dynamic model simulations on tets with DFWR. Energy spectra at t_{98} are shown on the left and temporal evolution of the filter width ratios squared are shown on the right. — : DFWR with $(\tilde{\Delta}/\hat{\Delta})^2 = 2.9$ and filters S1 and W1; ---- : DFWR with $(\tilde{\Delta}/\hat{\Delta})^2 = 2.6$ and filters S2 and W2.

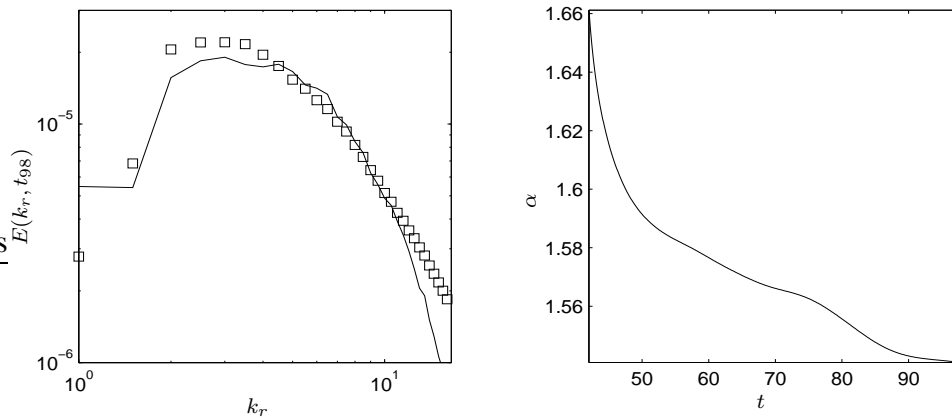


Figure 5.3: Dynamic model simulations on wedges with DFWR and $(\tilde{\Delta}/\hat{\Delta})^2 = 2.6$. Energy spectra at t_{98} are shown on the left and temporal evolution of the filter width ratio squared is shown on the right. DFWR uses filters S2 and W2.

turbulence. This shows the robustness of the model.

5.1.2 Test filter widths in the DFWR

The only information required in the formulation of DFWR is the width of the finite element-based test filters used. More specifically, we need the ratio between the widths of the standard and wide filters used, $\tilde{\Delta}/\hat{\Delta}$, referred to as the test filter width ratio. Recall that the width of these filters may be defined as π/k_r^* , where k_r^* is the average radial

$G(\mathbf{k}^*)$	(width of W1) ² /(width of S1) ²	(width of W2) ² /(width of S2) ²
0.5	2.75	2.37 \approx 2.4
0.65	2.86 \approx 2.9	2.43 \approx 2.4
0.75	2.87 \approx 2.9	2.44 \approx 2.4
0.85	2.91 \approx 2.9	2.5

Table 5.1: Limiting values of test filter width ratios $\tilde{\Delta}/\hat{\Delta}$ for filters on hexes.

$G(\mathbf{k}^*)$	(width of W1) ² /(width of S1) ²	(width of W2) ² /(width of S2) ²
0.5	2.71	2.51
0.65	2.82 \approx 2.8	2.57 \approx 2.6
0.75	2.89 \approx 2.9	2.59 \approx 2.6
0.85	2.92 \approx 2.9	2.63 \approx 2.6

Table 5.2: Limiting values of test filter width ratios $\tilde{\Delta}/\hat{\Delta}$ for filters on tets.

wavenumber for which the filter transfer function is a specified value. Here, we discuss how we choose this value. In Tables 3.1 and 3.2 in Chapter 3 we presented test filter widths for various specified values of the transfer functions of standard and wide filters on hexes and tets. From these tables we see that as the specified value of the transfer functions varies between 0.5 and 1.0, the ratio between the filter widths of W1 (viz. W2) and S1 (viz. S2) is roughly constant. We choose this constant as the test filter width ratio in DFWR. The constant behavior of the test filter width ratios is made clear by Tables 5.1 and 5.2. A similar behavior was found between standard and wide test filters on wedges. Although the test filter widths depend on a specified value of the filter transfer functions, remarkably this dependence is practically non-existent in the test filter width ratios.

5.2 Dynamic formulation of the filter width ratio. Part II: A parameter-free model

The dynamic model with dynamic estimation of the filter width ratio derived in the previous section is only valid for isotropic turbulence for which the assumption in (5.19) was shown to hold. In the case of wall-bounded flows this was not the case. Thus, we would like to derive a more general formulation of the filter width ratio with less restrictions. To that extent, consider the stresses at the $G_{\tilde{\Delta}}$ -level, the $G_{\hat{\Delta}}$ -level and the $G_{\tilde{\tilde{\Delta}}}$ -level

in (5.6), (5.7) and (5.8), respectively. Let us model these stresses using the Smagorinsky model, but this time without making the scale-invariance assumption. In that case, we obtain at the $G_{\bar{\Delta}}$ -level

$$\tau_{ij}^d = -2(C_s^{\bar{\Delta}} \bar{\Delta})^2 |\bar{S}| \bar{S}_{ij}, \quad (5.23)$$

at the $G_{\hat{\Delta}}$ -level

$$T_{ij}^d = -2(C_s^{\hat{\Delta}} \hat{\Delta})^2 |\hat{S}| \hat{S}_{ij}, \quad (5.24)$$

and at the $G_{\tilde{\Delta}}$ -level

$$\mathcal{T}_{ij}^d = -2(C_s^{\tilde{\Delta}} \tilde{\Delta})^2 |\tilde{S}| \tilde{S}_{ij}. \quad (5.25)$$

where none of the Smagorinsky coefficients, $C_s^{\bar{\Delta}}$, $C_s^{\hat{\Delta}}$ and $C_s^{\tilde{\Delta}}$ are equal to each other. Least-squares minimization of the difference between the modeled and resolved expressions for the Germano identity between the stresses at the $G_{\hat{\Delta}}$ -level and the $G_{\bar{\Delta}}$ -level with respect to $C_s^{\bar{\Delta}}$ leads to

$$(C_s^{\bar{\Delta}} \bar{\Delta})_{\text{std}}^2 = \frac{1}{2} \frac{\langle L_{ij} M_{ij} \rangle}{\langle M_{kl} M_{kl} \rangle} \equiv \Theta_1(\alpha \zeta), \quad (5.26)$$

where L_{ij} is given in (2.19) and now M_{ij} becomes

$$M_{ij} = |\widehat{S}| \widehat{S}_{ij} - \alpha \zeta |\hat{S}| \hat{S}_{ij}. \quad (5.27)$$

Parameter $\alpha \equiv (\hat{\Delta}/\bar{\Delta})^2$ is the square of the filter width ratio as before, and $\zeta \equiv (C_s^{\hat{\Delta}}/C_s^{\bar{\Delta}})^2$. The subscript ‘‘std’’ in (5.26) symbolizes that the over-hat notation, $\widehat{\cdot}$, denotes potential application of one of the standard finite element-based filters (S1 or S2). Next, least-squares minimization of the difference between the modeled and resolved expressions for the Germano identity between the stresses at the $G_{\bar{\Delta}}$ -level and the $G_{\tilde{\Delta}}$ -level yields

$$(C_s^{\bar{\Delta}} \bar{\Delta})_{\text{wide}}^2 = \frac{1}{2} \frac{\langle \mathcal{L}_{ij} \mathcal{M}_{ij} \rangle}{\langle \mathcal{M}_{kl} \mathcal{M}_{kl} \rangle} \equiv \Theta_2(\beta \eta), \quad (5.28)$$

where

$$\mathcal{L}_{ij} = \widetilde{\widetilde{u_i u_j}} - \widetilde{u_i} \widetilde{u_j}, \quad (5.29)$$

$$\mathcal{M}_{ij} = |\widetilde{\widetilde{S}}| \widetilde{\widetilde{S}}_{ij} - \beta \eta |\widetilde{\widetilde{S}}| \widetilde{\widetilde{S}}_{ij}, \quad (5.30)$$

$\beta \equiv (\widetilde{\widetilde{\Delta}}/\widetilde{\Delta})^2$, and $\eta \equiv (C_s^{\widetilde{\widetilde{\Delta}}}/C_s^{\widetilde{\Delta}})^2$. The subscript “wide” in (5.28) symbolizes that the over-hat-tilde notation, $\widetilde{\widetilde{\cdot}}$, denotes potential application of one of the wide, finite element-based filters (W1 or W2).

For the moment, let us digress and assume scale-invariance, thus $\zeta = 1$ and $\eta = 1$ implying $C_s^{\widetilde{\Delta}} = C_s^{\widehat{\Delta}} = C_s^{\widetilde{\widetilde{\Delta}}} = C_s$. Furthermore, let us take the assumption for the filter width ratio in (4.2), thus

$$\alpha \equiv \left(\frac{\widehat{\Delta}}{\widetilde{\Delta}} \right)^2 = \kappa_1 \left(\frac{\widehat{\Delta}}{h} \right)^2 \quad (5.31)$$

and

$$\beta = \left(\frac{\widetilde{\widetilde{\Delta}}}{\widetilde{\Delta}} \right)^2 \equiv \kappa_2 \left(\frac{\widetilde{\widetilde{\Delta}}}{h} \right)^2 \quad (5.32)$$

with $\kappa_1 = \kappa_2 = \kappa$. In Chapter 4 it was shown that under these assumptions, the dynamic model coefficients in (5.26) and (5.28) give nearly identical results, as long as test filter widths $(\widetilde{\widetilde{\Delta}}/h)$ and $(\widehat{\Delta}/h)$ are computed consistently. For example, tracking the temporal behavior of model coefficients given by (5.26) and (5.28) in our simulations of decaying isotropic turbulence on hexes performed in sub-section 4.2.2 in Chapter 4, we can see that the ratio between these coefficients, $(C_s \widetilde{\Delta})_{\text{std}}^2 / (C_s \widetilde{\Delta})_{\text{wide}}^2$, is nearly one, as is shown in Figure 5.4. For isotropic turbulence, the classic dynamic model produces nearly identical model coefficients regardless of the finite element-based filter used. In the case of wall-bounded flows, a similar conclusion was made for the core region far from walls, based on results shown in Figure 4.7 in Chapter 4. However, this conclusion did not hold in near-wall regions, suggesting that $\kappa_1 = \kappa_2$ is not valid and that both parameters need to be

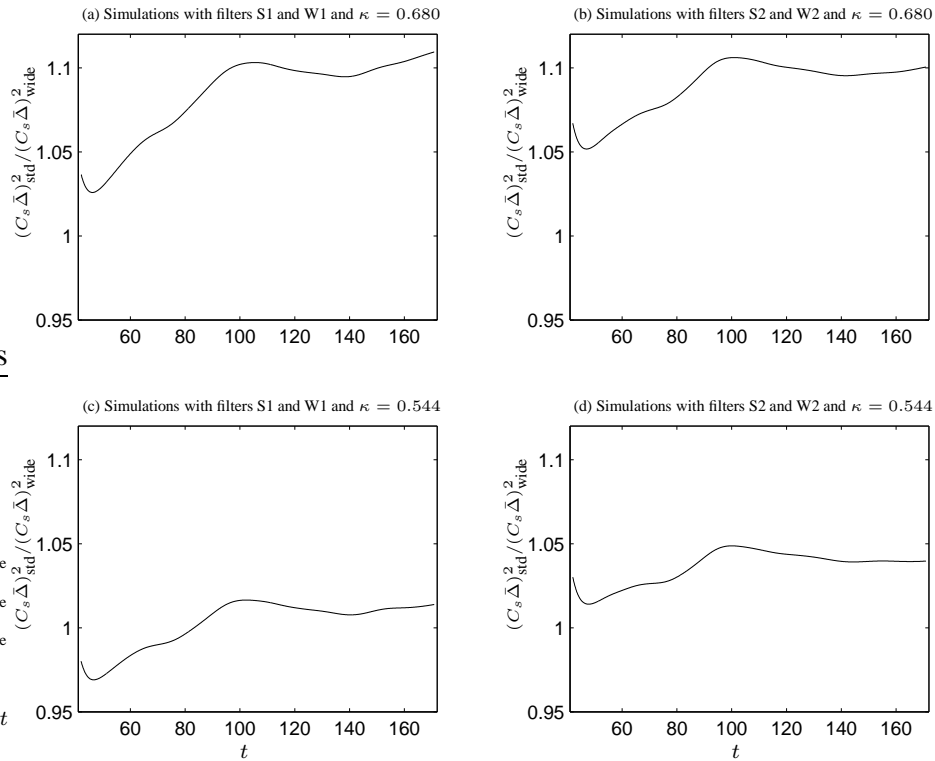


Figure 5.4: Ratio between dynamic model coefficients in decaying isotropic turbulence on hexes obtained using standard and wide filters. These results correspond to the simulations in sub-section 4.2.2 of Chapter 4.

functions of the in-homogenous direction(s) in order to obtain nearly the same dynamic model coefficient regardless of the finite element-based test filter. Consequently, the filter width ratios α and β in (5.31) and (5.32) would have to be functions of the in-homogeneous direction(s) as well.

Let us return to the full expressions for the model coefficient based on a standard filter in (5.26) or on a wide filter in (5.28) without invoking scale-invariance nor assuming a form for the filter width ratio squared as done in (5.31) and (5.32). Looking at the dynamic model coefficients with standard and wide test filters in (5.26) and (5.28), respectively, we have two unknowns, namely $\alpha\zeta$ and $\beta\eta$. Results shown in Figure 5.4 motivate equating (5.26) and (5.28) thus giving us the first equation for the two unknowns ($\alpha\zeta$ and $\beta\eta$):

$$\Theta_1(\alpha\zeta) = \Theta_2(\beta\eta). \quad (5.33)$$

Equation (5.33) establishes the idealistic principle that if $\alpha\zeta$ and $\beta\eta$ (involving filter width

ratios and Smagorinsky coefficients at different residual stress levels) are properly computed as functions of the in-homogeneous direction(s) and time, then the dynamic model coefficient should be independent of the test filter.

In deriving a scale-dependent model in [54], Porté-Angel *et al.* arrive at a similar equation to that in (5.33), involving two test filters, one being twice wider than the other. Within the context of our expressions in (5.26), (5.28), and (5.33), they set their filter width ratios as $\alpha = 2^2$ and $\beta = 4^2$ and use different test filters from the ones described here. Their motivation is obtaining a scale-dependent model, and not obtaining a model with a dynamic filter width ratio. Our equation in (5.33) is more general than their scale-dependent equation, given that in addition to being scale-dependent, it does not assume any values for the filter width ratios. Furthermore, even after setting values for the filter width ratios, expression (5.33) still has two unknowns, namely ζ and η . To that extent, Porté-Angel *et al.* assume a power law behavior for $C_s^{\hat{\Delta}}$, which in our notation leads them to the form $\eta = \zeta^2$. Here, we will obtain a second scale-dependent equation that coupled with equation (5.33) can be used to solve for the pair of unknowns $\alpha\zeta$ and $\beta\eta$, without the need to assume a power law behavior for the Smagorinsky coefficient.

A second equation complementing (5.33) for the unknowns $\alpha\zeta$ and $\beta\eta$ is obtained by considering the analogous identity to that of Germano between the stresses at the $G_{\hat{\Delta}}$ -level and the $G_{\tilde{\Delta}}$ -level, first proposed in the previous section in (5.12). Least-squares minimization (with respect to $C_s^{\tilde{\Delta}}$) of the difference between the modeled and resolved expressions for the deviatoric portion of Q_{ij} in (5.12), leads to

$$(C_s^{\hat{\Delta}})^2 = \frac{1}{2} \frac{\langle Q_{ij} N_{ij} \rangle}{\langle N_{kl} N_{kl} \rangle}, \quad (5.34)$$

where

$$N_{ij} = |\widetilde{\widetilde{S}}|_{\tilde{S}_{ij}} - \gamma \vartheta |\widetilde{\widetilde{S}}|_{\tilde{S}_{ij}} \quad (5.35)$$

and Q_{ij} is given in (5.12). The modeled expression for Q_{ij} is obtained following (5.12) and using (5.24) and (5.25). The resolved expression for Q_{ij} is given in (5.13). In (5.35), $\gamma = (\tilde{\Delta}/\hat{\Delta})^2$ and $\vartheta = C_s^{\tilde{\Delta}}/C_s^{\hat{\Delta}}$. Expression (5.34) seemingly introduces one more unknown in

the form of $\gamma\vartheta$ until we re-express it as

$$\begin{aligned}
\gamma\vartheta &= \left(\frac{\widetilde{\hat{\Delta}}}{\hat{\Delta}} \right)^2 \left(\frac{C_s^{\hat{\Delta}}}{C_s^{\bar{\Delta}}} \right)^2 \\
&= \frac{(\widetilde{\hat{\Delta}}/\bar{\Delta})^2 (C_s^{\hat{\Delta}}/C_s^{\bar{\Delta}})^2}{(\hat{\Delta}/\bar{\Delta})^2 (C_s^{\hat{\Delta}}/C_s^{\bar{\Delta}})^2} \\
&= \frac{\beta\eta}{\alpha\zeta} = \frac{\beta\eta}{\alpha\zeta}.
\end{aligned} \tag{5.36}$$

Recall that $\alpha\zeta$ and $\beta\eta$ are the unknowns in (5.33). Letting

$$(C_s^{\hat{\Delta}} \hat{\Delta})^2 = \frac{1}{2} \frac{\langle Q_{ij} N_{ij} \rangle}{\langle N_{kl} N_{kl} \rangle} \equiv \Phi \left(\frac{\beta\eta}{\alpha\zeta} \right) \tag{5.37}$$

and dividing the expression in (5.37) by the expression in (5.26), we obtain

$$\left(\frac{C_s^{\hat{\Delta}}}{C_s^{\bar{\Delta}}} \right)^2 \left(\frac{\hat{\Delta}}{\bar{\Delta}} \right)^2 \equiv \alpha\zeta = \frac{\Phi \left(\frac{\beta\eta}{\alpha\zeta} \right)}{\Theta_1(\alpha\zeta)}. \tag{5.38}$$

Thus, we have our second equation for the unknowns $\alpha\zeta$ and $\beta\eta$. In what we refer to as DFWR2, we solve the full versions of the nonlinear algebraic coupled equations in (5.33) and (5.38) for $\alpha\zeta$ and $\beta\eta$ giving rise to a parameter-free, scale-dependent dynamic model in (5.26) or equivalently (5.28). The coupled nonlinear equations can be solved iteratively using Newton's method as described in [16]. Letting $\alpha\zeta = \xi_1$ and $\beta\eta = \xi_2$, the Newton iterations become

$$\begin{bmatrix} \xi_1^{i+1} \\ \xi_2^{i+1} \end{bmatrix} = \begin{bmatrix} \xi_1^i \\ \xi_2^i \end{bmatrix} - \begin{bmatrix} \Theta_{,\xi_1}(\xi_1^i, \xi_2^i) & \Theta_{,\xi_2}(\xi_1^i, \xi_2^i) \\ \Psi_{,\xi_1}(\xi_1^i, \xi_2^i) & \Psi_{,\xi_2}(\xi_1^i, \xi_2^i) \end{bmatrix}^{-1} \begin{bmatrix} \Theta(\xi_1^i, \xi_2^i) \\ \Psi(\xi_1^i, \xi_2^i) \end{bmatrix}, \tag{5.39}$$

where

$$\Theta(\xi_1, \xi_2) \equiv \Theta_1(\xi_1) - \Theta_2(\xi_2) \tag{5.40}$$

and

$$\Psi(\xi_1, \xi_2) \equiv \frac{\Phi(\xi_2/\xi_1)}{\Theta_1(\xi_1)}. \quad (5.41)$$

In our efforts to derive a dynamic formulation for the filter width ratio, we have arrived at a scale-dependent model in the same spirit as the scale-dependent model of Porté-Angel *et al.*, yet more general. In the scale-dependent model of Porté-Angel *et al.*, scale-dependency is associated only with the Smagorinsky coefficients in the models for the stresses at different filter levels such as (5.23), (5.24), and (5.25), while the filter width ratios are assumed known. However, in our scale-dependent model the filter widths are very much related to scale-dependency, as they can be absorbed into the Smagorinsky coefficients at the different filter levels.

5.2.1 Numerical results with decaying isotropic turbulence

In this sub-section we present dynamic model results with DFWR2 and compare them with those of the dynamic model with DFWR1, the first version of the dynamic filter width ratio formulation in the previous section. We test DFWR2 on the decay of isotropic turbulence using the same hexahedral, tetrahedral and wedge grids described earlier. The domain is a 2π -periodic cube with a grid of 33 evenly spaced vertices in all three directions. For all the simulations presented, different initial guesses used in Newton's method for DFWR2 led to practically equal solutions.

First, in Figure 5.5 we present the energy spectrum of decaying isotropic turbulence on hexes at the non-dimensional time station t_{98} . Figure 5.6 shows the evolution of $\alpha\zeta$, herein referred to as simply the filter width ratio squared. For both DFWR2 and DFWR1, the energy spectrum at t_{98} is similar. Furthermore, the temporal evolution of the filter width ratio squared is roughly the same for DFWR1 and DFWR2 both using filters S1 and W1. In the case when both use filters S2 and W2, the filter width ratio squared corresponding to DFWR2 is slightly higher than that of DFWR1. However, this slight difference hardly impacts the energy spectrum for these two cases.

In Figure 5.7 and Figure 5.8, we present results of the same problem but on the tetrahedral grid, mentioned earlier. The results parallel those of the simulations performed on the hexahedral grid.

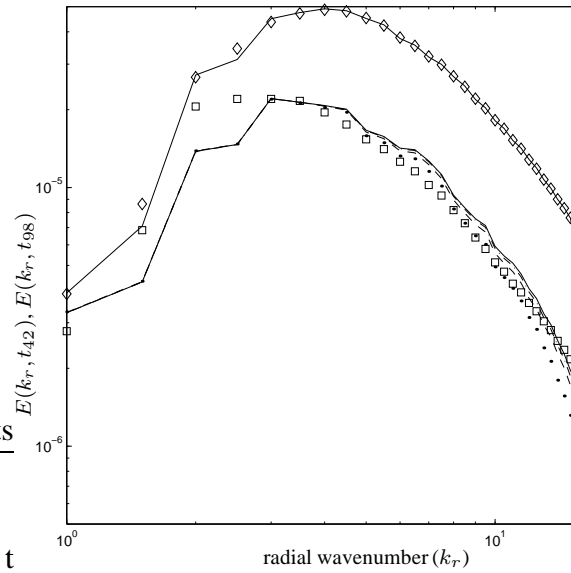


Figure 5.5: Energy of the initial condition at t_{42} and energy at t_{98} after simulations with DFWR1 and DFWR2 on the hexahedral grid. — : initial energy for all simulations; — : DFWR2 with filters S1 and W1; ---- : DFWR2 with S2 and W2; - · - : DFWR1 with S1 and W1; · · · : DFWR1 with S2 and W2; \diamond : data at t_{42} ; \square : data at t_{98} .

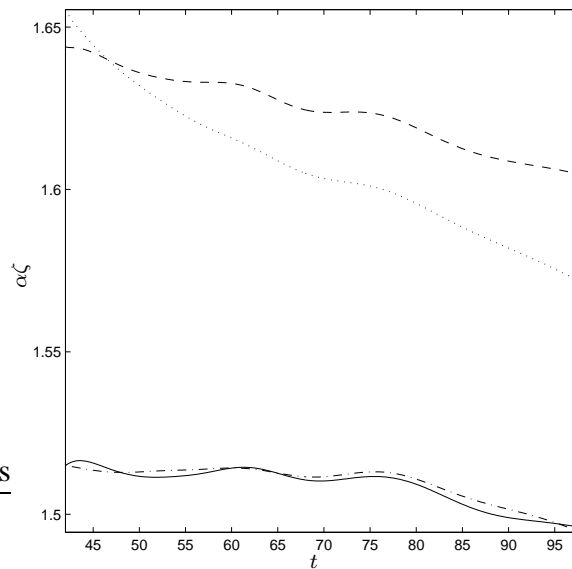


Figure 5.6: Temporal evolution of predicted filter width ratios in the simulations on the hexahedral grid. — : DFWR2 with filters S1 and W1; ---- : DFWR2 with S2 and W1; - · - : DFWR1 with S1 and W1; · · · : DFWR1 with S2 and W2. In DFWR1 $\zeta = 1$.

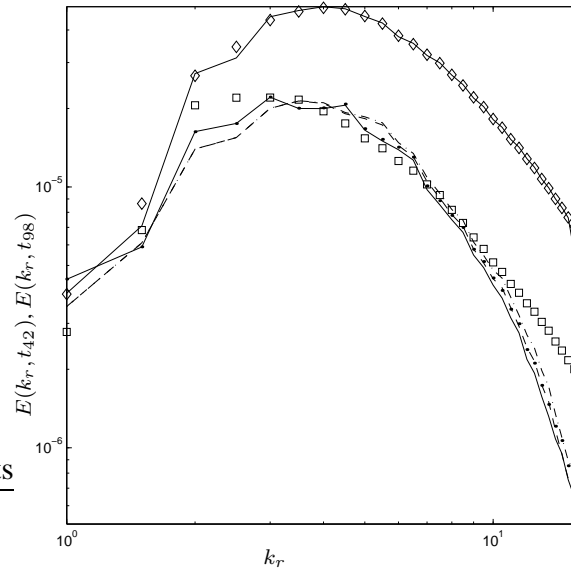


Figure 5.7: Energy of the initial condition at t_{42} and energy at t_{98} after simulations with DFWR1 and DFWR2 on the tetrahedral grid. — : initial energy for all simulations; — : DFWR2 with filters S1 and W1; ---- : DFWR2 with S2 and W2; - · - : DFWR1 with S1 and W1; · · · : DFWR1 with S2 and W2; \diamond : data at t_{42} ; \square : data at t_{98} .

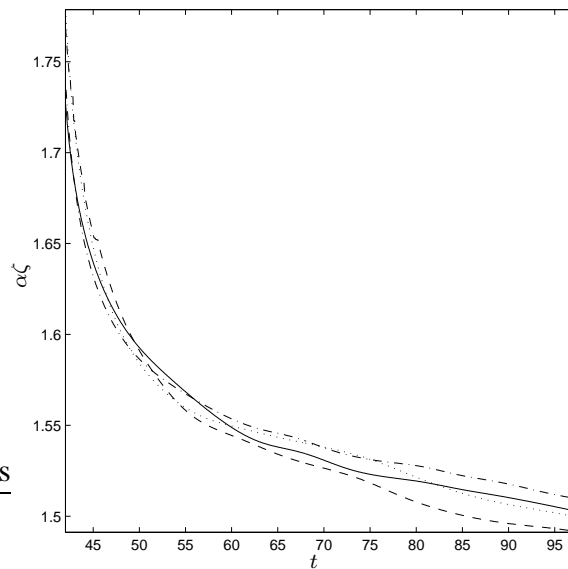


Figure 5.8: Temporal evolution of predicted filter width ratios in the simulations on the tetrahedral grid. — : DFWR2 with filters S1 and W1; ---- : DFWR2 with S2 and W2; - · - : DFWR1 with S1 and W1; · · · : DFWR1 with S2 and W2. In DFWR1 $\zeta = 1$.

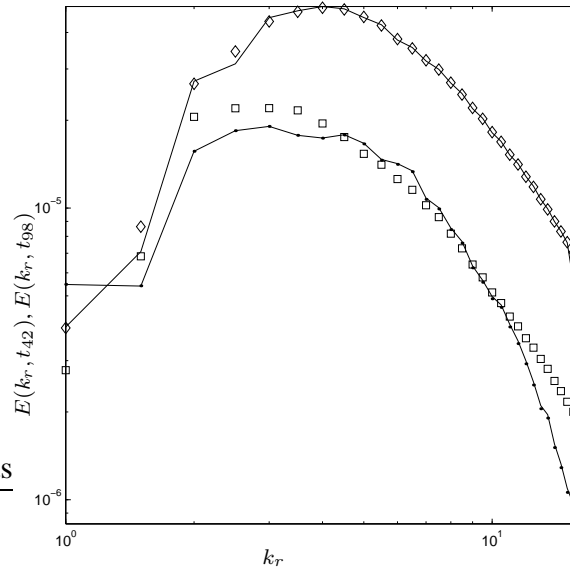


Figure 5.9: Energy of the initial condition at t_{42} and energy at t_{98} after simulations with DFWR1 and DFWR2 on the wedge grid. — : initial energy for all simulations; — : DFWR2 with filters S2 and W2; ---- : DFWR1 with S2 and W2.

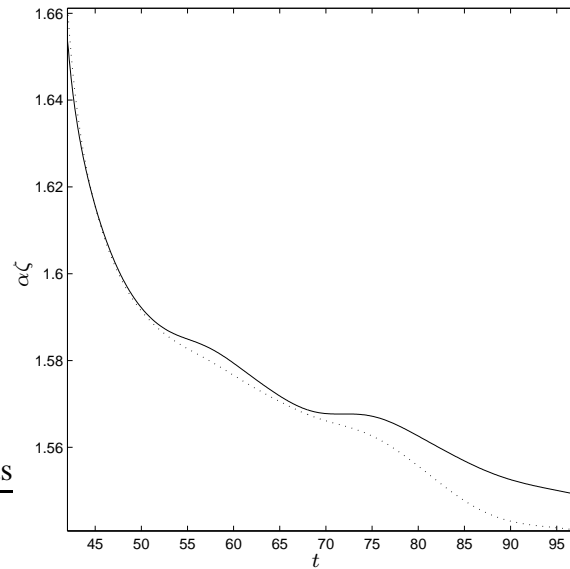


Figure 5.10: Temporal evolution of predicted filter width ratios in the simulations on the wedge grid. — : DFWR2 with filters S2 and W2; ---- : DFWR1 with S2 and W2. In DFWR1 $\zeta = 1$.

Finally, Figure 5.9 and Figure 5.10 show results using the wedge grid, mentioned earlier. In this case nearly identical energy spectra are obtained with DFWR1 and DFWR2 using filters S2 and W2. This is due to the roughly equivalent filter width ratios predicted by both methods, especially in the earlier part of the simulations.

5.2.2 Numerical results with wall-modeled turbulent channel flow

In this section we test the parameter-free dynamic model characterized by dynamic computation of the filter width ratio (DFWR2) on a wall-modeled turbulent channel flow at $Re_\tau = 180$ in which the near-wall regions are not fully resolved. (One of the assumptions made in DFWR1 is invalid in near-wall regions, thus we do not test DFWR1 on this problem.) The reason for not resolving the near-wall regions is that we would like to understand the behavior of DFWR2 in a setting where dissipation due to the numerical method is not as strong as in the wall-resolved channel of Chapter 4. Due to strong gradients and thus strong convection near walls, characteristics which are not fully resolved in the wall-modeled channel, numerical dissipation associated to the SUPG method plays an important role in dynamic model results of the wall-resolved channel. In the next chapter, we will understand the role of numerical dissipation associated to SUPG, and thus will postpone testing DFWR2 on the wall-resolved channel until then.

The domain for the wall-modeled channel is the same as described in Chapter 4, Figure 4.5 with $L_x = 4\pi h$ and $L_z = 4\pi h/3$. The grid is composed of 33 equally spaced vertices in the x - and z -directions. Unlike the grid for the wall-resolved channel, which uses a stretching function to distribute more points in the near-wall region normal to the walls (the y -direction), here the grid is composed of 31 equally spaced vertices in the y -direction. Thus, the first vertex off the wall is at a distance of $\Delta y^+ = 12$. Recall that in the wall-resolved channel the first vertex off the wall is at a distance of $\Delta y^+ = 1$. For the current channel problem, we employ the slip-velocity near-wall model described in [71] and [51] typically used to model the wall.

It is insightful to compare compare results obtained with DFWR2 with filters S1 and W1 to those obtained with the classical dynamic models with finite element-based test filters S1 and W1. For the classical dynamic models, the filter width ratios are fixed, just as it was done in Chapter 4 for the wall-resolved channel simulations. The fixed filter width

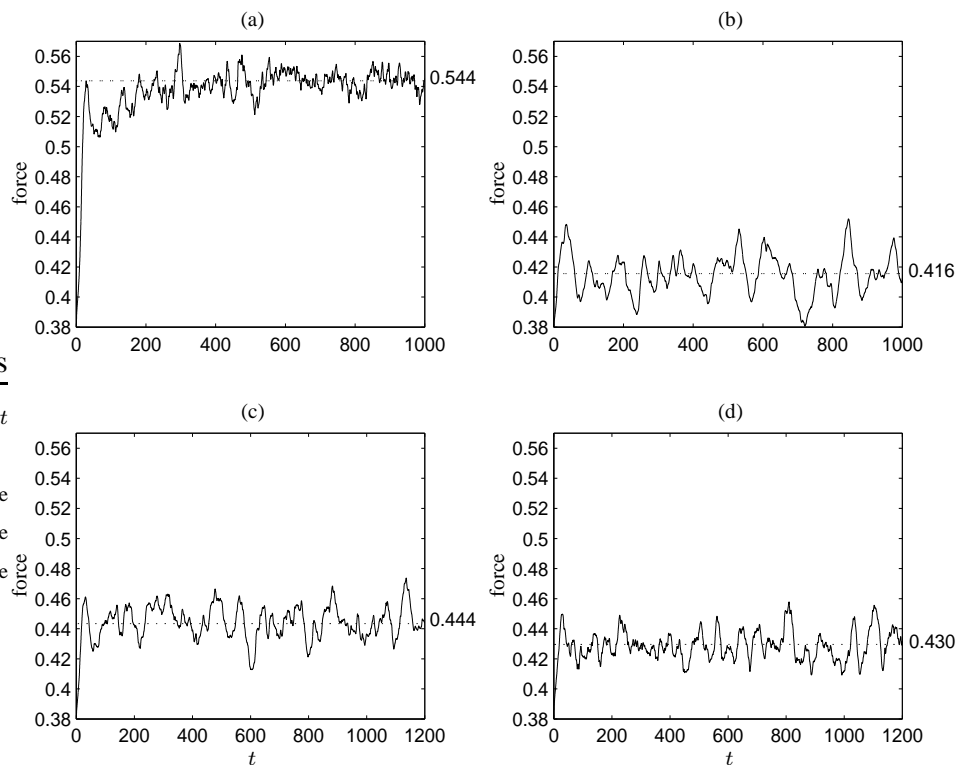


Figure 5.11: Wall force histories with (a) no model, (b) classical model with standard filter S1, (c) classical model with wide filter W1, (d) DFWR2. The mean wall force should be approximately 0.435.

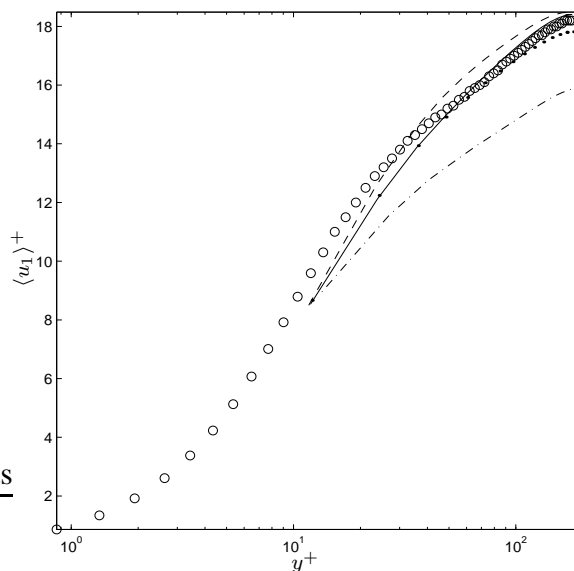


Figure 5.12: Mean streamwise velocities in wall coordinates with DFWR2 (—), classical dynamic model with standard filter S1 (---), classical model with wide filter W1 (-·-), and no model (-·-). \circ : mean velocity in the DNS in [34].

ratios are based on the assumption in (5.2) with $\kappa = 1$ while using the second moment of filter kernels to obtain filter widths. For the case using standard filter S1, with model coefficient denoted as $(C_s^{\hat{\Delta}} \bar{\Delta})_{\text{std}}^2$ in (5.26) with $\zeta = 1$, α is taken as $\alpha = (\hat{\Delta}/h)^2 = (\sqrt{3})^2$. For the case using wide filter W1, with model coefficient denoted as $(C_s^{\hat{\Delta}} \bar{\Delta})_{\text{wide}}^2$ in (5.28) with $\eta = 1$, α is taken as $\alpha = (\hat{\Delta}/h)^2 = (\sqrt{9})^2$. Recall that $\zeta = 1$ and $\eta = 1$ correspond to dynamic models under scale-invariance, in other words the classical dynamic models.

We restrict attention to mean wall forces and mean streamwise velocities, as higher order quantities such as root-mean-square of velocity fluctuations and Reynolds stresses are not well represented in wall-modeled channel flow compared to wall-resolved channel flow. In Figures 5.11 and 5.12 we plot mean wall forces and mean streamwise velocities in wall coordinates. The DFWR2 model gives a closer approximation of the expected mean wall force compared to the the classical dynamic models with fixed filter width ratios. DFWR2 also does well in approximating the mean velocity, especially near the core of the channel. Note that it is difficult to assess the performance of DFWR2 with respect to the classical models with fixed filter width ratios given that results with the latter are subject to change if a different definition of the test filter width is taken or if a different assumption for the filter width ratio (other than the one in (5.2)) is made. On the other hand, results of DFWR2 are not subject to change given that it has no parameter inputs. Recall that in the classical dynamic models, the filter width ratio is assumed to be $\alpha \equiv (\hat{\Delta}/\hat{\Delta})^2 = \kappa(\hat{\Delta}/h)^2$, with $\kappa = 1$. If we were to change κ , results with the classical dynamic models would change. Furthermore, we have computed test filter widths, $\hat{\Delta}$, based on the filters' second moments. However, other definitions of filter widths can be taken, such as those based on filter transfer functions, leading to different values of $\hat{\Delta}$, and thus different results with the classical dynamic models. In summary, the question of how to set the filter width ratio in the classical dynamic models is an open one. This is not the case for DFWR2 as its filter width ratio is dynamically computed.

In practice, the model coefficient, $(C_s \bar{\Delta})^2$, is averaged over spatially homogenous directions and allowed to vary in time and in y , the in-homogenous direction in the current problem. For presentation purposes, in Figure 5.13a, and b, we plot the space- and time-average of $(C_s \bar{\Delta})^2$. In the case of DFWR2, we are really plotting the space- and time-averaged $(C_s^{\hat{\Delta}} \bar{\Delta})^2$. In these figures we see that in the core region, the model coefficient

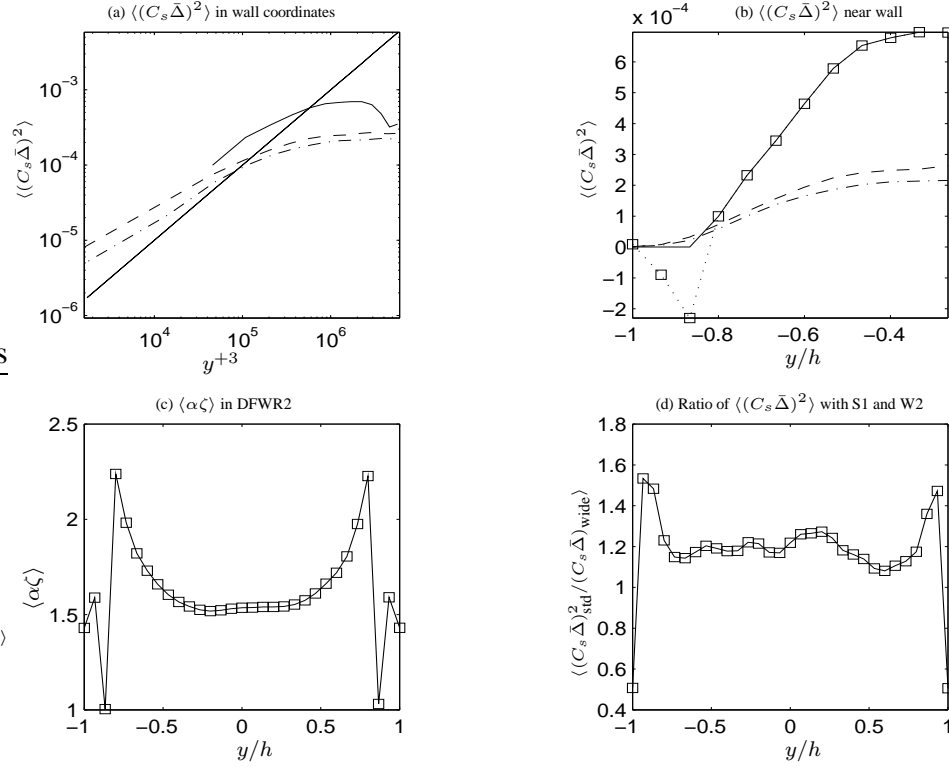


Figure 5.13: (a), (b) $\langle (C_s \bar{\Delta})^2 \rangle$ in DFWR2 (—), in the classical dynamic model with S1 (----), and in the model with W1 (-·-·). In (a), the solid, straight line denotes the theoretical y^{+3} profile. (c) Filter width ratio in DFWR2, $\langle \alpha \zeta \rangle \equiv \langle (C_s^{\hat{\Delta}}/C_s^{\bar{\Delta}})^2 (\hat{\Delta}/\bar{\Delta})^2 \rangle$. In (b), —: clipped DFWR2 coefficient used in simulations; ···: DFWR2 coefficient showing negative values.

in DFWR2 is much greater than those in the classical models, but decays to zero faster near the walls. This is consistent with isotropic turbulence results, for which DFWR2 led to a higher value of the model coefficient than the classical models. In Figure 5.13(c) we plot the space- and time-average of the computed filter width ratio in DFWR2. In the first three planes of vertices normal to the walls (at $y/h = \pm 1$), we see that the filter width ratio behaves much differently than in other planes. The computed values of the filter width ratio for these first three planes off the walls lead to negative values of $(C_s^{\hat{\Delta}} \bar{\Delta})^2$, depicted by the dotted line in Figure 5.13(b). The decay of $(C_s^{\hat{\Delta}} \bar{\Delta})^2$ is so fast that it becomes zero before reaching the walls and becomes negative for the first three planes off the walls. Instead of using a negative value for the model coefficient, we take it as zero (in other words, we clip it) to prevent backscatter. Specifically, we clip the model coefficient for the first three planes off the walls, the furthest ones being at $y/h = \pm 0.83$. The clipped

coefficient is depicted in Figure 5.13(b) by the solid curve. The negative values of the model coefficient near the walls might be attributed to the large difference between the classical dynamic model coefficients with filters S1 and W1 in the near-wall region. Recall that the DFWR2 tested here uses test filters S1 and W1. In Figure 5.13(d), we plot the ratio between the classical dynamic model coefficients. Just as was observed in Chapter 4 in the case of the wall resolved channel, the model coefficient with filter S1 is slightly larger than that with filter W1 in the core region. This difference increases rapidly near the walls and behaves much different in the region of the first three planes off the walls for which the DFWR2 model coefficient is negative and consequently clipped. In addition to preventing backscatter, clipping the model coefficient near the walls is appealing from the point of view that in the near-wall region, numerical energy dissipation due to SUPG stabilization tends to be stronger, and potentially could be enough to represent the required subgrid dissipation.

5.3 Chapter summary

In this chapter we have derived two new dynamic models in which the filter width ratio is dynamically computed. In the classical model the filter width ratio parameter is not calculable, due to the un-defined, implicit, numerical filter associated to the discretization, in our case the SUPG method. However, the two new models proposed here are able to spectrally sample the resolved field and extract the necessary information regarding the length scale or width characterizing the un-defined, numerical filter. For both models, a second test filter is needed in addition to the original test filter used in the classical dynamic model. The second of the new models presents a major advantage in that it is completely parameter-free, in addition to being scale-dependent. The new models were tested successfully in isotropic turbulence. The parameter-free model, denoted as DFWR2, was tested in wall-modeled turbulent channel flow, as well. DFWR2 led to good results in terms of mean wall force and mean streamwise velocity. In the next chapter, DFWR2 will be tested in wall-resolved turbulent channel flow.

CHAPTER 6

A MODIFIED DYNAMIC MODEL BASED ON SUPG STABILIZATION

The classical Galerkin method for the incompressible Navier-Stokes equations is well-known to be unstable in the convective dominated limit, as discussed in [5]. A second instability can occur for certain interpolation combinations of the velocity and pressure which violate the so-called Babuška-Brezzi condition. In References [5] and [25] among others, streamline upwind / Petrov-Galerkin (SUPG) stabilization has been shown to remedy these instabilities through the addition of numerical diffusion along streamlines. In [24] and more recently in [8], the origins of such stabilized methods are brought to light, being interpreted as subgrid-scale (SGS) numerical models which account for the effect of small scales, unresolvable by the discretization, on the resolvable large scales. More precisely, as discussed in [3], stabilization can be thought of as the enrichment of the finite dimensional space underlying the discretization (which can only represent scales larger than a certain size) through the addition of a higher order function, the so called residual-free bubble.

In LES of turbulent flows a spatial filter is applied to the Navier-Stokes equations with the purpose of filtering out small scales and thereby allowing coarser discretizations to solve for the large (resolved) scales governed by the filtered equations. The filtering operation splits a field into filtered and residual components, and furthermore, in the case of the filtered Navier-Stokes equations, this operation generates a residual stress tensor reflecting the effect of the residual scales on the filtered scales. In practice, the discretization (in our case the SUPG method) assumes the role of the spatial filter, thus the residual component of the original field can be regarded as the subgrid component and the residual stress can be regarded as the subgrid stress. The latter has traditionally been referred to as the subgrid-scale stress. Throughout this work we have been using the dynamic coefficient Smagorinsky model (dynamic model), developed in [18] and [40], in addition to two new dynamic models based on dynamic computation of the models' filter width ratio, accounting for the implicit filtering nature of the SUPG method.

It is clear from the previous interpretations that although motivated by different needs, subgrid-scale models in LES and stabilization operators in otherwise unstable classical Galerkin discretizations share similar purposes. Both aim at representing the effect of unresolved small scales on resolved large scales by introducing proper dissipative mechanisms. The phrase “proper dissipative mechanisms” deserves special attention. In the case of stabilized methods, artificial energy dissipation is introduced for the purpose of achieving a stable, consistent and convergent discretization, thereby making the stabilization operator strictly grid dependent. In the case of LES, dissipation is introduced not to provide stability but to model the cascading transfer of energy that occurs between large and small scales in a turbulent flow. As viewed in [55] and later noted in [53], although the physical SGS model can be effected by numerical issues, in principle it should be independent of the numerical method. The effectiveness of the physical model should be based solely on how well it describes the residual stress. For example, the dynamic mixed model developed in [72] and references within is well known to be superior than the classic dynamic model because the modeled residual stress is better aligned with the true residual stress which can be measured through direct numerical simulation.

There are differing viewpoints on the role of numerical dissipation in LES. The simplest is that grid spacing should be chosen sufficiently small so that numerical dissipation is negligible compared to physical dissipation. In the variational multi-scale approach to LES in [27] the roles of numerical and physical dissipation are hypothesized. In the previous work, the substitution of numerical dissipation (applied to the smallest resolvable scales) by physical dissipation is considered. The remark is made that physical dissipation could be sufficient to stabilize the smaller resolvable scales, but artificial dissipation is still required to stabilize the larger resolvable scales. The authors in [27] conjecture that ideally, artificial, numerical dissipation should not greatly degrade or interfere with the behavior of the physical model. However, it is noted that tuning of parameters associated to numerical dissipation might be required to produce the desired energy transfer between the larger and smaller resolved scales. In principle, this should not be the case.

The opposite viewpoint, advocated by Boris *et al.* in [4], is that no explicit physical SGS model is required if an appropriate method providing sufficient, proper numerical dissipation is used. Boris *et al.* refer to this approach as monotone integrated large-eddy

simulation (MILES). In addition to the works cited by Boris *et al.*, other works using the MILES approach are [62], [35], and [49]. The main advantage of the MILES approach is that the effort required to develop physical SGS models is eliminated. However, physical modeling and the numerics are inseparably intertwined. For a given LES, results depend on the numerical method and on the grid used, as it is not possible to refine the grid to obtain grid-independent solutions. Refining the grid in search of grid-independence would lead to a DNS, no longer LES. Furthermore, not all numerical methods are suited for the MILES approach. The SUPG method used here is certainly not, as can be seen in the isotropic turbulence results of Chapter 4 for which the method by itself is not able to properly represent the energy cascade from large to small scales when the influence of the model is decreased.

There have been some researchers that have tried to understand the behavior of the physical SGS model in the presence of numerical dissipation. In Reference [48], the effect of artificial dissipation on the physical SGS model is investigated by tracking the dynamic model's eddy viscosity when dissipative and non-dissipative discretizations are used. The influence of the model increases when the non-dissipative solver is used instead of the dissipative solver, suggesting that the model is robust enough to adjust for numerical diffusion.

Given the un-avoidable coupling between the physics and the numerics, in this work we explore the interaction between physical and numerical subgrid-scale models by tracking the physical model dissipation, as well as our own definition of numerical dissipation due to SUPG stabilization. It is seen that for low Reynolds number channel flow simulations on relatively coarse grids, which lead to numerical dissipation on the same order but still smaller than physical model dissipation, numerical dissipation does play a role. It will be shown that the model does not adjust well enough in the presence of changing numerical dissipation, contrary to previous belief. To this end, we will introduce a correction to the model, which will serve essentially as a coupling between the model and stabilization at the energy dissipation level. This coupling will lead to a model independent of the amount of numerical subgrid-scale energy dissipation present in the simulations performed here, as it should be in principle. To date, this is the first attempt at physical modeling of the subgrid-scale stress taking into account the presence of numerical, subgrid-scale dissipa-

tion.

6.1 Mathematical preliminaries

6.1.1 Resolved kinetic energy

To study the effect of the physical SGS dynamic model and its interaction with numerical dissipation, dissipation due to the physical SGS stress is of importance. To that extent, we consider the transport equation for the resolved energy $\bar{q}^2 = \bar{u}_i \bar{u}_i$, found by dotting the filtered momentum equation in (2.9) with the velocity vector and making use of the filtered continuity equation in (2.3), as shown in [52]:

$$\bar{q}_{,t}^2 + (\bar{q}^2 \bar{u}_j)_{,j} = (-2\bar{p}\bar{u}_j - 2\bar{u}_i \tau_{ij} + \nu \bar{q}_{,j}^2)_{,j} - 2\nu \bar{u}_{i,j} \bar{u}_{i,j} + 2\tau_{ij}^{(d)} \bar{S}_{ij}, \quad (6.1)$$

where the simplification $\overline{\tau_{ij}^{\nu}} = \nu \bar{u}_{i,jj}$ (due to the filtered continuity equation) has been made. If the term $\tau_{ij}^{(d)} \bar{S}_{ij}$ (the last term in (6.1)) is negative, the subgrid-scales remove energy from the resolved ones, often referred to as forward scatter or dissipation. On the other hand, if this term is positive, the subgrid-scales give energy to the resolved ones, often referred to as backscatter. In the dynamic model considered here, the majority of instances the eddy viscosity is positive due to averaging of the numerator and denominator in the model coefficient in (2.23), resulting in

$$\tau_{ij}^d \bar{S}_{ij} = -2\nu_T \bar{S}_{ij} \bar{S}_{ij} < 0, \quad (6.2)$$

thus only forward scatter or dissipation. In (6.2) we have used the fact that the trace-free residual stress tensor is expressed through the Smagorinsky model as $\tau_{ij}^d = -2\nu_T \bar{S}_{ij}$. The eddy viscosity ν_T is obtained dynamically as $\nu_T = (C_s \bar{\Delta})^2 |\bar{S}|$. Herein we refer to $-2\nu_T \bar{S}_{ij} \bar{S}_{ij}$ as the physical subgrid-scale (SGS) energy dissipation, traditionally referred to as simply SGS dissipation. This is a misnomer given that in some instances numerical dissipation is also a type of SGS dissipation, such as is the case with the SUPG method.

6.1.2 Weak form – Finite element discretization with the SUPG method

Next, we proceed with the stabilized finite element discretization of the weak form of the modeled, filtered Navier-Stokes equations (the filtered continuity (first) equation in

(2.3) and the filtered momentum equation in (2.9)). First, we introduce the discrete weight and solution function spaces that are used. Let $\bar{\Omega} \subset \mathbf{R}^N$ represent the closure of the physical spatial domain, $\Omega \cup \Gamma$, in N dimensions; only $N = 3$ is considered. The boundary, Γ , is decomposed into portions with natural boundary conditions, Γ_h , and essential boundary conditions, Γ_g , i.e., $\Gamma = \Gamma_g \cup \Gamma_h$. In addition, $H^1(\Omega)$ represents the usual Sobolev space of functions with square-integrable values and derivatives on Ω (see Hughes [29]).

Subsequently Ω is discretized into n_{el} finite elements, $\bar{\Omega}_e$. To be precise, the previous notation denotes the closure of a finite element. With this, we can define the discrete trial solution and weight spaces for the semi-discrete formulation as

$$\begin{aligned} \mathcal{S}_h^k &= \{ \mathbf{v} | \mathbf{v}(\cdot, t) \in H^1(\Omega)^N, t \in [0, T], \mathbf{v}|_{x \in \bar{\Omega}_e} \in P_k(\bar{\Omega}_e)^N, \mathbf{v}(\cdot, t) = \mathbf{g} \text{ on } \Gamma_g \}, \\ \mathcal{W}_h^k &= \{ \mathbf{w} | \mathbf{w}(\cdot, t) \in H^1(\Omega)^N, t \in [0, T], \mathbf{w}|_{x \in \bar{\Omega}_e} \in P_k(\bar{\Omega}_e)^N, \mathbf{w}(\cdot, t) = \mathbf{0} \text{ on } \Gamma_g \}, \\ \mathcal{P}_h^k &= \{ p | p(\cdot, t) \in H^1(\Omega), t \in [0, T], p|_{x \in \bar{\Omega}_e} \in P_k(\bar{\Omega}_e) \} \end{aligned} \tag{6.3}$$

where $P_k(\bar{\Omega}_e)$ is the piecewise polynomial space, complete to order k , defined on $\bar{\Omega}_e$. Throughout this work we have performed and will continue to perform simulations with piecewise tri-linear basis functions, restricting to $k = 1$. Let us emphasize that the local approximation space, $P_k(\bar{\Omega}_e)$, is the same for both the velocity and pressure variables. This is possible due to the stabilized nature of the formulation to be introduced below. These spaces represent discrete subspaces of the spaces in which the weak form is defined.

The stabilized formulation used in the present work is an alternative to that described in [63] and furthermore used in [68] with great success. The authors in the previous two references work with the convective form of the incompressible equations. Here we will work with the conservative form of these equations for reasons to become apparent in the next sub-section.

The current weak formulation of the conservative form of the incompressible, modeled, filtered equations proceeds as follows. Given the spaces previously defined, we first present the semi-discrete Galerkin finite element formulation applied to the weak form of the modeled, filtered equations as:

Find $\mathbf{u} \in \mathcal{S}_h^k$ and $P \in \mathcal{P}_h^k$ such that

$$B_G(w_i, q; u_i, P) = 0$$

$$B_G(w_i, q; u_i, P) = \int_{\Omega} \{w_i \dot{u}_i + w_{i,j} (-u_i u_j - P \delta_{ij} + \tau_{ij}^*) - q_{,i} u_i\} dx$$

$$+ \int_{\Gamma_h} \{w_i (u_i u_n + P \delta_{in} - \tau_{in}^*) + q u_n\} ds$$
(6.4)

for all $\mathbf{w} \in \mathcal{W}_h^k$ and $q \in \mathcal{P}_h^k$. Note that the stress τ_{ij}^* is given as the viscous stress plus the modeled deviatoric component of the residual stress:

$$\tau_{ij}^* = 2(\nu + \nu_T) S_{ij}. \quad (6.5)$$

As mentioned before, the trace component of the residual stress can be absorbed by the pressure. Furthermore, the bar notation denoting resolved variables (\bar{u}_i, \bar{P}) has been omitted for simplicity. The boundary integral term arises from the integration by parts and is only carried out over the portion of the domain without essential boundary conditions. Since the Galerkin method is unstable for the equal-order interpolations given above, we add additional stabilization terms which yields:

Find $\mathbf{u} \in \mathcal{S}_h^k$ and $P \in \mathcal{P}_h^k$ such that

$$B(w_i, q; u_i, P) = 0$$

$$B(w_i, q; u_i, P) = B_G(w_i, q; u_i, P)$$

$$+ \sum_{e=1}^{n_{el}} \int_{\tilde{\Omega}_e} \{w_{i,j} \tau_M (u_j \mathcal{L}_i + u_i \mathcal{L}_j) + q_{,i} \tau_M \mathcal{L}_i + \tau_C w_{i,i} u_{j,j}\} dx$$
(6.6)

for all $\mathbf{w} \in \mathcal{W}_h^k$ and $q \in \mathcal{P}_h^k$. Symbol $\tilde{\Omega}_e$ denotes element interiors, excluding their closure. We have used \mathcal{L}_i to represent the residual of the i^{th} momentum equation,

$$\mathcal{L}_i = \dot{u}_i + (u_i u_j)_{,j} + P_{,i} - \tau_{ij,j}^* \quad (6.7)$$

The second line in the stabilized formulation, (6.6), represents streamline upwind / Petrov-Galerkin (SUPG) stabilization added to the Galerkin formulation of the compressible equations in conservation variables in the incompressible limit. As is shown in [22], this limit of the compressible equations in conservation variables $(\rho, \mathbf{u}, e_{\text{tot}})$ under a change of variables to (p, \mathbf{u}, T) is well-defined, leading to a conservative incompressible formulation. Variables e_{tot} and T are total energy and temperature, respectively.

The stabilization parameters for continuity and momentum are defined as given in [63],

$$\tau_M = \frac{1}{\sqrt{(2c_1/\Delta t)^2 + u_i g_{ij} u_j + c_2(\nu + \nu_T)^2 g_{ij} g_{ij}}}, \quad (6.8)$$

$$\tau_C = \frac{1/\tau_M}{\text{tr}(g_{ij})}. \quad (6.9)$$

where c_2 is obtained based on the one-dimensional, linear advection-diffusion equation using a linear finite element basis and $g_{ij} = \xi_{k,i} \xi_{k,j}$ is the covariant metric tensor related to the mapping from global to element coordinates. The constant c_1 (associated to the temporal influence on the stabilization) is obtained by considering the local gradient in element space-time coordinate systems, as is done in [58]. However, for the purely spatial coordinate system used in our semi-discrete formulation, this constant is not well-defined. In this work we will study the dependence of simulation results on stabilization by varying c_1 . Specifically, we will use c_1 as a parameter with which we will control dissipation due to stabilization making it weaker or stronger.

6.1.3 Numerical dissipation

Of importance in this chapter will be numerical dissipation due to the SUPG stabilization, presented in the previous sub-section. Not much emphasis has been placed on this topic in past literature, and furthermore, this is the first time (to the best of our knowledge) that a dissipation due to stabilization has been defined. Consider the filtered momentum equation in (2.9) where the term $[\overline{\tau_{ij}^\nu} - \tau_{ij}^d]_{,j}$ appears in the right hand side. In terms of

molecular and eddy viscosities, this term can be expressed as

$$[\overline{\tau_{ij}^v} - \tau_{ij}^d]_{,j} = [2\nu\bar{S}_{ij} - (-2\nu_T\bar{S}_{ij})]_{,j}. \quad (6.10)$$

In deriving the weak form of the filtered equations, the previous term is brought to the left hand side and dotted by a weight function. The resulting term is integrated by parts resulting in a term of the form $w_{i,j} \{2\nu_T\bar{S}_{ij}\}$ in the integrand of the integral equation in (6.4). This can be seen by inserting τ_{ij}^* in (6.5) into the second line in (6.4). Note that in the Galerkin weak form in (6.4) the over-bar notation in (\bar{u}_i, \bar{p}) has been dropped for simplicity. The SUPG advection stabilization term of the integrand in (6.6) is of the form $w_{i,j} \{\tau_{ij}^{\text{SUPG}}\}$, where

$$\tau_{ij}^{\text{SUPG}} = \tau_M(\bar{u}_j\mathcal{L}_i + \bar{u}_i\mathcal{L}_j), \quad (6.11)$$

and \mathcal{L}_i is given in (6.7). Again, the over-bar notation has been dropped in (6.7). Thus, analogous to physical SGS energy dissipation defined in sub-section 6.1.1 as $-2\nu_T\bar{S}_{ij}\bar{S}_{ij}$, we define SUPG (numerical) dissipation as $-\tau_{ij}^{\text{SUPG}}\bar{S}_{ij}$. We would like to work with positive quantities, thus we denote

$$\epsilon_{\text{SGS}} = 2\nu_T\bar{S}_{ij}\bar{S}_{ij} \quad \text{and} \quad \epsilon_{\text{SUPG}} = \tau_{ij}^{\text{SUPG}}\bar{S}_{ij} \quad (6.12)$$

as physical SGS dissipation and SUPG dissipation, respectively. To summarize, the *ad hoc* definition of SUPG dissipation is motivated by looking at the Galerkin and SUPG terms of the weak formulation in (6.4) and (6.6), respectively. After integration by parts is performed while deriving the weak form, the stress τ_{ij}^* is multiplied by the gradient of the weight function which leads it to appear in the same form as the SUPG tensor τ_{ij}^{SUPG} . It is important to note that by considering the incompressible limit of the compressible stabilized formulation (leading to an incompressible formulation in conservative form), as discussed earlier, we are led to a symmetric SUPG tensor, a property also shared by τ_{ij}^* . If we had considered SUPG stabilization for the incompressible formulation in the advective form as is done in [63] and [68], our SUPG tensor and thereby our SUPG dissipation would have been more complicated to define due to the presence of extra stabilization terms.

6.2 A modification to the dynamic model based on SUPG

In this section we will present simulation results with the wall-resolved channel flow at $Re_\tau = 180$ of Chapter 4. We aim to vary the strength of SUPG stabilization through the parameter associated with the temporal portion of the intrinsic time scale τ_M, c_1 . We also aim to vary the strength of the classical dynamic model. To that extent, we use the finite element-based filters S1 and W1. From the results of Chapter 4 we see that the magnitude of the dynamic model coefficient with wide filter W1 is less than that with standard filter S1, especially in the near-wall regions. Thus, we will refer to the classical dynamic model with filter S1 as the strong physical model and to the dynamic model with filter W1 as the weak physical model. Throughout this chapter, the filter width ratio parameter appearing in the dynamic model through (2.22) is taken as $\alpha = 3$ when filter S1 is used and as $\alpha = 9$ when filter W1 is used. Recall that these choices are based on the assumption in (4.2), where the second moment of the test filter kernels are used to compute filter widths.

6.2.1 Channel flow at $Re_\tau = 180$

Our goal is to understand the behavior of the dynamic model (physical) SGS dissipation in the presence of SUPG (numerical) dissipation and vice-versa. We begin by looking at Figure 6.1, where we show the components of the SUPG tensor, τ_{ij}^{SUPG} , averaged over spatially homogenous directions and over time for simulations with different combinations of SUPG stabilization and dynamic model. We present the four non-zero (in the mean) components of the SUPG tensor. Notice that τ_{11}^{SUPG} and τ_{12}^{SUPG} are dominant over τ_{22}^{SUPG} and τ_{33}^{SUPG} . Although not shown, all components are symmetric about the channel centerline at $y/h = 0$, except for τ_{12}^{SUPG} , which is anti-symmetric.

The influence of the SUPG stabilization decreases as constant c_1 is increased, as expected from looking at the expression for τ_M in (6.8). We also change the strength of the dynamic model by changing the width of the test filter. From Figure 6.1, we see that by switching the dynamic model from strong to weak while leaving c_1 unchanged, the peaks of the SUPG tensors increase in magnitude to account for lack of physical SGS energy dissipation. SUPG stabilization seems to be at least partially adjusting to the strength of the model. The previous conclusions can be drawn as well from Figure 6.2a, where we show SUPG dissipation in wall units. Note that for the first five planes of vertices off the

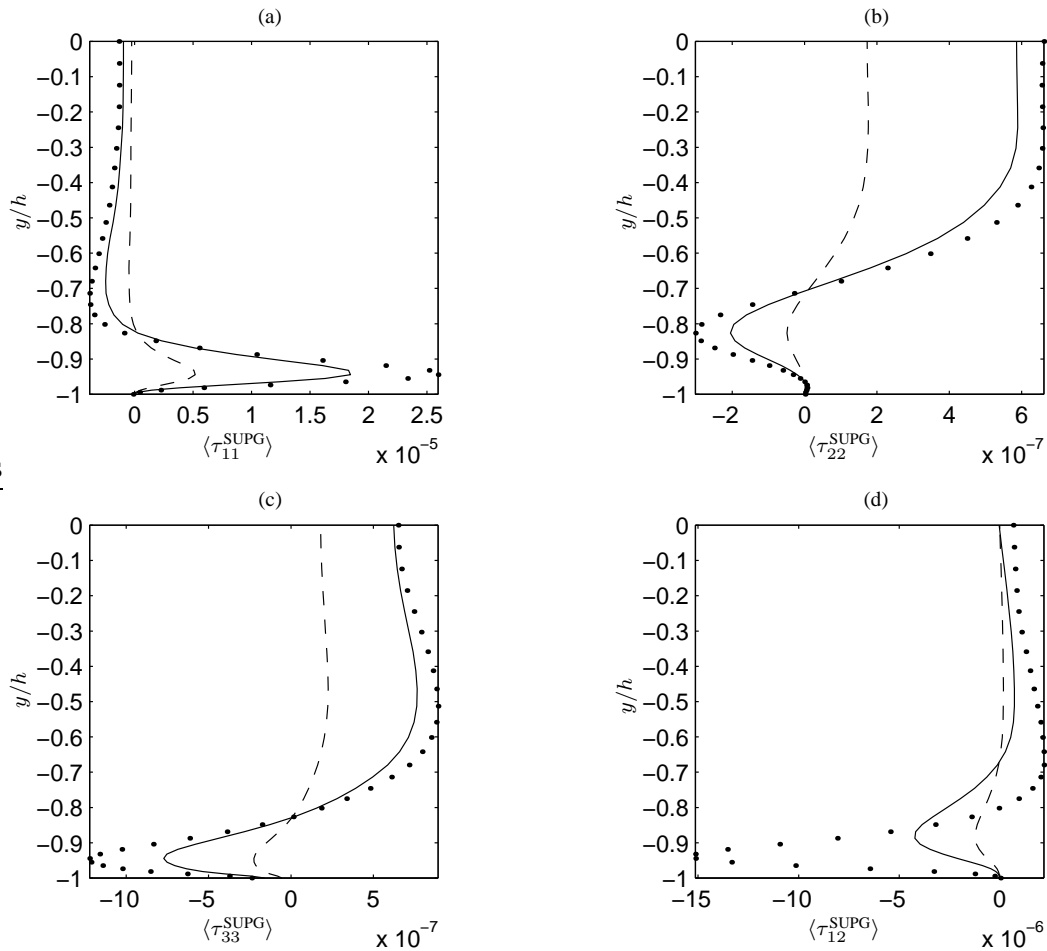


Figure 6.1: Components of the SUPG tensor τ_{ij}^{SUPG} . — : $c_1 = 16$ (strong SUPG) and strong dynamic model; ---- : $c_1 = 64$ (weak SUPG) and strong model; · · · : $c_1 = 16$ (strong SUPG) and weak model.

walls, SUPG dissipation is negative. In Figure 6.2b we see that the weaker model near the wall gives rise to smaller physical SGS dissipation in this region.

Of great importance, as seen in Figure 6.2b, is that keeping the model fixed and changing the influence of SUPG stabilization by varying c_1 between 16 and 64, does not seem to effect physical SGS dissipation by much. However, looking at Figure 6.3, we see that actually there is some adjustment of the eddy viscosity when keeping the model fixed and varying the SUPG strength. A strong SUPG gives rise to a lower eddy viscosity. The reason for this can be explained by first recalling the eddy viscosity as

$$\nu_T = (C_s \bar{\Delta})^2 |\bar{S}|. \quad (6.13)$$

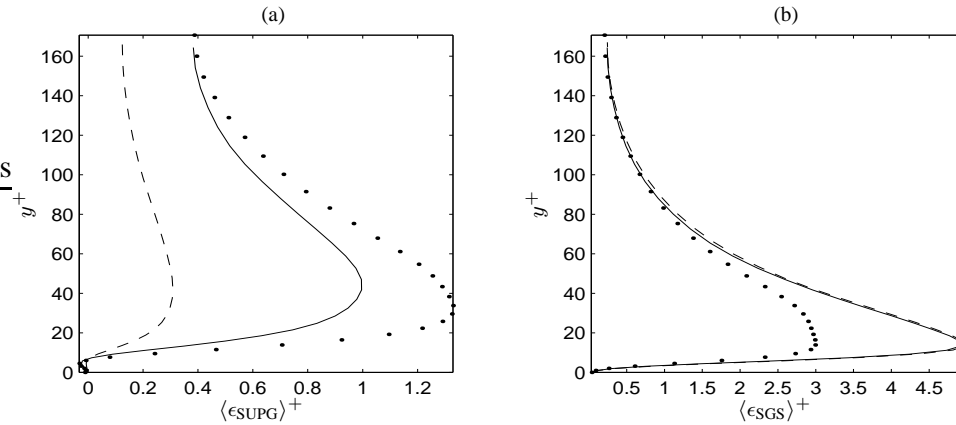


Figure 6.2: (a) SUPG dissipation on the left and (b) dynamic model/SGS dissipation on the right, both in wall units. Solid: $c_1 = 16$ (strong SUPG) and strong model; dashed: $c_1 = 64$ (weak SUPG) and strong model; dotted: $c_1 = 16$ (strong SUPG) and weak model.

A strong SUPG leads to a less energetic flow due to higher numerical dissipation. In turn, a less energetic flow leads to lower values of the norm of the filtered strain-rate tensor ($|\bar{S}|$), appearing in (6.13), thus a lower eddy viscosity. However, this adjustment of the physical model to a stronger SUPG is not enough as evinced by the time history of the force exerted by the flow on the channel walls, shown in Figure 6.4a. In this figure we see that increasing SUPG, slightly decreases the wall force. Although the physical SGS model weakens to account for the stronger SUPG stabilization, this adjustment is not enough to keep the mean wall force the same between both simulations. The reason for this is that even though there is an adjustment of the eddy viscosity through the filtered strain-rate tensor, there is hardly any adjustment at all by the physical model coefficient $(C_s \bar{\Delta})^2$, as seen in Figure 6.5. A possible reason for the non-adjusting nature of the physical model is that the model coefficient is computed based on sampling larger resolved components of the flow than those believed to be affected by SUPG stabilization. Changing SUPG stabilization does not greatly affect the larger resolved components used in computing the model coefficient, consequently leaving it relatively unchanged. This hypothesis should be tested in future. As mentioned earlier, the wide filter W1, leads to lower values of the dynamic model coefficient, which reflects through much higher wall forces due to a more energetic flow. This can be seen by comparing the solid curves in Figure 6.4a and Figure 6.4b. Here, SUPG is not able to adjust enough so as to keep the forces the same

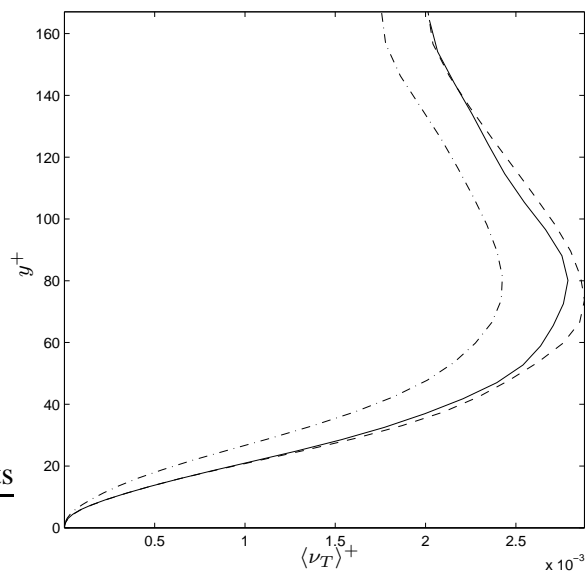


Figure 6.3: Eddy viscosity in wall units. Solid: $c_1 = 16$ and strong model; dashed: $c_1 = 64$ (weak SUPG) and strong model

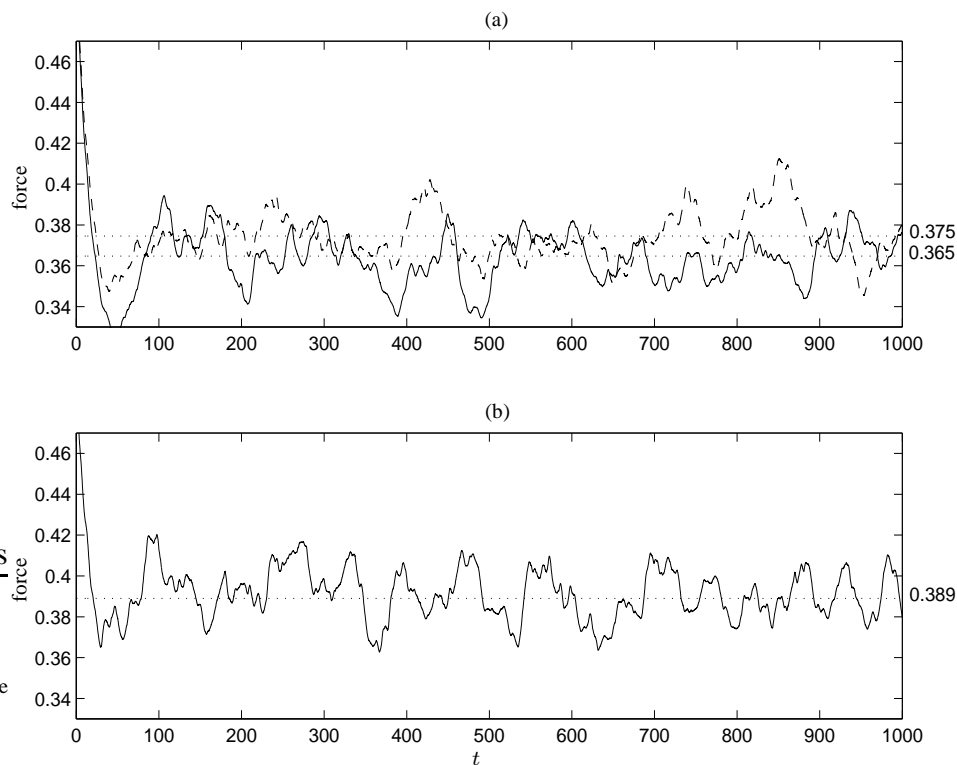


Figure 6.4: (a) Force histories with strong model and with varying SUPG. — : $c_1 = 16$ (strong SUPG); ---- : $c_1 = 64$ (weak SUPG). (b) Force history with weak model and with $c_1 = 16$ in the stabilization (strong SUPG). The mean wall force should be approximately 0.435.

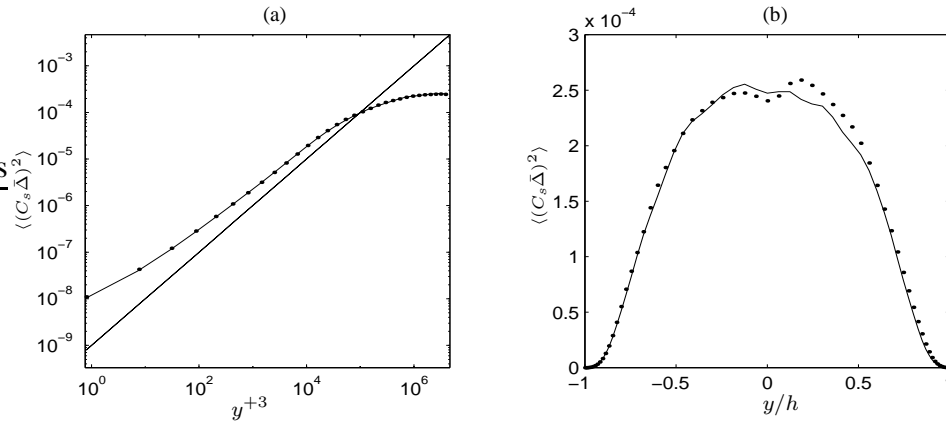


Figure 6.5: (a) Dynamic model coefficient versus y^{+3} . (b) Dynamic model coefficient versus y . For (a) and (b), — : strong model and $c_1 = 16$ (strong SUPG); ··· : strong model and $c_1 = 64$ (weak SUPG).

between the two cases.

Here, we aim to modify the physical model such that at least when keeping the filter fixed and changing the SUPG strength, the model can adjust enough to retain nearly the same mean wall force. We propose to account for SUPG stabilization in the physical SGS dynamic model at the energy dissipation level by setting the new, corrected physical SGS dissipation to be

$$\epsilon_{\text{SGS}}^* = \epsilon_{\text{SGS}} - \epsilon_{\text{SUPG}} \equiv 2\nu_T \bar{S}_{ij} \bar{S}_{ij} - \tau_{ij}^{\text{SUPG}} \bar{S}_{ij}. \quad (6.14)$$

The previous corrected physical SGS dissipation implies a corrected eddy viscosity (ν_T^*), thus a corrected dynamic model coefficient $(C_s \bar{\Delta})^{*2}$. The corrected eddy viscosity and model coefficient are related as

$$\epsilon_{\text{SGS}}^* = 2\nu_T^* \bar{S}_{ij} \bar{S}_{ij} = 2(C_s \bar{\Delta})^{*2} |\bar{S}| \bar{S}_{ij} \bar{S}_{ij}, \quad (6.15)$$

where the first equality follows from our definition of physical SGS dissipation in (6.12), and the second equality follows from the modeled eddy viscosity in (6.13). Recalling the corrected physical SGS dissipation in (6.14) and making use of the fact that $|\bar{S}|^2 = 2\bar{S}_{ij} \bar{S}_{ij}$,

we can solve for the corrected dynamic model coefficient from (6.15) as

$$(C_s \bar{\Delta})^{*2} = \frac{\epsilon_{\text{SGS}}^*}{|\bar{S}|^3} = \frac{2\nu_T \bar{S}_{ij} \bar{S}_{ij} - \tau_{ij}^{\text{SUPG}} \bar{S}_{ij}}{|\bar{S}|^3}. \quad (6.16)$$

In terms of the original model coefficient, $(C_s \bar{\Delta})^2$ we have

$$(C_s \bar{\Delta})^{*2} = \frac{\epsilon_{\text{SGS}}^*}{|\bar{S}|^3} = \frac{(C_s \bar{\Delta})^2 |\bar{S}|^3 - \tau_{ij}^{\text{SUPG}} \bar{S}_{ij}}{|\bar{S}|^3}. \quad (6.17)$$

For stability purposes, the numerator and denominator in (6.16) or (6.17) are averaged over spatially homogenous directions of the flow, analogous to the averaging performed for the uncorrected, classical dynamic model coefficient. In practice, if the spatially averaged SUPG dissipation is negative, such as is the case for the first few planes off the walls, the SUPG correction is not made and the classical dynamic model is left unmodified. The corrected eddy viscosity is obtained as

$$\nu_T^* = (C_s \bar{\Delta})^{*2} |\bar{S}|. \quad (6.18)$$

The corrected model coefficient in (6.16) is motivated from the result that the uncorrected dynamic model does not seem to be aware of numerical dissipation, mostly due to an unaffected model coefficient. In the case were $\epsilon_{\text{SUPG}} \ll \epsilon_{\text{SGS}}$, the correction to the SGS physical dissipation becomes negligible (which can be seen by inspecting (6.14)), essentially leading to the usual dynamic model. However, if these two dissipations are of the same order, the modification plays a stronger impact. Regardless of the difference between physical SGS and numerical SUPG dissipations, the total subgrid dissipation will always be due to the physical SGS model alone and not due to SUPG since

$$\text{total subgrid dissipation} = \epsilon_{\text{SGS}}^* + \epsilon_{\text{SUPG}} = \epsilon_{\text{SGS}}. \quad (6.19)$$

This can be seen by substituting ϵ_{SGS}^* given by the first equality in (6.14) into (6.19). Hence, as a result of the modification in (6.14), SUPG stabilization is used for stabilization purposes only. This is a desirable feature since in principle, numerical dissipation should not interfere with subgrid dissipation meant to be provided by the physical SGS model only.

6.3 Turbulent channel LES with the SUPG-modified dynamic model

In the up-coming sub-sections we will see the effect of the corrected or modified dynamic model coefficient in (6.17) on simulation results of wall-resolved turbulent channel flow. Specifically, we will study the effect of SUPG correction in three cases distinguished by the difference between SUPG and SGS dissipation. In the first case, we will study SUPG correction in the $Re_\tau = 180$ channel with the dynamic models using filter S1. In the second case we perform simulations of the $Re_\tau = 180$ with the models using filter W1. In the second case, with filter W1, the difference between peak SGS dissipation and SUPG dissipation is less than in first case with filter S1. In the third case, we perform simulations of an $Re_\tau = 395$ channel flow with dynamic models using filter S1. For this case the peak difference in SGS and SUPG dissipations is slightly greater than in the first case. It will be seen that when the difference between peak SGS and SUPG dissipations is low, the model correction introduced in (6.14) can play an important role.

6.3.1 Channel flow at $Re_\tau = 180$ with model using filter S1

Here we study cases in the channel at $Re_\tau = 180$ for which the corrected and non-corrected dynamic models are computed using filter S1 under different strengths of the SUPG stabilization. We begin by looking at Figure 6.6. Comparing the curves with $c_1 = 64$, we see that when SUPG correction is employed, the magnitude of the components of the SUPG tensor are higher due to the reduction of the dynamic model coefficient. In other words, the magnitude of the components of the SUPG tensor increase due to a more energetic flow resulting from a lower eddy viscosity given by a corrected dynamic model. This is more noticeable in the case of strong SUPG dissipation (when $c_1 = 16$). Furthermore, the adjustment of the model due to a change in SUPG strength is much more pronounced as seen in the plots of SGS energy dissipations and viscosities in Figure 6.7b and Figure 6.8, respectively. As expected, the SUPG correction introduces lesser changes in the cases for which SUPG is weak corresponding to $c_1 = 64$. The reason for this is that when $c_1 = 64$, ϵ_{SUPG} is much smaller than when $c_1 = 16$, hence it does not affect ϵ_{SUPG}^* in (6.14) as much. This can be clearly seen by comparing mean wall forces (Figure 6.9) and SGS dissipations (Figure 6.7b) in the corrected and uncorrected model cases under weak SUPG.

In Figure 6.9 we plot time histories of the forces on the channel walls with and with-

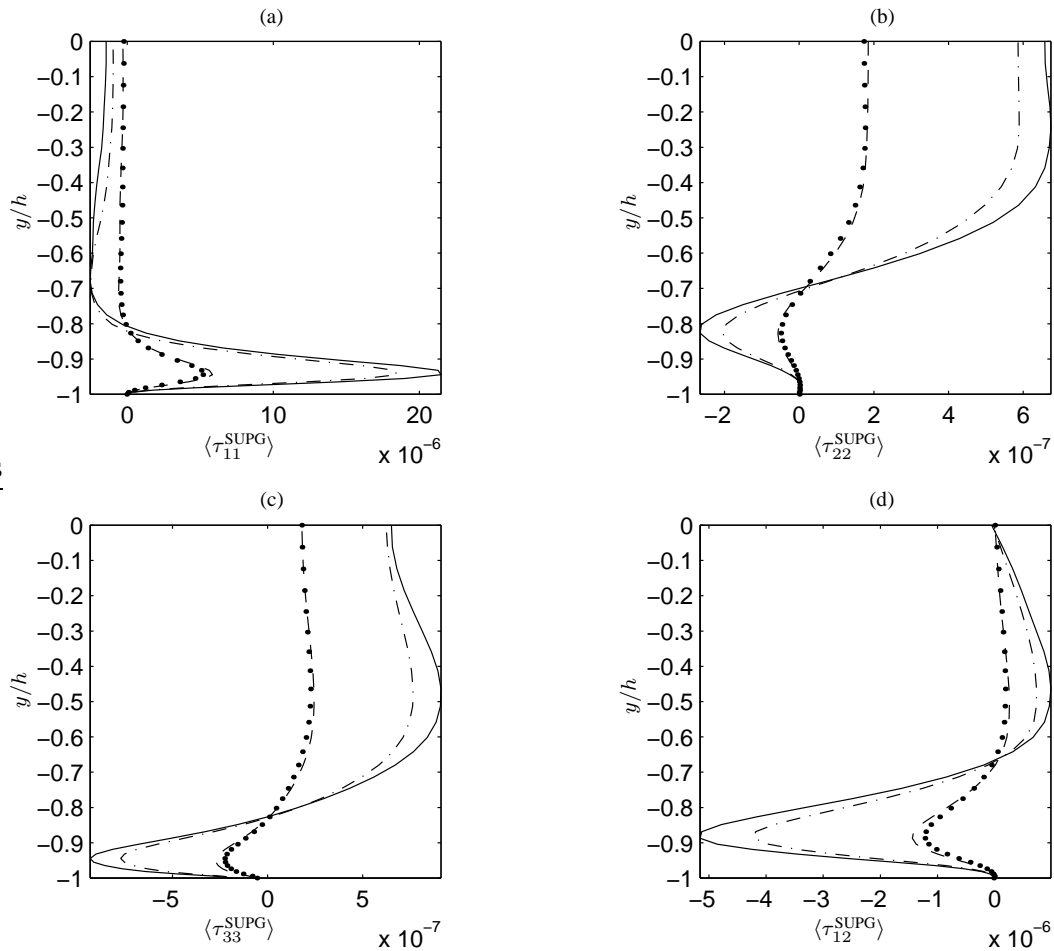


Figure 6.6: Components of the SUPG tensor τ_{ij}^{SUPG} with and without SUPG correction in the dynamic model with filter S1. — : $c_1 = 16$ and SUPG correction; ---- : $c_1 = 64$ and SUPG correction. - · - : $c_1 = 16$ and no SUPG correction; · · · : $c_1 = 64$ and no SUPG correction.

out SUPG correction. Notice that when the dynamic model does not have SUPG correction, corresponding to Figure 6.9a, the peaks and troughs of the force recorded with $c_1 = 16$ are lower than those of the force with $c_1 = 64$. The relative difference between the two mean forces, defined as $(f_{high} - f_{low})/f_{low}$, is three percent. In this case, as c_1 goes from 16 to 64, SUPG dissipation decreases while SGS dissipation remains nominally the same, giving rise to a more energetic flow, and consequently a higher wall force. When the dynamic model does have SUPG correction, corresponding to Figure 6.9b, the model adjusts to the change in SUPG stabilization, giving rise to nearly similar force histories for which the relative mean difference is one percent.

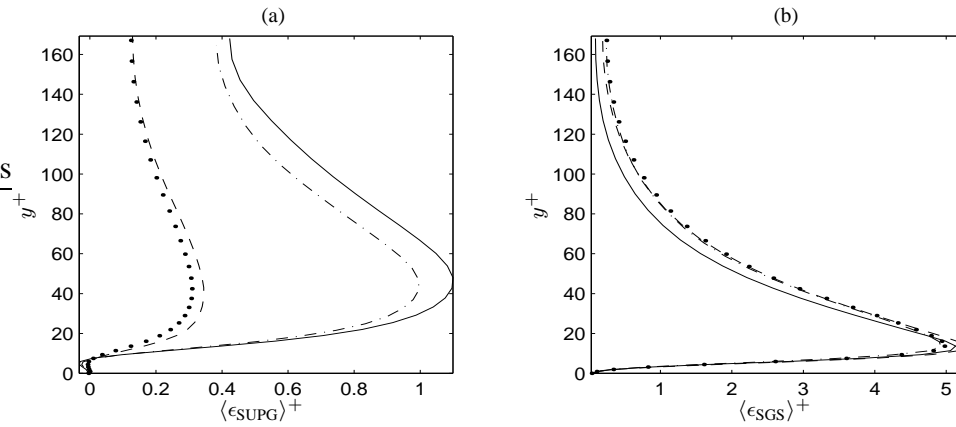


Figure 6.7: (a) SUPG dissipation on the left and (b) dynamic model/SGS dissipation on the right, both in wall units. Here results are with and without SUPG correction in the dynamic model with filter S1. — : $c_1 = 16$ and SUPG correction; ---- : $c_1 = 64$ and SUPG correction. - · - : $c_1 = 16$ and no SUPG correction; · · · : $c_1 = 64$ and no SUPG correction.

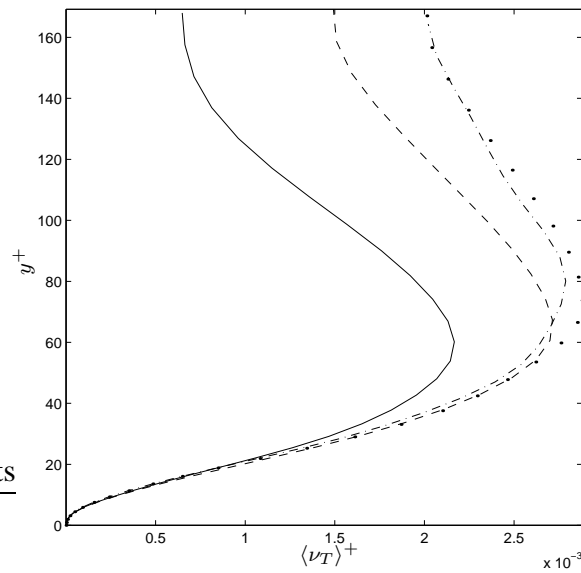


Figure 6.8: Eddy viscosity in wall units with and without SUPG correction in the dynamic model with filter S1. — : $c_1 = 16$ and SUPG correction; ---- : $c_1 = 64$ and SUPG correction. - · - : $c_1 = 16$ and no SUPG correction; · · · : $c_1 = 64$ and no SUPG correction.

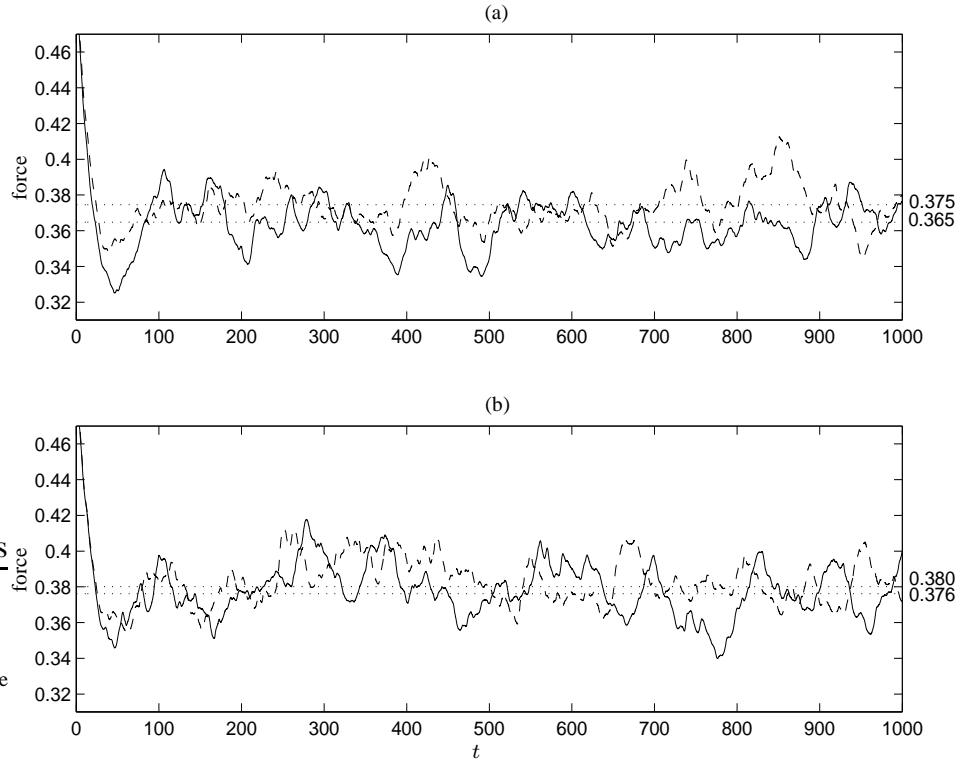


Figure 6.9: (a) Wall forces without SUPG correction on the top and (b) wall forces with SUPG correction on the bottom. In all cases the model was computed with filter S1. — : $c_1 = 16$; dashed: $c_1 = 64$.

6.3.2 Channel flow at $Re_\tau = 180$ with model using filter W1

In this sub-section we study cases in the channel at $Re_\tau = 180$ for which the corrected and non-corrected dynamic model are computed using wide filter W1 under different strengths of the SUPG stabilization.

Looking at Figure 6.10 we see that once again the magnitude of the components of the SUPG tensor increase due to a more energetic flow resulting from a lower eddy viscosity given by a corrected dynamic model. This is more noticeable in the case of strong SUPG dissipation (when $c_1 = 16$). Furthermore, with SUPG correction the adjustment of the model due to a change in SUPG strength is greater as seen in the plots of SGS energy dissipations and viscosities in Figure 6.11b and Figure 6.12, respectively. Similar to the case presented in the previous sub-section, the SUPG correction introduces lesser changes in the cases for which SUPG is weak corresponding to $c_1 = 64$.

In Figure 6.13 we plot wall force histories for when the model is corrected and uncor-

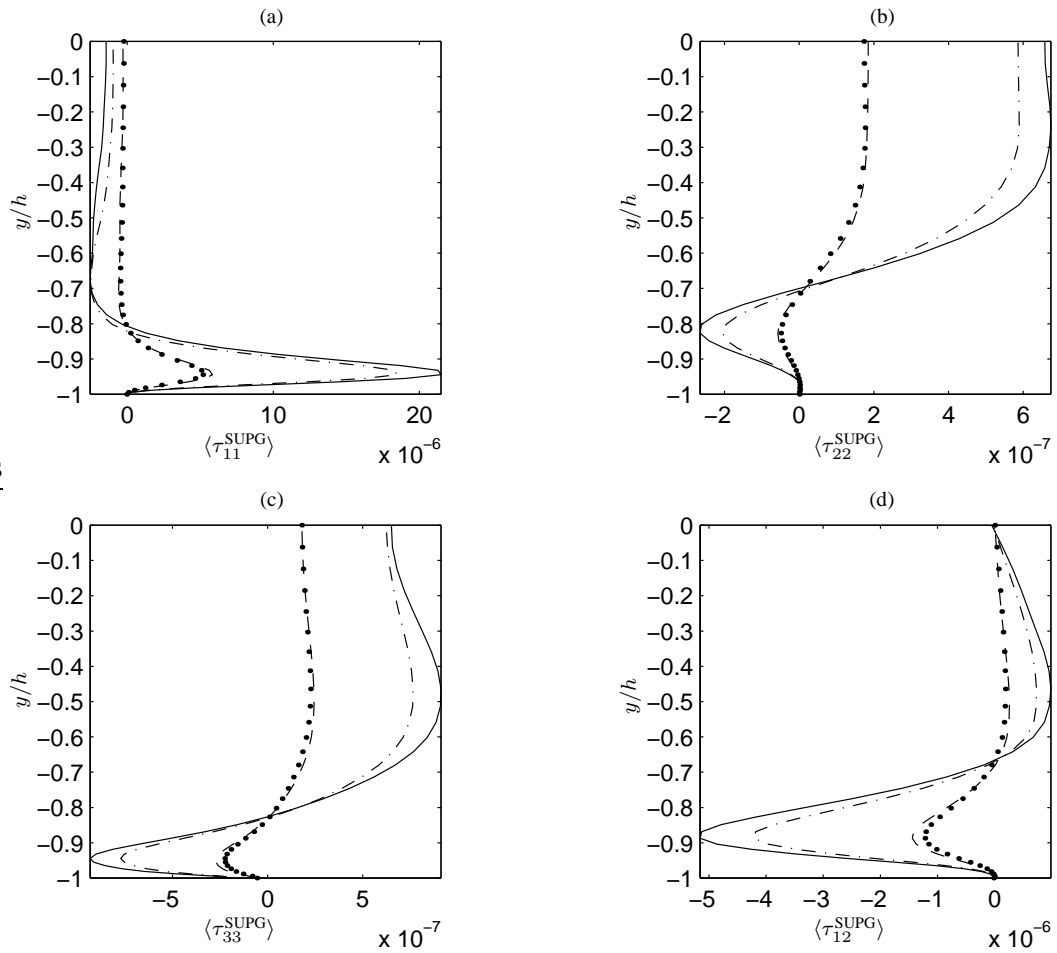


Figure 6.10: Components of the SUPG tensor τ_{ij}^{SUPG} with and without SUPG correction in the dynamic model with the filter W1. — : $c_1 = 16$ and SUPG correction; ---- : $c_1 = 64$ and SUPG correction. - · - : $c_1 = 16$ and no SUPG correction; · · · : $c_1 = 64$ and no SUPG correction.

rected. Once again, the uncorrected model leads to a lower mean force when the SUPG stabilization is increased. On the other hand, the corrected model keeps the mean wall force constant under changes of SUPG strength. Prior to SUPG correction, the relative mean difference in the forces is six percent, and after SUPG correction the difference is negligible.

It is important to note that for the cases considered in this sub-section that have strong SUPG stabilization, the peak SGS dissipation is approximately two times greater than the peak SUPG dissipation. In the previous sub-section, for the case of strong stabilization, the peak SGS dissipation is approximately five times greater than the peak SUPG

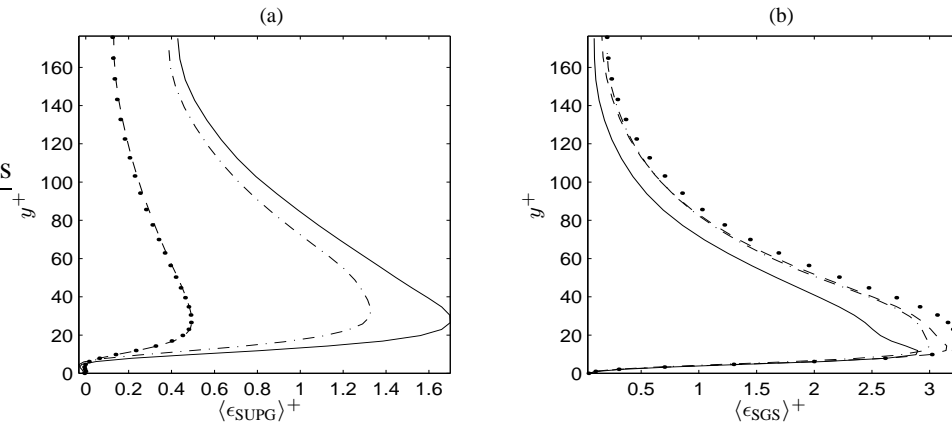


Figure 6.11: (a) SUPG dissipation on the left and (b) dynamic model/SGS dissipation on the right, both in wall units. Here results are with and without SUPG correction in the dynamic model with filter W1. — : $c_1 = 16$ and SUPG correction; ---- : $c_1 = 64$ and SUPG correction. - · - : $c_1 = 16$ and no SUPG correction; · · · : $c_1 = 64$ and no SUPG correction.

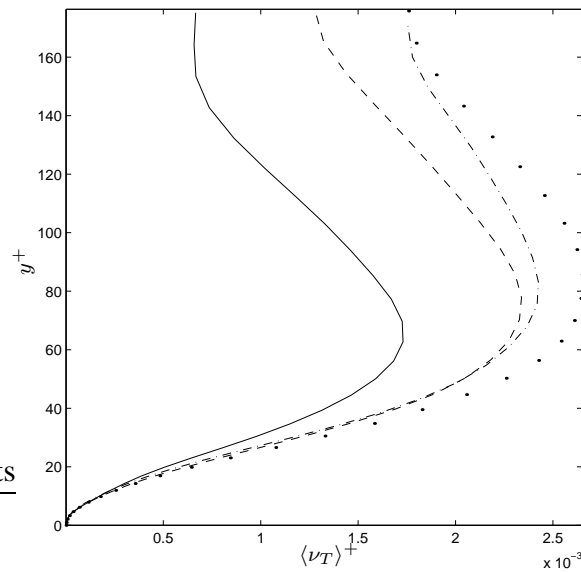


Figure 6.12: Eddy viscosity in wall units with and without SUPG correction in the dynamic model with filter W1. — : $c_1 = 16$ and SUPG correction; ---- : $c_1 = 64$ and SUPG correction. - · - : $c_1 = 16$ and no SUPG correction; · · · : $c_1 = 64$ and no SUPG correction.

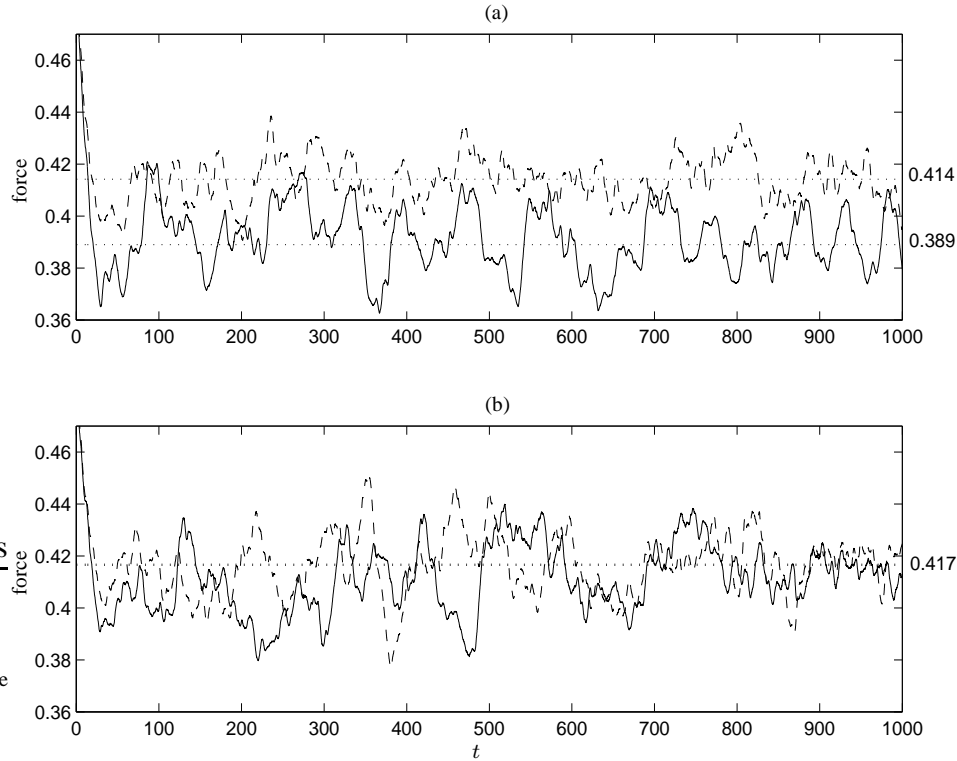


Figure 6.13: (a) Wall forces without SUPG correction on the top and (b) wall forces with SUPG correction on the bottom. In all cases the model was computed with filter W1. — : $c_1 = 16$; ---- : $c_1 = 64$.

dissipation. In the scenario of relatively small difference between the strengths of SGS and SUPG dissipations, the dynamic model correction is seen to have a greater impact on the results than in cases when the maximum difference between SGS and SUPG dissipations is greater. This can be seen by comparing the mean wall force between the corrected and uncorrected models under high difference between maximum SGS and SUPG dissipations (Figure 6.9) and under low difference between these two (Figure 6.13). In Figure 6.9, the difference in the force histories caused by changing the SUPG strength is less pronounced than in Figure 6.13. Thus, having a corrected dynamic model proves to be more significant in cases where the maximum difference between SGS and SUPG dissipations is low.

Next, in Figures 6.14, 6.15, and 6.16 we compare mean streamwise velocity, root-mean-square of velocity fluctuations and Reynolds stresses between strong and weak dynamic models with and without SUPG correction. For all cases SUPG dissipation is strong at $c_1 = 16$. In the case of the weak dynamic model, which uses filter W1, the SUPG cor-

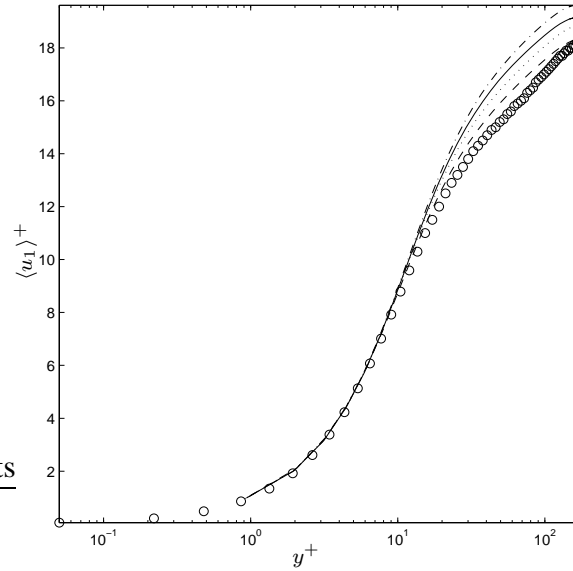


Figure 6.14: Mean streamwise velocity in wall coordinates with dynamic model using filter S1 and SUPG correction(—), filter W1 and SUPG correction(----), filter S1 and no SUPG correction(-·-), and filter W1 and no SUPG correction(···). \circ : mean velocity in the DNS in [34].

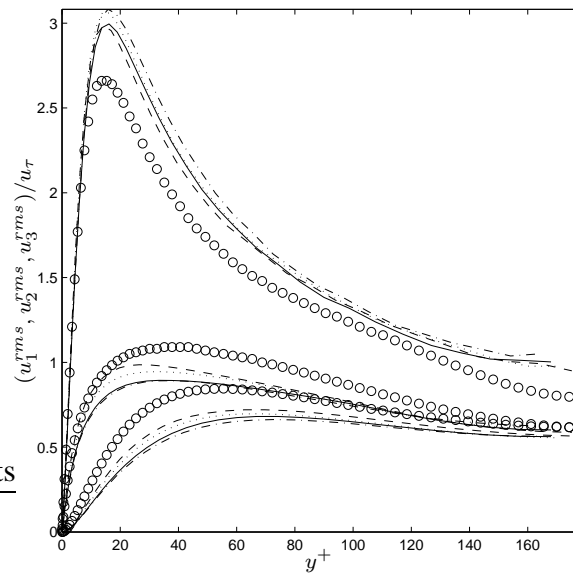


Figure 6.15: Rms of velocity fluctuations in wall coordinates. Rms of velocities with dynamic model using filter S1 and SUPG correction(—), filter W1 and SUPG correction(----), filter S1 and no SUPG correction(-·-), and filter W1 and no SUPG correction(···). \circ : rms of fluctuations in the DNS in [34].

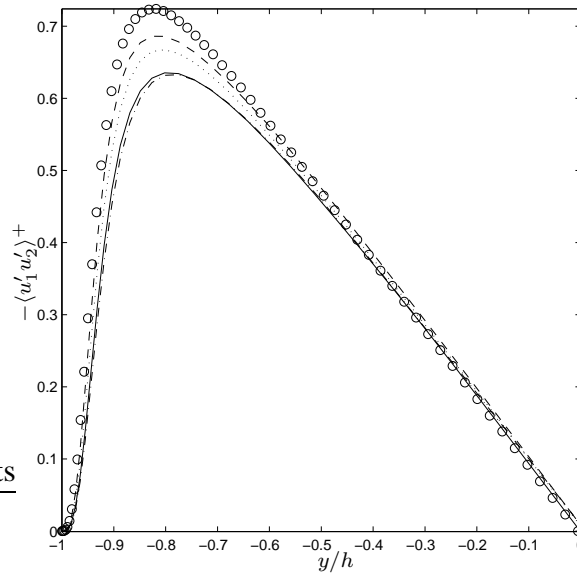


Figure 6.16: Reynolds stress component $\langle u'_1 u'_2 \rangle$ with dynamic model using using filter S1 and SUPG correction (—), filter W1 and SUPG correction (----), filter S1 and no SUPG correction (- · -), and filter W1 and no SUPG correction (···). \circ : Reynolds stress component in the DNS in [34].

rection introduces greater changes, especially in terms of mean streamwise velocity and Reynolds stress component $\langle u'_1 u'_2 \rangle$. This is due to the small difference between SGS and SUPG energy dissipation. From these figures we can clearly say that the dynamic model with SUPG correction using test filter W1 is the top performer, which can be directly attributed to its better approximation of the mean wall force.

6.3.3 Channel flow at $Re_\tau = 395$ with model using filter S1

Here, we study numerical results for the case when the difference between peak SGS and SUPG dissipations is larger than in the previous simulations. This occurs in turbulent channel flow at $Re_\tau = 395$ with the dynamic model using filter S1. By Dean's suggested correlation, as given in [34], $Re_\tau = 395$ corresponds to a bulk Reynolds number, Re , based on the bulk velocity and channel half-width of 6800. Referring back to Figure 4.5, for this problem $L_x = 2\pi h$ and $L_z = \pi h$. Here, the domain is split by 33 vertices in the streamwise direction, 49 vertices in the spanwise direction and 65 vertices in the direction normal to the walls. Similar to the wall-resolved channel flow at $Re_\tau = 180$, a hyperbolic stretching function is employed in the y -direction such that the first vertex off the wall is

set at a distance $\Delta y^+ = u_\tau \Delta y / \nu = 1$ away from the wall, where y is non-dimensionalized by h , and $\nu = 1/Re$.

Due to the more energetic nature of this flow compared to the flow at $Re_\tau = 180$, the dynamic model is expected to cause stronger SGS dissipations. SUPG dissipation is also greater in the current flow compared to the $Re_\tau = 180$ case. With an uncorrected model, the maximum SGS dissipation is approximately five and one-half times greater than then maximum SUPG dissipation. This difference is slightly greater than that studied in sub-section 6.3.1, in which the factor was approximately five. Given previous results, one would expect for the corrected dynamic model to impact results less than it did in earlier simulations.

In Figure 6.17 and Figure 6.18, we plot the SUPG tensor and dissipations due to SGS and SUPG. Looking at the SGS dissipation, the corrected dynamic model does not adjust as much as in earlier cases. This is further evinced by looking at the mean forces in Figure 6.19. As seen in this figure, the mean forces in the uncorrected model cases do not differ by much (especially in the last third of the simulations) as the strength of SUPG stabilization is changed. Over the last third of the simulations, the mean forces differ by less than two percent. The SUPG corrected dynamic model brings them even closer.

6.4 Turbulent channel LES with the SUPG-modified, parameter-free dynamic model

Now that we have a clearer understanding of the interaction between physical and numerical subgrid-scale modeling, we proceed to test the parameter-free dynamic model (DFWR2) (derived and studied in Chapter 5) with the wall-resolved turbulent channel flow at $Re_\tau = 180$. Earlier, we tested DFWR2 with a wall-modeled channel flow at $Re_\tau = 180$ as well, in which SUPG dissipation played a small role compared to SGS dissipation due to the non-resolution of the near-wall region. We begin by comparing the mean wall force between DFWR2 with and without SUPG correction. Looking at Figures 6.20c and 6.20d we see that SUPG correction helps towards achieving a steady mean of the wall force. In Figure 6.20c, DFWR2 without SUPG correction leads to forces which do not seem to settle down about a steady mean. Instead of a steady mean, a low frequency mode appears in the force history, uncharacteristic of stationary turbulent flows such as the current one.

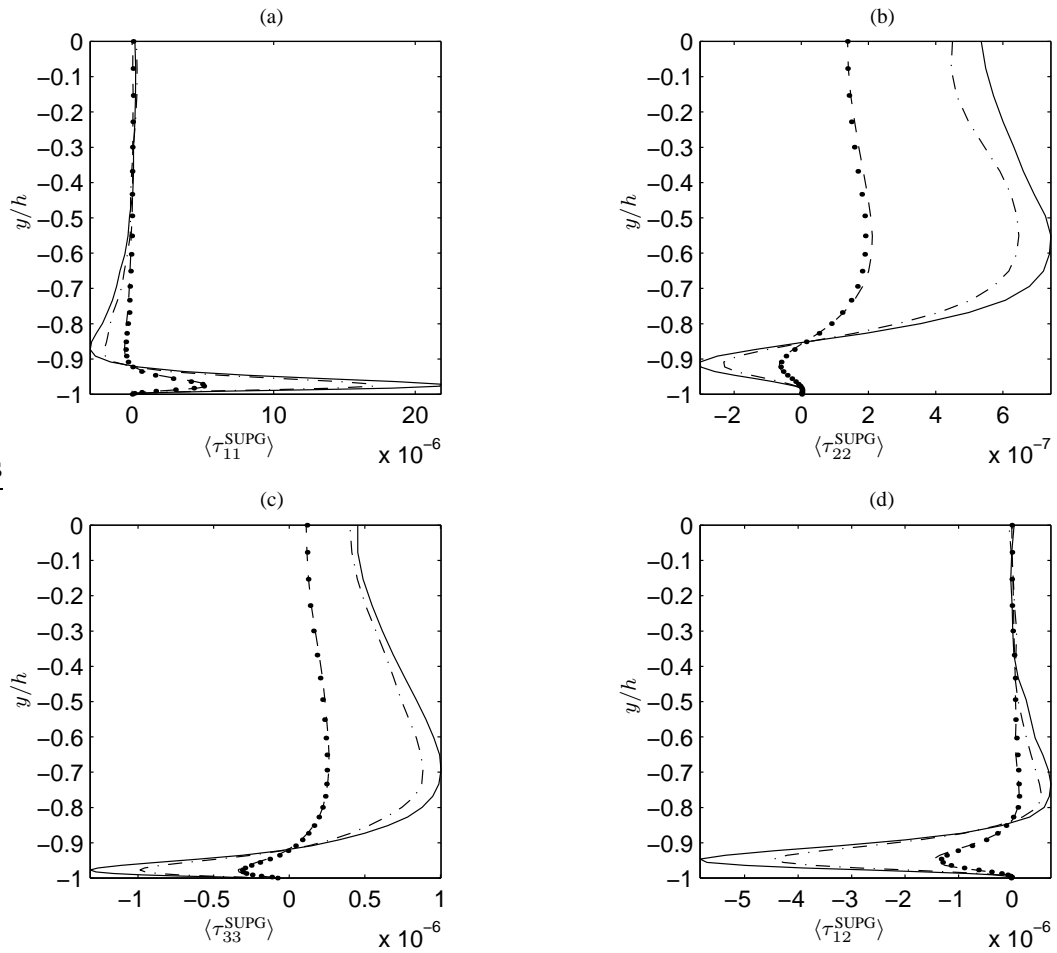


Figure 6.17: Components of the SUPG tensor τ_{ij}^{SUPG} with and without SUPG correction in the dynamic model with filter S1. — : $c_1 = 16$ and SUPG correction; ---- : $c_1 = 64$ and SUPG correction. - · - : $c_1 = 16$ and no SUPG correction; · · · : $c_1 = 64$ and no SUPG correction.

Introducing SUPG correction in the DFWR2 model certainly helps towards achieving a steady mean force, as evidenced by Figure 6.20d.

The instability of DFWR2, reflected through a non-settling behavior of the wall force history, may be explained by looking at the space- and time-averaged model coefficient $(C_s^{\bar{\Delta}} \bar{\Delta})^2$. In Figure 6.21b we see that $(C_s^{\bar{\Delta}} \bar{\Delta})^2$ behaves irregularly near the wall. Specifically, as $|y/h| \rightarrow 0.7$ from the channel center line at $y/h = 0$, it decays at a faster rate than the model coefficients of the classical dynamic models. However, for the region $|y/h| > 0.7$, $(C_s^{\bar{\Delta}} \bar{\Delta})^2$ no longer behaves in the same fashion, as its decay rate is slowed until it finally re-assumes a rapid decay to zero. For $|y/h| > 0.93$, DFWR2 predicts neg-

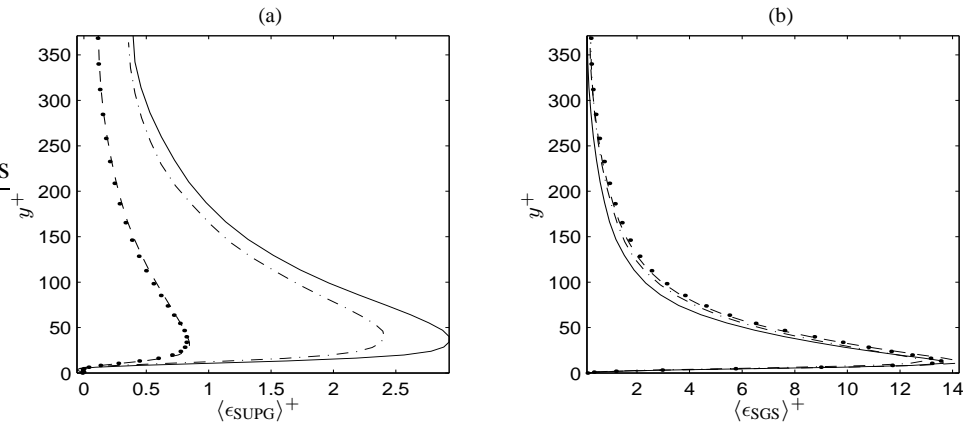


Figure 6.18: (a) SUPG dissipation on the left and (b) dynamic model/SGS dissipation on the right, both in wall units. Here results are with and without SUPG correction in the dynamic model with filter S1. — : $c_1 = 16$ and SUPG correction; ---- : $c_1 = 64$ and SUPG correction. - · - : $c_1 = 16$ and no SUPG correction; · · · : $c_1 = 64$ and no SUPG correction.

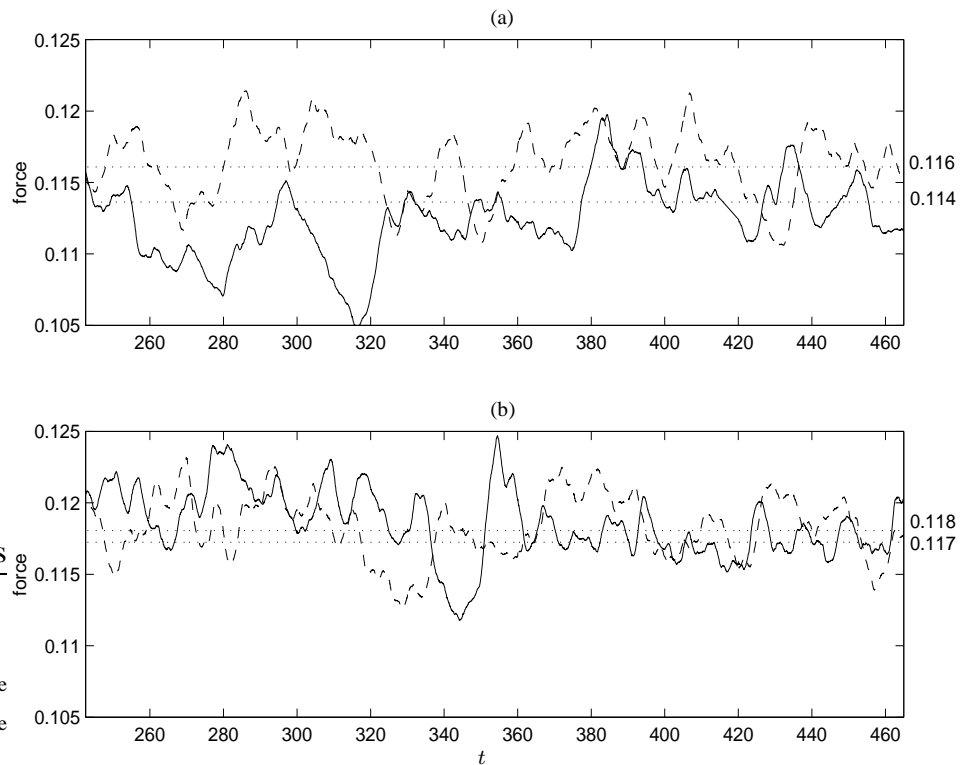


Figure 6.19: (a) Wall forces without SUPG correction on the top and (b) wall forces with SUPG correction on the bottom. In all cases the model was computed with filter S1. The expected mean wall force is approximately 0.133. — : $c_1 = 16$; dashed: $c_1 = 64$.

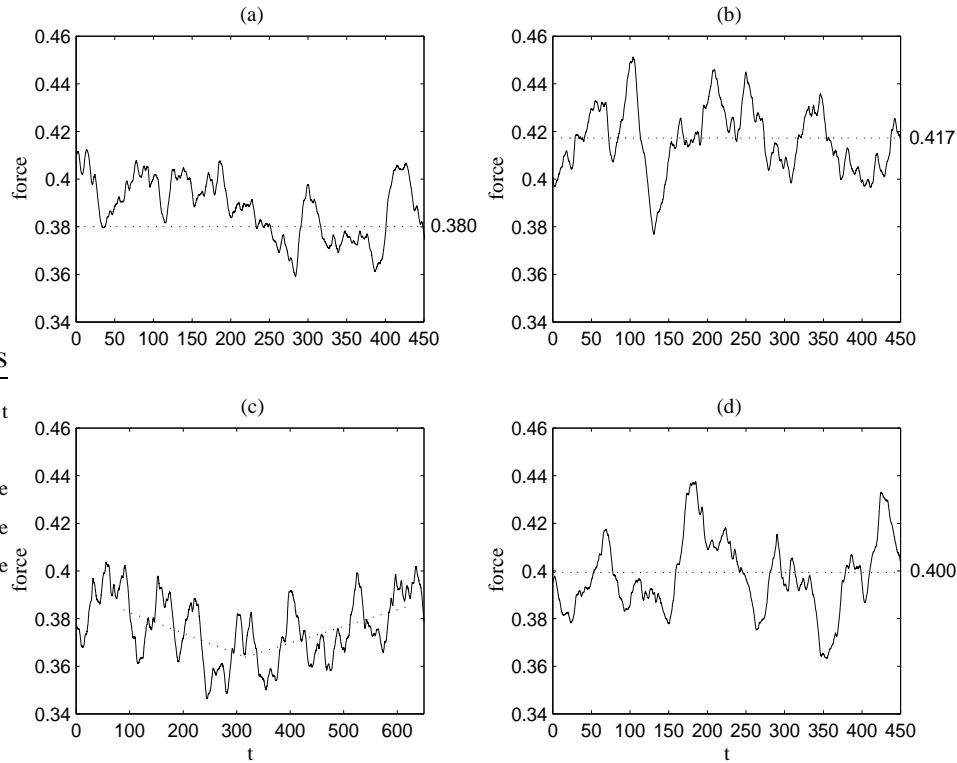


Figure 6.20: Wall force histories with classical dynamic models (CDM) and with DFWR2. Forces with (a) CDM with filter S1 and SUPG correction, (b) CDM with filter W1 and SUPG correction, (c) DFWR2 with no SUPG correction, and (d) DFWR2 with SUPG correction. The mean wall force should be approximately 0.435.

ative values of $(C_s^{\bar{\Delta}} \bar{\Delta})^2$, and thus it is clipped in this range. As discussed in the previous chapter, clipping the model coefficient is done to prevent backscatter. The negative values of $(C_s^{\bar{\Delta}} \bar{\Delta})^2$ near the wall result from its fast decay. However, the main issue with the DFWR2 model coefficient is the irregular behavior of its decay rate. If the coefficient were to decay uniformly as it does in the region $|y/h| > 0.7$, the predicted mean force would be higher, and possibly free of instability. Perhaps, the region of irregular behavior in the decay of $(C_s^{\bar{\Delta}} \bar{\Delta})^2$ can be associated to the region in which a sudden jump is exhibited by the ratio between the classical dynamic model coefficients (shown in Figure 6.21d) with filters S1 and W1, denoted with the subscripts “std” and “wide”, respectively. This indicates that the pathological behavior of DFWR2 near walls can be attributed to differences in test filters S1 and W1 near the walls, and not to the model itself, or the basic principles underlying the model.

Note that the jump exhibited in the ratio between the classical dynamic model co-

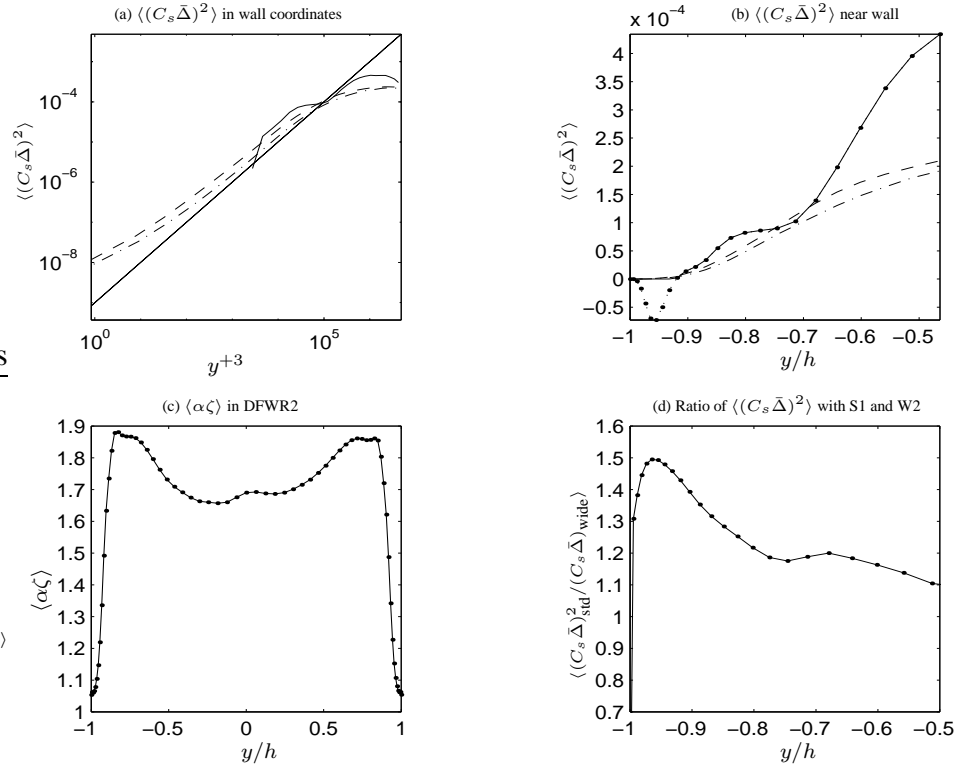


Figure 6.21: (a), (b) $\langle (C_s \bar{\Delta})^2 \rangle$ in DFWR2 with SUPG correction (—), in CDM with S1 and SUPG correction (----), and in CDM with W1 and SUPG correction (- · -). In (a), the solid, straight line denotes the theoretical y^{+3} profile. (c) Filter width ratio in DFWR2, $\langle \alpha \zeta \rangle \equiv \langle (C_s \hat{\Delta} / C_s \bar{\Delta})^2 (\hat{\Delta} / \bar{\Delta})^2 \rangle$. In (b), — : clipped DFWR2 coefficient used in simulations; · · · : DFWR2 coefficient showing negative values.

efficients with finite element-based test filters S1 and W1 is not observed if instead finite difference-based filters FD1 and its wider version are used. This can be seen in Figure 4.13. DFWR2 was implemented with these two finite difference-based filters, however, it was found to be beset by instabilities in its prediction of the model coefficient, possibly due to the lack of smoothness in the filters compared to the finite element-based filters. For example, as noted in Table 3.1, filter W1 involves 64 function evaluations, leading to much smoother filtered fields compared to the wide version of filter FD1, which only involves 25 function evaluations.

In the wall-modeled channel, the region exhibiting the sudden jump in the ratio between classical dynamic model coefficients using finite-element based test filters is not well resolved, thus the irregularity of the model coefficient is not well resolved (as can be seen from Figures 5.13b and 5.13d), leading to a well-behaved model coefficient.

For the wall-resolved channel studied here, SUPG correction applied to DFWR2 certainly does not eliminate the irregularity of the model coefficient, $(C_s^{\bar{\Delta}}\bar{\Delta})^2$, near the walls. However, SUPG correction decreases the adverse effect of this irregular behavior by lowering the SGS dissipation, leading to a more stable model.

In Figures 6.22 and 6.23 we plot dissipations and eddy viscosities, respectively, for DFWR2 and compare them to those of the classical dynamic models. The irregularity of DFWR2's model coefficient is not reflected through SGS dissipation, but it is clearly reflected through the eddy viscosity. Furthermore, given that DFWR2 produces a greater dynamic coefficient compared to the coefficients of the classical models, SGS dissipation due to DFWR2 is greater than that of the classical models, especially in the region $y^+ > 60$. As expected, SUPG stabilization adjusts as its dissipation is less in the case of the DFWR2. The peak SGS dissipations occur in the region $y^+ < 60$, where we see that the classical dynamic model with filter S1 leads to the highest SGS dissipation peak, followed by DFWR2. The lowest peak is obtained with the classical dynamic model using filter W1. The order of the SGS dissipation peaks is reflected through the mean forces in Figure 6.20. Because peak SGS dissipation with the classical model with filter W1 is the lowest of all cases, this model leads to a more energetic flow, and thus higher wall forces compared to DFWR2 and the classical model with filter S1. Because peak SGS dissipation with DFWR2 is less than with the classical model with filter S1, the former leads to a higher wall force than the latter.

In the final three figures (Figures 6.24, 6.25, and 6.26) we compare DFWR2 to the classical dynamic models, all with SUPG correction, in terms of mean streamwise velocity fluctuations, root-mean-square of velocity fluctuations, and Reynolds stress component $\langle u'_1 u'_2 \rangle$. In terms of these three quantities, DFWR2 does better than the classical dynamic model with filter S1. In terms of mean streamwise velocity and root-mean-square of velocity fluctuations, the classical dynamic model with filter W2 does slightly better than DFWR2. However, in terms of Reynolds stress, both lead to similar results. Note that a comparison between these three models is difficult given that classical dynamic model results are subject to variation if the assumptions made for their filter width ratios are changed. This is not the case for the parameter-free model, DFWR2, as its filter width ratio is dynamically computed. Recall that in the classical dynamic models, the filter width

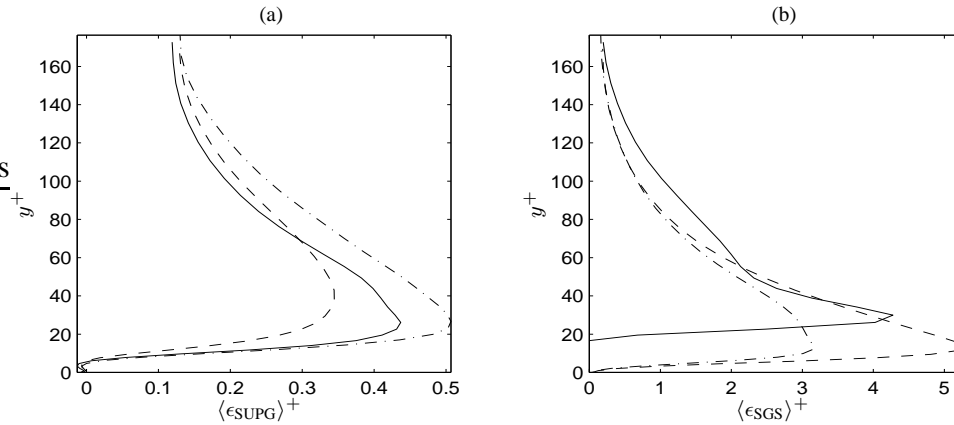


Figure 6.22: (a) SUPG dissipation on the left and (b) dynamic model/SGS dissipation on the right, both in wall units. — : DFWR2 with SUPG correction; ---- : classical dynamic model (CDM) with filter S1 and SUPG correction; - · - : CDM with filter W1 and SUPG correction.

ratio is assumed to be $\alpha \equiv (\hat{\Delta}/\hat{\Delta})^2 = \kappa(\hat{\Delta}/h)^2$, with $\kappa = 1$. If we were to change κ , results with the classical dynamic models would change. Furthermore, we have computed test filter widths, $\hat{\Delta}$, based on the filters' second moments. However, other definitions of filter widths can be taken, such as those based on filter transfer functions, leading to different values of $\hat{\Delta}$, and thus different results with the classical dynamic models. In summary, the question of how to set the filter width ratio in the classical dynamic models is an open one. This is not the case for DFWR2 as its filter width ratio is dynamically computed.

6.5 Chapter summary

In this chapter we have presented a modification to the Smagorinsky dynamic subgrid-scale stress model for the purpose of allowing the model to adjust itself in the presence of varying numerical dissipation due to SUPG stabilization. The success of the SUPG modification was shown on LES of turbulent channel flows with Reynolds numbers Re_τ of 180 and 395. It was concluded that for cases when the maximum difference between SGS and SUPG dissipation is low, the modification to the model plays an important role in allowing the model to adjust properly under different amounts of SUPG dissipation. In cases where this difference is large, SUPG dissipation does not have a strong impact on results and the modification to the model becomes almost negligible. Furthermore, it was shown that the SUPG modification applied to the parameter-free model, DFWR2, helps to improve re-

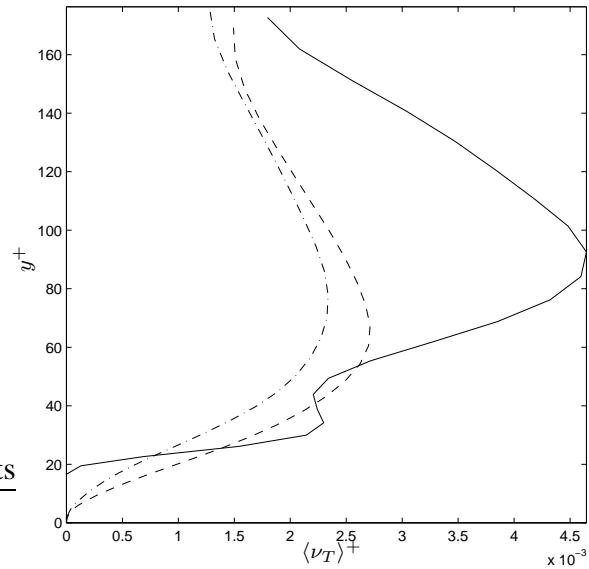


Figure 6.23: Eddy viscosity in wall units. — : DFWR2 with SUPG correction; ---- : classical dynamic model (CDM) with filter S1 and SUPG correction; - · - : CDM with filter W1 and SUPG correction.

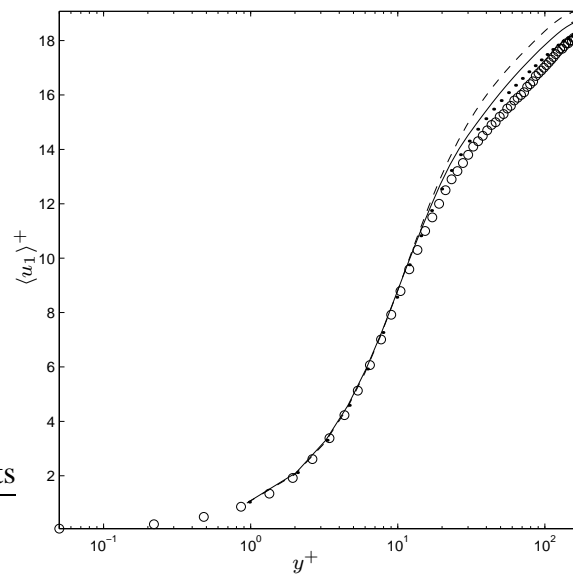


Figure 6.24: Mean streamwise velocity in wall coordinates with DFWR2 and SUPG correction (—), classical dynamic model (CDM) with filter W1 and SUPG correction (· · ·), and CDM with filter S1 and SUPG correction (----). \circ : mean velocity in the DNS in [34].

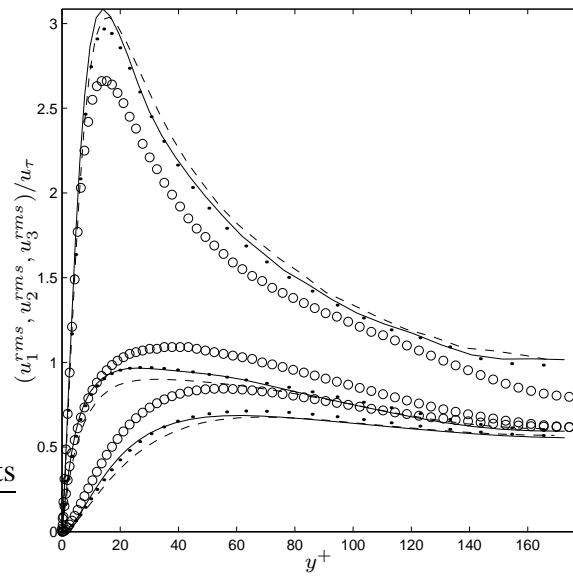


Figure 6.25: Rms of velocity fluctuations in wall coordinates. Rms of velocities with DFWR2 and SUPG correction (—), classical dynamic model (CDM) with filter W1 and SUPG correction ($\cdot \cdot \cdot$), and CDM with filter S1 and SUPG correction (----). \circ : rms of fluctuations in the DNS in [34].

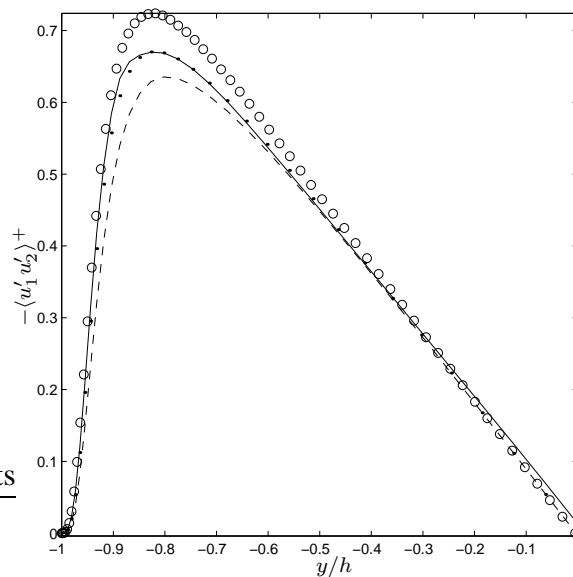


Figure 6.26: Reynolds stress component $\langle u_1' u_2' \rangle$ with DFWR2 and SUPG correction (—), classical dynamic model (CDM) with filter W1 and SUPG correction ($\cdot \cdot \cdot$), and CDM with filter S1 and SUPG correction (----). \circ : Reynolds stress component in the DNS in [34].

sults. Due to differences between finite element-based standard and wide filters, DFWR2 suffers from a de-stabilizing irregularity in its model coefficient in the near-wall region. By decreasing SGS dissipation, and thus the influence of a poorly behaved DFWR2 near walls, SUPG correction suppresses adverse effects brought about by DFWR2. The irregularity of the DFWR2 model coefficient was not observed in the wall-modeled channel flow of Chapter 5 because the near-wall region in which the irregularity occurs is not completely resolved.

CHAPTER 7

DISCUSSION AND CONCLUSION

In this thesis, several novel approaches to dynamic subgrid-scale modeling for LES of turbulent flows have been proposed and studied with a stabilized finite element method, namely the streamline upwind / Petrov-Galerkin (SUPG) method. Historically, the majority of dynamic subgrid-scale modeling in LES has dealt with accurate physical representation of the effect of unresolved, subgrid-scales, filtered out by the discretization, on resolved scales. Thus, one of the major goals in subgrid-scale modeling has been to correctly represent the amount of energy extracted from the resolved scales by the modeled, unresolved ones. To that extent, we have proposed new models in which the dissipative nature and thus the implicit filter characteristic of the stabilized method representing the discretization have been taken into account. Our approach has been to better model the subgrid-scales by understanding the stabilized method's impact on a given physical model, instead of traditional approaches which often focus on the introduction of more complex physics. LES models will be inevitably coupled with the numerics. For this reason, it is the author's belief that before introducing models which can better represent the physics behind subgrid-scales, it is best to fully understand the behavior of simpler models within their numerical setting.

In the first part of this work, the popular dynamic Smagorinsky model was introduced and the major difficulty in setting the sole model parameter, denoted as the filter width ratio, was discussed. It was made clear that this parameter requires knowledge of the characteristic length scale, or better yet, the width of the primary filter, G_{Δ} , which is not calculable because it is implicitly set by the discretization method. The explicit test filter, $G_{\hat{\Delta}}$, present in dynamic model computations was discussed and it was seen that knowledge of the width of a second filter resulting from successive applications of the primary and test filter, $G_{\hat{\Delta}}$, is required as well. Just like the primary filter, this second filter is implicitly set by the discretization method, making it impossible to directly determine its shape and width. To be precise, the model parameter (or the filter width ratio) involves the widths of G_{Δ} and $G_{\hat{\Delta}}$, both set by the discretization method, thus not calculable.

For use in the test filtering operation required in the dynamic model, new filters appropriate for LES with finite element discretizations were introduced. These “finite element-based” filters are obtained from Gauss quadrature approximations of the generalized box filter on a given topology. Furthermore, the finite element-based filters are characterized by their filter widths, obtained from different possible definitions. Two definitions considered here were based on the filters’ second moments and transfer functions, respectively. It was seen that filter widths depend on the definition taken, and thus are not unique for a given filter. In addition to the finite element-based filters, other filters based on finite dimensional projections were proposed. These filters, better suited for finite element discretizations with hierarchic basis functions, are based on L_2 -projections and interpolations.

Based on dynamic model simulations of decaying isotropic turbulence and turbulent channel flow, the role of the test filter type on dynamic model results was understood. First, a form of the unknown filter width ratio in the dynamic model was assumed. The form took the filter width ratio as proportional to the width of the explicit test filter divided by the grid size. Under this assumption, isotropic turbulence results were shown to be independent of the filter used as long as the width of the test filter is consistently computed following one of the definitions proposed. The quality of results relied on the proportionality constant in the assumed form of the filter width ratio.

In the case of wall-bounded turbulence, the previous conclusion regarding the independence of dynamic model results to filter choice was not observed. It was seen that under the assumption for the filter width ratio previously mentioned, wide finite element-based filters performed better compared to their narrower counterparts, due to the former’s tendency to cause the dynamic model coefficient to decay faster in the near-wall region. The filters with narrower widths led to model coefficients which decayed slower near walls, thereby causing more dissipation than required. Additionally, the three-dimensionality of the finite element-based filters in turbulent channel flow was observed not to cause adverse affects compared to the traditional in-plane filters used in finite difference discretizations. Commonly, the filtering operation is applied over directions of flow homogeneity, such as is the case of the in-plane filters in channel flow. However, here the three-dimensional finite element-based filters were used because many turbulent flows would not have direc-

tions of homogeneity.

The filter width ratio was seen to have a strong impact on dynamic model results, demonstrating the importance of its accurate determination. To that extent, new dynamic models characterized by dynamic determination of their filter width ratios were derived. The first of these models, denoted as DFWR1, is based on the invariance of isotropic turbulence results regardless of the test filter. The success of DFWR1 was demonstrated on LES of isotropic turbulence on various topologies of hexahedral, tetrahedral and wedge elements. For the three topologies, DFWR1 was able to represent the correct transfer of energy between the larger and smaller resolved scales in the simulations. A key component of DFWR1 is the explicit application of a second test filter in addition to the test filter used in the classical dynamic model. With DFWR1, the resolved field is sampled twice by the test filters in order to determine the filter width ratio parameter, thereby accounting for the implicit filter characteristic of the stabilized finite element method. Unlike in the classical dynamic model, the filter width ratio parameter is no longer an input, and the only input is the ratio of the width of the two explicit test filters used. This is an advantage over the classical dynamic model because in the case of DFWR1, the test filters are explicit and consequently their widths can be determined. Although filter widths depend on the definition used, it was seen that for a given definition, the ratio between test filters widths is nearly constant, independent of the definition taken. This was the case when filter width definitions were based on transfer functions.

DFWR1 makes use of the assumption for the form of filter width ratio discussed earlier, which breaks down in near-wall regions. Consequently, a second model was derived, denoted as DFWR2, again characterized by its dynamic calculation of the filter width ratio. DFWR2 does not use any assumption for the form of the filter width ratio. Instead, it relies on the more general, idealistic principle that if the filter width ratio is properly obtained, the dynamic model coefficient should be independent of the test filter used. A second advantage of DFWR2 is that it is parameter-free, unlike the classical dynamic model and DFWR1. This can play a role in unstructured-grid simulations for which test filter widths can be cumbersome to obtain. Thirdly, DFWR2 is derived without the scale-invariance assumption made in the classical dynamic model and in DFWR1, making it a scale-dependent model suitable for a broader range of flow conditions. DFWR2 was first tested on isotropic

turbulence and produced similar results as those of DFWR1. In the near-wall region of turbulent channel flow, DFWR2 was observed to have a difficulty associated to the difference in the widths of the two test filters used. This difficulty came about due to an irregularity in the decay rate of the model coefficient as it approached the walls. It was shown that for wall-modeled turbulent channel flow, the region in which the irregularity of the model coefficient occurs is not resolved, resulting in a well-behaved coefficient. For this problem, DFWR2 led to good approximations of the mean streamwise velocity and the mean force exerted on the channel walls by the flow.

In the latter part of this work, a modification was made to the dynamic model in an effort to account for the dissipative nature of the stabilized method. To that extent, an *ad hoc* definition of the numerical dissipation due to the stabilized method was proposed. Studies of the energy dissipations associated to the dynamic model and the stabilized method were used to motivate a modified dynamic model able to properly adjust to parameter changes in SUPG stabilization controlling the strength of numerical dissipation. The SUPG-modified dynamic model was validated on wall-resolved turbulent channel flow, for which it led to improved results in terms mean wall force, mean streamwise velocity, root-mean-square of velocity fluctuations, and Reynolds stress.

As discussed earlier, DFWR2 suffers from an irregularity of the model coefficient decay as it approaches the walls. In the case of wall-resolved channel flow, this irregularity was conjectured to cause an instability, manifested in an unsteady mean of the wall force. However, when the SUPG modification was applied to the DFWR2 model, this instability was no longer present. This led to the conclusion that by effectively decreasing the strength of the DFWR2 model, the SUPG modification was able to lessen the adverse effect created by the irregular decay of the model coefficient. Application of the SUPG modification to DFWR2 represents the most general form of dynamic subgrid-scale modeling proposed here, in which, up to some degree, LES is ideally thought of as independent of

1. a change in the physical (dynamic) model brought about by changing the spatial filter required in the dynamic model, and
2. a change in the numerical model brought about by the tuning of SUPG parameters so as to provide sufficient stabilization.

Recall the introductory statements of Chapter 1, which first put forth these modeling tenets. DFWR2 enforces the first one while the SUPG modification satisfies the second.

There are limitations to the current research. The clearest one is that in near-wall regions, DFWR2 is sensitive to the difference between the widths of the two test filters required. This suggests that new filters closer in width than the ones proposed here should be developed. Perhaps the finite dimensional projections/filters introduced in Chapter 3 can serve for this purpose, given that their widths are easily controlled, as was shown for the L_2 -projection filters. Furthermore, these projections/filters could be used to extend DFWR2 to hierarchic grids.

All dynamic model results in this work have been presented on grids which are either uniform or slightly non-uniform. As discussed in Chapter 4, non-uniformity can cause asymmetries in the three-dimensional finite element-based filters leading to potential adverse effects. Studies on grids with greater non-uniformity than those used here should be performed to quantify any negative impact on results. In addition to more studies with non-uniform grids, studies with tetrahedral and wedge topologies should be performed and the reason for the inability of these topologies to represent near-wall turbulence at the same quality as hexahedral topologies should be well understood. As was discussed at the end of Chapter 4, tetrahedral and wedge elements introduce a directional bias which negatively impact the near-wall numerical solution. In the case of isotropic turbulence, these elements introduce directional bias, but the bias does not affect the solution because the flow is isotropic and thus directionally independent.

The models proposed in this work have great potential to be further developed and achieve far-reaching capabilities. The dynamic filter width ratio formulation in DFWR2 can be extended to other models other than the dynamic Smagorinsky model, such as the modified dynamic mixed (Bardina) model of Moranishi and Vasilyev in [47]. As mentioned in an earlier chapter, the dynamic mixed subgrid-scale stress model has yielded better alignment of its components with the true subgrid-scale stress measured *a priori* through direct numerical simulations, and overall does a better job in representing the root-mean-square of velocity fluctuations and the Reynolds stress than the dynamic Smagorinsky model.

Due to its scale-dependency, DFWR2 in itself has potential applicability to numer-

ous flow and simulation conditions, where the traditional model is known to fail. For example, in hybrid Reynolds-averaged Navier-Stokes / large-eddy simulations the local grid scale may become larger than the inertial scales and may approach the integral scale, thus breaking the scale-invariance assumption. A second example is when LES approaches DNS and the grid scale approaches the dissipative, viscous scales, the model should reflect this change by causing less energy dissipation. For the simulation conditions previously discussed, one would expect scale dependence of the model near a certain length scale, thereby making the traditional model invalid. In brief, for complex flow conditions, one does not necessarily know before hand how the model should change with scale, thus motivating the need for a scale-dependent model.

The dynamic formulation of the filter width ratio in DFWR1 and DFWR2 and the SUPG modification to the dynamic models prove that subgrid-scale modeling taking into consideration the interaction between physical and numerical models is indeed a possibility and not just an unrealizable, theoretical notion. The present work can certainly serve as basis for future

- improved physical subgrid-scale models which reflect the possible interaction between physical and numerical energy dissipation and
- improved stabilized methods designed to take into account the presence of physical subgrid-scale dissipation, in addition to providing the usual requirements of stability, consistency, and convergence.

In conclusion, to be able to utilize the full potential of LES for numerical simulation of large-scale turbulent flow problems of the present and future, methods capable of describing such target problems must be explored and thoroughly understood. Stabilized finite element methods coupled with proper physical subgrid-scale models can potentially meet this challenge. The developments put forth in this work leading to versatile, better designed subgrid-scale modeling represent a move towards this future.

REFERENCES

- [1] A. A. Aldama. Filtering techniques for turbulent flow simulation. In C. A. Brebbia and S. A. Orszag, editors, *Lecture Notes in Engineering*, volume 56. Springer-Verlag, 1990.
- [2] M. Antonopoulos-Domis. Large-eddy simulation of a passive scalar in isotropic turbulence. *J. Fluid Mech.*, 104:55–79, 1981.
- [3] C. Baiocchi, F. Brezzi, and L. P. Franca. Virtual bubbles and the Galerkin/least squares method. *Comp. Meth. Appl. Mech. Engng.*, 105:125–142, 1993.
- [4] J. P. Boris, F. F. Grinstein, E. S. Oran, and R. L. Kolbe. New insights into large eddy simulation. *Fluid Dyn. Res.*, 10:199–228, 1992.
- [5] A. N. Brooks and T. J. R. Hughes. Streamline upwind / Petrov-Galerkin formulations for convection dominated flows with particular emphasis on the incompressible Navier-Stokes equations. *Comp. Meth. Appl. Mech. Engng.*, 32:199–259, 1982.
- [6] D. Carati and E. Vanden Eijnden. On the self-similarity assumption in dynamic models for large eddy simulations. *Physics of Fluids*, 9(7):2165–2167, 1997.
- [7] D. Carati, K. E. Jansen, and T. S. Lund. A family of dynamic models for large-eddy simulation. In *Annual Research Briefs*, pages 35–40, NASA Ames / Stanford University, 1995. Center for Turbulence Research.
- [8] R. Codina and J. Blasco. Analysis of a stabilized finite element approximation of the transient convection-diffusion-reaction equation using orthogonal aubscales. *Computing and Visualization in Science*, 4:167–174, 2002,.
- [9] G. Comte-Bellot and S. Corrsin. Simple Eulerian time-correlation of full and narrow-band velocity signals in grid-generated ‘isotropic’ turbulence. *Journal of Fluid Mechanics*, 48:273–337, 1971.

- [10] J. W. Deardorff. A numerical study of three-dimensional turbulent channel flow at large Reynolds numbers. *Journal of Fluid Mechanics*, 41:453–480, 1970.
- [11] J. W. Deardorff. On the magnitude of the subgrid scale eddy viscosity. *J. Comput. Phys.*, 7:120–133, 1971.
- [12] M. Van Dyke. *Album of Fluid Motion*. Parabolic Press, 1982.
- [13] U. Frisch. *Turbulence*. Cambridge University Press, 1995.
- [14] G. P. Galdi, T. Iliescu, and W. J. Layton. Mathematical analysis for a new large eddy simulation model. Preprint, 2000.
- [15] G. P. Galdi and W. J. Layton. Approximating the larger eddies in fluid motion: A model for space filtered flow. *Math. Methods and Models in Applied Sciences*, 10(3):343–350, 2000.
- [16] C. F. Gerald and P. O. Wheatley. *Applied Numerical Analysis*. Addison-Wesley Publishing Company, Inc., 5th edition, 1994.
- [17] M. Germano. Turbulence: the filtering approach. *Journal of Fluid Mechanics*, 238:325–336, 1992.
- [18] M. Germano, U. Piomelli, P. Moin, and W. H. Cabot. A dynamic subgrid-scale eddy viscosity model. *Physics of Fluids*, 3:1760, 1991.
- [19] J. Gleick. *Chaos: Making a New Science*. Penguin, New York, 1988.
- [20] J. Gullbrand. Explicit filtering and subgrid-scale models in turbulent channel flow. In *Annual Research Briefs*, pages 31–42, NASA Ames / Stanford University, 2001. Center for Turbulence Research.
- [21] P. Hansbo and A. Szepessy. Velocity-pressure streamline diffusion finite element method for the incompressible Navier-Stokes equations. *Comp. Meth. Appl. Mech. Engng.*, 1990.

- [22] G. Hauke and T. J. R. Hughes. A comparative study of different sets of variables for solving compressible and incompressible flows. *Comp. Meth. Appl. Mech. Engng.*, 153:1–44, 1998.
- [23] J. O. Hinze. *Turbulence*. McGraw-Hill, New York, 1975.
- [24] T. J. R. Hughes. Multiscale phenomena: Green’s functions, the Dirichlet-to-Neumann formulation, subgrid scale models, bubbles and the origins of stabilized methods. *Comp. Meth. Appl. Mech. Engng.*, 127:387–401, 1995.
- [25] T. J. R. Hughes, L. P. Franca, and M. Balestra. A new finite element formulation for fluid dynamics: V. A stable Petrov-Galerkin formulation of the Stokes problem accommodating equal-order interpolations. *Comp. Meth. Appl. Mech. Engng.*, 59:85–99, 1986.
- [26] T. J. R. Hughes, L. P. Franca, and G. M. Hulbert. A new finite element formulation for fluid dynamics: VIII. The Galerkin / least-squares method for advective–diffusive equations. *Comp. Meth. Appl. Mech. Engng.*, 73:173–189, 1989.
- [27] T. J. R. Hughes, L. Mazzei, and K. E. Jansen. Large-eddy simulation and the variational multiscale method. *Computing and Visualization in Science*, 3:47–59, 2000.
- [28] T. J. R. Hughes and J. Stewart. A space-time formulation for multiscale phenomena. *J. Comput. Appl. Math.*, 74:217–229, 1996.
- [29] Thomas J. R. Hughes. *The finite element method: Linear static and dynamic finite element analysis*. Prentice Hall, Englewood Cliffs, NJ, 1987.
- [30] K. E. Jansen. Private communication. 1998.
- [31] K. E. Jansen. A stabilized finite element method for computing turbulence. *Comp. Meth. Appl. Mech. Engng.*, 174:299–317, 1999.

- [32] K. E. Jansen and A. E. Tejada-Martínez. An evaluation of the variational multiscale model for large-eddy simulation while using a hierarchical basis. Number 2002-0283, Reno, NV, Jan. 2002. 40th AIAA Annual Meeting and Exhibit.
- [33] K. E. Jansen, C. H. Whiting, and G. M. Hulbert. A generalized- α method for integrating the filtered Navier-Stokes equations with a stabilized finite element method. *Comp. Meth. Appl. Mech. Engng.*, 1999. Contributed to a special volume devoted to the Japan-US Symposium on F.E.M. in Large-Scale C.F.D., SCOREC Report 10-1999.
- [34] J. Kim, P. Moin, and R. Moser. Turbulence statistics in fully developed channel flow at low Reynolds number. *Journal of Fluid Mechanics*, 177:133, 1987.
- [35] D. Knight, G. Zhou, N. Okong'o, and V. Shukla. Compressible large eddy simulation using unstructured grids. Number 98-0535. AIAA Annual Meeting and Exhibit, 1998.
- [36] D. Kwak, W. C. Reynolds, and J. H. Ferziger. Three dimensional time-dependent computation of turbulent flow. Technical Report Rep. TF-5, Thermosciences Div., Stanford University, Dept. Mech. Eng., Stanford, CA 94305, 1975.
- [37] H. Le, P. Moin, and J. Kim. Direct numerical simulation of turbulent flow over a backward-facing step. *Journal of Fluid Mechanics*, 330:349–374, 1997.
- [38] A. Leonard. On the energy cascade in large-eddy simulations of turbulent fluid flows. Technical Report Rep. TF-1, Thermosciences Div., Stanford University, Dept. Mech. Eng., Stanford, CA 94305, 1973.
- [39] D. K. Lilly. On the application of the eddy viscosity concept in the inertial subrange of turbulence. NCAR Manuscr. 123, NCAR, 1966.
- [40] D. K. Lilly. A proposed modification of the Germano subgrid-scale closure. *Physics of Fluids*, 3:2746–2757, 1992.
- [41] T. S. Lund. On the use of discrete filters for large-eddy simulation. In *Annual Research Briefs*, pages 83–95, NASA Ames / Stanford University, 1997. Center for Turbulence Research.

- [42] T. S. Lund and H.-J. Kaltenbach. Explicit filtering for LES. In *Annual Research Briefs*, pages 91–105, NASA Ames / Stanford University, 1995. Center for Turbulence Research.
- [43] A. L. Marsden, O. V. Vasilyev, and P. Moin. Construction of commutative filters for LES on unstructured meshes. *Journal of Computational Physics*, 175:584–603, 2002.
- [44] C. Meneveau and J. Katz. Scale-invariance and turbulence models for large-eddy simulation. *Annu. Rev. Fluid Mech.*, 415:1–32, 2000.
- [45] P. Moin, K. Squires, W. H. Cabot, and S. Lee. A dynamic subgrid-scale model for compressible turbulence and scalar transport. *Physics of Fluids*, 3:2746–2757, 1991.
- [46] F. C. Moon. *Chaotic and fractal dynamics: an introduction for applied scientists and engineers*. Wiley, New York, 1992.
- [47] Y. Morinishi and O. V. Vasilyev. A recommended modification to the dynamic two-parameter mixed subgrid scale model for large eddy simulation of wall bounded turbulent flow. *Physics of Fluids*, 13:3400–3410, 2001.
- [48] F. M. Najjar and D. K. Tafti. Study of discrete test filters and finite difference approximations for the dynamic subgrid-stress model. *Physics of Fluids*, 8:1076–1088, 1996.
- [49] Okong’o and D. Knight. Compressible large eddy simulation using unstructured grids: channel and boundary layer flows. Number 98-3315. AIAA Annual Meeting and Exhibit, 1998.
- [50] U. Piomelli, W. H. Cabot, P. Moin, and S. Lee. Subgrid-scale backscatter in turbulent transitional flows. *Physics of Fluids*, 3:1766–1771, 1991.
- [51] U. Piomelli, J. Ferziger, and P. Moin. New approximate boundary conditions for large eddy simulations of wall-bounded flows. *Physics of Fluids*, 6:1061, 1989.

- [52] S. B. Pope. Large-eddy simulation using projection onto local basis functions. In J. L. Lumley, editor, *Fluid Mechanics and the Environment: Dynamical Approaches*. Springer, 2000.
- [53] S. B. Pope. *Turbulent Flows*. Cambridge University Press, 2000.
- [54] F. Porté-Agel, C. Meneveau, and M. B. Parlange. A scale-dependent dynamic model for large-eddy simulation: application to the atmospheric boundary layer. *Journal of Fluid Mechanics*, 415:261–284, 2001.
- [55] W. C. Reynolds. The potential and limitations of direct and large eddy simulations. In J. L. Lumley, editor, *Whither Turbulence? Turbulence at the Crossroads*, volume 357 of *Lecture Notes in Physics*, pages 313–343. Berlin: Springer Verlag, 1990.
- [56] R. S. Rogallo and P. Moin. Numerical simulation of turbulent flows. *Annual Review of Fluid Mechanics*, 16:99–137, 1984.
- [57] S. Shaanan, J. H. Ferziger, and W. C. Reynolds. Numerical simulation of turbulence in the presence of shear. Technical Report Rep. TF-6, Thermosciences Div., Stanford University, Dept. Mech. Eng., Stanford, CA 94305, 1975.
- [58] F. Shakib. *Finite element analysis of the compressible Euler and Navier-Stokes equations*. PhD thesis, Stanford University, 1989.
- [59] J. Smagorinsky. General circulation experiments with the primitive equations, I. The basic experiment. *Monthly Weather Review*, 91:99–152, 1963.
- [60] E. T. Spyropoulos and G. A. Blaisdell. Evaluation of inhomogeneous formulations of the dynamic subgrid-scale model. In M. Y. Hussaini, T. B. Gatski, and T. L. Jackson, editors, *Transition, Turbulence, and Combustion*, volume II, pages 51–60. Kluwer Academic Publishers, 1993.
- [61] K. R. Sreenivasan. On the universality of the Kolmogorov constant. *Phys. Fluids A*, 7:2778–2784, 1995.

- [62] T. Tamura and K. Kuwahara. Numerical analysis on aerodynamic characteristics of an inclined square cylinder. Number 89-1805. AIAA Annual Meeting and Exhibit, 1989.
- [63] C. A. Taylor, T. J. R. Hughes, and C. K. Zarins. Finite element modeling of blood flow in arteries. *Comp. Meth. Appl. Mech. Engng.*, 158:155–196, 1998.
- [64] A. E. Tejada-Martínez and K. E. Jansen. Spatial test filters for dynamic model large-eddy simulation on finite elements. *Communications in Numerical Methods in Engineering*, 2002. In press.
- [65] O. V. Vasilyev. Computational constraints on large eddy simulation of inhomogeneous turbulent complex geometry flow. In C. Liu, L. Sakell, and T. Beutner, editors, *Proceedings of the Third AFOSR International Conference on DNS/LES*, Arlington, Texas, August 2001.
- [66] O. V. Vasilyev and T. S. Lund. A general theory of discrete filtering for LES in complex geometry. In *Annual Research Briefs*, pages 67–82, NASA Ames / Stanford University, 1997. Center for Turbulence Research.
- [67] C. H. Whiting. *Stabilized finite element methods for fluid dynamics using a hierarchical basis*. PhD thesis, Rensselaer Polytechnic Institute, Sep. 1999.
- [68] C. H. Whiting and K. E. Jansen. A stabilized finite element method for the incompressible Navier-Stokes equations using a hierarchical basis. *International Journal of Numerical Methods in Fluids*, 35:93–116, 2001.
- [69] C. H. Whiting, K. E. Jansen, and S. Dey. Hierarchical basis in stabilized finite element methods for compressible flows. *Comp. Meth. Appl. Mech. Engng.*, submitted. SCOREC Report 11-1999, Scientific Computation Research Center, Rensselaer Polytechnic Institute, Troy, NY.
- [70] G. S. Winckelmans, A. A. Wray, and O. V. Vasilyev. Testing of a new mixed model for LES: the Leonard model augmented by a dynamic Smagorinsky term. In *Proc. Summer Program VII (Center for Turbulence Research)*, pages 367–387, Stanford, CA, 1998. Stanford University.

- [71] M. Yaworski. Near-wall modeling in RANSS. Master's thesis, Rensselaer Polytechnic Institute, Dec. 2001.
- [72] Y. Zang, R. L. Street, and J. R. Koseff. A dynamic mixed subgrid-scale model and its application to turbulent recirculating flows. *Physics of Fluids A*, 5:3186, 1993.